Photonic metasurfaces for integrated optical trapping applications

Tomasz Tytus Plaskocinski

A thesis submitted for the degree of PhD
at the
University of St Andrews

2024

Full metadata for this thesis is available in
St Andrews Research Repository
at:
https://research-repository.st-andrews.ac.uk/

Identifier to use to cite or link to this thesis:

DOI: https://doi.org/10.17630/sta/1103

This item is protected by original copyright

This item is licensed under a
Creative Commons Licence

https://creativecommons.org/licenses/by/4.0/

Abstract

Through optical trapping, we aim to replicate the ease and precision of macroscopic level manipulation, such as holding, observing, squeezing, rotating, and probing biological specimens in microfluidic environments. Optical beams access these environments through narrow apertures of bulky and expensive microscopic objectives. These limitations increase the complexity and cost of optical trapping, keeping it out of clinical settings.

To address these constraints, this thesis presents a new biophotonic platform integrating nano- and micro-fabricated optical elements into the microfluidic environment. Arrays of custom parabolic micromirrors are rapidly patterned into glass using CO_2 laser ablation and used to form optical traps. Holographic metasurfaces, flat optical elements capable of arbitrary photonic response, operating in reflection and transmission are used to create optical traps with an equivalent efficiency to commercial microscope objectives. The metasurfaces are then used to generate photonic landscapes with multiple trapping sites without the need for diffractive optical elements.

Very stable 15×15 μm^2 square polymeric membranes are fabricated and decorated with handles for optical manipulation and mirrors. This creates a steerable, microscopic mirror, allowing full control over the delivery and collection of light around samples in the microfluidic chamber without the need for multiple microscope objectives. This is, in turn, used for refractive index sensing by selective planar excitation of a whispering gallery mode laser.

This cross-disciplinary project bridges photonics, material sciences, and biology, enabling the adoption of advanced photonic designs in microfluidic environments, with transformative benefits for microscopy and biophotonic applications at the interface of molecular and cell biology.

Candidate's declaration

I, Tomasz Tytus Plaskocinski, do hereby certify that this thesis, submitted for the degree of PhD, which is approximately 35,000 words in length, has been written by me, and that it is the record of work carried out by me, or principally by myself in collaboration with others as acknowledged, and that it has not been submitted in any previous application for any degree. I confirm that any appendices included in my thesis contain only material permitted by the 'Assessment of Postgraduate Research Students' policy.

I was admitted as a research student at the University of St Andrews in September 2020.

I received funding from an organization or institution and have acknowledged the funder(s) in the full text of my thesis.

Date: 11/09/2024 Signature of candidate

Supervisor's declaration

I hereby certify that the candidate has fulfilled the conditions of the Resolution and Regulations appropriate for the degree of PhD in the University of St Andrews and that the candidate is qualified to submit this thesis in application for that degree. I confirm that any appendices included in the thesis contain only material permitted by the 'Assessment of Postgraduate Research Students' policy.

Date: 11/09/2024 Signature of supervisor

Permission for publication

In submitting this thesis to the University of St Andrews we understand that we are giving permission for it to be made available for use in accordance with the regulations of the University Library for the time being in force, subject to any copyright vested in the work not being affected thereby. We also understand, unless exempt by an award of an embargo as requested below, that the title and the abstract will be published, and that a copy of the work may be made and supplied to any bona fide library or research worker, that this thesis will be electronically accessible for personal or research use and that the library has the right to migrate this thesis into new electronic forms as required to ensure continued access to the thesis.

I, Tomasz Tytus Plaskocinski, have obtained, or am in the process of obtaining, third-party copyright permissions that are required or have requested the appropriate embargo below.

The following is an agreed request by candidate and supervisor regarding the publication of this thesis:

Printed copy

No embargo on print copy.

Electronic copy

No embargo on electronic copy.

Date: 11/09/2024 Signature of candidate

Date: 11/09/2024 Signature of supervisor

Underpinning Research Data or Digital Outputs

Candidate's declaration

I, Tomasz Tytus Plaskocinski, understand that by declaring that I have original research data or digital outputs, I should make every effort in meeting the University's and research funders' requirements on the deposit and sharing of research data or research digital outputs.

Date: 11/09/2024 Signature of candidate

Permission for publication of underpinning research data or digital outputs

We understand that for any original research data or digital outputs which are deposited, we are giving permission for them to be made available for use in accordance with the requirements of the University and research funders, for the time being in force.

We also understand that the title and the description will be published, and that the underpinning research data or digital outputs will be electronically accessible for use in accordance with the license specified at the point of deposit, unless exempt by award of an embargo as requested below.

The following is an agreed request by candidate and supervisor regarding the publication of underpinning research data or digital outputs:

No embargo on underpinning research data or digital outputs.

Date: 11/09/2024 Signature of candidate

Date: 11/09/2024 Signature of supervisor

Acknowledgements

General acknowledgments

Since starting in St Andrews in 2015, my time as a student here is finally ending. I’ve had the opportunity to meet and work with many amazing people who have impacted my life. I want to thank you all here and express how grateful I am for you.

Beginning with Andrea Innocent Di Falco, whom I had the pleasure of working with from my very first year when he was my tutor, followed by many summer projects, and finally, this PhD. He supported me fully every step of the way, with much more patience than I had ever earned. His supervising style allowed me to grow as a person and a researcher, and I’m glad to have chosen St Andrews to work with him. I hope to carry the same passion and curiosity for research that he has demonstrated over all the years I’ve known him.

I would also like to extend my gratitude to Jianling Xiao, whom I have worked closely with for the past couple of years and who has also exhibited tremendous patience. I believe we achieved some incredible results together and taught each other many valuable skills. Her work ethic and enthusiasm have inspired me and repeatedly kept me going over my PhD. I would also like to thank all past and present members of the Synthetic Optics Group, in particular Mohammad Biabanifard, Yuhui Gan and Saydulla Persheyev, Libin Yan, and Meisam Askari. It’s been a pleasure working with you all, you’ve made my time here both interesting and special.

My thanks go to a few staff members who, while not directly involved in my projects, I considered my mentors throughout my PhD. Chris Hooley for our monthly chats, Yoshihiko Arita for all the mentorship in optical trapping, and Graham Bruce and Sebastian Schultz for always having solutions for any problems I could come up with. Next, my thanks go to the cleanroom technicians and the store managers, particularly Scott Johnston.

Finally, my thanks go to the people who have been there for me outside of the University. My flatmates and PhD co-companions Anindya and Aswin looked after our house during my lab disappearances and kept us all going. To my parents, who have shown nothing but love and support from the very first day I started this journey.

To Sofiia, who has been my reason to keep going from the very start.

Place: St Andrews

Date: 11/09/2024 **Tomasz Plaskocinski**

Funding

This work was supported by the EPSRC DTP 2020-2021 University of St Andrews [grant number 2458969]; European Research Council under the Horizon 2020 Framework Programme Research and Innovation Program [grant number 819346].

Research Data/Digital Outputs access statement

Research data underpinning this thesis are available at:

https://doi.org/10.17630/1907da8b-4e1f-4422-aa2c-3928218243fe
https://doi.org/10.17630/e1745c6c-3042-4b14-be26-5506fe2ca247
https://doi.org/10.17630/393b6b47-cca8-40df-b2e7-81ba46fb0cfb
https://doi.org/10.17630/413a0461-d941-43db-bb7f-379dc05ec0bc
https://doi.org/10.17630/e5371e49-ecc5-42f7-9b74-5dcc96011199
https://doi.org/10.17630/7d90ba28-cd6a-4bc5-a4e1-d5a3d7314dd6
https://doi.org/10.17630/3bd2a243-71be-4667-b8ee-ded7be7e472e

Collaboration Statement

I collaborated with Libin Yan, Jianling Xiao, Mohammad Biabanifard, Saydulla Persheyev, Meisam Askari, and Andrea Di Falco from the Synthetic Optics Group at the University of St Andrews on the paper entitled “Two-tier manipulation of holographic information” described in Chapter 2. I assisted with optical setup, characterization, and manuscript preparation.

I collaborated with Jianling Xiao, Mohammad Biabanifard, Saydulla Persheyev, and Andrea Di Falco from the Synthetic Optics Group at the University of St Andrews on the paper entitled “On-Chip optical trapping with high NA metasurfaces” described in Chapter 5. I assisted in the project direction. I built the optical setup and performed the metasurface characterization and trapping data acquisition and analysis. I prepared the draft of the manuscript together with Jianling Xiao.

I collaborated with Yoshihiko Arita, Graham D. Bruce and Kishan Dholakia from the Optical Manipulation Group at the University of St Andrews, Saydulla Persheyev and Andrea Di Falco from the Synthetic Optics Group at the University of St Andrews and Hamid Ohadi from the Quantum Light-Matter Group at the University of St Andrews on the paper entitled: “Laser writing of parabolic micromirrors with a high numerical aperture for optical trapping and rotation” described in Chapter 4. This was a completion of a project begun in 2020 during my Master’s thesis. I modified and automated the CO_2 optical ablation setup for which I also wrote the control software. I characterized and fabricated the majority (300+) mirrors. I performed the trapping experiments, data acquisition, and analysis. I prepared the manuscript draft.

I collaborated with Libin Yan and Andrea Di Falco from the Synthetic Optics Group at the University of St Andrews and Marcel Schubert and Malte C. Gather from the Humboldt Centre for Nano and Biophotonics at the University of Cologne on the publication entitled “Optically manipulated micromirrors for precise excitation of WGM microlasers” described in Chapter 6. I assisted with the membrane fabrication and design, built the optical setup, performed the experiments, and acquired and analyzed subsequent data. I also prepared the manuscript draft.

I collaborated with Mohammad Biabanifard, Jianling Xiao and Andrea Di Falco from the Synthetic Optics group at the University of St Andrews on the paper entitled “ZrO_2 holographic metasurfaces for efficient optical trapping in the visible range” described in Chapter 5. I assisted with data analysis, design of the optical setup and manuscript preparation.

I collaborated with Jianling Xiao, Mohammad Biabanifard, and Andrea Di Falco from the Synthetic Optics Group at the University of St Andrews on the paper entitled "Self-calibrated flexible holographic curvature sensor" described in Chapter 2. I assisted with the metasurface characterization, data analysis, and manuscript preparation.

It’s still magic even if you know how it’s done.

Publications and Awards

Publications Resulting from this Work

- **Tomasz Plaskocinski***, Jianling Xiao*, Mohammad Biabanifard, Saydulla Persheyev, and Andrea Di Falco, "On-Chip optical trapping with high NA metasurfaces", ACS Photonics 10 (5), 1341-1348 (2023). (*Equal Contribution)

- **Tomasz Plaskocinski**, Yoshihiko Arita, Graham D. Bruce, Saydulla Persheyev, Kishan Dholakia, Andrea Di Falco and Hamid Ohadi, "Laser writing of parabolic micromirrors with a high numerical aperture for optical trapping and rotation" Applied Physics Letters 123 (8), 081106 (2023).

- **Tomasz Plaskocinski**, Libin Yan, Marcel Schubert, Malte C Gather and Andrea Di Falco "Optically manipulated micromirrors for precise excitation of WGM microlasers", Advanced Optical Materials, 12 (7), 2302024, (2024)

- Mohammad Biabanifard, **Tomasz Plaskocinski**, Jianling Xiao, and Andrea Di Falco, "ZrO_2 holographic metasurfaces for efficient optical trapping in the visible range", Advanced Optical Materials, 2400248 (2024).

Other Publications

- Libin Yan*, Jianling Xiao*, **Tomasz Plaskocinski**, Mohammad Biabanifard, Saydulla Persheyev, Meisam Askari, and Andrea Di Falco, "Two-tier manipulation of holographic information", Optics Express 30 (11), 19145-19151 (2022). (*Equal Contribution)

- Jianling Xiao, **Tomasz Plaskocinski**, Mohammad Biabanifard, and Andrea Di Falco, "Self-calibrated flexible holographic curvature sensor", Advanced Materials Technologies, 2301851 (2024).

- Yuhui Gan, Jianling Xiao, **Tomasz Plaskocinski**, Saydulla Persheyev, Mohammad Biabanifard, and Andrea Di Falco, "See-through Conformable Holographic Metasurface Patches for Augmented Reality", (under review in Laser and Photonics Reviews, 2024)

Conferences

- **Tomasz Plaskocinski**, Jianling Xiao, Saydulla Persheyev, Mohammad Biabanifard, and Andrea Di Falco, “Photonic Metasurfaces for optical manipulation applications”, European Optical Society Annual Meeting (EOSAM 2022), Porto Portugal. Invited presentation, presented by **Tomasz Plaskocinski**.
- **Tomasz Plaskocinski**, Jianling Xiao, Saydulla Persheyev, Mohammad Biabanifard, and Andrea Di Falco, “Holographic optical metasurfaces with high trap stiffness”, Biophotonics Congress: Optics in the Life Sciences 2023, Vancouver Canada. Presentation, presented by **Tomasz Plaskocinski**.
- **Tomasz Plaskocinski**, Jianling Xiao, Mohammad Biabanifard, Saydulla Persheyev, and Andrea Di Falco, “Holographic Optical Metasurfaces with High Trap Stiffness”, Conference on Lasers and Electro-Optics/Europe (CLEO/Europe 2023) and European Quantum Electronics Conference (EQEC 2023), Munich Germany. Poster, presented by **Tomasz Plaskocinski**.
- **Tomasz Plaskocinski**, Jianling Xiao, Mohammad Biabanifard, Saydulla Persheyev and Andrea Di Falco, “Photonic metasurfaces for biophotonics”, SPIE Nanoscience + Engineering 2023, San Diego United States. Presentation, presented by **Tomasz Plaskocinski**.
- **Tomasz Plaskocinski**, Libin Yan, Marcel Schubert, Malte C. Gather and Andrea Di Falco, “Optically Manipulated Photonic Membranes for Biophotonics”, SPIE Photonics Europe 2024, Strasbourg France, Presentation, presented by **Tomasz Plaskocinski**.
- **Tomasz Plaskocinski**, Libin Yan, Marcel Schubert, Malte C. Gather and Andrea Di Falco, “Photonic Metasurfaces for Biophotonics”, SUPA Annual Gathering 2024, Glasgow United Kingdom, Presentation, presented by **Tomasz Plaskocinski**.
- Jianling Xiao, Libin Yan, **Tomasz Plaskocinski**, Mohammad Biabanifard, Saydulla Persheyev, Meisam Askari, and Andrea Di Falco, “Environment-Dependent Holographic Metasurfaces In The Visible Range”, Conference on Lasers and

Electro-Optics/Europe (CLEO/Europe 2023) and European Quantum Electronics Conference (EQEC 2023), Munich Germany. Presentation, presented by Jianling Xiao.

- Mohammad Biabanifard, **Tomasz Plaskocinski**, Jianling Xiao, and Andrea Di Falco, "High Numerical Aperture ZrO_2 Holographic Metasurfaces for Biophotonics Applications." Photonic technology for biomedical applications, CLEO Europe 2023, Munich, Germany. Presentation, presented by Mohammad Biabanifard.
- Mohammad Biabanifard, **Tomasz Plaskocinski**, Jianling Xiao, and Andrea Di Falco, "ZrO_2 Holographic Metasurfaces for Biophotonics Applications." Metasurfaces and their Applications, META 2023, Paris, France. Presentation, presented by Mohammad Biabanifard.
- Mohammad Biabanifard, **Tomasz Plaskocinski**, Jianling Xiao, and Andrea Di Falco, "High numerical aperture ZrO2 holographic metasurfaces for imaging and optical trapping applications in the visible range", SPIE Photonics Europe 2024, Strasbourg France, Poster, presented by Mohammad Biabanifard.
- Yuhui Gan, Jianling Xiao, **Tomasz Plaskocinski**, Saydulla Persheyev, Mohammad Biabanifard and Andrea Di Falco, "Flexible holographic metasurfaces for augmented reality near-eye display", SPIE Photonics Europe 2024, Strasbourg France, Poster, presented by Yuhui Gan.
- Jianling Xiao, **Tomasz Plaskocinski**, Robert I Hunter, Mohammad Biabanifard, Duncan A Robertson, Graham M Smith, Simon Horsley, Sebastian A Schulz and Andrea Di Falco, "Flexible holographic metasurfaces for shape dependent imaging and curvature sensing", SPIE Photonics Europe 2024, Strasbourg France, Presentation, presented by Jianling Xiao.

Awards and miscellaneous

- Founder and President of the St Andrews Optica Student Chapter and the St Andrews Optics Society. Vice President of the St Andrews SPIE Student Chapter (2022-2024).

- Cover issue of ACS Photonics titled “On-Chip Optical Trapping with High NA Metasurfaces” (2023).
- Recipient of the Caroline Fitzmaurice Trust Award (2023).
- Cover issue of Advanced Optical Materials titled “Optically manipulated micromirrors for precise excitation of WGM microlasers” (2024).
- Founder and main organizer of the 1st Scottish Conference in Optical Technologies (SCOT 2024) in St Andrews United Kingdom (2024).

Table of Contents

CHAPTER 1

Introduction

This Chapter contains the motivational background for this thesis and the broader context. This includes lab-on-chip, metasurfaces, and optical trapping. The Chapter concludes with the thesis structure.

The story of light-matter interaction is almost as old as that of science — seeing is believing! Whether it is through observing how a material absorbs and scatters light, its response to the electromagnetic field, or how the light's properties change throughout the interaction, many of the answers to our questions begin with directing a source of light at the object of interest and recording what happens.

As this object decreases in size, we turn to optical elements to see what our eyes can no longer resolve, and our tools are too large to touch without causing damage. In the case of observing the building blocks of life, such as cells, proteins, and bacteria, we use the microscope objective. This tool allows us to magnify and easily observe the microscopic world, send in light to probe the environment, and touch and sense whatever we please. The variables in this process can be broken down to the **light** we send in through the objective, the sample **environment**, the **sample** itself, and our **detection and data processing methods**.

As the field of biophotonics matured, progress has focused on the light we send into this objective. According to Abbe's principle, imaging resolution is constrained by the diffraction limit of this light, equal to $d = \frac{\lambda}{2NA}$ [1] where d is the minimum resolvable spot size, λ is the light wavelength and NA is the numerical aperture of the microscope objective. This dimensionless number characterizes the range of angles over which the system can accept or emit light. Mathematically, it is defined as

$$NA = n \sin(\theta), \tag{1.1}$$

where n is the refractive index of the medium in which the lens or optical system is working, and θ is the half-angle of the maximum cone of light that can enter or exit the system. The NA is critical in determining the resolving power of an imaging system, with higher values indicating a greater ability to gather light and resolve finer details [1]. Initially, it would seem like all we have to do is decrease the wavelength and increase the NA to achieve the required resolution. However, lower wavelengths result in phototoxicity, while NA cannot be increased over the theoretical value of n. This equation also doesn't account for the many complexities of real-life microscopy, including the low contrast between the medium and samples and scattering through media, which affects both signal strength and resolution [2]. To address these issues at the most basic level, we can control the phase and frequency components of the light, increasing the contrast of the images [3]. Light can be sculpted into complex beams, improving its ability to penetrate deeper into biological samples [4]. Pinholes are used in confocal microscopy to enhance resolution, with spinning disks used to speed up the process [5]. Cylindrical lenses shape light into a sheet, allowing whole volumes to be scanned in seconds [6]. We can go further with active optical elements and use spatial light modulators (SLMs) or digital micromirror devices to shape the beam to adapt to real-time imaging [7]. Furthermore, the momentum of the shaped light itself can be harnessed through optical trapping, allowing for investigation of the most minute forces present at these scales [8].

Next, the environment around the objects of interest can be modified to investigate individual specimens, increase the sensitivity of our measurements, or select a specific signal. Channels on the scale of 100s of microns are used to guide individual cells, which undergo multi-parametric analysis at high throughput rates using flow cytometry [9]. Biomolecules such as deoxyribonucleic acid (DNA) can be immobilized next to resonant structures [10] or particles to increase the signal by up to a factor of 10^{11} [11] in surface-enhanced Raman spectroscopy. Another sensing avenue is photonic crystals, engineered materials designed to control light propagation through periodic variations in the dielectric constant. The exact period of these variations results in the formation of a photonic bandgap, meaning only select wavelengths can pass through the crystal. This enables selective reflection, guidance, or total suppression of light across distinct wavelength ranges [12]. They can slow down the light near the samples, increase the light-matter interaction time [13], and achieve directional emission, increasing the signal-to-noise ratios [14] (SNRs).

The samples can also be labeled for precise measurements and tracking over long periods. One of the best-explored labeling modalities is the use of fluorophore reporters, which can be excited at a specific wavelength and re-emit at another, separating the pump beam from the data collected through dichroic mirrors [2]. The fluorophores can be designed to bind to the object of interest, or living organisms can be genetically modified to produce them internally [15]. The precision of measurements can be increased through fluorescence resonance energy transfer — by tagging objects with multiple types of compatible acceptor and donor fluorophores, molecular interactions on the scale of < 10 nm can be measured [16]. Techniques using blinking fluorophores activated at different wavelengths, such as photoactivated localization microscopy and stochastic optical reconstruction microscopy [17], increase the imaging resolution past the diffraction limit [18]. Fluorophores also play a crucial role in experiments where the evolution of the cell over time is tracked. They enable optical barcoding, where combinations of genetically expressed reporters are used to track lineages of cells [19]. Another method for modifying the samples is through using radially symmetric resonators such as toroids, rings, and spheres. Through phagocytosis, these resonators can be embedded in cells [20], allowing for simultaneous barcoding and tracking of thousands of cells over days [21, 22] as well as direct sensing of intracellular forces [20]. This is enabled through their exceptional sensitivity to changes in their shape [23] through whispering gallery modes (WGM), which exist in the boundary between the resonator and its environment.

All these methods culminate in the last part of the process — detection of the light received back after interacting with the samples. Event-driven microscopy is used to preserve the ‘photon budget’ [24] of the samples, where wide-field imaging is combined with single-molecule imaging techniques through machine learning, meaning that samples are exposed to less light, allowing them to preserve the fluorophores [25].

One object remains constant in each of these studies: the microscope objective. While not problematic in isolated research contexts, the transition of these methods from laboratory to real-world applications is hindered by the objective’s cost, fragility, and size. High-quality objectives, often costing thousands, are susceptible to damage and are significantly larger than their subjects, limiting interaction. As the number of objectives grows, so does the complexity of setup alignment and the challenge of sample positioning, keeping many innovative methods confined to optical labs and beyond the reach of many biologists and healthcare professionals.

This work aimed to develop methods for replacing the microscope objective or providing additional functionality. It combines two complementary modalities of light-matter interaction: optical manipulation, where structured light is used to control matter, and metamaterial design, where structured matter is used to control light. In this thesis, a specific two-dimensional (2D) subset of metamaterials — holographic metasurfaces (HMSs) — is used. HMSs consist of arrays of sub-wavelength structures known as meta-atoms. These meta-atoms’ size, shape, arrangement, and composition are engineered to produce the desired electromagnetic response, such as changing the polarization, phase, or amplitude of the light passing through or reflecting from them.

The overview of this work is summarised in Figure 1.1, showing (HMSs) and microstructures engineered to efficiently focus light in a manner equivalent to a high NA microscope objective. The HMSs are used to trap individual particles and more complex extended objects. Also shown are polymeric membranes, which extend the microscopes' ability to deliver and collect light to samples inside the microfluidic chamber, with all of the work striving towards a fully integrated on-chip platform for biological sample analysis.

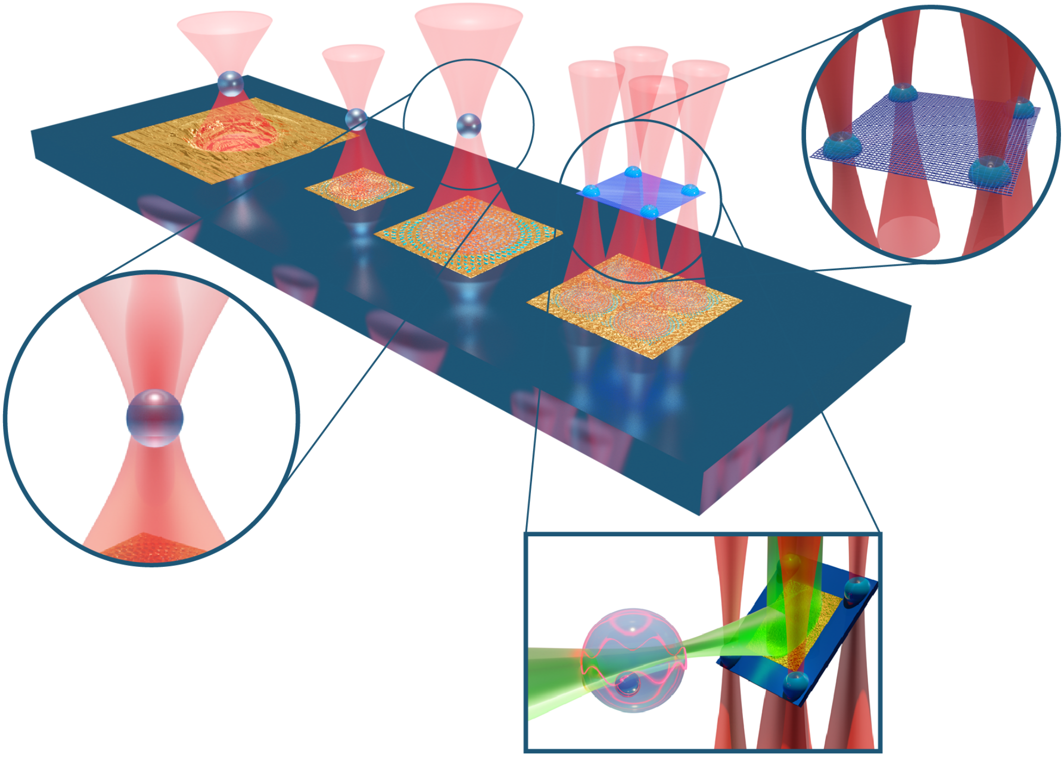

Figure 1.1 Concept design for using microstructures and HMSs to enhance or replace the microscope objective. HMSs are used to trap particles and extended objects such as polymeric membranes. Each membrane has handles allowing for easy control, and a HMS is patterned on top of it.

1.1 Lab-on-chip

Integration and miniaturization have driven the modern technological revolution [26]. This is most clearly embodied by the smartphones in our pockets, comprising a mobile phone, camera, personal computer, navigation system, and portable media player into a compact, highly integrated device. This is primarily enabled by the rise of the system-on-chip technology, which places the processing units, memory, and input/output ports into a single microchip when, just a few decades ago, the same architecture would fill a room. The result is a device where the end user can access the full computational power through a simple interface without necessarily understanding how the individual components function [27].

Lab-on-chip systems strive to give the user the full capability of a biological and chemical 'lab' in a compact form factor. A drop of analyte can be presented, and the required information can be read in minutes in a manner similar to a home pregnancy test [27]. It is an interdisciplinary field, combining the work of physicists, biologists, chemists, and engineers into a cheap, simple device that anyone can use. One of the first lab-on-chip systems was fabricated in 1979 at Stanford and was a gas chromatography chip [28], while the most recent high-profile example was the lateral flow tests used during the COVID-19 pandemic [29].

The lab-on-chip platform is closely linked with developing integrated circuits and microelectronics [30]. Together with the invention of the transistor in 1947 [31], photolithography was a key process used in the miniaturization and creation of on-chip systems. Shown in Figure 1.2, it allows for precise patterning of substrates, including the silicon crystal that would go on to create the first-ever integrated circuit [32].

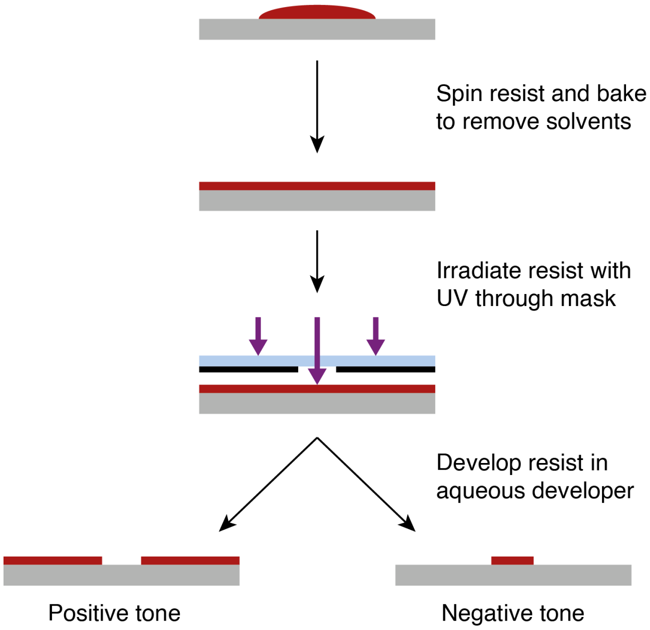

Figure 1.2 A standard procedure for photolithography is outlined as follows: The process begins with the application of a photoresist layer onto the substrate, then by spinning it to reach the required thickness. This step is followed by a heating process that eliminates any solvents present. Subsequently, the resist undergoes exposure to ultra violet (UV) light through a photomask. In the case of negative tone photoresists, the development stage removes areas that were not exposed to the radiation, whereas for positive tone photoresists, the unexposed areas remain intact. Adapted from [33].

As fabrication technologies matured, the channels and valves comprising lab-on-chip systems could be fabricated on the scales of hundreds of nanometers. They could deliver picolitres of fluids through compact chambers, simplifying and parallelizing analysis. This minuscule volume has multiple advantages, primarily through enforcing a predictable laminar flow within the fluid passing through the channels, giving exact control over the position and velocity of analytes [34]. The use of materials such as silicon [35, 36], glass [36], which can be machined and etched, and polydimethylsiloxane (PDMS), cast into arbitrary shapes with molds made using photolithography [37], has been pivotal in this development. The use of PDMS microfluidics introduced sophisticated systems with reconfigurable 3D channels and valves, further enhanced by innovations like paper microfluidics, which utilize capillary action for fluid transport [38].

Implementing such small volumes is also particularly beneficial for handling scarce samples. The precise control over the analytes extends to the development of organ-on-chip systems, where cell cultures grown directly on the device mimic the physiological conditions of blood cells moving through veins, and optofluidics, which makes use of the laminar flow to guide light and analytes concurrently [27]. Understanding fluid physics at these scales, exemplified by the Reynolds number (Re), reveals how reduced system dimensions favor a laminar flow regime characterized by predictable flow patterns and diffusion-based molecular transport instead of the turbulent mixing seen in larger-scale systems. This principle underpins the efficient design and operation of lab-on-chip devices [39]:

$$Re = \frac{\rho \nu L}{\mu}, \tag{1.2}$$

where ρ is the fluid's density, ν its velocity, L the characteristic linear dimension of the system, and μ the dynamic viscosity. In such systems, laminar flow simplifies modelling efforts and enhances the predictability and efficiency of molecular interactions and analyses [33].

Waveguides are now commonly used to deliver and collect light efficiently, maximizing the interaction with analytes [40]. Furthermore, the incorporation of photonic crystals has been pivotal in increasing the contact time of light with analytes, substantially improving the detection sensitivity of these systems [41]. The development of optofluidic cavities and surface plasmon resonance sensors represents a leap forward, offering strong light confinement for sensing, lasing, and nonlinear optics applications alongside high sensitivity for biomolecular detection [42]. Microfluidics can be coupled with light-sheet microscopy to obtain full three-dimensional (3D) imaging of cells at high-throughput rates [43]. Additionally, introducing digital microfluidics with integrated optics has opened new avenues for manipulating light and conducting high-throughput screening and analysis [44]. As the system scales down even more, we turn to components that give a tailored photonic response, such as HMSs [45, 46, 47].

1.2 Metasurfaces

As new frontiers are reached, we discover new methods of manipulating the very light we use as a probe, controlling its spatial and temporal properties through lenses, polarisers, waveplates, and materials that give nonlinear responses. In all these cases, we rely on the intrinsic properties of materials from which we manufacture these optical elements from, such as their refractive index and crystalline structure. With the revolutionary discovery of lasers in 1960 [48], demand has grown for greater control over light. Diffraction limits hold back traditional optics along with a lack of tunability, intrinsic optical aberrations, and bulky size. [49]

The solution to these problems comes from electromagnetic metamaterials (EMM). These comprise sub-wavelength-sized and spaced metallic [50] and/or dielectric [51] structures that couple to the incoming electromagnetic field. These EMM building blocks are commonly referred to as meta-atoms. Their size, composition and shape allow for controlled manipulation of the electromagnetic field response not possible in natural materials [52]. This may initially seem similar to the well-established field of composites, where two or more distinct constituents are used to create a new material with improved and unique properties, but there are two key distinctions. The first is that the EMM derives its properties from both the composition of the meta-atoms and their physical architecture [53] resulting in properties not found in the constituent materials [54]. The other key difference with EMM lies in the scale of the meta-atoms being considerably smaller than the wavelength of the incoming field in free space, at which point the structure is deemed an effective medium. This homogenization of the EMM allows for the definition of effective constitutive parameters, such as electric permittivity ε and magnetic permeability μ, to describe these artificial structures [55].

While one of the first theoretical use cases was proposed by Viktor Veselago in 1968 [56], in his consideration of material with negative permittivity and permeability resulting in a negative refractive index $n = \sqrt{\varepsilon\mu}$, the first experimental realization of an EMM did not occur until 2001 when Shelby *et al.* observed negative refraction in microwaves [57]. Aided by nanofabrication techniques, the first optical EMM with a real part of the refractive index of -0.6 at a 780 nm wavelength was realized by Soukoulis *et al.* in 2007 [58].

This has since led to surpassing of the diffraction limit through superlenses [59, 60] based on negative refraction, as well as zero-index materials [61], perfect absorption [62] and tunability [63].

These early EMMs, while revolutionary in their ability to control light, were not without their faults. To achieve this control, they used metals and resonant responses, leading to dispersion and losses [64]. While progress has been made since through the use of all-dielectric EMM [51] and metal EMM design can be optimized for higher efficiencies, fabrication at scales required for optical response is also a significant challenge, as most nanofabrication systems are not well suited for 3D fabrication [65].

HMSs — a subset of EMM, — allow for much of the similar ability to control the properties of light while greatly simplifying the fabrication and reducing the bulk. [66] This is due to HMSs being made of meta-atoms arranged into an optically thin layer. Unlike metamaterials, which focus on the effective permittivity and permeability of the homogenized medium, HMSs aim to control the phase, amplitude, and polarisation through engineering boundary conditions that the electromagnetic field must obey. One of the first examples of this was shown experimentally by Capasso *et al.* [67], who expanded Fermat's principle to consider a sudden phase shift between two media, as shown in Figure. 1.3 and arrived at a general Snell's law of the form:

$$n_t \sin(\theta_t) - n_i \sin(\theta_i) = \frac{\lambda_0}{2\pi}\frac{d\phi}{dx}, \tag{1.3}$$

$$\sin(\theta_r) - \sin(\theta_i) = \frac{\lambda_0}{2\pi n_i}\frac{d\phi}{dx}, \tag{1.4}$$

where n_t and n_i are the refractive indices of the two media, λ_0 is the vacuum wavelength, θ_i, θ_r and θ_r are respectively the angle of incidence, reflection, and transmission and $\frac{d\phi}{dx}$ is the phase gradient. This meant that as long as the phase discontinuity was correctly engineered, an arbitrary angle of reflection and transmission could be demonstrated. They then went on to show that this is possible by constructing gold V-shaped resonant elements supporting symmetrical and anti-symmetrical modes. By changing the length size and orientation of the resonators, they achieved full 2π phase modulation over the incoming light and demonstrated anomalous refraction. A detailed explanation of this phase control scheme can be found in Chapter 2.

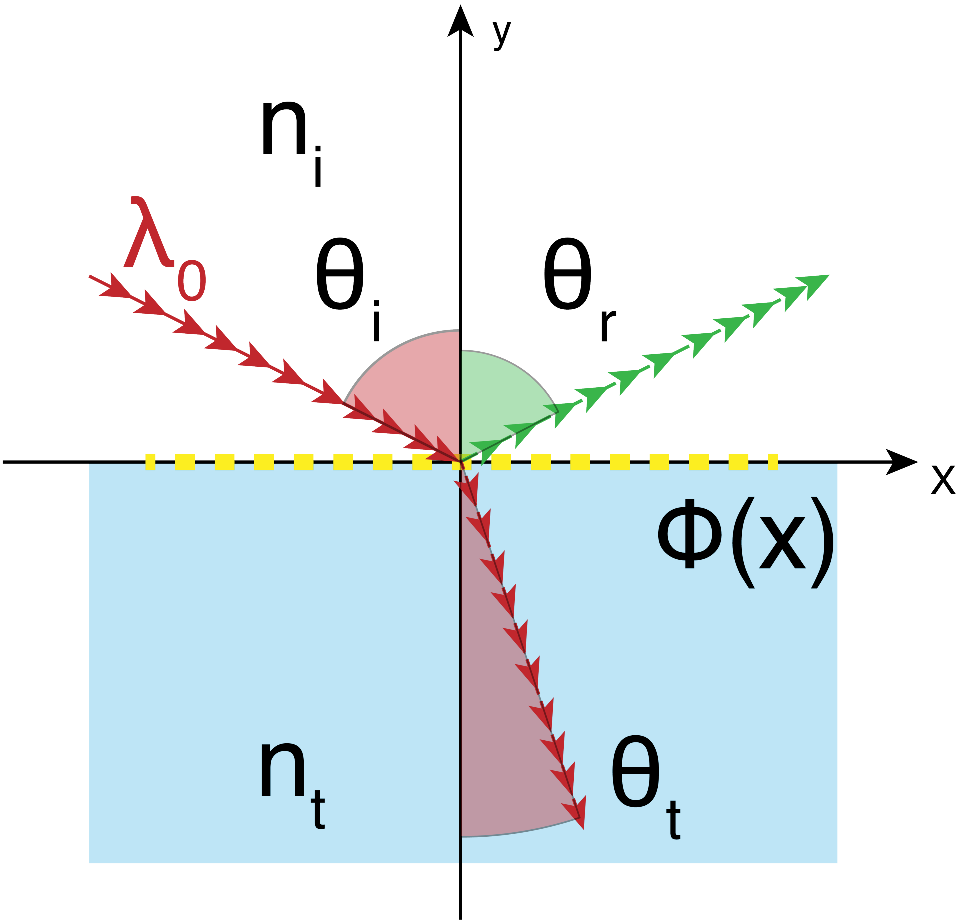

Figure 1.3 Diagram used to demonstrate generalised Snell's law. Adapted from [67].

Since then, the field of HMSs has proliferated, with demonstrations of applications of holograms [68, 69] and holographic encryption [70, 71], flat lenses [72] and active beam steering [73, 74]. The HMSs can be made flexible [75, 76, 77, 78], adding a degree of freedom to the applications. These flexible HMSs can be tuned using micro-electromechanical systems (MEMS), resulting in adaptive optics [79]. Similarly, liquid crystals [80], voltage-sensitive materials such as indium tin oxide (ITO) [81], and 2D materials such as graphene [82] are incorporated into HMSs for refractive index tunability.

These qualities make HMSs an appealing candidate in biophotonics applications, such as biomolecule sensing [83]. HMSs can be integrated with and enhance existing imaging techniques such as confocal microscopy [84] and broadband super-resolution imaging [85]. They can be patterned on endoscopes for optical coherence tomography [86]. Furthermore, HMSs can focus multiple wavelengths at the same distance for two-photon microscopy [87], allowing for efficient excitation and collection of signals from samples with a single objective. Chiral HMSs have significant potential in the sensing of chiral biomolecules [88], a crucial process for identifying the pharmacological effects and toxicity that differ between biomolecules of varying handedness [89]. HMS-based lenses with NA ~ 1 have been demonstrated [90], making them an ideal candidate for replacing the microscope objective.

There are two properties of HMSs we want to focus on in this body of work. The first is the HMSs' ability to generate arbitrary aberration-free holographic images that can be used to create a complex optical field [91]. The second is the ability to control the transfer of momentum of light, which is the fundamental concept behind optical manipulation.

1.3 Optical Manipulation

Ever since the demonstration of the single beam gradient force trap by Arthur Ashkin in 1986 [92], optical manipulation has been at the forefront of biological and atomic physics — a versatile tool capable of anything from measuring forces exerted by proteins [93], cells [94] and DNA [95], to cooling atoms for quantum computing [96] and atomic clocks [97].

One of the most compelling examples of physical light-matter interaction is through optical trapping, whereby focusing a coherent laser focused by a high NA objective, microscopic objects can be freely manipulated in 3D space as they oscillate around the beam waist, typically inside a dampening medium such as water [98]. The particle is trapped in equilibrium and experiences a combination of the scattering force, the gradient force, and Brownian motion due to the constant bombardment of molecules comprising the medium around it. The overall motion is comparable to an overdamped simple harmonic oscillator, as shown in Figure 1.4, with a restorative force:

$$F_{trap} = -k_{trap}x, \tag{1.5}$$

where x is the displacement from the equilibrium position and k_{trap} is the equivalent of the spring constant, referred to as the trap stiffness of the system, and is on the order of $pN/\mu m$ [99].

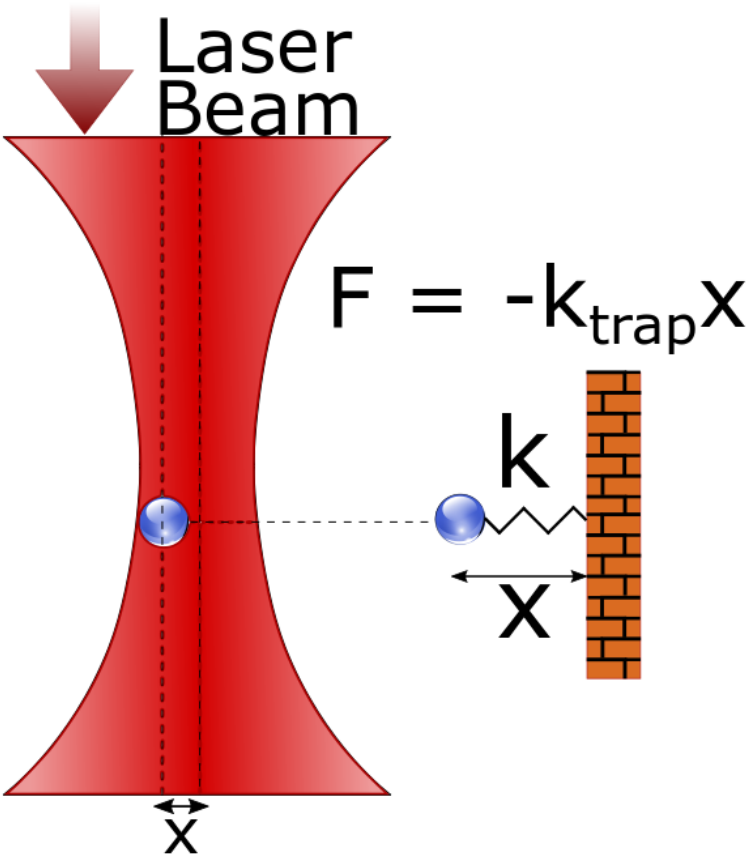

Figure 1.4 Simplified model of the force experienced by an optically trapped particle in a medium of lower refractive index than that of the particle, where k_{trap} is the trap stiffness.

When used in a biological context, typically, the object trapped by the laser is a glass or latex sphere. The sphere is attached by a tether to the molecule of interest and used as a handle, with changes to its motion indicative of a force exerted by the molecule [100]. The most common use for optically trapped particles in a biological context is through single-molecule force spectroscopy [101] — along with magnetic tweezers [102, 103, 104] and atomic force microscopy [105, 106] it allows for precise measurement of physical properties of biological molecules. Another common use case is embedding the particle inside a cell's cytoplasm [107] or even nucleus [108, 109] for rheology measurements.

The isotropy of the sphere allows us to predict its movement and solve for the forces it experiences analytically [99]. Limitations exist regardless of the strength of the trapping beam; the Brownian motion of the sphere introduces an impenetrable noise floor along with a measurement delay, making it necessary to wait up to seconds for the motion of the particle to average out [110].

Optical trapping can be realized across a range of particle sizes, typically with a diameter on the same order of magnitude as the trapping laser wavelength. These limitations can be surpassed by combining optical trapping with other techniques. When larger objects need to be trapped, the technique is combined with acoustic tweezers [111], and near-field plasmonic tweezers are used to trap nano-sized particles [112, 113, 114, 115, 116].

On-Chip Optical Manipulation

As Chapters 4 and 5 will be dealing with on-chip trapping, it is key to establish that the single gradient trap is not the only way to implement optical trapping. Counter-propagating beams have been used from the technique's inception [117]. More sophisticated geometries, such as the optical stretcher, have also been used to distinguish cancerous cells from healthy ones through force measurements alone [118]. Microfluidics can be integrated for high throughput particle and cell sorting [119], with some examples shown in Figure 1.5.

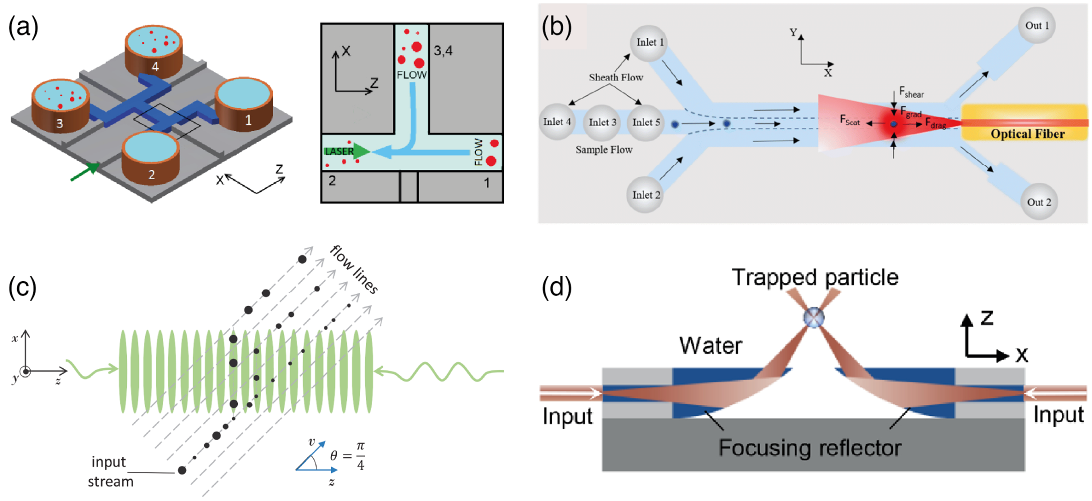

Figure 1.5 Examples of on-chip optical manipulation. (a) shows channels combining optical trapping and optofluidics for direction of particles. Taken from [120] (b) shows an example of hydrodynamic tweezers used to redirect particles after keeping still for analysis. Taken from [121]. (c) Shows an example of passive sorting of particles of different sizes and refractive indices. Taken from [122]. (d) Shows free-space optics being used to trap particles on-chip for analysis. Taken from [123].

Advanced nanophotonics techniques have also been applied to optical trapping through HMSs. HMSs have been used to produce complex beams which allow for exertion of anomalous lateral forces [124], spinning particles using angular momentum generated by the HMS [125], and traps with arbitrary depth of focus [126]. A range of HMSs have been used for optical trapping without the need for a microscope objective [127, 128, 129], including HMSs patterned on top of optical fibers [130], A recent full review of HMSs for optical trapping can be found at ref. [131]. More intricate optical fields can also be created to manipulate multiple particles as well as more complex objects.

Optical Manipulation of Extended Objects

Much of this thesis is based around the optical manipulation and use of microscopic membranes for interaction with biological samples, as outlined in Chapter 6. Several advanced techniques exist nowadays to trap multiple objects, including using time and polarisation shared traps [132], speckle tweezers [133], and trapping with structured light [134]. The last is most often facilitated by the use of digital micromirror devices [135] and SLMs, first demonstrated by Grier *et al.* [136].

Given the ability for several points in the trapping plane to be controlled, the field of optical trapping began to progress towards more complex objects than just polymer and glass spheres with the advent of microtools and micromachines. Spheres were great force probes but their ability to interact with other objects in the microfluidic chamber was limited. Over the past decade, there has been an increased interest in creating optically manipulated micromachines capable of complex interactions with the biological samples inside the chamber [137].

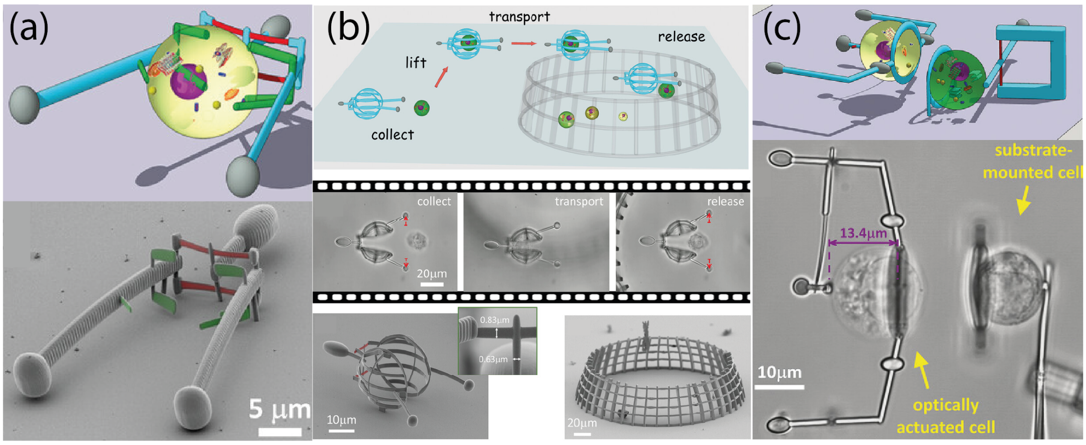

Figure 1.6 Examples of optically steerable microrobot designs: (a) was employed for generating a natural convection flow in a closed microfluidic channel [138], (b) can be used for cell maneuvering [139], while (c) and (d) can be used to interact with cells directly. Taken from from [140].

Optical trapping can easily result in heating the medium surrounding the trapped object by light absorption. To address this, force probes capable of interacting with samples far from the trapping site have been demonstrated [141]. Some examples are shown in Figure 1.6. Optically controlled microrobots have been shown capable of delivering biological samples to different parts of the microfluidic chamber [140], waveguides for tip-enhanced Raman scattering [142], and structures capable of converting the scattering force of light to an angular torque [143, 144, 145]. Currently, most such microtools are made using two-photon polymerisation [140], where a pulsed laser is scanned through a photosensitive resist containing two-photon chromophores, which emit at a wavelength the photoresist is sensitive to, leading to cross-linking [146].

Over the remainder of this thesis, I will present the inherent synergy of lab-on-chip techniques, HMSs, and optical trapping of particles and extended objects.

1.4 Thesis Summary and Structure

The three key outcomes of this thesis are:

1. Creation of static optical trapping landscapes using microstructures and HMSs, reducing the need for multiple objectives during the microfluidic analysis of cells, and particle and cell sorting as well as other lab-on-chip applications.
2. Creation of optically controllable micro-optical elements, which allow for delivery and collection of light anywhere in the microfluidic chamber.
3. Foundational work towards the use of these same elements for extremely sensitive force measurements of DNA denaturation and supercoiling.

The first Chapter of this thesis describes the motivation behind this work. The second Chapter focuses on the background theory behind the optical trapping of individual particles and the holographic optical trapping of complex objects. The principles behind reflective and transmissive HMSs are then explained, along with the design strategies for the individual meta-atoms and holograms these HMSs form. Examples of HMS applications developed throughout this thesis are discussed. These include HMSs for curvature sensing and encoding multiple images into cryptographic HMSs (where each image can only be accessed using a combination of the correct wavelength and medium refractive index). Then, in the third Chapter, the fabrication of the microscopic membranes used in Chapter 6 as in-situ optics and force probes is covered. Also covered is the development of the optical trapping system, fluorescence detection, and imaging used in the following experiments needed to manipulate them. This includes the details of the software used to steer the holographic optical tweezers, the software used to analyze the particle motion, sample, and microfluidic chamber design and preparation, and the principles of data analysis underpinning this thesis. The design and components of a separate complex optical setup built for precise force measurement are described. The setup consists of an optical trapping system integrated with a commercial microscope, a homodyne interferometer, and a stable optical trapping system designed to calibrate the integrated system.

The next section of the thesis deals with structuring materials for an arbitrary photonic response to replace the microscope objective for optical trapping applications. This is used to create arrays of optical elements that perform the trapping function. Two approaches to this are explored, one with fabrication on the scale of tens of microns and the other on a scale of tens of nanometers. Both approaches resulted in a publication. The first approach, described in the fourth Chapter, uses rapid carbon dioxide (CO_2) laser ablation to create $\sim$ 60 µm diameter parabolic cavities in glass, which serve as parabolic mirrors following gold deposition. The advantages of this platform include ease of fabrication, the ability to tune the trapping parameters through adjustment of fabrication parameters, and a broadband photonic response. The fabrication and characterization of the micromirrors are covered, including the automated ablation setup and multiple methods of characterization of the micromirror profile and optical trapping performance compared to a microscope objective. To demonstrate the ability to preserve the original characteristics of the incoming light, such as angular momentum, this platform is used to rotate a birefringent particle using the objective, then reverse the direction of rotation by using light reflected from the micromirror. The second approach, described in the fifth Chapter, uses HMSs of sizes ranging from 315×315 µm^2 down to just 30×30 µm^2 to achieve trapping with equivalent efficiency to an NA = 1.2 microscope objective. For this purpose, HMSs with NA ranging from 0.9 to 1.3 were designed, fabricated, and characterized by trapping the same 2 µm particle. The best performance is seen in 1.2NA HMSs, which are fabricated in various sizes and systematically characterized. The full capability of the HMSs is then demonstrated by trapping an extended object (a polymeric net measuring 15×15 µm^2) using an optical trapping landscape created by a single HMS, a feat typically requiring an SLM. Approaches for trapping using HMS operating in both reflection and transmission are demonstrated. The design of a microfluidic chamber used to flow and trap the polymeric nets is also discussed, along with some preliminary results.

Inspired by the microtools, the sixth Chapter of this thesis describes the work undertaken using square polymeric membranes with optically trappable handles at each corner, which give complete control over the membranes' 3D position, tilt, pitch, and yaw. As the membrane is a flat canvas, it can decorated with arbitrary optical elements such as mirrors or HMSs. Three experiments using the membranes are presented, each using the membranes decorated with a reflective gold layer acting as a mirror. The mirror-decorated membranes are used as *in-situ* optical elements, placed in a microfluidic chamber with optically active beads, and used to illuminate them at arbitrary angles, which can typically only be achieved when multiple objectives are used. The first optical phenomenon explored using this geometry is refractive index sensing using WGM microlasers. The microlasers are 15 µm polystyrene beads, which lase along one plane when excited with a pulsed nanosecond source. This results in a single WGM mode that probes the microlaser's interface and the surrounding medium. Using a combination of a WGM laser on a glass substrate and an optically trapped steerable mirror membrane, this WGM plane is changed by altering the illumination angle, and we show the ability to probe both the refractive index of the glass substrate as well as that of the water surrounding the microlaser. Furthermore, we demonstrate the ability to probe the refractive index around the microlaser by performing a time-resolved experiment where the microlaser illuminated by the membrane micromirror is orbited by a polystyrene bead, resulting in a detectable change in the local refractive index. The experiment setup and geometry are described, along with data analysis methods. The second optical phenomenon explored is that of a photonics jet, where the incoming light is focused using a microscopic dielectric sphere. A high field enhancement at the focal spot is achieved when using a beam with a waist size close to the diameter of the focusing sphere. The mirror membranes steer this photonics jet to selectively excite nitrogen-vacancy nanodiamonds embedded in TiO_2 spheres. The light emitted by the nanodiamonds is then redirected towards the microscope objective using a second mirror membrane. The experiment geometry, collected spectra, and experimental procedures are discussed. Finally, optical trapping from an arbitrary angle is shown by redirecting the trapping beam using a membrane micromirror.

The eventual goal of optical trapping and HMS integration is for applications in biological experiments, and the preliminary work to that end is shown. Two experiments are proposed to explore the mechanical breaking of the bonds in the DNA helix, replicating the enzymatic activity of helicase and measuring the forces involved. The first proposed experiment focuses on another advantage of the polymeric membrane form factor, the significantly dampened motion in the z-direction, as demonstrated in recent work [147]. This dampening means that force measurements can be more finely resolved and taken more quickly as the membrane reaches an equilibrium position much faster than a spherical bead. The second proposed experiment is based on another way in which DNA will unwind its helix through supercoiling. Supercoiling occurs as the DNA tightens or loosens its helical turns beyond a relaxed state, resulting in torque applied to the helix's sections, making it easier to split. To mechanically induce this supercoiling, paddle-like microtools were designed and fabricated. The design of these paddles allows them to convert the linear momentum of light into an angular torque, and the experimental rotation of the paddles is demonstrated. The next step is to attach these paddles to functionalized DNA strands. The thesis ends with a discussion of the work done.

The thesis is split into 8 Chapters:

- Chapters 1 and 2 introduce the key motivation for this thesis and background physics of optical trapping and HMSs required to understand the thesis.
- Chapter 3 describes the fabrication methods as well as the optical setup used for the experiments.

- Chapter 4 covers a published result on fabrication and trapping using micromirrors.
- Chapter 5 covers a published result on using HMSs to trap particles and extended objects.
- Chapter 6 covers a published result on using holographic optical tweezers to manipulate polymeric membranes and decorate them as *in-situ* optics. It also contains preliminary work on the use of the membranes as sensitive force sensors, and fabrication of micropaddles for DNA supercoiling.
- Chapter 7 is the conclusion.

CHAPTER 2

Background and Theory

This Chapter will focus on the basics of the two overarching themes behind this thesis: optical manipulation and metasurfaces.

I will cover the theory behind optical manipulation, the forces involved at the different wavelength scales, force measurement, and calibration methods, as well as the basics behind MS. Here, I describe in detail the method used in this thesis for all of the optical trapping data analysis, based on the power density spectrum analysis. The methods used to generate complex optical patterns using diffractive optical elements for holographic optical tweezers are described, focusing on the superposition of lenses and gratings algorithm used in trapping complex objects. More sophisticated hologram generation using the Gerchberg-Saxton algorithm (GSA) behind all HMSs used in this work is summarised. The theory behind the working principles of HMSs is described, their many applications, and the HMS design process and the difference between different types of HMSs used throughout this thesis. While I have not been designing HMSs during this work, these details are required to follow the thesis and for completeness.

2.1 Optical Manipulation Theory

At the core of optical manipulation is the interplay between two distinct types of forces acting on a trapped object (typically a glass, latex or polystyrene sphere) when exposed to incident light in a context where the medium's refractive index is lower than that of the particle. A non-conservative force, referred to as the scattering force, arises from the reflection of photons off the particle's surface, manifesting as radiation pressure. This phenomenon was theorized by Kepler as far back as 1619 [148] to explain the formation of comet tails. The force is deemed non-conservative as it does not conserve the system's mechanical energy but instead imparts momentum to the particle, pushing it away from the light source.

The balancing force is a conservative one, known as the gradient force. This force opposes the scattering force by drawing the particle back towards the laser's focal point [99]. The conservative nature of the gradient force means it derives from a potential energy gradient within the field, working to minimize the system's potential energy and thus conserving the system's mechanical energy.

An important consideration for optical manipulation is also the medium the particle is surrounded by, as it determines the refractive index contrast as well as the Brownian forces incident on the particle. While optical trapping can be performed in different environments (including air and vacuum) and has gained attention in recent years due to its applications in studying fundamental physics [149], the work in this thesis will focus on optical trapping in liquid media. The use of a commonly preferred wavelength of 1064 nm for optical trapping can lead to increased heating when working with water. In such instances, opting for heavy water D_2O is advantageous due to its lower absorption than regular water across typical trapping wavelengths. Research by Peterman *et al.* [150] has underscored that heating the medium around a trapped object significantly influences experimental outcomes. It harms biological specimens being investigated, alters the thermal motion of the trapped bead, and decreases the medium's local viscosity. This choice becomes even more apparent when we consider the full equation of the one-dimensional motion of a spherical particle inside of a viscous medium, described by the Langevin equation [151]:

$$m\ddot{x}(t) + \gamma_0 \dot{x}(t) + k_{trap} x(t) = \sqrt{\frac{2k_B T}{\gamma_0}} \eta(t), \tag{2.1}$$

where $x(t)$ represents the trajectory of the Brownian particle, $m\ddot{x}(t)$ is related to the particle's inertia and is negligible at high acquisition speeds, $k_{trap}x(t)$ the force exerted by the optical trap, and $\sqrt{\frac{2k_B T}{\gamma_0}}\eta(t)$ a random Gaussian process symbolizing Brownian forces at absolute temperature T, with $\eta(t)$ being white noise satisfying:

$$(\langle \eta(t) \rangle = 0) \text{ and } (\langle \eta(t)\eta(t') \rangle = \delta(t - t')), \tag{2.2}$$

for all t and t' and γ_0 is the drag coefficient given by the Stokes relation:

$$\gamma_0 = 6\pi\rho\nu r, \tag{2.3}$$

where $\rho\nu$ is the dynamic viscosity of the medium, and r is the radius of a spherical particle. The consequence of this relation is that the system will reach an equilibrium over a sufficiently long time, t, setting the right-hand side of the equation to 0. As this term depends on the trapping medium's temperature, keeping the additional heating due to light absorption as low as possible is paramount. The particle size also plays an important role — not only are small particles more affected by the surrounding medium, but the way in which we treat the optical forces will depend on the relative sizes of the particle and trapping wavelength.

Optical Forces and Trapping Regimes

The way optical forces affect the particle depends on the particle size relative to the wavelength λ of the laser used to trap it. There exist three regimes: the Mie regime, where the particle size is on the order of multiple wavelengths; the Rayleigh regime, which relies on the particle being much smaller than the wavelength of the light; and finally, the Mie-Lorentz regime, where the wavelength and particle size are comparable. Most of the trapping described in this report relies on the latter. Although it is significantly more mathematically complex, requiring multipole wave expansion and electromagnetic wave theory (which is outside the scope of this work [152, 153]). A sufficient understanding can be gained from examining the Mie and Rayleigh regimes.

Mie Regime

Employing a ray optics framework, as depicted in Figure 2.1, we analyze the interaction of photons with a spherical particle within the Mie regime, treating the particle as a refracting lens. Each photon incident upon the particle possesses momentum $\hbar k$, where k is the wavenumber, and $\hbar$ represents Planck's constant divided by 2π. This interaction involves reflection and refraction, given the particle's higher refractive index than the surrounding medium, leading to changes in the photon momentum's direction and magnitude. According to the momentum conservation principle, this results in an equivalent and opposite change in the particle's momentum. Notably, the particle experiences a net force directed towards areas of higher intensity due to uneven momentum change, especially in the transverse direction. Moreover, in the axial direction, the highest intensity region, typically the beam's focal point, the light exerts an attractive force on the particle. This dynamic is quantified through the scattering (F_S) and gradient (F_G) forces, as formulated by Ashkin *et al.* [154]:

$$F_S = \frac{n_m P}{c}\left[1 + \frac{R\cos 2\theta - T^2\left(\cos\left(2\theta - 2\epsilon\right) + R\cos 2\theta\right)}{1 + R^2 + 2R\cos 2\epsilon}\right], \tag{2.4}$$

$$F_G = \frac{n_m P}{c}\left[R\sin 2\theta - \frac{T^2\left(\sin\left(2\theta - 2\epsilon\right) + R\sin 2\theta\right)}{1 + R^2 + 2R\cos 2\epsilon}\right], \tag{2.5}$$

where P is the power of the single ray hitting the particle, n_m denotes the medium's refractive index, and R and T represent the Fresnel reflection and transmission coefficients, respectively, with θ and ϵ being the angles of incidence and refraction. This analysis underlines the influence of the light's refraction through the sphere, aligning with Newton's third law by generating a net force that pushes the sphere towards the beam's focus, particularly as light entering through the particle's edges is refracted more intensely.

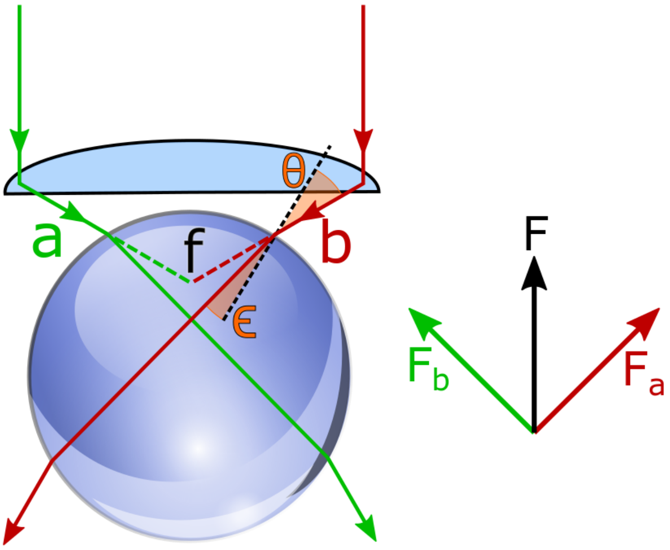

Figure 2.1 Optical forces F_a and F_b on a dielectric bead in the Mie regime due to refraction of two light beams, a and b. θ is the angle of incidence, and ϵ is the angle of refraction. Momentum transfer from the beams results in total force F near f, the focal point of the lens.

Rayleigh Regime

In the Rayleigh regime, particles significantly smaller than the trapping wavelength are influenced by their polarizability, the measure of how much the electron cloud of a molecule is affected by an external electric field. When an electric field is applied, the distribution of electrons around the nucleus shifts slightly, inducing a dipole moment proportional to the strength of the electric field. Due to their high polarizability, the particles behave as dipole oscillators within an electromagnetic field, as illustrated in Figure 2.2. This interaction, governed by the Lorentz force, attracts particles towards regions of highest intensity—typically the beam's focal point where the electromagnetic field's intensity gradient, and consequently the gradient force, is maximized. This phenomenon is quantitatively described by the scattering force, F_S, and the gradient force, F_G, articulated by Ashkin *et al.* [155]:

$$F_S = \frac{I n_m}{c} \frac{128\pi^5 r^6}{3\lambda^4} \left(\frac{m^2 - 1}{m^2 + 2} \right), \tag{2.6}$$

$$F_G = \frac{n_m}{2} \alpha \nabla E^2, \tag{2.7}$$

where I denotes the laser beam's intensity, m is the ratio of the refractive indices between particle and medium (n_p/n_m), α is the particle's polarizability and ∇E^2 represents the intensity gradient of the electric field. The gradient force, thus named for its reliance on the electric field's gradient, encourages particles to migrate towards the beam's center when a TEM_{00} Gaussian profile is used, reflecting a direct correlation between force and the laser's spatial intensity distribution.

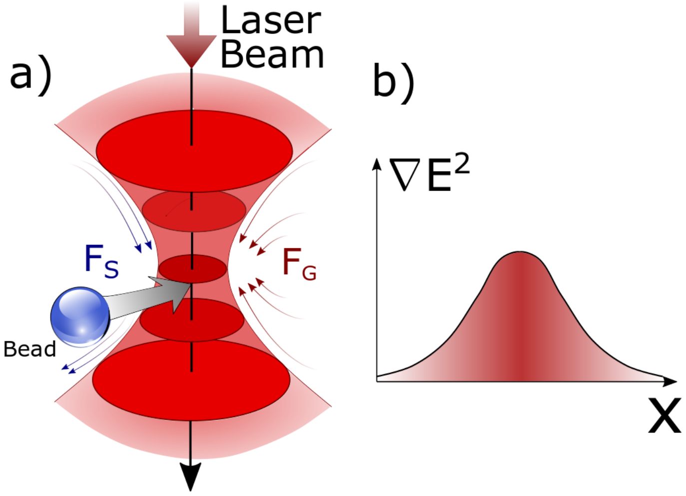

Figure 2.2 (a) Gradient force F_G and the scattering force F_S felt by a particle in the Rayleigh regime, (b) Spatial electric field gradient of a TEM_{00} Gaussian beam. Adapted from [156]

Force Measurement and Calibration

There exists a range of methods developed for extracting the particle's trap stiffness [157], which informs us about the quality of the optical trapping and dictates the system's lowest force resolution. These include analysis of the optical potential, autocorrelation function, Bayesian inference, and mean square displacement of the particle [157]. Here, we will focus on the three most commonly used methods. They give us a baseline of how the particle is moving in equilibrium and later allow us to extract force incident on the particle from the deviation from this baseline.

The simplest method to implement is the equipartition method. This approach takes advantage of the uniformity of random Brownian motion, leading to a Boltzmann distribution of $\rho(x) = \rho_0 e^{-\frac{U(x)}{k_B T}}$, where ρ_0 is the normalization factor, $U(x)$ is the potential of the particle, k_B is the Boltzmann constant, and T is the absolute temperature of the medium. For small displacements in x, the potential trapping the particle resembles that of a harmonic oscillator with $U = \frac{1}{2}k_{trap}(x - x_{eq})^2$, where x_{eq} is the equilibrium position.

This means the equipartition theorem allows us to equate the position probability density to the thermal average of the potential of $\langle U(x) \rangle$:

$$\frac{1}{2}k_{trap}\langle x - x_{eq}\rangle^2 = \frac{1}{2}k_B T, \tag{2.8}$$

meaning the trap stiffness can be extracted through plotting and fitting of the position distribution, with standard deviation $\sigma^2 = \langle x - x_{eq} \rangle^2$.

The second is the force drag method. In this case, we rely on moving the sample plane at a known velocity v. When the force of the medium is larger than that of the trapping, the particle escapes, and the known escape drag force for a low Reynolds number medium can be used to equate the two:

$$F_{drag} = -\gamma_0 v_f = F_{trap}, \tag{2.9}$$

where v_f is the fluid velocity.

The last method, which will be used throughout this project, is looking at the power spectrum density of the particle. Due to using frequency analysis it's the most robust to any external sources of vibrational noice. As described above, the particle motion inside the fluid is well characterized by the Langevin equation of motion. Recording the displacement again, the resulting data can be Fourier transformed and squared to obtain the power spectrum density. By relying on the characteristic shape of this spectrum for a spherical particle being a Lorentzian of the form:

$$PSD(f) = \frac{k_B T}{2\pi^2 \gamma_0 (f^2 + f_c^2)}. \tag{2.10}$$

We can then extract the corner frequency f_c, which is related to the trap stiffness through:

$$k_{trap} = 2\pi\gamma_0 f_c \tag{2.11}$$

Once the particle is trapped in the optical potential, there are several methods to track and analyze its motion — the simplest being the use of a bright light emitting diode (LED) to illuminate the particle and setting up an imaging system using a charged-coupled device (CCD) or complementary metal–oxide–semiconductor (CMOS) camera, taking advantage of the fact that the particle is trapped near the focus of the microscope objective, and so it can be used to both trap and image it [158].

By using software such as ImageJ [159] or MATLAB [160] to analyze the footage frame by frame, tracking the center of mass of the particle relative to an average displacement, allowing for motion detection, which can be limited by the resolution of the images. Even at relatively slow framerates and with readily available CCD cameras, sub-pixel resolution, and precise measurements can be made [161]. This can be taken further, with convolutional neural networks such as DeepTrack [162] used to predict the motion and allow for observation of the motion even in low light or with multiple light sources used to create a stereoscopic view of the particle motion in 3D [163]. This method has its advantages in being able to selectively choose which particle or object is being analyzed, as well as being relatively inexpensive and straightforward to set up;

however, under normal conditions, it is limited by the amount of light that can be used to illuminate the sample, which is directly tied to the exposure time and frame rate [157] resulting in inaccurate analysis of the motion. In general, this method is also confined to the x-y plane, as the particle is being imaged from a top-down perspective — this can be solved using principal component analysis [164] PCA.

Backplane interferometry is another primary particle detection method, with either a single-section photodiode or a quadrant photodiode (QPD). This generally allows for a much higher bandwidth detection of the particles with 10s of kHz bandwidths [157], where the scattering profile of the trapped sphere is used to detect the 3D motion of the particle, with calibration required to convert the voltage seen to a physical distance. Often, a combination of the CCD and QPD is used [159, 161, 165], to allow for cross-calibration as well as being able to see the trapping site with the CCD and precisely measure the motion using the QPD.

Another notable method is direct force measurement [166]. By measuring all of the light before and after the microscope objective, the exact forces can be inferred from the light scattering between the objective and the condenser. This method allows for the force analysis of not only individual beads but also to characterize the stretching forces incident on a blood cell trapped using multiple tightly focused beams formed using holographic optical trapping.

Holographic Optical Trapping

In holographic optical tweezers, diffractive optical elements are used as a programmable diffraction grating to create multiple traps from a single beam, allowing for precise control of multiple particles within the field of view of the microscope objective. While a broader list of methods used to generate multiple optical traps with a single laser source can be found in Chapter 1, a phase-only reflective SLM was used throughout this thesis for trapping more complex objects.

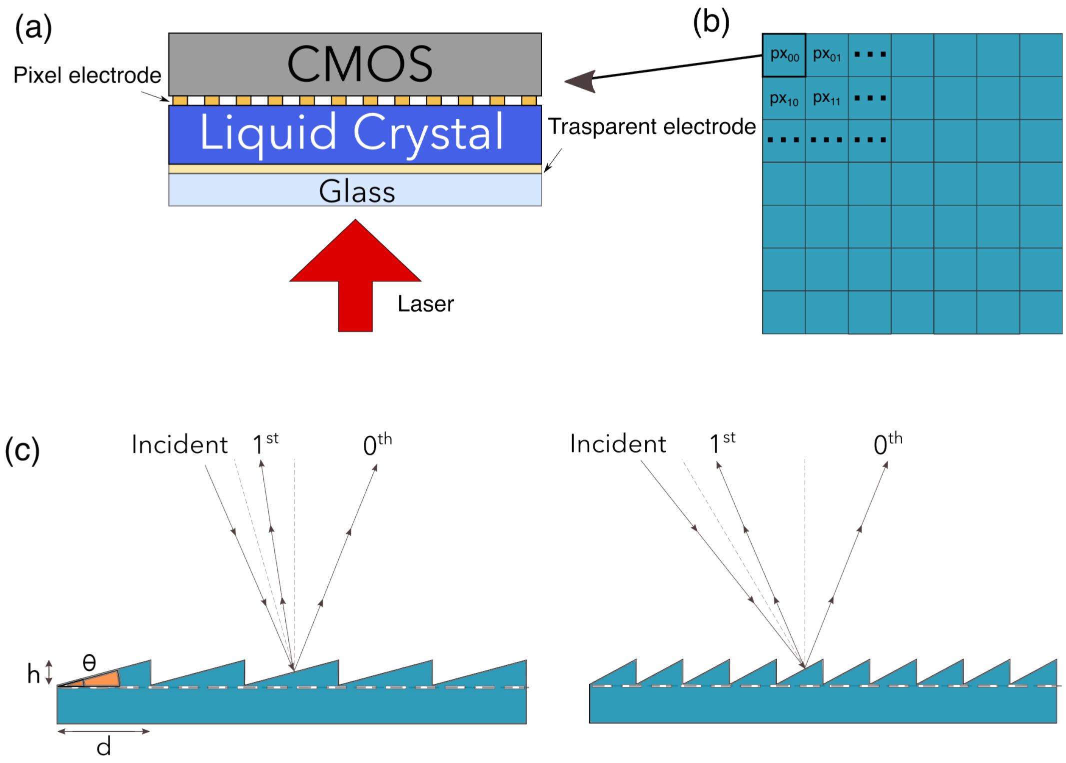

Figure 2.3 Schematic of the SLM (a) individual pixel and (b) the entire addressable grid of pixels (c) show how projecting a blazed grating onto the SLM allows to use it to move the position of the first order of the diffracted beam.

As shown in Figure 2.3 (a) and (b), an SLM consists of an array of thousands of liquid crystal pixels, wherein each pixel is addressable. The voltage across each pixel determines the phase delay experienced by light passing through it, meaning the diffraction of the light through the SLM is dynamically shaped in any way desired in transmission and reflection.

The SLM is placed at the conjugate plane to the back aperture of the objective used for trapping using a 4f lens system. A 4f system consists of two lenses with focal lengths f_1 and f_2 with the SLM being f_1 away from the first lens, the lenses separated by $f_1 + f_2$ and the microscope objective back focal plane placed f_2 away from the second lens [1]. A blazed grating is projected to create an interference pattern as shown in Figure 2.3 (c), with the amplitude of the gratings and lenses modulated to divert as much power as possible to the first order. Then, by changing the grating and lens height, size, and angle, the absolute position of the first order can be freely altered, and an aperture is placed in the center of the 4f system to block the zeroth and higher orders.

This control scheme combines discretized blazed diffraction gratings and Fresnel lenses [158, 167], as shown in Figure 2.4.

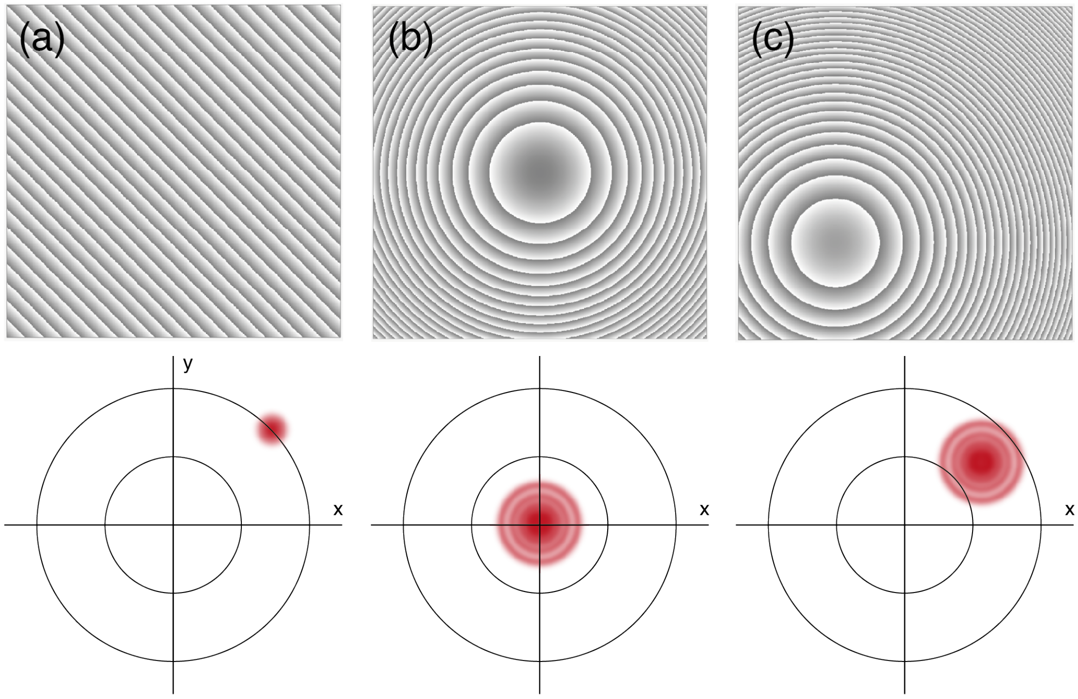

Figure 2.4 Gratings and Fresnel lenses hologram scheme used in this thesis for holographic optical tweezers, with the corresponding focal spot intensity shown below them. (a) simple displacement in x and y (b) positive Fresnel lens displacing the beam in z (c) superposition of the two creating a displacement in x,y and z. Adapted from [99].

The simplest configuration involves a single trap, i.e., $N = 1$, positioned at $[x_{ot,1}, y_{ot,1}, z_{ot,1}]$. Consequently, the phase modulation of the pixels is defined as:

$$\phi^{S}_{m_x,m_y} = \frac{2\pi}{\lambda_0 f}\left(x_{m_x,m_y}x_{ot,1} + y_{m_x,m_y}y_{ot,1}\right) + \frac{\pi z_{ot,1}}{\lambda_0 f^2}\left(x^2_{m_x,m_y} + y^2_{m_x,m_y}\right), \tag{2.12}$$

λ_0 is the vacuum wavelength, f is the focal distance of the trapping lens, $m_{x,y}$ are the SLM pixel indices and $x_{m_{x,y}}, y_{m_{x,y}}$ are the pixel's coordinates.

The first term corresponds to a blazed diffraction grating phase pattern, facilitating lateral spot shifting shown in Figure 2.4 (a), and the second term introduces a phase retardation akin to that produced by a Fresnel lens, enabling axial spot displacement shown in Figure 2.4 (b). The integration of these elements allows for three-dimensional trap manipulation shown in Figure 2.4 (c). Given the computational efficiency of generating the holographic mask, this methodology offers an effective means to dynamically position a single optical trap in three dimensions in real time [99].

Another efficient algorithm that outperforms random mask encoding with only a marginally increased computational demand is the superposition of gratings and lenses method. This approach dictates that the phase of each pixel is determined by the argument of the complex sum of single-trap holograms as described by Eq.2.1, that is

$$\phi_{m_x,m_y} = \arg\left(\sum_{n=1}^{N} e^{i\phi^S_{m_x,m_y}(x_m,y_m;x_{ot,n},y_{ot,n},z_{ot,n})}\right). \tag{2.13}$$

This formula consolidates the phases from individual trap holograms to generate a composite phase pattern for multiple traps.

The scheme described is a relatively simple example of a computer-generated hologram, relying on a superimposed set of gratings where the image is simply a series of a few discrete points in 3D space that can be solved analytically. While computationally fast, allowing for a 10 Hz hologram refresh rate using the setup used in this thesis, the method suffers from unwanted energy diversion to higher order diffraction, especially when high symmetry geometries are used. This can be solved by adding a certain amount of random noise to each superimposed layer of the mask, decreasing the amount of interference and diverting the energy back to the desired traps.

When dealing with complex optical trap distributions, methods for calculating the phase required to generate the image become more sophisticated. More optically efficient but computationally expensive methods to generate the holograms exist, outlined in reference [158]. The holograms can be pre-calculated using an iterative approach such as the Gerchberg-Saxton algorithm [168] (GSA), outlined below in Figure 2.5.

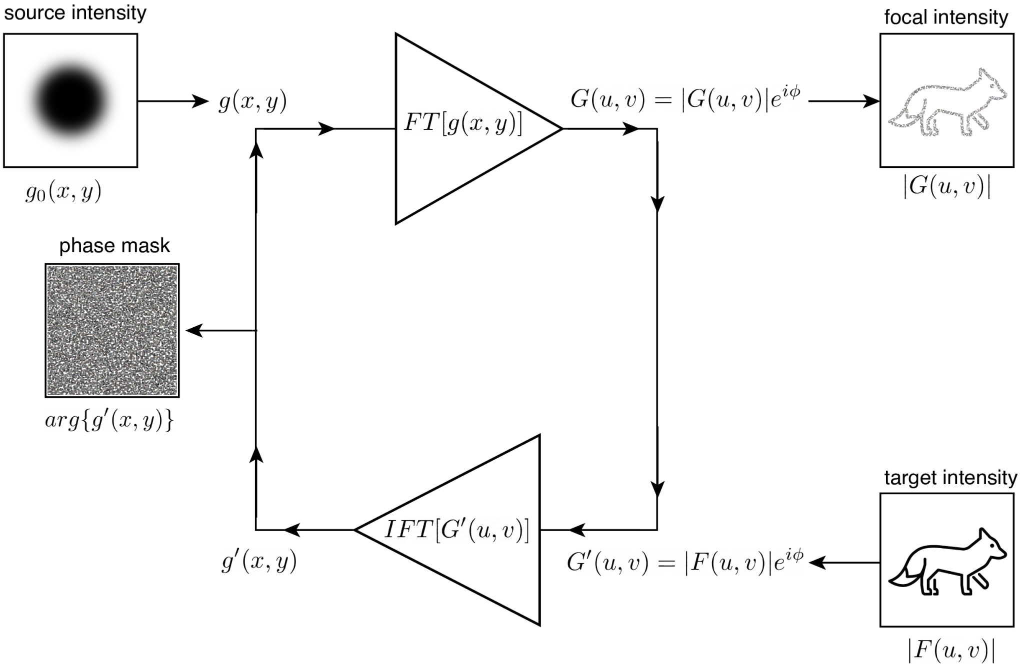

Figure 2.5 Gerchberg–Saxton algorithm. FT—Fourier transform, and IFT—inverse Fourier transform. Adapted from [169].

The GSA, developed by Gerchberg and Saxton in 1972, utilizes iterative procedures to compute the phase distribution that will transform a specified input intensity distribution at the SLM plane into a desired target intensity distribution at the trapping plane. This iterative method cyclically propagates complex amplitudes between these two planes. At each cycle, the intensity at the trapping plane is replaced with the target intensity. In contrast, the intensity at the SLM plane is substituted with the actual intensity profile of the laser, typically modeled by a plane wave or a Gaussian beam profile denoted as $g_0(x, y)$ in Figure 2.5.

The process begins by using the target image as the holographic image and propagating it to the hologram plane, where the intensity information is replaced with that from the illumination source. This modified hologram is then propagated back to the holographic image plane, and the intensity information is again substituted with the target image. This procedure is repeated until the difference between the holographic and target images, typically measured by a least squares metric, falls below a set threshold.

The Fourier Transform (FT) is key to the GSA by enabling the propagation of the complex amplitude between the SLM and trapping planes. The equations below describe the algorithm's iteration process, where the FT and its inverse (IFT) are used to compute the necessary phase distributions [169]:

$$G_{j-1}(u,v) = \mathcal{F}[g_{j-1}(x,y)] = |G_{j-1}(u,v)|e^{i\phi_{j-1}(u,v)}, \tag{2.14}$$

Here, $G_{j-1}(u, v)$ represents the FT of the amplitude distribution $g_{j-1}(x, y)$ at iteration $j - 1$, with $\mathcal{F}$ denoting the FT. The magnitude $|G_{j-1}(u, v)|$ and phase $\phi_{j-1}(u, v)$ are maintained at the Fourier plane.

$$G'_j(u,v) = |F(u,v)|e^{i\phi_{j-1}(u,v)}, \tag{2.15}$$

$G'_j(u, v)$ is the updated complex amplitude in the Fourier plane, combining the fixed magnitude $|F(u, v)|$ (from the reference image) with the previously calculated phase $\phi_{j-1}(u, v)$.

$$g'_j(x,y) = \mathcal{F}^{-1}[G'_j(u,v)] = |g'_j(x,y)|e^{i\phi_j(x,y)}, \tag{2.16}$$

This equation applies the IFT ($\mathcal{F}^{-1}$) to $G'_j(u, v)$, yielding $g'_j(x, y)$, the updated amplitude distribution in the spatial domain, with its magnitude and new phase $\phi_j(x, y)$.

$$g_j(x,y) = |g(x,y)|e^{i\phi_j(x,y)}. \tag{2.17}$$

Finally, $g_j(x, y)$ adjusts the amplitude to match the original input ($|g(x, y)|$) while updating the phase to $\phi_j(x, y)$ for the next iteration.

In these equations, $j = 1, 2, \cdots, n$ indexes the iteration steps, (u, v) are the coordinates in the Fourier plane, and (x, y) are the coordinates in the spatial domain. The calculated phase $\phi_j(x, y)$ can then be applied to the SLM to achieve the desired intensity at the trapping plane.

While the ability of SLMs to dynamically change the phase masks is key in optical trapping, when it comes to higher diffraction orders, SLMs face notable challenges. One significant limitation is the reduced diffraction efficiency for these higher orders, attributable to the discrete nature of their pixelated surface. This reduction in efficiency becomes more pronounced with an increase in the diffraction order, adversely affecting control and efficiency in applications that depend on these higher orders. Furthermore, the capability of SLMs to manage higher diffraction orders is constrained by the minimum grating period that can be achieved, which is inherently limited by the size of the pixels. One key technology we use to address these issues is HMSs.

2.2 Holographic Metasurfaces

HMSs, composed of arrays of subwavelength-sized structures, offer significant advantages for manipulating light with high efficiency across various diffraction orders. This is due to the HMSs' ability to operate on scales smaller than the wavelength of light, effectively addressing the limitations associated with SLMs. Most notably, HMSs overcome grating period constraints, which result in some light being diffracted into higher orders, limiting SLM's efficiency. HMS applications go far beyond wavefront shaping, including full control of the light polarization [170], amplitude [67], angular and spin momentum [125, 171], tunable HMSs capable of working at a wide range of wavelengths [82], and perfect reflectors [172] and absorbers [173]. Since HMSs were used throughout this thesis, this section will introduce the necessary background to understand their operation.

The utility of HMSs extends to the efficient generation of high-quality holograms, where each meta-atom serves as a sub-wavelength pixel, akin to those in an SLM, but with enhanced control over the phase of the incident light, thereby dictating the characteristics of the resulting far-field image. The GSA is similarly used for designing HMS holograms mentioned throughout this thesis. This typically comes at a later stage of the HMS design process, outlined in Figure 2.6.

The design process begins with deciding the application of the HMS. This includes determining the operational wavelength and required bandwidth, the medium by which the HMS will be surrounded, whether it will work in transmission or reflection and whether the HMS will need to focus light at high angles (such as those required in optical trapping). The main structural components of the meta-atoms is also chosen. Metals typically have high reflectivity at visible wavelengths. They are typically easier to deposit but less efficient due to higher losses brought about by plasmonic resonances and a small cross-section [174], leading to poor performance in transmission. Dielectrics tend to be much more transparent in the visible range and more efficient but more challenging to fabricate [175]. The phase control scheme (explained in detail in the following section) is then chosen. Simulation tools such as COMSOL Multiphysics or CST Microwave Studio are used to model and optimize the nanostructured materials' electromagnetic properties. In this stage, meta-atom unit cell parameters such as shape, size, and material refractive index undergo iterative parameter sweeps, ensuring the desired response at specific light wavelengths. Depending on the materials, this process can be time-consuming as physical fabrication limitations have to be considered. A set of at least eight meta-atoms is chosen, with a phase response that allows for linear mapping between 0 and 2π. GSA is then used to form a holographic phase mask of the target image, with the mask discretized to the eight levels chosen in the previous step. The periodicity of the meta-atoms is chosen to be less than half of the operational wavelength to satisfy the Nyquist-Shannon sampling theorem [176] for high NA applications. This phase mask is then fabricated using various cleanroom techniques, described in Chapter 5.

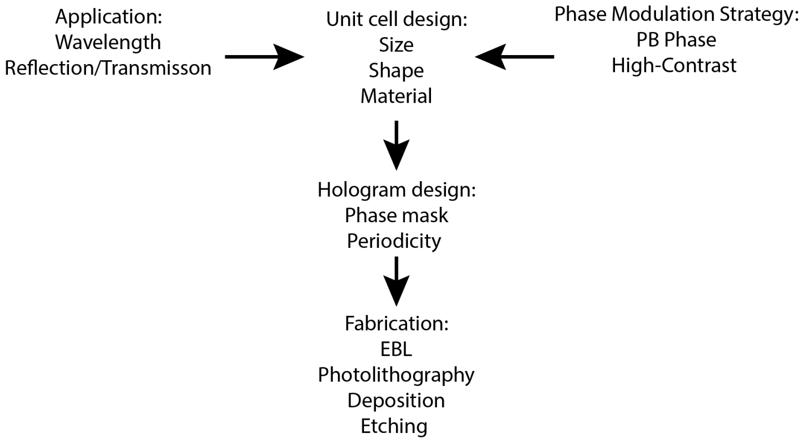

Figure 2.6 Example flow chart of the design process of the HMSs presented throughout this thesis. The unit cell design is informed by the operational wavelength of the HMS, whether it will be used in transmission or reflection, and the phase modulation scheme chosen. The parameters of the HMS atoms are then simulated to provide the desired electromagnetic response. The GSA algorithm is then used to produce a discretized phase mask with a given periodicity, with meta-atoms acting as pixels of the mask. Finally, the HMS is fabricated using well-established cleanroom techniques, including electron beam lithography (EBL), photolithography, metal and dielectric deposition, and dry and wet etching.

Phase Modulation

The core objective of meta-atom design is to enable modulation of the phase of incident light across a full 0 to 2π range, achieved through a detailed phase mapping strategy. The imparted phase shift is systematically adjusted by varying the meta-atom's dimensions, refractive index, or orientation. The specific nature of this phase control is closely linked to the meta-atom's material composition. This modulation is discretized into eight or more levels, ensuring clear phase differentiation without interference and allowing for precise manipulation of light's wavefront [177].

While structuring materials like glass into varying thicknesses can mimic some metasurface functions, this approach has limitations. Metasurfaces use sub-wavelength-sized resonators to induce abrupt phase shifts, enabling precise control over not just phase, but also the direction, polarization, and amplitude of light. This phase discontinuity allows metasurfaces to surpass traditional optics, offering multifunctionality, compactness, and integration with modern photonic devices, which traditional optics cannot achieve.

How the phase is modulated largely depends on the meta-atom's component materials. There are multiple mechanisms for phase modulation, each with its subcategories. As HMSs operate at various wavelengths and scales, in this thesis I will focus on the ones able to operate efficiently in the visible regime. A full review of the operational schemes can be found in ref. [178].

The first scheme is fundamentally based on plasmonic resonances within metallic nanostructures. Analogous to mechanical oscillators, these structures respond when exposed to an external electric field. This interaction prompts the displacement of conduction electrons relative to the fixed positive ions within the metal, causing a polarization of the structure. This polarization, in turn, generates a restorative depolarizing field reminiscent of the restoring force in a displaced mechanical oscillator.

The dynamic behavior of these electron oscillations is described by the Lorentz oscillator model, which predicts an amplification in the system's polarizability at a certain resonance frequency. This resonance is characterized by a peak in the polarizability profile and a phase shift of π across its spectral range [179].

Linearly polarized light and the meta-atom's geometry are exploited to achieve full 2π phase control. Examples include the one of the first optical HMS demonstrated by the Capasso group in 2011, using linearly polarised light and v-shaped meta-atoms supporting symmetric and antisymmetric modes [67] as shown in 2.7(a). The dephasing of the light depends on the angle of the antenna β and its orientation relative to the polarization axis of the incoming light. Another example includes the gap-plasmon HMS, where the meta-atom is comprised of a metal-dielectric-metal structure. The dielectric spacer results in a strong coupling of the electric field between the top cap and reflective backplane, and allow for 2π phase modulation by changing the length of the meta-atom [180].

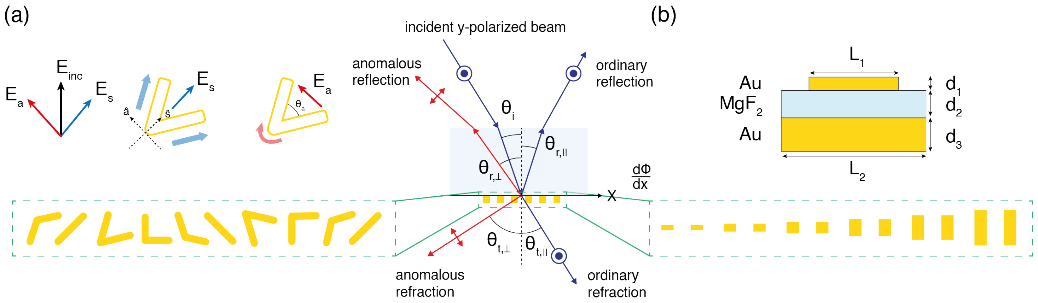

Figure 2.7 (a) V-shaped plasmonic antenna supporting symmetric and antisymmetric modes triggered by the incident field's components along the ŝ and â axes, respectively. The incident polarization forms a 45° angle with the antenna's axis of symmetry. The distribution of currents within the antenna is visually encoded using colors (blue for the symmetric mode and red for the antisymmetric mode). Here, the orthogonal components of the scattered electric fields are distinguished by a phase shift of π. Adapted from [67]. (b) Schematic of a gap-plasmon HMS. The left inset shows the unit cell made of a gold nanorod and a continuous gold film separated by a MgF_2 spacer. Adapted from [180].

The two other phase control schemes were used throughout this work, prompting a more detailed introduction. The first was reflective plasmonic metal-dielectric-metal HMSs based on the Pancharatnam-Berry (PB) geometric phase, requiring circularly polarized light and meta-atoms acting as nano-sized half waveplates to achieve 2π phase modulation [178]. The second was dielectric HMSs operating in transmission where meta-atoms act as truncated waveguides, which locally imposes the desired phase shift. [181, 182].

Pancharatnam-Berry Phase Metasurfaces

To fully understand the PB HMSs, we consider the representation of the polarization of light through a Poincaré sphere, suggested by Poincaré in 1892 to solve the issues of indistinguishability of degenerate states of elliptically polarized light. On a Poincaré sphere, the polarisation state of light is represented as a point P on the surface of the unit radius sphere with the Cartesian coordinates [183]:

$$x = \cos(2\chi)\cos(2\psi), 0 \leq \psi < \pi, \tag{2.18}$$

$$y = \cos(2\chi)\sin(2\psi), -\pi/4 \leq \chi < \pi/4, \tag{2.19}$$

$$z = \sin(2\chi), \tag{2.20}$$

where χ and ψ are the ellipticity angle and spherical orientation angles respectively. As shown in Figure 2.8 (a), in the most straightforward cases of the point in the x-y plane, this corresponds to linearly polarised light, and the poles of the sphere correspond to circularly polarised light.

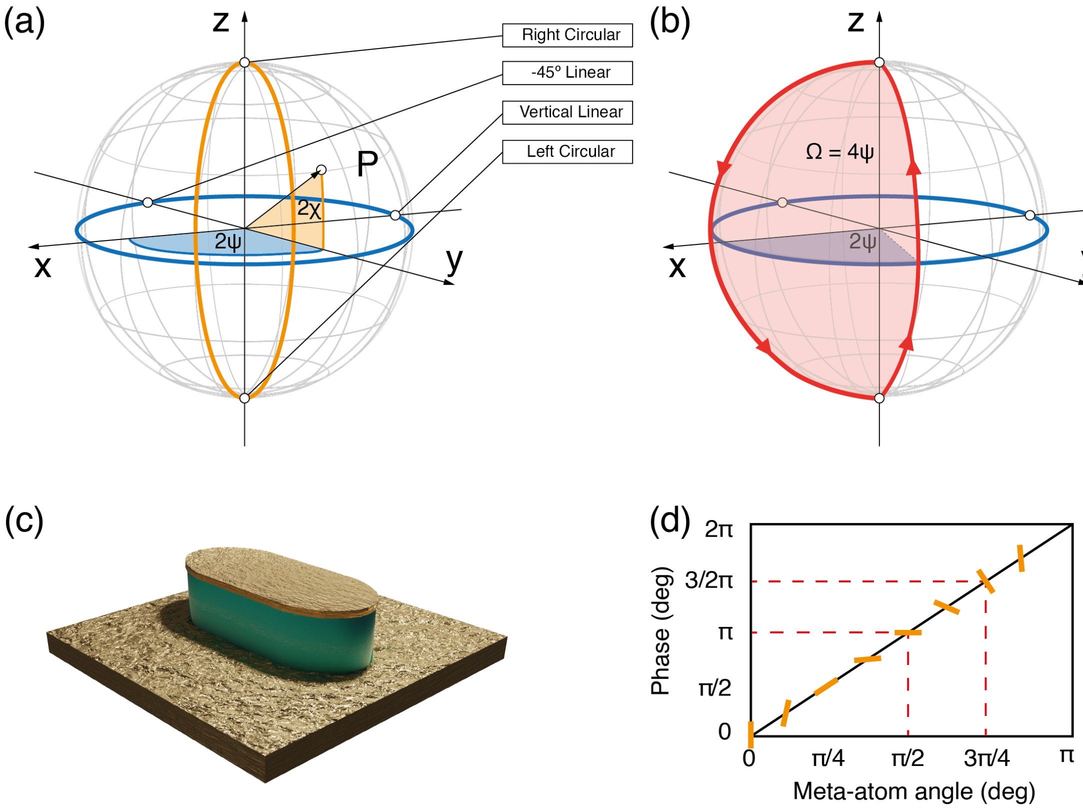

Figure 2.8 (a) Poincaré sphere, representing the polarisation state of light, (b) closed path on the surface of the sphere, resulting in a PB phase shift equal to half of the solid angle Ω, adapted from [183] (c) example PB meta-atom used throughout the work, and (d) simple phase to orientation mapping of the meta-atoms.

The PB phase is derived from the geometry of the Poincaré sphere. A phase delay is acquired when the polarization state of light completes a closed path across the sphere's surface. The resulting phase shift acquired equals half of the solid angle Ω swept by the closed path [184, 185] as shown in Figure 2.8(b).

In PB phase HMSs, incident light is either left or right circularly polarized, meaning the path taken on the surface of the Poincaré sphere must take place between the two poles, as the polarization is reversed upon reflection. The anisotropic meta-atom (Figure 2.8(c)) dimensions along the long and short axis are engineered to ensure resonances π out of phase with each other, characteristic of a half-wave plate. The meta-atoms' rotation angle then results in twice the phase delay as indicated by the red dashed line in2.8(d). Because the scattering amplitude depends on the meta-atom geometry, not the orientation [186], PB phase HMSs can be engineered to work across a broad range of wavelengths with high conversion efficiencies of 80-90% [83, 187] when used in reflection.

Additionally, the sign on the phase shift depends on the incoming field's handedness, meaning multiple holograms can be encoded using the same configuration of meta-atoms by simply changing the polarization. This presents the PB scheme as a great candidate for multiplexed HMSs. Multiplexing is a method used in telecommunications and networking that combines multiple signals or data streams into one signal over a shared medium [188]. In the context of HMSs, it's a method that allows multiple images to be encoded into the same structure, greatly increasing the information density. Information can be encoded through polarization [189], propagation direction [190], and wavelength [191] among other properties of light.

During this work, I assisted in a publication [71] that used this property to encode two images into a frequency-selective HMS for cryptography purposes. I contributed to building the optical setup needed to characterize the HMS, assisted in the HMS fabrication, and collected a portion of the published spectra.

The work demonstrated a two-tier manipulation of holographic information, where each image would only be revealed when the correct combination of wavelength and the surrounding medium was used, as shown in Figure 2.9. The media chosen were that of air and water, and the wavelengths were 705 nm and 750 nm.

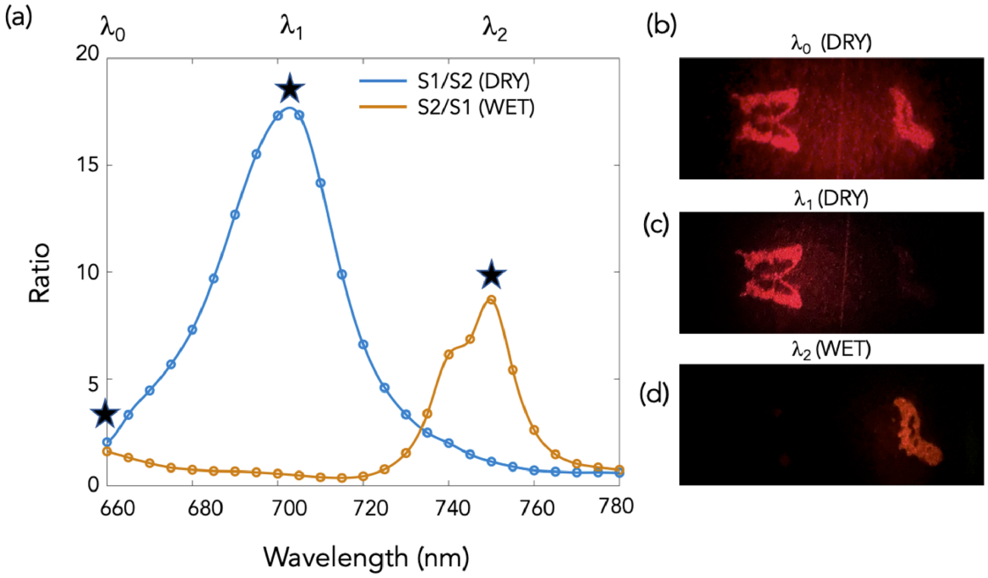

Figure 2.9 Experimental measurements of the HMSs under different conditions. (a) Solid blue and orange lines demonstrate the relative efficiency of Subcell-1 to Subcell-2 in dry and wet conditions. From left to right, the stars correspond to wavelength and medium of (b-d). Taken from [71].

This was achieved by designing two different subcells with varying dielectric lengths and heights, resulting in vastly different electromagnetic responses, as shown in Figure 2.10, giving ratios of over 1:50 at the selected wavelengths in air and water.

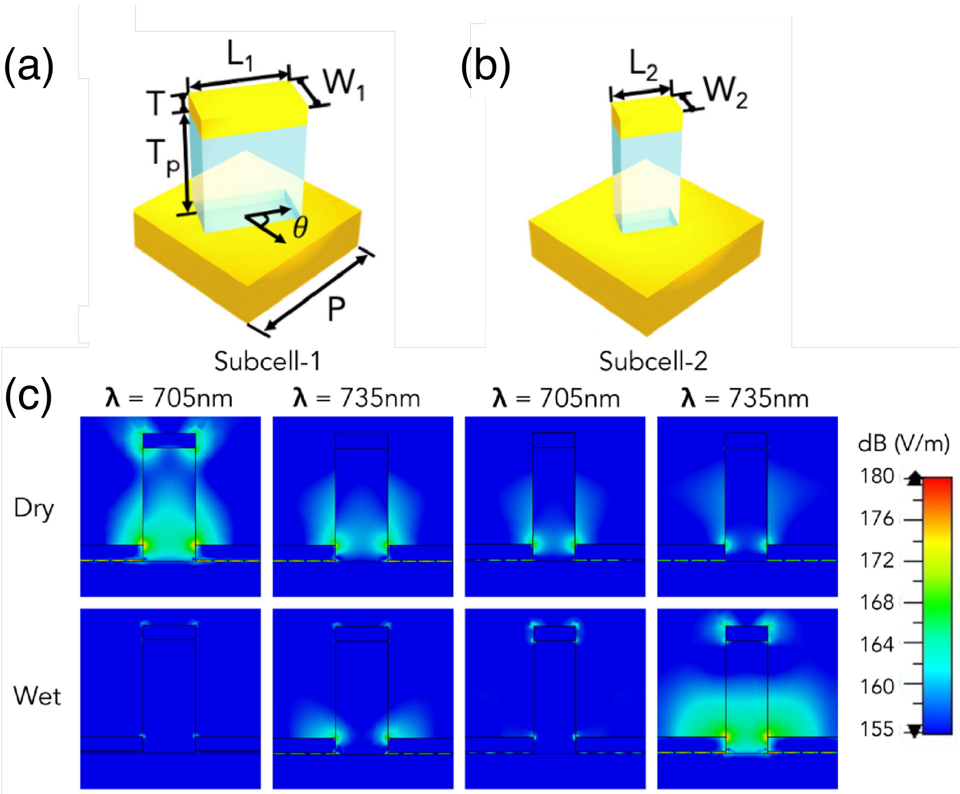

Figure 2.10 Example of using the dependence of the scattering of PB phase meta-atoms on unit cell geometry. (a) and (b) show the individual meta-atom subcells with lengths $L_{1,2}$, widths $W_{1,2}$ dielectric height T_p, metal cap thickness of T, rotation angle θ and periodicity P. (c) Shows a side view of the electric field fields of Subcell-1 and Subcell-2 of the HMS, where the resonant condition for Subcell-1 is an incoming wavelength of 705 nm and the effective medium is air. The resonant condition of Subcell-2 is an incoming wavelength of 735 nm, and the effective medium is water. Taken from [71].

Another advantage of the PB scheme is the relative ease of fabrication, as all of the scatterers comprise simple nano-rods. This enables more sophisticated geometries, including making the substrate flexible to form a conformal HMS using PDMS [76, 77, 78, 182].

During this work, I also contributed a publication [78] that described using a conformal HMS as a self-calibrated flexible holographic curvature sensor. I helped build the optical setup needed for the characterization of the HMS, and assisted with the data collection and analysis. The schematic and main result are shown in Figure 2.11.

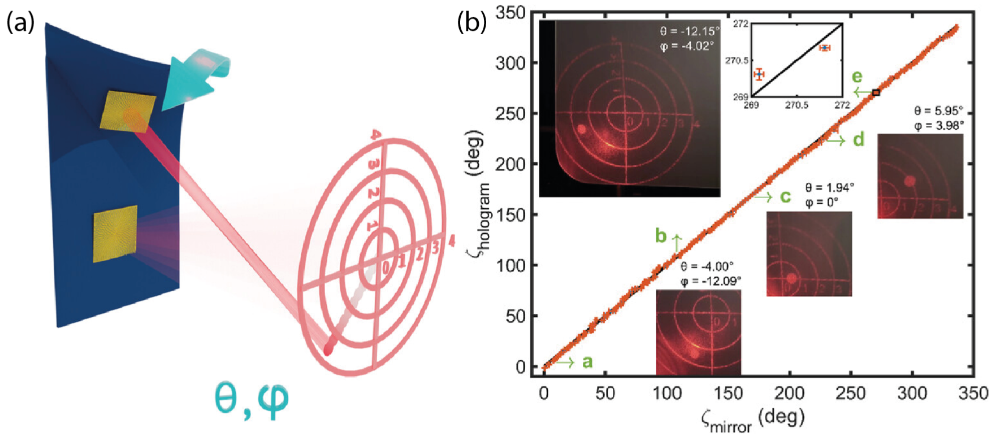

Figure 2.11 Self-calibrated flexible holographic curvature sensor. (a) A schematic representation of the flexible curvature sensor is presented, highlighting two patterned regions (depicted in gold) that correspond to the HMS responsible for generating the two-dimensional scale image and the dot indicator image. As the patterned areas undergo displacement relative to one another, the position of the dot transitions across the 2D scale, correlating the movement to specific displacement angles θ and ϕ, which are annotated directly on the scale for reference. (b) Parametric plot of the angle accuracy of the HMS when compared to a mirror, with the two angles θ and ϕ combined into one parameter ζ. Insets a–d display the holographic images captured at designated points. Inset e provides a magnified perspective of the graph, accentuating the alignment between the two methodologies (illustrated by blue dots), the associated uncertainty (depicted with orange error bars), and the linear regression (represented by a solid black line). Taken from [78].

The flexible, self-calibrated holographic curvature sensor operates within the visible spectrum and can detect the deformation of target objects. Unlike existing methods, this sensor eliminates the need to map specific observables to the substrate's curvature. It features a holographic display encompassing a reference scale and an indicator cursor, facilitating an immediate readout of curvature. As illustrated in Figure 2.11 (a), the sensor's holographic image is composed of a 2D scale and a dot that serves as the curvature indicator. The displacement of this dot is directly proportional to the deformation angle, shifting in response to changes in the HMS's form. This system's validation against external calibration measures is shown in Figure 2.11 (b), obtained by independently calibrating the object's curvature by collecting the beam's angle reflected from an un-patterned area acting as a simple mirror.

Propagating Mode Metasurfaces

In propagating mode HMSs, regions of high and low refractive index are used to enhance light confinement and give a more significant phase modulation depending on the engineered geometry of the meta-atoms. This confinement is also advantageous by limiting cross-talk between neighboring atoms [182]. Propagating mode HMSs typically take advantage of the high refractive indices of dielectrics such as silicon [182] or zirconia [129] and high transmissivity in the visible spectrum. They can be realized using the PB phase with polarized light and the usual phase-orientation dependence described above for wavelength-specific applications [192]. However, their most significant advantage comes when the phase is modulated through the size of the features in the unit cells, which is polarization-independent. This is the key difference between propagating mode HMSs and plasmonic HMSs, as the elements don't need to be at resonance to control the light phase, dramatically increases their versatility [181]. As the HMSs are made up entirely of dielectrics, they overcome the critical issue of heat dissipation, reaching much higher efficiencies and polarization conversions when compared to plasmonic-based devices [51] and allowing for applications such as 100% efficient mirrors [193].

Below in Figure 2.12 is an example of a propagating mode HMS used for optical trapping. The phase is modulated by controlling the pillars' height, which acts as truncated waveguides supporting multiple low-quality Fabry-Perot resonant modes that interfere, resulting in a high transmission [129]. More details can be found in Chapter 5, where this propagating mode HMS was used to trap particles using wavelengths of 532 nm and 488 nm.

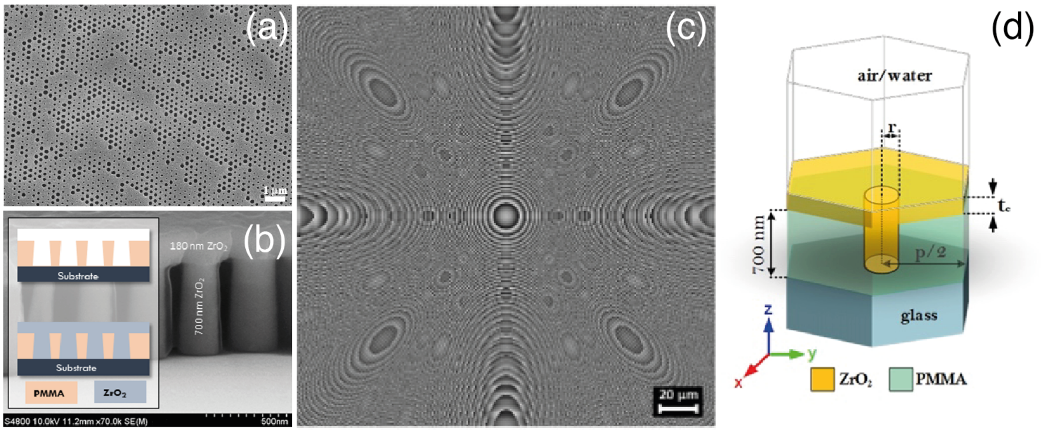

Figure 2.12 Example of a propagating mode HMS lens.(a) and (b) Scanning electron microscope images of the zirconia posts forming the micro-lens. (c) Phase mask of a lens. (d) Schematic of truncated waveguides used to create high-NA micro-lens. Taken from [129].

2.3 Contribution

The examples in the HMS section cover two publications where I contributed to the experimental characterization and fabrication of the HMSs and the data analysis. The first publication demonstrates a HMS capable of encoding multiple holographic images, which can only be retrieved using the correct combination of wavelength and medium refractive index [71]. The second publication concerns a self-calibrated flexible holographic curvature sensor capable of displaying an instantly readable surface curvature reading [78].

2.4 Conclusion

This Chapter covered the theory of optical manipulation and metasurfaces, outlining the underlying theories and methodologies that facilitate precise control over light-matter interactions at both macroscopic and microscopic scales.

All analysis of the optically trapped particles in Chapters 4 and 5 was done based on the PSD method outlined here. The manipulation of membranes in 6 was done using the SLM algorithm defined in this Chapter, and the design of their features was informed by optical trapping theory. All HMS design in Chapter 5 was completed using the GSA, and following the flow chart outlined above.

With the basic theory covered, the following Chapter will describe the methods used for fabricating the membranes and metasurfaces, the physical setup used for optical trapping, the software used to control it as well as the data analysis methods.

CHAPTER 3

Materials and Methods

With the key theory behind metasurfaces and optical trapping covered in the previous Chapter, I will now focus on how the metasurfaces and membranes were made, and the optical setups used to characterize and manipulate them. The machines and setups described here formed the backbone of this thesis.

All metasurfaces used in Chapter 5 and membranes used in Chapter 6 were fabricated using the electron beam lithography process and other cleanroom methods and tools. I will thoroughly explain the fabrication protocols here. The membranes were designed to be optically manipulated, and I will cover the design process here.

To use them, I designed and built multiple optical setups, for HMS characterization in Chapters 4 and 5, manipulation, interaction with biological objects, and force sensing as described in Chapter 6. I will cover the intricacies of each of those setups and the software I developed over the years to control them and analyze the data used in characterization.

3.1 Fabrication

Most my time fabricating (roughly the first 12 months of this PhD work) was spent on refining the design and methodology of making optically trappable membranes for use as in-situ optics and force sensors described fully in Chapter 6. These were 15×15 μm^2 polymeric membranes with a gold film evaporated in their center. The membranes had handles in the corners, which could be optically manipulated at will. Their planar shape makes them exceptionally stable (this allows for sensitive force detection), and leaves an area in the center of the membrane to pattern (this allows for use of the membranes to redirect and collect light sent into the microfluidic chamber).

3.2 Membrane Design

The membrane designs are shown below in Figure 3.1. This final design is the result of multiple iterations of fabricated membranes, experimenting with different processes, and figuring out the exact dimensions to optimize the membranes for optical trapping. The handles have undergone several iterations, starting as cubes for easy fabrication. We then experimented with each membrane having two long handles, which can be seen in some images throughout the thesis. This was done to take advantage of the fact that anisotropic objects will align along the long axis in an optical trap, allowing us to position the membranes vertically using just two traps. The design has since been changed to hemispherical domes using greyscale lithography to resemble the shape of hemispheres, with a handle at each corner of the membrane to allow for full control over the motion of the membrane in 3D.

Each parameter shown in Figure 3.1 was iteratively optimized. The round handle shape is chosen to maximize the amount of restorative force due to the refraction of light. The handle size, w_h, and t_h are chosen to be similar to the waist size of the trapping beam, increasing the trapping stability. The thickness of the membrane t_m was chosen to be 200 nm to keep the membrane as lightweight as possible without it bending. The side length of the membrane was chosen as it was the largest size which still allowed for the membrane to be tilted at 45 °, requiring a translation of the traps by ±7.5 µm in z. The side length w_g of the gold patch was chosen to be as large as possible without interfering with the trapping of the handles. The thickness of the gold layer was chosen to be 35 nm, creating a reflective and lightweight surface.

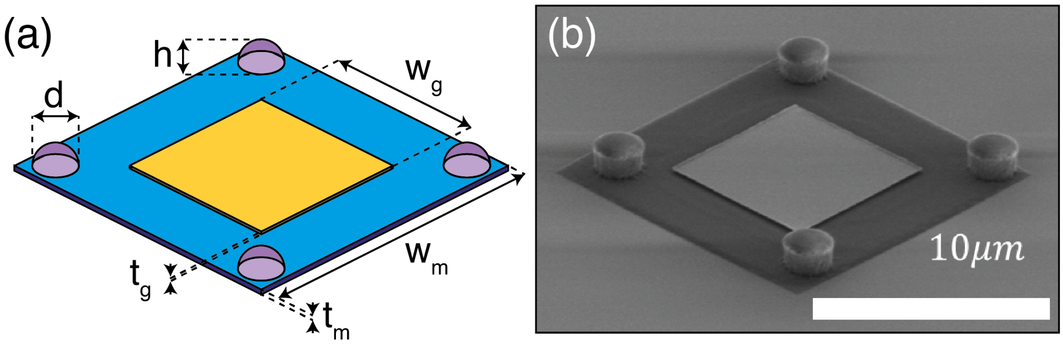

Figure 3.1 Current membrane designs. (a) shows the semi-spherical handle design, where h is the handle height, d is the diameter, w_g is the side length of the gold film square, t_g is the gold thickness, w_m is the square membrane width, and t_m is the membrane thickness. (b) shows the cylindrical handle design, where l_h, t_h and w_h are the handle length, thickness and width respectively. Adapted from [194].

Current design parameters are outlined in table 3.1:

Feature	**Size (μm)**
w_m	15
t_m	0.2
w_g	8
t_g	0.035
w_h	2
t_h	2
l_h	10
h	1.5
d	2.5

Table 3.1 Membrane design parameters.

3.3 Membrane Fabrication

Nanofabrication involves multiple steps, as each sample takes weeks to fabricate. The first year of the work on this thesis was spent on learning and optimizing the fabrication procedure of the membranes, as a consistent recipe and design had to be formulated and constantly refined.

Fabrication Equipment

The main equipment used in this process were:

1. Spin coater — used to spread out a resist to a desired thickness depending on the spin speed and duration.
2. Hot plate — used to bake the resist to evaporate the solvents inside and promote cross-linking.
3. Reactive Ion Etching (RIE) system — used to remove material through the use of charged ions directionally.
4. Electron Beam Lithography (EBL) system — used to directly write desired patterns into the resist using a focused beam of electrons. The energy the sample is exposed to in this process is known as the dose.
5. Electron Beam Evaporator (EBE) — used to deposit metal onto the sample directionally.

As the last two pieces of equipment made up the bulk of fabrication, I will introduce each one briefly:

Electron Beam Lithography

By far the most common method of fabricating metamaterials and HMS is through EBL [49, 195]. Similar in principle to scanning electron microscopy, EBL began with the discovery of the first electron-sensitive resist, PMMA, in 1968 [196]. Utilizing electron optics, unburdened by the diffraction limits of light, EBL can achieve resolutions on the scale of 10 nm feature sizes [197]. Resists used in EBL can be either positive or negative tone. Positive resists consist of long molecular chains that break up when exposed to a high-energy electron beam, allowing exposed regions to be washed away by the developer. Negative resists work oppositely, with short chains linking together through exposure and heating, creating permanent hard features [49].

Crucial to the process is the sensitivity of each resist, which depends on several variables such as substrate type, resist type, thickness, and electron energy. The EBL system used in this project was a Raith eLINE Plus, operating at 30 kV with a 10 µm aperture. A rough schematic of the system is shown in Figure. 3.2.

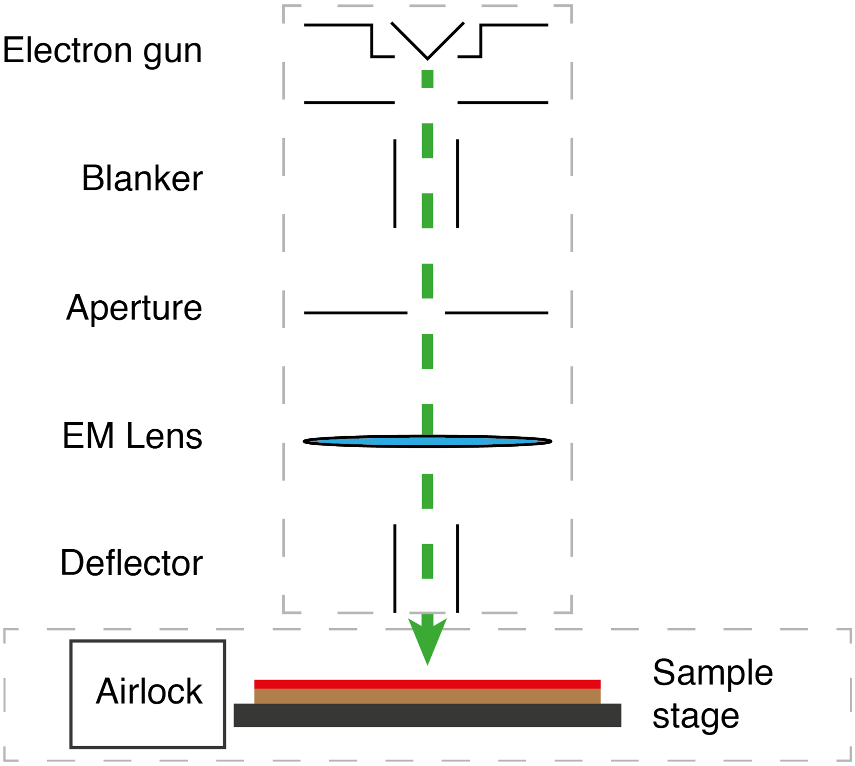

Figure 3.2 EBL system schematic.

System alignment, including focus, aperture, and stigmation adjustments, was conducted before each writing. Initial beam optimization involved burning contamination spots into the resist to fine-tune the beam's quality. A customized dose test was used to verify the outcome after development, ensuring the target structure was fully developed. The e-beam dose, measured in micro coulombs per square centimeter (µC/cm^2), is crucial for achieving the desired pattern fidelity.

Due to the multiple steps the process requires, the key step at the beginning of fabrication was writing alignment markers shown in Figure 3.3 (d) and (e), which through 3-point alignment allow for lining up of the global x-y and design u-v coordinates using the EBL software.

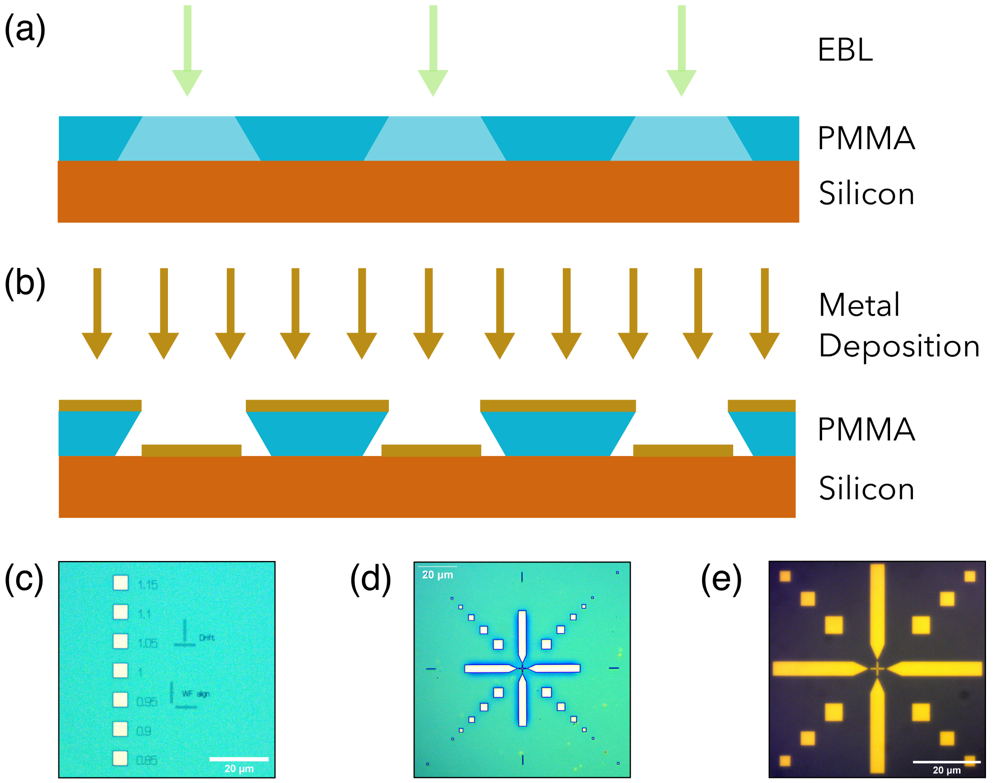

Figure 3.3 Fabrication using PMMA and gold. (a) and (b) show the undercut from secondary electron scattering, allowing thin film deposition. (c) shows a dose test used for optimizing development time. (d) shows what the undercut looks like from the top, it appears as a faint shadow around the structure. (e) shows a successfully evaporated gold alignment marker.

Metal Deposition

For both the alignment markers shown in Figure 3.3 and metallic features on the membranes, metal evaporators are used to deposit exact thin layers of metal. Currently, these are nickel-chromium alloy (NiCr) and gold. NiCr is used as an adhesive layer for the gold — due to its exceptional stability; gold is unlikely to oxidize and bond with the substrate, which contributes to low adhesion [198]. Its very low absorption and high reflectivity are needed to create functional mirrors. The metal is deposited in one of two ways, either through EBE or through thermal evaporation, both of which are based on the Edwards Auto 306 Evaporator system. The principles of operation are almost identical, with the main difference being the thermal evaporator heats the crucible through resistive heating, while the EBE uses a stream of high-energy electrons to bombard and evaporate the material, which then redeposits on top of the substrate. A high vacuum is needed to achieve directional deposition — the random path length of the molecules scales inversely with the pressure inside the chamber [197].

Methods

The membranes, along with the handles they were trapped by, were made using the negative photoresist SU8, which for decades has found use in MEMS and integrated circuit (IC) design [199, 200], due to its ability to form high aspect ratio structures and exceptional strength once cross-linked. While its high sensitivity makes it less suitable for high-precision EBL [201], for the micron-scale of membranes currently fabricated, the high sensitivity means a much faster writing time. To achieve the round shape of the handles, greyscale lithography [202] was used as shown in Figure 3.4 — by varying the exposure dose, the wall profile of the feature could be made non-vertical.

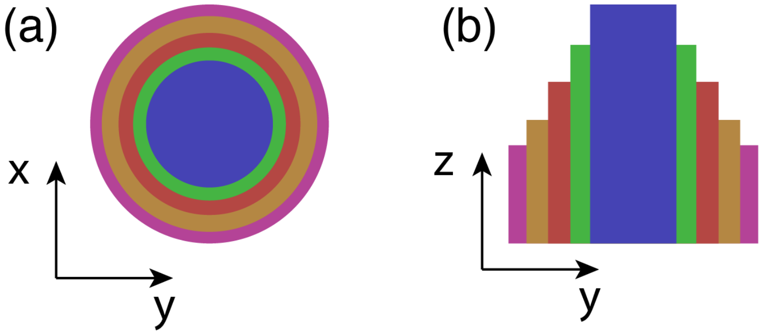

Figure 3.4 Greyscale lithography process. (a) shows a top-down view, (b) shows a side view of how the hemispherical handles are fabricated by gradually decreasing the dose used to write the handles to taper off the edges.

A positive resist of PMMA was used to create a mask, allowing for thin layers of material to be deposited in desired locations, as secondary electron scattering results in an undercut as seen in Figure 3.3 (a) and (b). To create this overhang, precise development was needed as too little or too much time for the developer would destroy the overhang. To ensure proper development, a 'dose test' shown in in Figure 3.3 (c) is used, which allows for precise tracking by showing the development of higher and lower doses (0.85 through to 1.15 of the base dose). Another indicator can be seen in Figure 3.3 (d), where the slight shadow around the features indicates an overhang.

The membrane fabrication protocol consisted of roughly ten steps, with the main steps outlined in Figure 3.5:

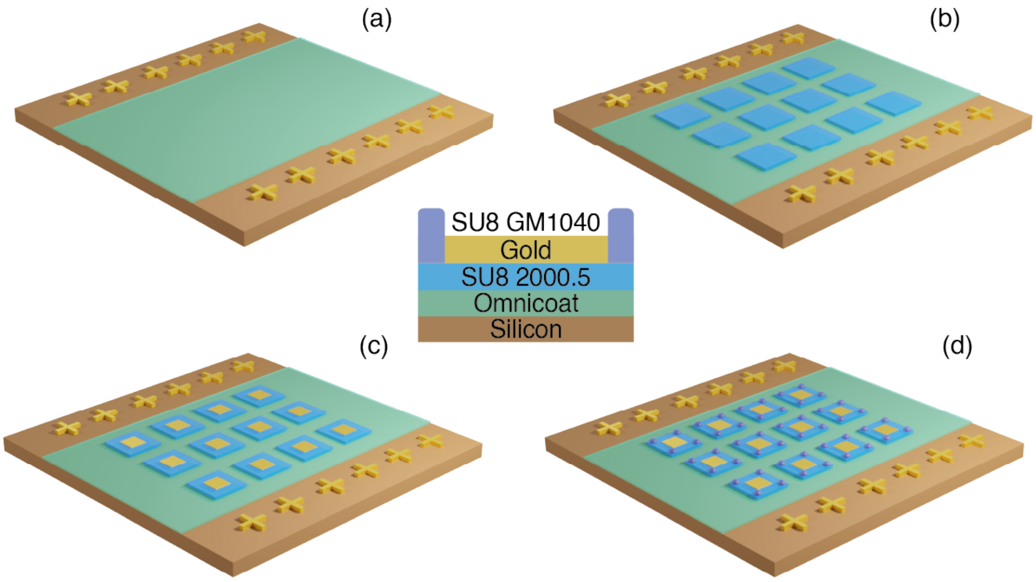

Figure 3.5 Key fabrication steps. Feature size is exaggerated to present them clearly. (a) Gold alignment markers are written and deposited, and a sacrificial layer of Omnicoat is spun. (b) SU8 membranes are written and developed. (c) Gold surface is deposited. (d) Handles are written and developed. Taken from [194].

1. First, a silicon substrate is prepared by scoring using a diamond scribe. The silicon substrate is then thoroughly cleaned using acetone in an ultrasonic bath, followed by cleaning with isopropyl alcohol (IPA), and the substrate is dried using nitrogen. The substrate surface must be pristine to avoid uneven coating with the resists. The substrate is then placed inside of an O_2 plasma asher and ashed for 3 minutes in 100% oxygen to promote the formation of oxygen-hydrogen groups on the substrate surface. The substrate becomes hydrophilic through this process, evenly spreading the resist.

2. The substrate is placed inside a spin coater, and a 100 nm thick sacrificial lift-off layer of Omnicoat (Dupont) is applied to the surface, spun, and baked according to values found in table 3.2. The flat sample is fixed to the spin coater using a vacuum pump. Hence, a consistent, exact thickness can be achieved. This was confirmed by measuring the resulting thickness using the DEKTAK profilometer.

3. A PMMA A7 950K (EM Resist) layer is then prepared according to values found in table 3.2. The sample is placed in the EBL, and alignment markers and a dose test are written. The PMMA is then developed in a 7:3 IPA: deionized (DI) water mixture for development. As PMMA is a positive-tone resist, the developer removes it in the areas exposed to the electron beam.

4. The sample is placed inside either the thermal or electron beam evaporator. A 5

nm adhesion layer of NiCr is deposited, followed by 35 nm of gold. The sample is then placed in acetone for lift-off, as the acetone dissolves the PMMA, leaving only the gold markers behind.

5. The alignment markers are then covered with dicing tape, and a 200 nm layer of SU8 2000.5 (Kayaku Advanced Materials) is prepared according to values found in table 3.2. The sample is then exposed in the EBL to write membranes and baked and developed in ethyl lactate (EC). As SU8 is a negative-tone resist, the developer washes away any unexposed SU8.
6. The alignment markers are covered again, and a layer of PMMA A7 950K is prepared according to values found in table 3.2 and written and developed as previously described.
7. 5 nm of NiCr and 35 nm of gold are again evaporated on the surface, and the remaining PMMA is washed away with acetone.
8. The alignment markers are taped again, and 2 µm SU-8 GM1040 (EM Resist) for the handles, which are then written in the EBL and developed with EC.
9. The sample is placed in the RIE and etched with oxygen plasma for 10 s at 20 W to remove a thin connective layer of SU8, which can sometimes form and join the membranes, making it impossible to lift them off.
10. Finally, the sample is cleaved to expose the Omnicoat, and MF319 (Dupont) is used to dissolve it. The submerged sample is placed in a 1.5 mL Eppendorf tube and left at 50 °C for several hours until the membranes are lifted into solution. The MF319 is then carefully skimmed off the top, and DI water is added to replace it.

Material	Omnicoat	PMMA A7 950K	SU8 2000.5	SU8 GM1040
Spin Speed RPM/time (s)	1000/45	4000/60	3000/45	2500/45
Resulting Thickness (nm)	100	400	200	1500
Pre-baking Temperature (°C)/ Time (s)	230/60	180/300	200/60	65/300 then 95/300
Exposure Dose (µC/cm^2)	N/A	150	3	3.5
Post-baking Temperature (°C)// Time (s)	N/A	N/A	100/120	100/300
Development Time (s)	N/A	60	60	45

Table 3.2 Resist parameters.

One sample would yield around 40,000 membranes, with membranes spaced by 30 µm away from each other, and a 200×200 array of membranes taking up ~ 6 mm^2. The final sample volume was 1 mL, giving a final membrane concentration of roughly 40 membranes per 1 µL, accounting for some of the membranes being lost during the liquid exchange. As the membranes would sink to the bottom of the sample, before a new sample of membranes and beads was prepared from trapping, the vial would be mixed using a vortex mixer to ensure an even concentration and to separate any membranes without damaging them. Fourteen membrane samples were prepared during the first ten months of this work. The fabrication time varied for each step. Steps involving sample preparation and resist deposition and development would take a few hours, metal deposition would take a day as it had to be prepared overnight to allow the evaporator to reach a sufficiently low vacuum while exposing the sample using the EBL would take one to three days. This is because each membrane and membrane feature was written individually, and the exposure time would depend on the sensitivity of the resist. The minimum preparation time for a single sample was two weeks, assuming an optimal process. However, once a sample is prepared, it is enough for hundreds of experiments, and once a successful batch was produced, shown in Figure 3.6 it was sufficient for the remainder of the work done in this thesis.

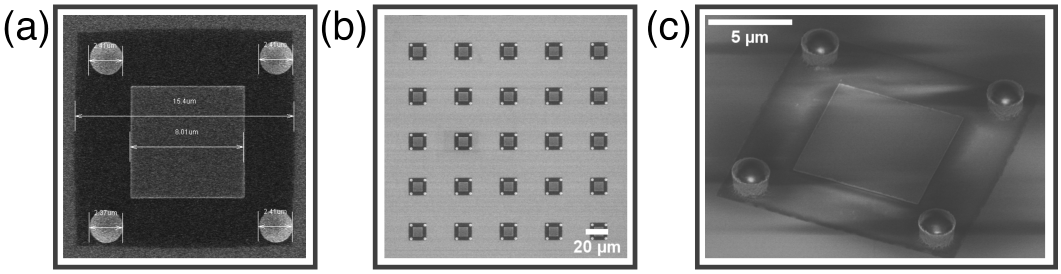

Figure 3.6 SEM images of successfully fabricated membranes with hemispherical handles as seen (a), (b) from above, and (c) at a 30 degree angle.

Although fourteen samples were fabricated throughout this thesis, only the last 2 out of 14 prepared samples were used in published results. This is due to experimenting with various membrane designs; first, to focus on creating the best membranes for optical trapping, different handles and membrane sizes were tested before settling on the current design. The metal element was then added, and different patterns were placed on the membranes, including diffraction gratings. The mask process shown in Figure 3.3 (a) and (b) needs to produce the correct overhang, otherwise the gold layer will not lift off as shown in Figure 3.7 (a). The precise EBL alignment required to place the elements on top of each other is very sensitive to temperature drifts, so during a long writing (such as for the PMMA mask for tens of thousands of membranes) the stage can move and produce a misalignment shown in Figure 3.7 (b). Different resists were experimented with, requiring optimizing the exposure dose and development each time. When too high of a dose is used on sensitive resist such as SU8 the features end up blown out as shown in Figure 3.7 (c). The fabrication was also stalled for a few months due to issues with metal deposition, as the electron beam would result in bubbling of the PMMA as shown in Figure 3.7 (d), making subsequent removal of the PMMA impossible. This was eventually discovered due to secondary electron scattering caused by the EBE, which would break up the PMMA chains resulting in outgassing [203].

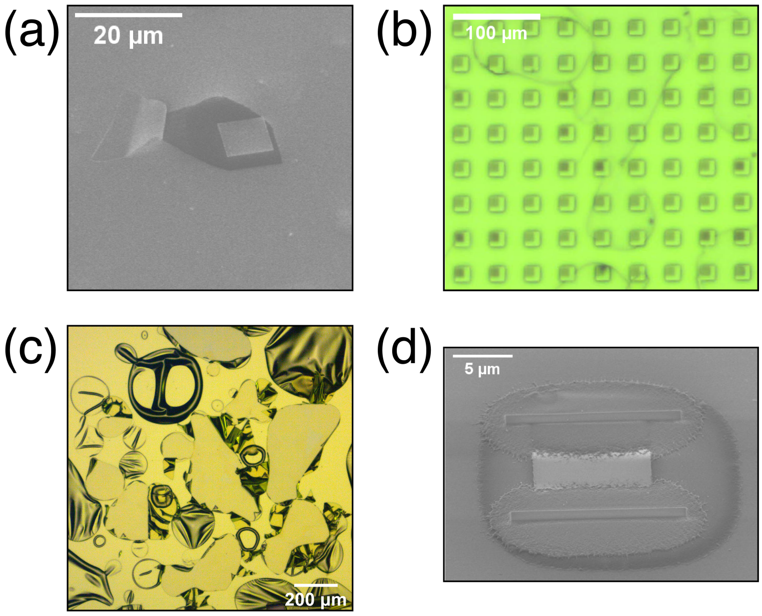

Figure 3.7 Different issues of membrane fabrication, (a) shows issues with gold lift-off after evaporation, (b) microscope image shows misalignment (c) gold bubbling due to exposure to PMMA off-gassing during evaporation and (d) effects of overdosing SU8.

In the end, all of these issues were solved, resulting in the two successful samples that lasted throughout the remaining work in this thesis. Once the membranes were fabricated, the first experiments they were used in were as movable microscopic optics inside a microfluidic chamber. For this, a holographic optical tweezers setup had to first be built.

3.4 Optical Trapping Setups

The majority of my time working on this thesis was spent in an optical lab, continuously rebuilding, improving, and using this trapping setup. The experiments performed using this setup can be likened to a balancing act, where the trapping and fluorescence pump beam's strengths must be continuously adjusted depending on the materials and objects being trapped and the required detection sensitivity. If metals, such as gold, were used, then there would be a threshold at which they would melt if the laser power were too high. If thin layers of metals exhibited localized heating, cavitation bubbles would form in the medium. Multiple traps could be generated using an SLM, but each new trap interfered with others, decreasing their power and efficiency. The experiments were all three-dimensional, with beads and membranes manipulated in x,y, and z around the imaging plane of the high NA 60x objective. With this high NA and magnification came a small depth of focus, so trapping anything displaced by more than ±7 μm away from the imaging plane was challenging. These optical trapping experiments would require undivided attention for hours, as all data had to be collected in a single session to ensure the environmental conditions were the same. The theory behind optical tweezers is simple: send an expanded laser beam through a high NA objective and focus it on a particle to achieve trapping. In this section, I will report on the added complexities of the process.

3.5 Single Objective Holographic Optical Tweezers

This section covers the main experimental setup: holographic optical tweezers enabled by an SLM, a motorized system that enabled switching between trapping with an objective and trapping using external structures such as metasurfaces. It describes the characterization section of the setup, including a fluorescence pump and detection and imaging system. It describes the experimental procedure for the trapping experiments and preparation of the microfluidic chambers. It introduces two pieces of software for the optical manipulation of multiple objects and particle motion analysis. This system was used in the experiments described in Chapters 4, 5, and 6, and three publications [128, 194, 204].

The trapping system was a single inverted microscope objective system, the basis of which was already in place when I started, together with a rudimentary version of the software. During a summer internship, an undergraduate student rewrote the software under my guidance, and I continued to add features to it as required by the experiments. I rebuilt this setup several times with different SLMs and optics to optimize the trapping efficiency further. I extended it using motorized mirrors to allow for trapping using microstructures and HMSs. I also added multiple fluorescence pump beams and spectrometers throughout this thesis for sensing experiments. The main challenge in maintaining and improving the setup was the limited space available on the optical table and the system being as low as possible relative to the optical table to ensure stability. These two limitations informed some choices, such as using 1-inch diameter optics instead of the recommended 2-inch diameter [157] as they decrease the spherical aberrations in holographic optical tweezers. To simplify the alignment of all sources and detectors (trapping laser, pump laser, imaging camera, spectrometer, and illumination source), a 30 mm cage system was used, which introduced its own complexities and spatial constraints.

Unless otherwise stated, all of the optical parts described were from Thorlabs. This greatly simplified the integration of the whole system, effectively standardizing all the component sizes, provided along with 3D models of the parts on the Thorlabs website. Additionally, free (for students, for now) computer-assisted design software such as Fusion360 by Autodesk could be used to assemble the parts virtually before purchase to ensure all components fit in the limited space.

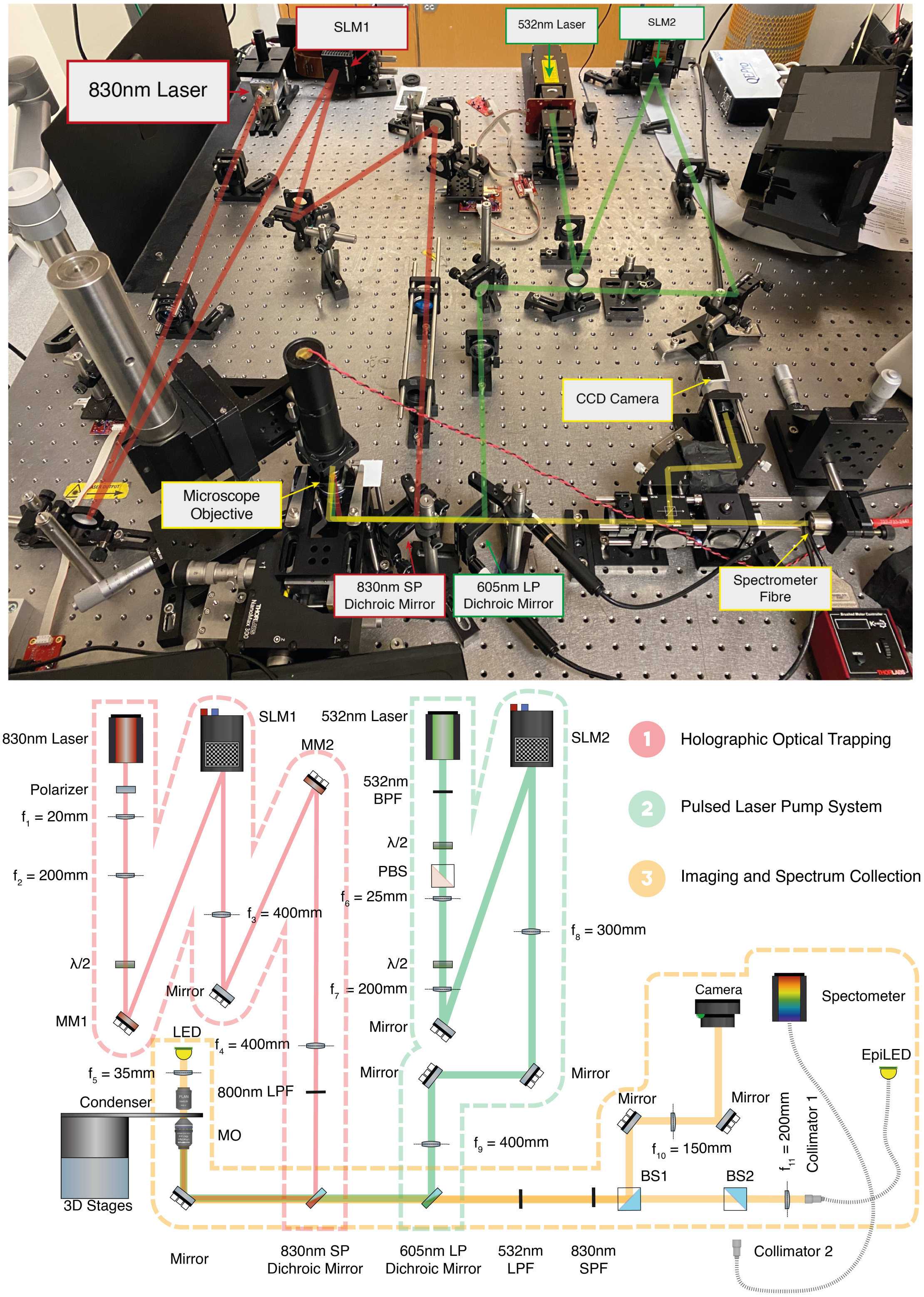

Figure 3.8 Single objective holographic optical trapping system (Section 1, left, outlined in pink), with a pump laser (Section 2, center, outlined in green) and imaging/sensing (Section 3, bottom, outlined in yellow). Here, $\lambda/2$ — half-wave plate, MM — motorized mirror, SLM — spatial light modulator, LED — light emitting diode, PBS — the polarising beam splitter, and BS — the beam splitter. BPF, LPF, and SPF refer to bandpass, long, and short pass filters, respectively. The distances are not drawn to scale. The automated mirror portion would be shown in Section 1 but is left out and shown in Figure 3.9 for visual clarity.

As shown in Figure 3.8, the final setup comprised two laser systems and an imaging system, each outlined by respective dashed lines.

Holographic Optical Trapping System

The first system consisted of a holographic optical tweezer setup. It started with a 230 mW continuous wave laser (LuxX 830–230, Omicron) with a wavelength of $\lambda_t =$ 830 nm, with a beam diameter of 1.1 ± 0.1 mm. The profile width of each laser was measured using a CCD Camera Beam Profiler. This laser was chosen due to its high pointing stability, ensuring high-quality trapping, and its power was sufficient for all performed experiments. It should be noted that typical optical trapping systems use lasers with a power of at least 1 W, especially when the beam power is split between multiple traps [8].

First, the laser polarization was filtered using a vertically aligned polariser matching the laser's polarization axis. Since the power of the laser was more than sufficient to trap, the focus was on creating the highest quality hologram using the SLM even if some of the power was lost. To this end, a half waveplate matched the laser polarisation to the polarisation axis of SLM1 (E-Series 1920×1152, Meadowlark). The beam was expanded using lenses, f_1 = 20 mm and f_2 = 200 mm, resulting in an expansion factor of $M = \frac{f_2}{f1} = 10$ to overfill SLM1, which measured 17.6×10.7 mm^2. A 1 mm diameter iris (not shown) was placed between f_1 and f_2 to spatially filter the beam as the profile was slightly elliptical in the vertical direction.

The beam was then sent through a 4f system consisting of lenses 3 and 4 with focal lengths f_3,f_4 = 400 mm. This configuration preserves the size and orientation of the input image at the output, meaning the phase mask on the SLM is perfectly relayed to the back focal plane of the objective. Additionally, the 4f system uses the Fourier transform property at the intermediate focal plane for spatial filtering. In the context of this trapping system, this meant the additional diffracted orders created by the SLM could be blocked using an iris (not shown) placed at the midpoint between f_3 and f_4. The iris was open up to 5mm, allowing for full control of the 1st order without interference from the 0th order.

The beam was aligned such that the first order reflected off SLM1 travelled through the center of the lenses, which minimizes spherical aberration. An 800 nm long-pass filter is used to remove some of the unwanted peaks in laser emission for spectroscopy experiments. The beam was then directed towards the back aperture of the water immersion objective (UPLSAPO60XW, NA = 1.2, Olympus) using a combination of an 830 nm short-pass dichroic and silver mirror. The dichroic allowed the light for imaging the sample to pass through to the camera while blocking the trapping beam to prevent damage to the CCD chip and oversaturation. The sample stage combined a manual

12.7 mm (562-XYZ, Newport) stage and an open-loop controlled Nanomax XYZ piezo stage, allowing for coarse and fine control of the sample plane in x,y, and z down to 50 nm precision. For visual clarity, the automated portion of the setup is not shown. It used motorized mirrors (indicated by MM1 and MM2) before and after the SLM to divert the trapping beam path and focus it on the back of the objective.

Switchable Optical Paths

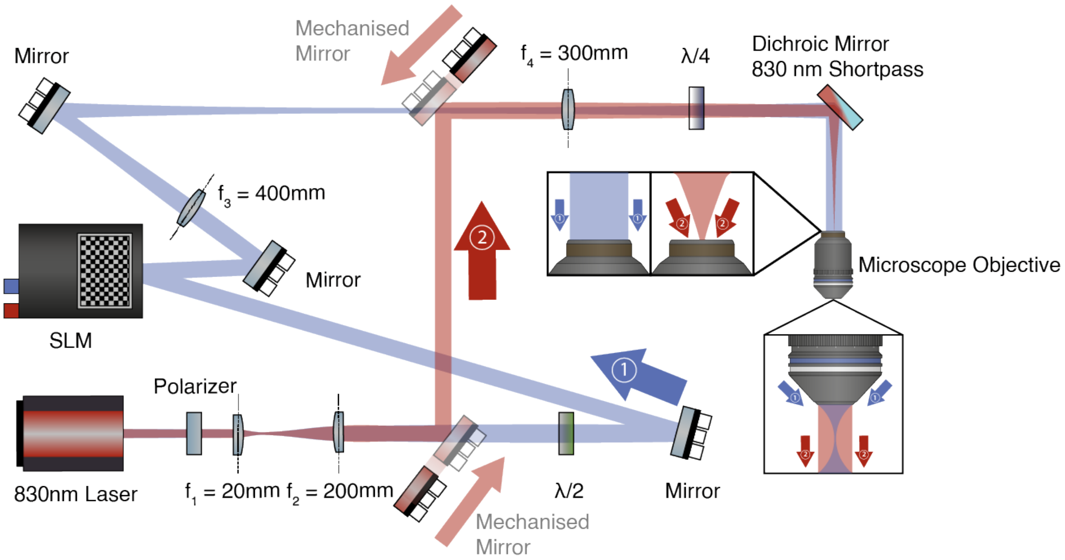

Figure 3.9 Modified optical setup allows for switching between two optical paths using two mechanized mirrors controlled by a computer. The first path results in typical holographic optical trapping. In the second path, the first lens of the 4f system, lens 3, is skipped, meaning that the trapping laser is focused on the back focal plane of the microscope objective. This results in a collimated beam coming out of the objective. The focal lengths and mirror position differ from Figure 3.8 because this is an earlier version of the trapping system, but the principle is identical. Adapted from [204].

Typically, in optical trapping, the laser beam is expanded as close as possible to the optimal size of 200% of the back aperture diameter of the microscope objective, which in this case was equal to 8 mm. This ensures the entire NA of the objective is used and results in optimal trapping strength [205].

In multiple cases throughout this work, sending a collimated trapping beam out of the objective was necessary while using the objective's high magnification to image trapped objects. The collimated beam illuminated gold-coated parabolic mirrors, which resulted in a focused spot at the focal point of the mirrors as described in Chapter 4. The collimated beam was also used to illuminate the reflective high NA HMSs used for trapping of particles and extended objects described in Chapter 5. The simple solution for generating this collimated illumination was to focus the trapping beam on the objective's back focal plane.

To this end, the capability of the trapping portion of the setup was extended using a pair of Elliptec™ 12 mm linear actuators controlled by the computer, which can displace the mirrors in less than 500 ms without misalignment due to repeated movement. Additionally, multiple actuators can be controlled using one board, meaning the mirror movement can be synchronized.

As shown in Figure 3.9, this allowed to skip lens f_3 in the 4f system and resulted in the trapping laser focusing on the back focal plane of the microscope objective using lens f_4. This resulted in a collimated beam coming out of the objective, which was used to illuminate the trapping micromirrors and the HMSs, as discussed in Chapters 5 and 6. Extra care had to be taken to ensure the beam would not damage the objective, given the maximum $\sim$180 mW power of the trapping laser (when the power out of the laser is the maximum of 230 mW) at the objective back aperture plane; it was empirically judged to be safe (the objective never cracked). The resulting beam profile is shown below in Figure 3.10.

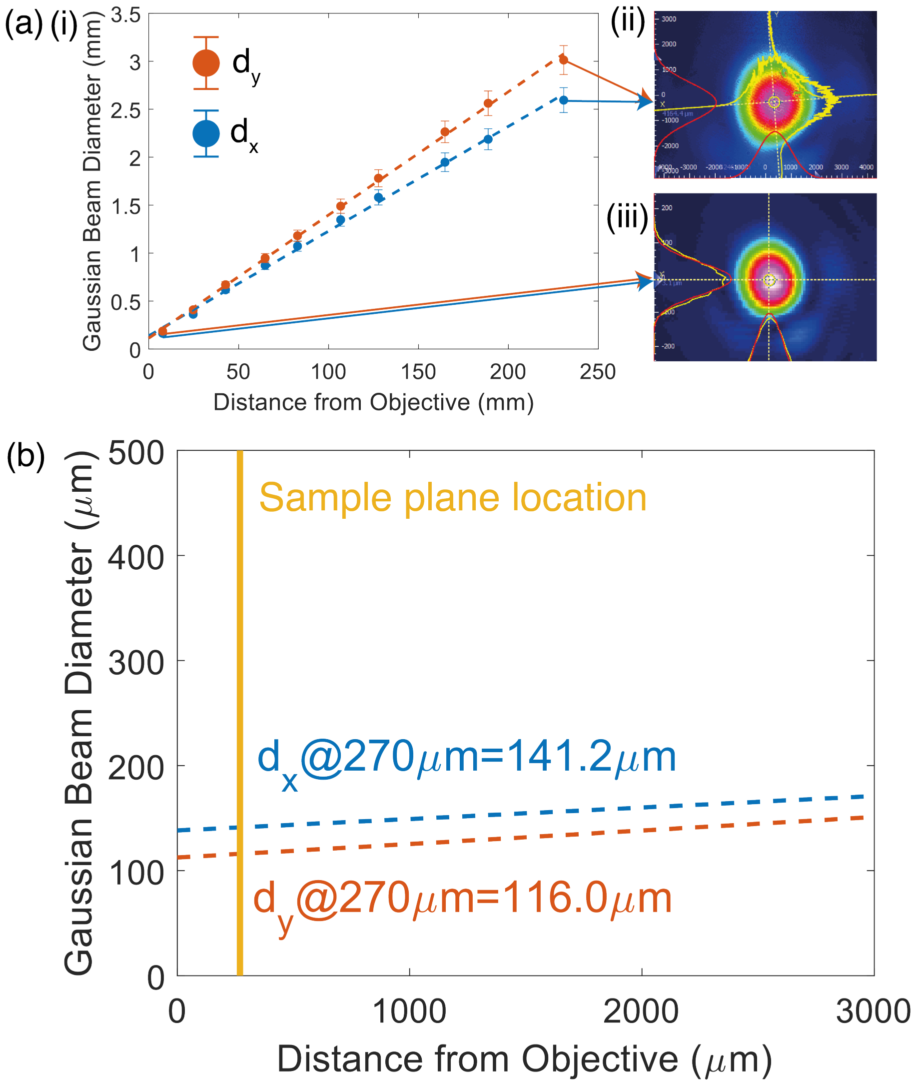

Figure 3.10 (a) (i) Beam size estimation with inset beam profiles at (ii) 7.7 mm and (iii) 230 mm away from the sample with (b) zooming in on the section where the micromirror traps would have been illuminated by the beam. Error bars show the standard deviation, as the beam diameter was measured three individual times. Taken from [204].

Simple flip mirrors were originally used, but they had two main issues. First, the slight shift due to the movement of the mirrors would result in a misalignment of the trapping beam. Second, for some of the trapping experiments, the switching from trapping using the objective to the illuminated structure had to be faster than the rate of sinking of the trapped object. Since the experiments were performed by me alone, this would also mean not monitoring the exact position of the trapped particle on the computer, which would often result in losing it and having to restart the experiment.

3.6 Pulsed Laser Pump System

The second laser system was a pump fluorescence excitation system consisting of a λ_p = 532 nm Q-switched pulsed laser, with a pulse duration of less than 1.3 ns (FDSS

532-Q3, Crylas) operating at repetition rates between 1 and 2500 Hz. A 1 nm bandpass filter centered on 532 nm was used after the beam to ensure a spectrally pure excitation.

The first few iterations of this setup used a 532 nm 400 mW continuous wave (CW) laser (MLL-III-532, CNI Laser) originally made for fiber-coupling, with a 1-inch focal length lens glued to the output. After it became apparent that work would be done using WGM lasers and nano-diamonds with nitrogen vacancies, the laser was replaced by a pulsed laser to enable time-resolved fluorescence measurements. Additionally, since pulsed lasers emit high peak power in brief bursts, they more efficiently induce fluorescence and lasing with decreased risk of photobleaching and damage compared to CW.

The laser power was controlled using a combination of a mechanized half-waveplate (using the same Elliptec™ software as mechanized mirrors) and a polarizing beam splitter (PBS). By measuring the power of the laser at the source and then in the side output of the PBS, the difference between the two was used to inform the power sent to the objective. As with the trapping beam, the pump beam polarization was straightened and rotated to match the SLM2 one, and the beam diameter was expanded to overfill SLM2 using lenses f_6 = 25 mm and f_7 = 200 mm.

The beam reflects from the 7.68×7.68 mm^2 SLM2 (512×512, BNS) active area and is expanded further by the 4f system formed by lenses f_8 = 300 mm and f_9 = 400 mm and sent to the microscope objective. This SLM has $\sim$ 4 times fewer pixels than the SLM used in the holographic optical tweezers, but since it was only used to displace a single beam, it was sufficient. The 605 nm dichroic is chosen due to fluorescent beads used in all pump experiments (PS-FluoRed, 15.35 µm particle diameter, Microparticles GmbH) having an excitation beak at 530 nm and and emission peak at 607 nm. The beam position was initially controlled by placing the mirror before lens f_9 at the midpoint of the 4f system to steer the beam, but for more advanced pumping schemes, there was a requirement to also displace the beam in z. Without an SLM, this meant shifting lens f_9, which would misalign the entire optical system.

3.7 Imaging and Spectrum Collection

Not all microfluidic chambers used in experiments were transparent, so sample illumination was implemented in both transmission and reflection. The transmission illumination system consisted of a white LED, lens f_5 = 35 mm, and a low NA objective (10x, NA = 0.8, New Focus) acting as a condenser. A fiber-coupled LED provided the reflection illumination focused on the back of the microscope using lens f_{11} = 200 mm.

The microscope objective collected the light from the sample plane and transmitted it through the two dichroic mirrors (830 nm short-pass and 605 nm long-pass), a long-pass 532 nm filter and a short-pass 830 nm filter removing the trapping and pump wavelengths. Despite multiple spectral filtering, some of the pump wavelengths would always make it through, especially during extremely sensitive measurements. the best solution to this was by slightly rotating the 830 nm filter, which resulted in more efficient blocking of the linearly polarized trapping beam. The light from the sample plane was then sent through a f_9 = 150 mm lens to a CCD camera (piA640–210gm, Basler), acquiring images at 1000 Hz for optical trapping experiments. Since the objective was designed for a 200 mm tube lens, this resulted in a $\frac{150mm}{200mm}$ = 0.75 reduction of the image size.

During the sensing experiments, the LEDs were turned off, and the fluorescence signal was sent to a spectrometer using a non-polarising 50:50 beamsplitter and then through a collimator attached to a multimode fiber (400–700 nm, 105 μm core diameter). Two different spectrometers were used throughout the experiments.

The first spectrometer (QE-Pro for Raman Spectroscopy, Ocean Optics) was a non-modifiable integrated module with an entrance slit size of 50 μm. As it was used for most experiments, it was integrated directly into the trapping software, typically operating at 1–5 Hz. Due to its relatively low resolution of 1.7 nm full width at half maximum (FWHM), another spectrometer was temporarily used during the WGM experiments described in Chapter 3.

That second spectrometer (Kymera 328i, Andor) was used with an integration time of 0.1 s, with a grating with 1200 L mm^{-1} with a 532 nm blaze. The entrance slit was 10 μm wide. This spectrometer was modular, with a separate spectroscopic camera (Newton 970 EMCCD, Andor) operating at 100 Hz with no electron multiplier gain and at a temperature of -70° C. This spectrometer had a much higher resolution of 35 pm.

3.8 Sample Preparation and Experimental Methods

Several experimental stages must be reached before the newly aligned optical system can be used to trap a membrane. To prepare the setup, the following protocol was used:

A sample was prepared by diluting a solution of beads in D_2O, which has a lower absorption at higher wavelengths, resulting in lower heating of the medium during trapping [206]. The exact dilution would depend on the initial concentration of the beads, and samples will be placed under the microscope and diluted further until, on average, less than two particles are visible in the 50×50 μm^2 field of view of the objective. This ensured multiple particles wouldn't be held in the same trap.

A 100 μm thick vinyl spacer sticker would be placed on a clean glass microscope slide, and $\sim$200 μL of the diluted solution of beads was placed in the center using a pipette (20 - 200 μL, Eppendorf Research). A 170 μm glass cover slip was attached on top using clear nail varnish, forming a sealed chamber as shown in Figure 3.11.

Particular care needs to be taken to prevent any air bubbles from forming at this step, as the compressible air introduces a lot of extra motion to the sample, and creates an area where trapping in not viable.

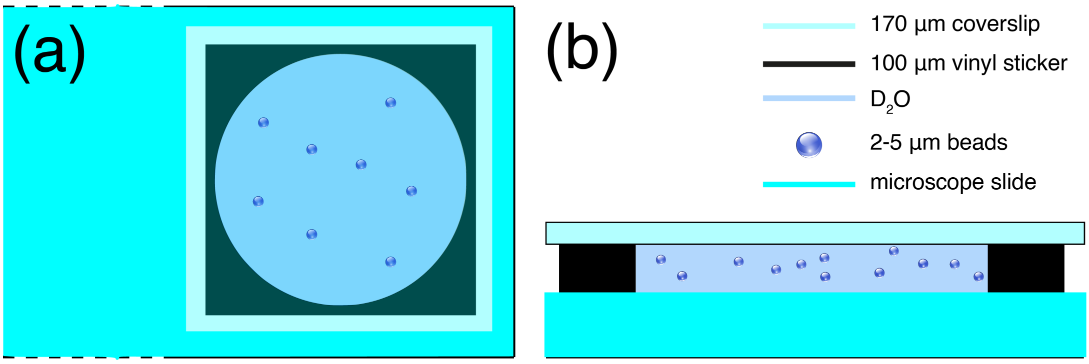

Figure 3.11 Schematic of the typical sample used in optical trapping experiments throughout this work from (a) the top and (b) the side.

All of the published results were acquired using the simple chamber described above. It has several limitations, starting with the large (relative to the field of view of the microscope objective) area. This simple limitation was what comprised the vast majority of experimental time during this thesis, especially when working with a variety of particle sizes and shapes. The samples need to be sparse enough to prevent multiple particles being attracted into one trap. This resulted in samples where just finding the correct combination of large and small particles and membranes could take hours, as the sample was scanned for the rarest component, which was then slowly dragged along in the optical trap until all of the required particles were within the field of view. This chamber design was also static in nature meaning once sealed no new particles could be introduced making each chamber single-use. Other microfluidic designs involving microfluidic channels for sample delivery were experimented with throughout this thesis, and they are described in Chapter 7.

Once the sample slide was prepared, it would be transferred to the optical setup for initial trapping. First, a drop of refractive index matching oil ($n_{oil} = 1.33$) was applied to both the surface of the coverslip and the top of the microscope objective. While the objective is a water immersion one and could in theory work with just water, the added viscosity of the oil aids with longevity of experiments as the objective was upside down.

The 830 nm laser would be turned on, and focused on the top of the glass coverslip. The reflection of the laser would serve as a very simple indicator of the z position in the microfluidic chamber, with the reflection appearing at the top and bottom of the coverslip as well as the top of the microscope slide. Using these reflections as guides, the laser would be focused in the centre of the microfluidic chamber and a particle would be found and trapped. The easiest way to establish if the particle is trapped is by translating the sample stage in x,y and z with other particles visible in the background. The appearance of the trapped particle should not change as the stage is translated, as it stays at the location of the laser focus.

This initial check is done to ensure the sample is still viable for trapping, as depending on the time since initial preparation, the size of the particles, the cleanliness of the sample, and the static charge of the coverslip, the electrostatic forces between the particles and the top and bottom of the chamber can be stronger than the trapping strength of the laser. This is particularly relevant when trapping larger particles (<5 µm), polarizable particles such as vaterite and of course the flat membranes which stick to the glass particularly well. To slow down this process the glass surfaces can be treated with oxygen plasma to remove any excess charges right before assembling the chamber. One method of releasing the particles is gently tapping the sample, with the trapping laser just below the particle. For membranes with a gold mirror on them this is much easier — simply by focusing the beam behind the membrane it can be lifted like a sail as the light is reflected and pushes the membrane up. Another advantage of the metal on the membranes is that when working with illumination in reflection, the membranes are clearly visible.

3.9 Optical Trap Control

While most of this Chapter deals with the physical components needed to realize optical trapping and subsequent analysis, a key piece of software was developed throughout this work to precisely manipulate the motion of the particles and membranes. The initial version was written Blair Kirkpatrick and Tomas Čižmár and refined by Meisam Askari. The code was then rehauled and rewritten from the ground up by Henry Archer and myself during a summer project. The full LABVIEW program can be found in the repository of this thesis at https://doi.org/10.17630/3bd2a243-71be-4667-b8ee-ded7be7e472e.

At the core of its function, the LABVIEW code controlled the SLMs' pixels and captured and recorded the data from the CCD and spectrometer.

The SLMs were controlled by projecting blazed gratings and Fresnel lenses on their surface, allowing for real-time 3D control of the optical traps and the pump laser. A phase mapping was manually adjusted by changing the offset and multiplier of the voltage of each pixel, resulting in a linear phase profile from 0 to 2π, with most of the power being diverted into the first positive diffracted order of the diffracted trapping beam. By combining the phase masks for the displacement of the beams, up to 6 traps could be simultaneously controlled with a refresh frequency of 10 Hz.

The software used an input from a PlayStation 4 game controller, chosen due to the joysticks being well-suited for the tilting of objects in 3D. An additional overlay of the imaging allowed for tracking the position of the traps and the pump laser even when filters were used.

The typical workflow for using the trapping software is shown in Figure 3.12. First, the imaging and overlay portion of the software was set up using calibration standard beads (9000 Series Glass Particle Standards, d = 2±0.05 µm, Thermo Scientific). The initial calibration was set by:

$$x_{real} = x_{pix}\frac{d_{img}}{d_{tube}}M \tag{3.1}$$

where x_{pix} is the pixel size of the camera, M is the rated magnification of the microscope objective, d_{img} is the focal length of the imaging lens and d_{tube} is the designed tube lens length [207]. The 830 nm long pass filter was removed, and the laser beam was focused on top of the coverslip. The final calibration was adjusted in the software by translating the first order of the beam using a blazed grating and matching the overlay to the final position of the beam. Afterwards, the filter was placed back in front of the CCD, finishing the x-y calibration. The pump laser position and multiplier were calibrated in a similar fashion, to account for the different scaling due to a shorter wavelength of 532 nm. The last portion of the calibration was to find the ”true center” of the trapping beam alignment. This was required due to the large defocusing of the trapping beam through Fresnel lenses when translating the beam in z. The defocusing results in slight astigmatism, i.e. a translation of the beam in x and y as the displacement in z increases. This astigmatism is 0 at the exact centre of the alignment, and gradually increases the further away from this centre it is. As such, when manipulating an object such as a membrane, to ensure stable trapping the centre of the membrane was placed at the exact position where aberrations would be minimal. When working with membranes, the calibration was further done by adjusting the distance between the four traps holding onto each corner of the membrane. This ensured the membrane could be lifted from the bottom of the sample into the middle of the microfluidic chamber and tilted by 45 degrees without the membrane falling out of the traps.

The software received input from the controller or mouse and processed them differently depending on whether it worked in the individual trap or membrane mode.

Up to 6 individual traps could be controlled in x,y, and z. The initial trap position could be set in-plane by either clicking that spot with a mouse, or translating the trap using a joystick. Each time a trap was moved, a new SLM mask would be calculated and multiplied with others. The traps were turned on and off using a single button. The laser power was dynamically altered depending on the number of traps as each new one shared the total available laser power, and relative trap power was set by a multiplier altering how prominent the holographic mask was for that trap. The imaging overlay tracked the exact position of the traps in x-y, and the numerical x,y,z position of each trap could be seen at all times.

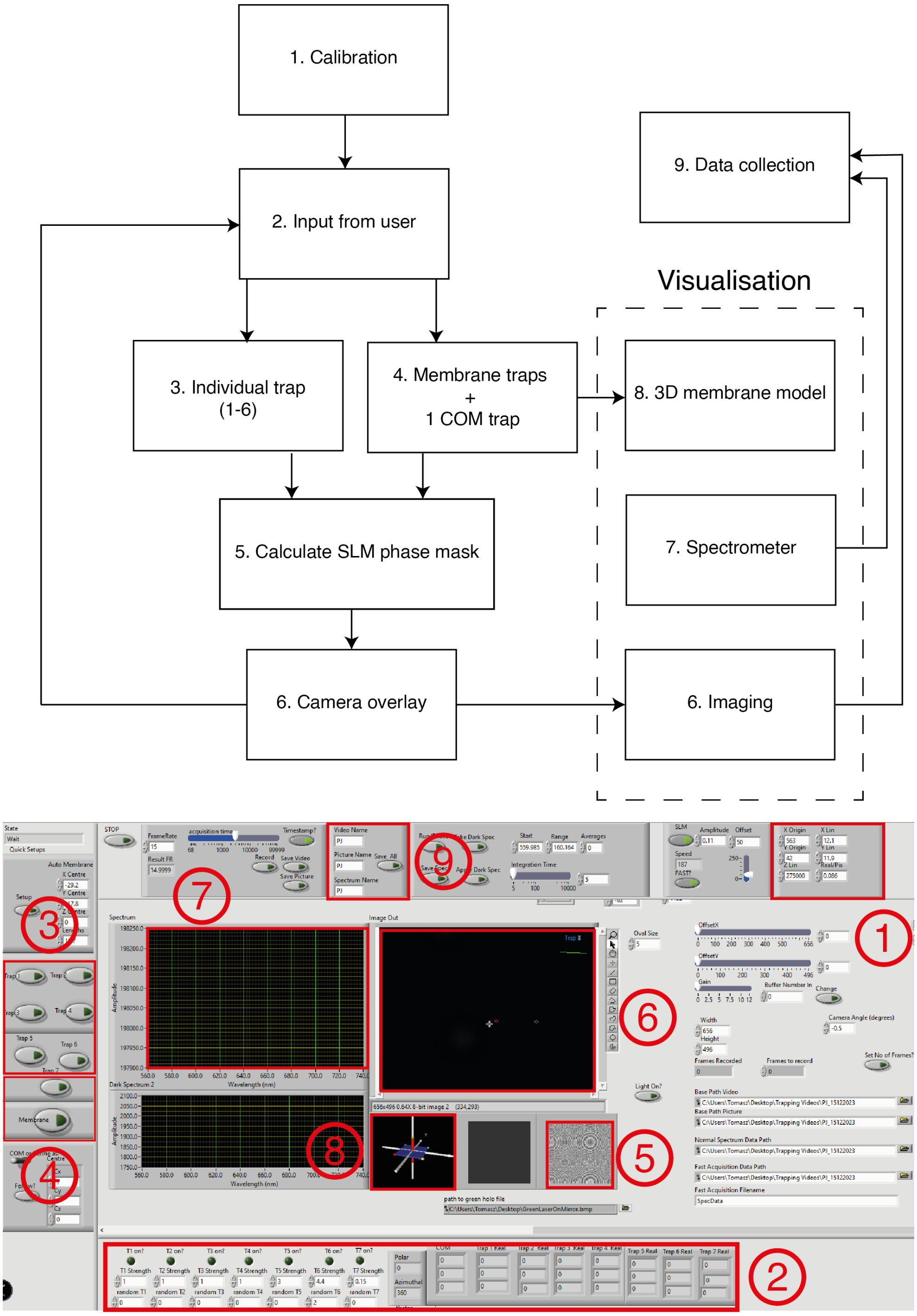

Figure 3.12 Flow chart of the LABVIEW software used to control the holographic optical tweezers. Below the flow chart is a screenshot of the front panel, with all steps marked with individual numbers. The full LABVIEW program can be found in the repository.

The membrane was controlled by coupling four traps together, placing them in a single plane as the corners of a square with a side length of 15 µm. By tracking the centre-of-mass (COM) and projecting the normal from it, an azimuthal and polar tilt angle could be calculated, allowing for not only in-plane rotation but also the pitch and yaw of the membranes. A comparison between the control of beads and membranes is shown below in Figure 3.13.

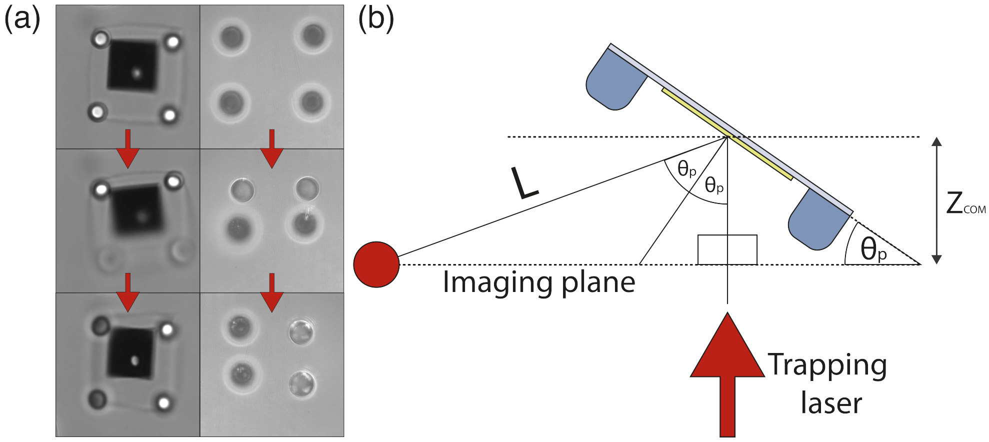

Figure 3.13 (a) Demonstration of full 3D control of multiple beads and membranes, with control over both pitch and yaw shown side-by-side. (b) Depiction of the beam reflected by the membrane, where θ_p denotes the polar angle at which the membrane is tilted. The membrane is shifted from the microscope's focal plane by a distance $\mathrm{Z_{COM}}$, and the reflected beam intercepts the imaging plane at the coordinate indicated by the large red dot.

As the membrane was commonly used as a mirror for reflecting beams, an extra 7th point was added to the overlay to track the intercept of the reflected beam and imaging plane, with the point having coordinates of:

$$x = X_{COM} + Z_{COM} \tan{(2\theta_p)}, \tag{3.2}$$

$$y = Y_{COM} + Z_{COM} \tan{(2\theta_a)}, \tag{3.3}$$

$$z = 0 \tag{3.4}$$

where θ_p and θ_a are the polar and azimuthal angles of the membrane, respectively, and X_{COM}, Y_{COM}, and Z_{COM} are the x,y, and z coordinates of the membrane COM.

Two types of data were also acquired using the software, videos and spectra. For the acquiring of videos, the interface allowed for the dynamic change of the framerate, exposure, gain, and cropping of the frame being imaged. For optical trapping experiments where the motion of the particle has to be analyzed high framerates of hundreds of Hz are required, ideally with no gain as it introduces artificial noise. This becomes more complicated, as the processing speed of the camera and the light entering the shutter decrease. To that end, to achieve the high acquisition speed the frame would be cropped to 128x128 or 64x64 pixels, with minimal exposure speed of ms and as much light as possible from the condenser illuminating the particle. In order to ensure the processing lag of the labview overlay didn't affect the high speed measurements, the camera's original software (Pylon Viewer) was used for data acquisition of all high speed footage.

Spectra were acquired by first taking a dark background reading, saving it for later reference and taking it away from the rest of the spectrum. The software was able to also control the boxing, averaging, and acquisition speed of the spectra, as well as display the position of the spectrum peaks. High-speed acquisition of the spectra could be set up, with hundreds of spectra being acquired consecutively for time-resolved experiments. While separate codes were developed for the analysis of the spectra in different cases, these will be covered in Chapter 6. The code used throughout the thesis to analyse videos and convert them to a measure of trap stiffness is described below.

3.10 Data Analysis

A MATLAB code was used to analyze the motion of trapped particles. The code is based on the shift property of the Fourier transform [164]. It was used to track the center of mass of the particles and convert them to a readable measure of trap stiffness. The flow chart of this code is shown in Figure 3.14.

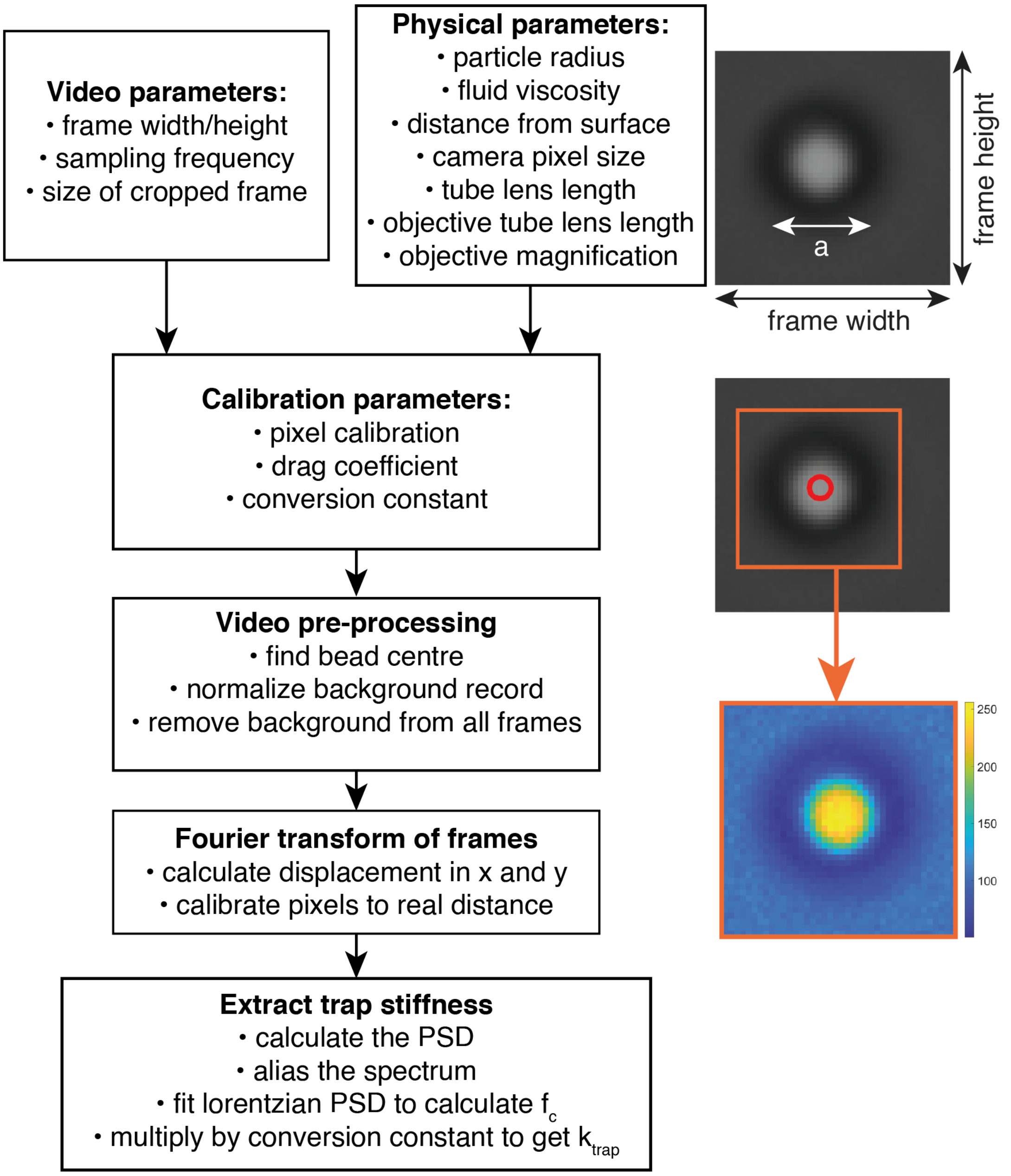

Figure 3.14 Flow chart of the MATLAB software used to analyze the motion of the trapped particles and calculate the trap stiffness. This software can be found in the repository.

Videos are loaded together in separate folders, with names containing important metadata such as trapping power and bead size. A background video without the particle is also loaded. The identical parameters for each video are set up - the size of the frame (typically 64x64 pixels), the framerate, and the approximate size of the particle in pixels which will decide how much further the video is cropped. The physical parameters are also set, and used to calibrate the pixel size (eq. 3.1), the drag coefficient γ_0 (eq. 2.3) and the conversion constant involving a correction for additional drag forces present near the surface of the glass (Faxen's correction [98]):

$$\beta = \frac{\gamma_0}{1 - \frac{9}{16}\left(\frac{a}{h}\right) + \frac{1}{8}\left(\frac{a}{h}\right)^3 - \frac{45}{256}\left(\frac{a}{h}\right)^4 - \frac{1}{16}\left(\frac{a}{h}\right)^5} \tag{3.5}$$

where h is the distance of the particle from the nearest surface.

Before the videos can be converted to a list of displacements in x and y, the software symmetrizes the frames. It looks for the brightest, most circularly symmetric spot indicative of the COM of the particle. This point serves as a reference, and the video is cropped around it. The background frames are then normalized and removed from the video, leaving only the particle at the center of the first frame.

Each consecutive frame of the video is then Fourier transformed, and the shift in x and y relative to the initial frame is recorded as a displacement. The resulting value is multiplied by the calibration constant, resulting in a time-distance plot such as the one shown in Figure 3.15 (a) and (b), where each graph has 10,000 points, corresponding to 10 s of footage recorded at 1000 fps.

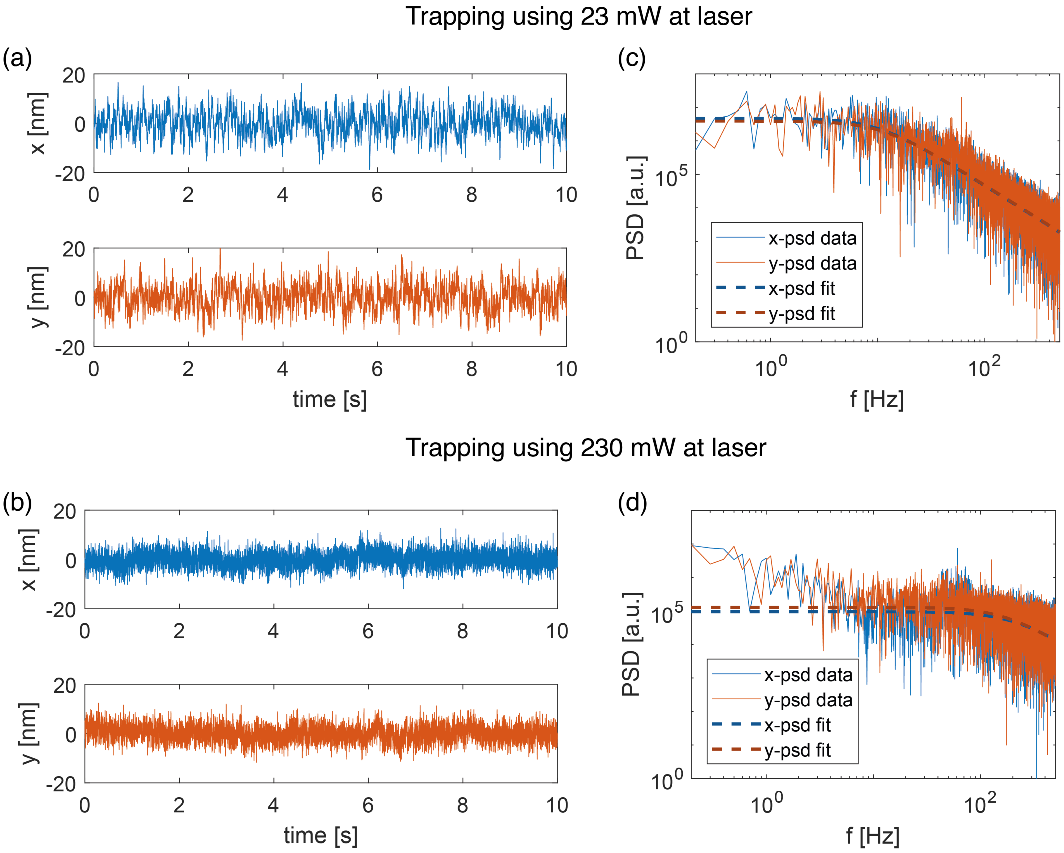

Figure 3.15 Trajectory comparison between the trapping laser at 10% (top) and 100% (bottom) power.

To extract the trap stiffness from the data, the power spectral density of the motion was analyzed, as described in Chapter 2. This method takes advantage of the spectrum having a characteristic shape of a Lorentzian of the form:

$$PSD(f) = \frac{k_B T}{2\pi^2 \beta (f^2 + f_c^2)}. \tag{3.6}$$

First, the absolute value of the particle motion in one direction is Fourier transformed and squared to acquire the power spectral density (PSD). The two halves of the spectrum are then averaged and plotted against the frequency on a log-log scale as shown in Figure 3.15 (c) and (d). An analytical Lorentzian is then fitted to this spectrum, yielding a corner frequency f_c, which is then converted to trap stiffness using:

$$k_{trap} = 2\pi \beta f_c. \tag{3.7}$$

This method means that the system is very sensitive to any sources of vibration. Peaks can often be seen at 50 Hz due to the mains frequency, as well as any undampened frequencies let through by the optical table such as that of heating pipes under the floor. To combat this, the optical tables which the experiments were always lifted using nitrogen to dampen any vibrations.

3.11 Further Optical Setups

The final plan for the optically trapped membranes is to use them to tether to a biological sample for single molecule force spectroscopy. The plan is to use the exceptional intrinsic stability of the membranes, coupled with the additional engineered stability brought about by the HMSs, to detect the minute forces involved in unzipping and ripping apart B-DNA molecules. This will be achievable due to the large size of the membranes — under normal circumstances, optically trapped beads have been tethered to DNA and used to test its spring constant, but the forces produced in tweezers are usually not enough to unzip the DNA.

For future experiments involving using the membranes and other structures to interact with biological specimens and using the flat profile of the membrane for extremely sensitive force detection, additional optical setups were designed, constructed, and calibrated throughout this PhD work. A high-quality imaging system was required alongside optical manipulation for biological work, so a custom optical tweezers system was incorporated into an existing commercial Nikon microscope. Two optical setups were constructed for work requiring precise force measurement, including one with a QPD for force measurement and one using homodyne interferometry to measure minute displacements.

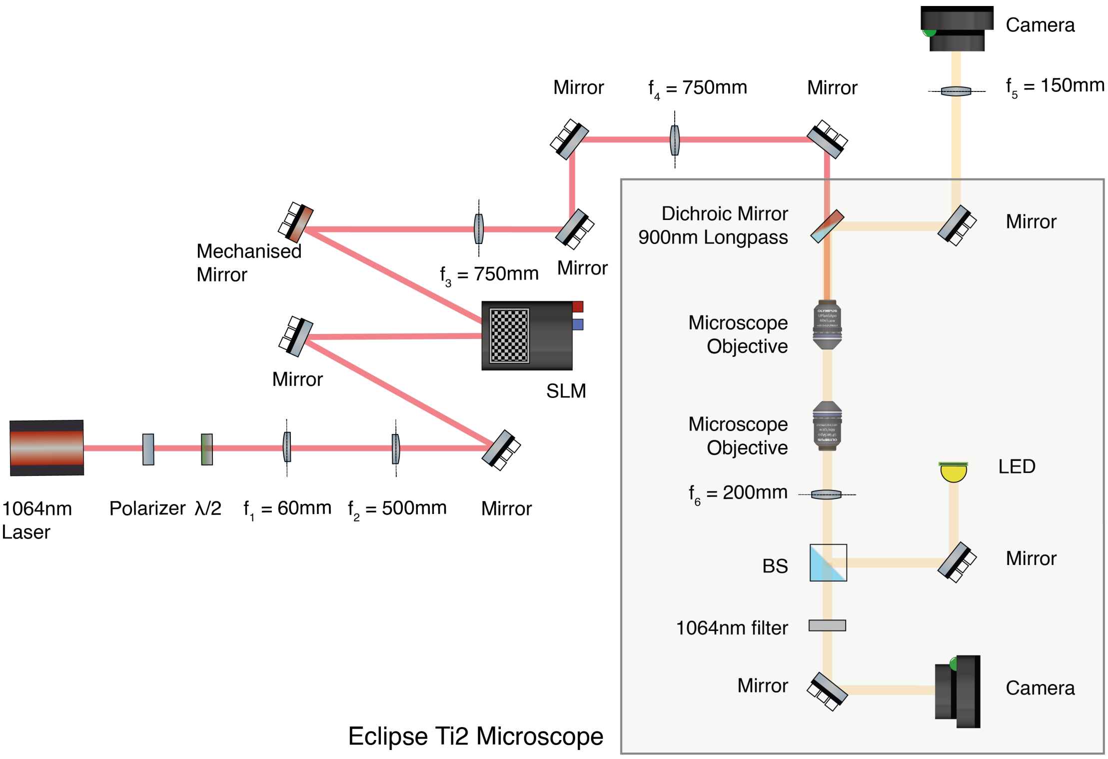

Figure 3.16 Double objective holographic optical trapping system built into a Nikon TiE2 microscope body,

3.12 Double Objective Trapping Setup

With an identical working principle as the setup described in the previous section, this system has two key differences, the first being that the microscope objectives, the stage upon which the sample is placed, illumination, and high-quality imaging are placed inside a Nikon TI2 Eclipse microscope body and controlled using the Nikon AR Elements software. This geometry also enforces the other key difference: the trapping in this setup is realized from above the sample.

The trapping setup here consists of a 10W CW (1064 nm, Opus) laser with a beam diameter of 1.85 ± 0.2 mm sent through an 8.3 beam expansion and polariser-waveplate combination, using lenses f_1 = 60 mm and f_2 = 500 mm. It is then reflected and modulated by the 1920×1152 SLM (Meadowlark) with a 17.6×10.7 mm pixel array, placed in the conjugate plane of the objective back aperture. It is then sent through a 4f system of lenses $f_3 = f_4$ = 750 mm. The trapping uses a 1.2 NA water immersion objective (C-Apochromat 63X UV-VIS-IR, Zeiss).

The system allows for simultaneous imaging from both above and below. This means one camera is dedicated to tracking the optical traps, and one can do both wide-field and single-molecule imaging depending on requirements. The first of the imaging systems is placed above the trapping objective, where the EPILED acts as a light source, the bottom objective acts as a condenser, with the visible light reflected by the 900 nm longpass dichroic mirror, through lens f_5 = 150 mm into the camera (piA640–210gm, Basler). The second imaging system uses the bottom objective and lens f_6 = 150 mm to relay the image through 2 sets of filter cubes for pump and probe experiments into the high-quality camera (iXon Ultra, Andor). This leaves another port in the microscope open for additional lasers to be added for fluorescence imaging. Due to its extreme sensitivity, the iXon Ultra camera was chosen for single-molecule imaging. The objectives can be displaced in z, while the stage can be displaced in x and y.

Calibration Trapping Setup

Before any biophotonics experiments can commence, the membrane motion must be characterized. A combination of CCD, QPD, and interferometer detection will be used to fully understand the membrane dynamic and the effect of membrane size, handle size, and shape on the stability of the membranes. The interferometer will be equipped with a single-frequency laser for better coherence length, and signals from the QPD and interferometer will be used to construct a PSD analysis of the membrane motion. Below is the summary of the work done so far to this end.

The setup shown in Figure 3.17 was built for calibration purposes, and the optical elements were chosen to be more suitable for holographic optical trapping. The large size of the SLM meant that standard 1-inch optics would result in spherical aberrations of the trapping beam, so all optical elements the trapping beam passes through were chosen to have a 2-inch diameter.

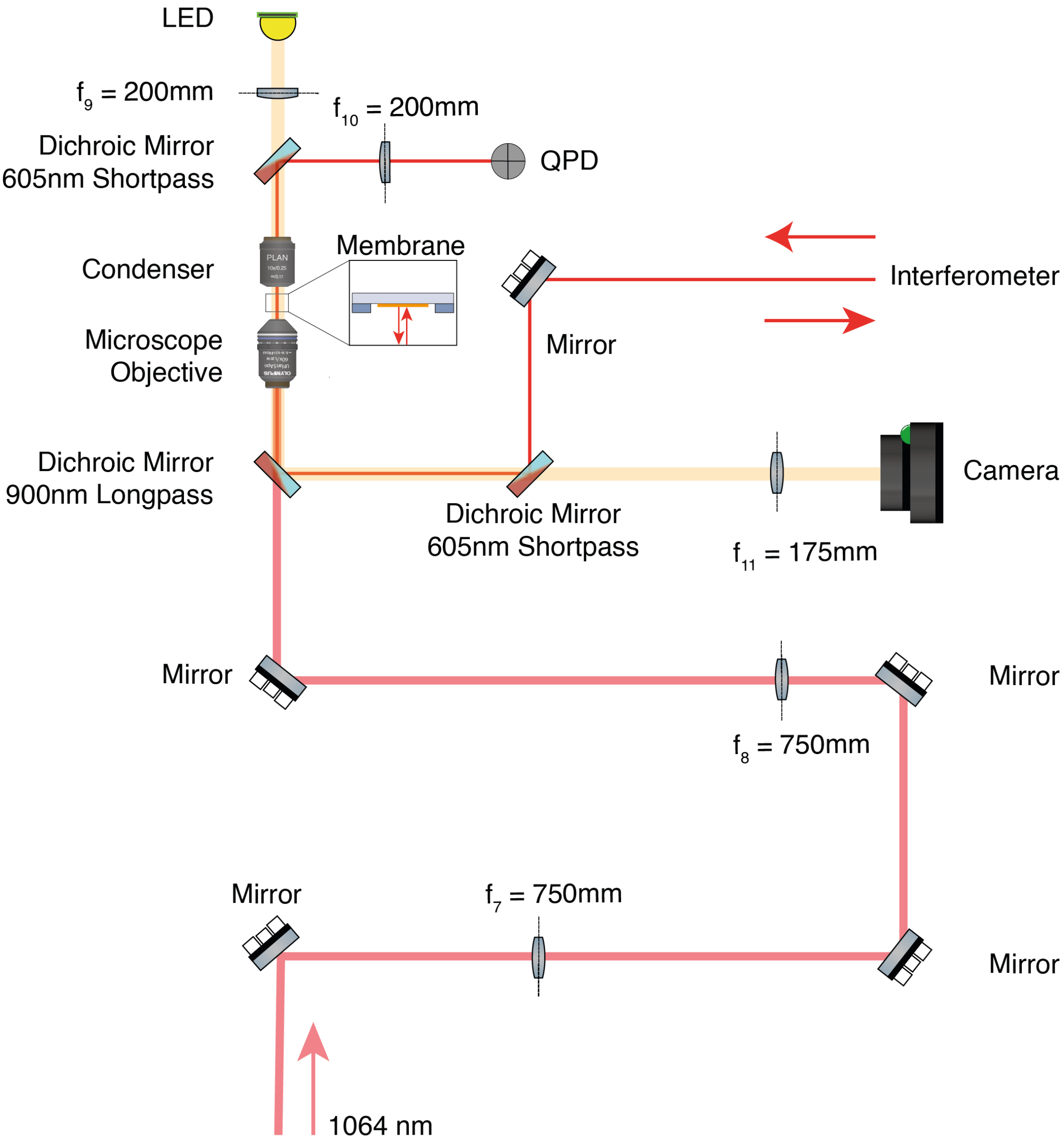

Figure 3.17 Trapping setup for detecting the membrane motion using a combination of interferometry and QPD.

A mechanized mirror was used to redirect the beam path and integrate it with the previous microscope-enabled setup. The SLM is coupled to the backplane of the trapping objective (UPLSAPO60XW, NA = 1.2, Olympus) using a 4f system consisting of lenses $f_7 = f_8 = 750$ mm. The microscope is mounted upside down, and a 5 nm precision stage with a closed loop piezo control is used to displace the samples. Imaging is done using light from an LED mounted above the condenser and focused on its backplane using lens $f_9 = 200$ mm, which is then reflected by a 900 nm dichroic mirror and focused on the CCD camera (piA640–210gm, Basler) using lens $f_{11} = 200$ mm.

Motion detection is split between three different methods. The first, as described in Chapter 3, is the high framerate footage of the beads, which we can extract individual motion in x,y, and z from. However, since this setup is focused on calibration of the membrane motion, a QPD is used to provide a high bandwidth means of measuring the bead displacement in x,y, and z. The laser used for this is a stable 633 nm laser with a coherence length of 10 m (Compact Red Laser, CryLaser), expanded by lenses f_{12} = 200 mm and f_{13} = 400 mm, delivered through the microscope objective to the sample plane and collected by the condenser and focused on the QPD using lens f_{10} = 200 mm. The other use of this laser is for homodyne interferometry, using the reflective gold mirrors on top of the polymeric membranes to detect their motion.

Phase Interferometry Setup and Implementation

Vibration measurement typically employs one of two schemes, homodyne or heterodyne [208, 209]. For this study, a homodyne Doppler vibrometer will be constructed, utilizing phase quadrature detection [210, 211, 212, 213]. This will involve encoding the membrane movement's direction directly into the light's phase. As conceptualized in Figure 3.18, the basic setup employs a Michelson interferometer configuration. The laser beam is split into orthogonal polarizations for the reference and measurement arms, recombined after reflection, and passed through a quarter-wave plate, producing circularly polarized beams. These are then split and sent through crossed polarizers to two photodiodes. After the offset is removed, the resulting detected signals are:

$$S_1 = const \cdot \sin\left(2\pi\frac{2\Delta d}{\lambda}\right), \tag{3.8}$$

$$S_2 = const \cdot \cos\left(2\pi\frac{2\Delta d}{\lambda}\right), \tag{3.9}$$

where Δd represents the membrane displacement and λ the wavelength of the laser. The displacement can be determined as:

$$\Delta d = \frac{\lambda}{4\pi}\arctan\left(\frac{S_1}{S_2}\right). \tag{3.10}$$

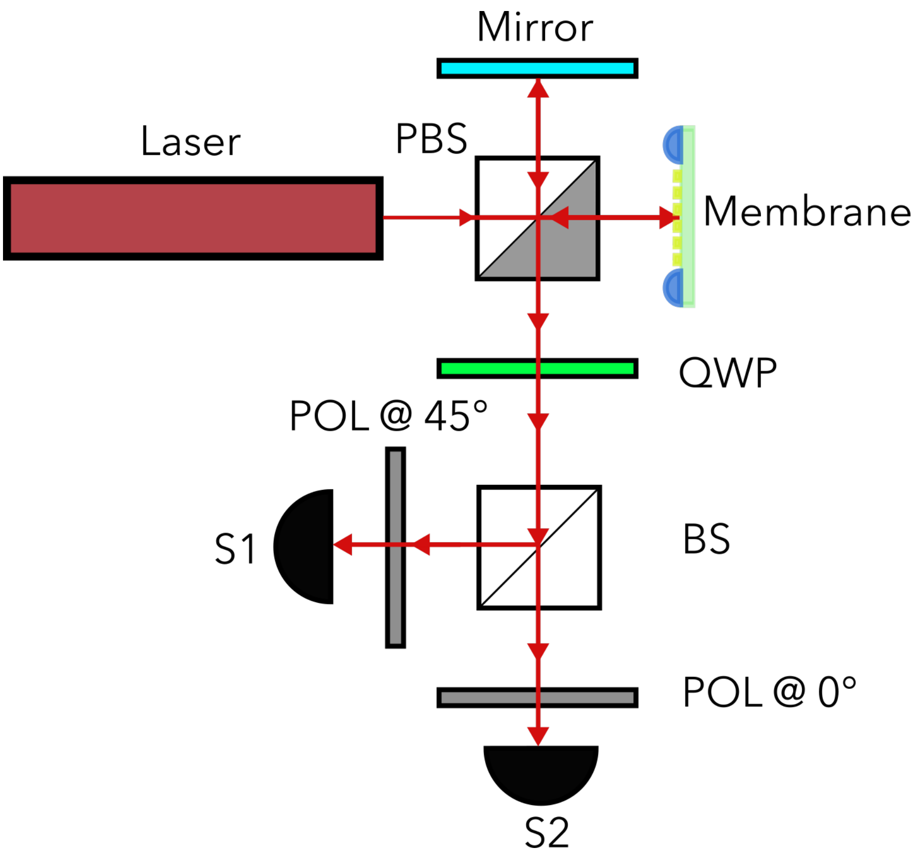

Figure 3.18 Basic schematic for the phase interferometer. PBS is a polarizing beam splitter, QWP is a quarter waveplate, BS is a beam splitter, S1 and S2 are signal 1 and 2, respectively.

The current test version of the interferometer, illustrated in Figure.3.19, operates with a 633 nm laser, expanded and collimated using lenses f_{12} = 200 mm and f_{13}= 400 mm. A half waveplate followed by a polarizing beam splitter divides the beam, while quarter waveplates prevent back reflection to the laser. The reference mirror and a piezo-attached mirror reflect the beams, which interfere with recombination at the polarizing beam splitter. The interfered beam then passes through another quarter wave plate, a non-polarizing beam splitter, and crossed polarizers. Lenses with focal lengths f_{14} = f_{15} = 50 mm focus the beams onto photodiodes (S3883,Hamamatsu) connected to photodiode amplifiers (C8366,Hamamatsu). The signals, in quadrature, are transmitted to a connector board via BNC cable and processed through a high-pass frequency filter.

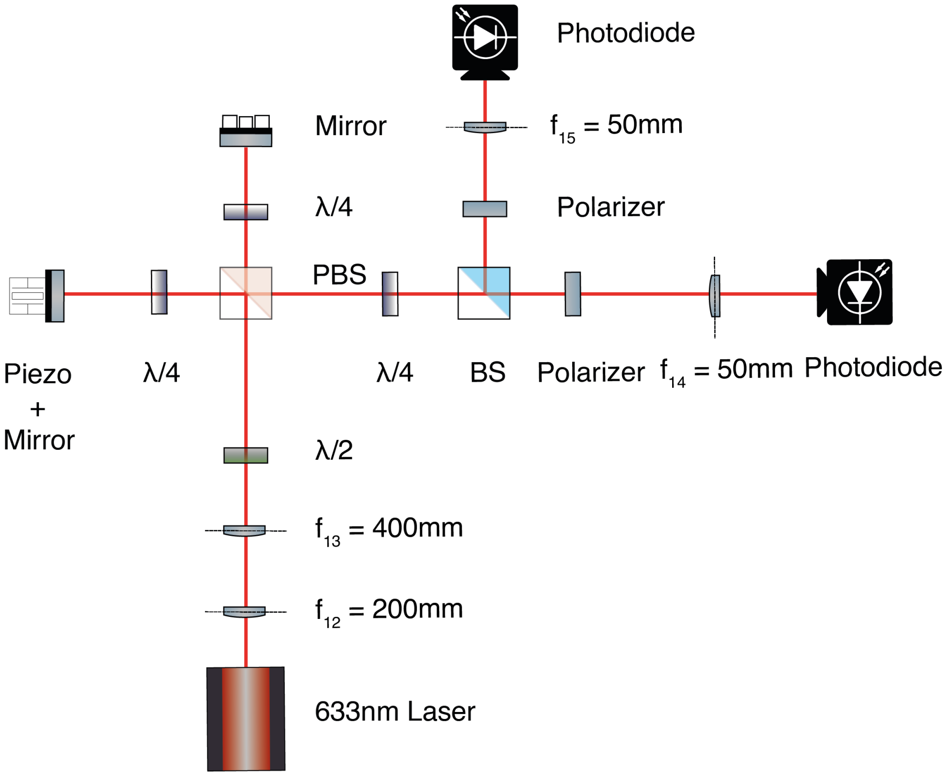

Figure 3.19 Optical setup for a test version of the interferometer.

Electronics and Signal Processing

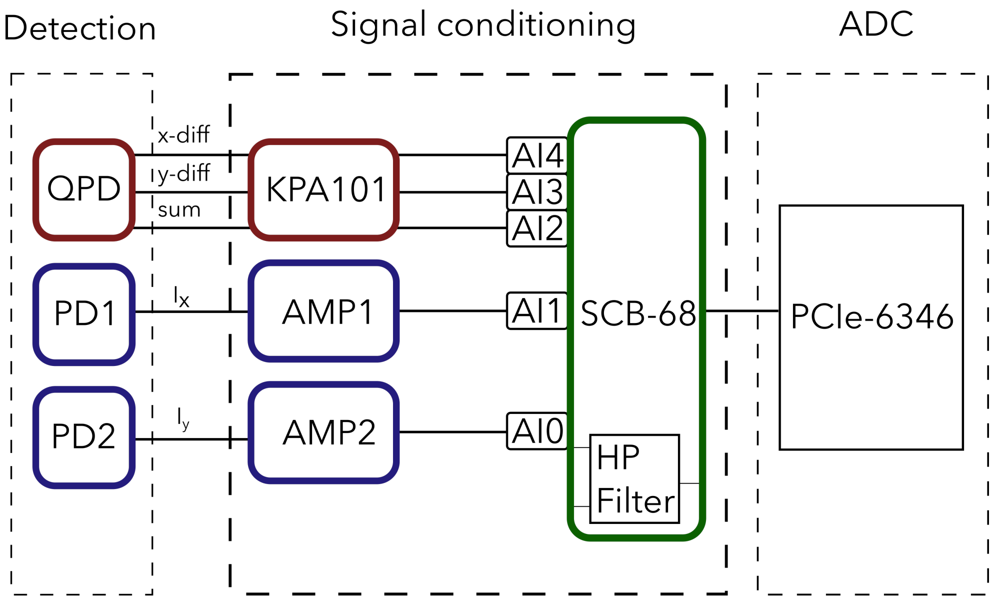

Figure 3.20 Data acquisition flow. QPD picks up 3 signals, which are transferred through a position aligner and the connector block to the data acquisition (DAQ) card without any conditioning. Photodiodes pick up a single signal each, which is amplified and filtered using the connector block before being passed to the DAQ.

As shown in Figure 3.20 The signals will be received through a 68-pin connector block (SCB-68, National Instruments), connected to a DAQ card (PCIe-6346, National Instruments) chosen due to its ability to sample 500 kS/s/ch, from 8 simultaneous differential analog inputs, leaving more than sufficient bandwidth for the expected motion of the membranes. LABVIEW will be used for signal processing of both the QPD signals and interferometer signals while integrating control over the Nikon microscope, as well as with the top camera, meaning the calibration process can be automated, and everything can be controlled and monitored using a single interface. While the QPD required no further conditioning, the photodiodes are connected to amplifiers which output an AC signal with a DC, which will be removed using a high pass filter placed in a signal conditioning section of the DAQ card.

The QPD will be used with the 633 nm laser, as shown in Figure 3.17 A separate laser was chosen as the trapping 1064 nm laser will be used in a holographic application, and the QPD is only capable of tracking one point at a time. The QPD outputs 3 raw signals, the x-diff, y-diff, and sum signals, which correspond to the displacement of the particle displacement in x, y, and z. The calibration requires sticking a bead to the bottom of the microfluidic chamber and moving the stage a known amount, which is achieved using the motorized microscope stage, which in turn produces a characteristic shape shown in Figure 3.21

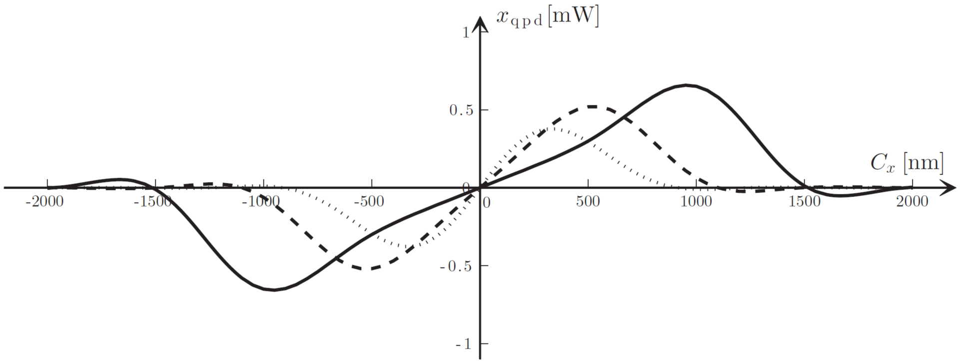

Figure 3.21 Characteristic shape of the spectrum detected when scanning along a bead. [99]

From there, the center linear slope is taken and used to convert between the voltage and displacement of the bead. The assumption is that the displacement will be limited to the linear portion of the calibration curve when the particle is trapped. The signal is then picked up by a Thorlabs KPA101 Position Aligner, which outputs the signal directly through an SMA connection to the connector block in a monitoring configuration with no further signal conditioning, where it is read and converted by the analog to digital converter. This should be compatible with the sphere-like features placed in the center of the membranes, where by analyzing the calibration curve left behind by the membrane when stuck to the bottom of the microfluidic chamber and moving the stage a known amount, we should be able to calibrate the membrane motion. However, since this method has its limitation in only working when there is a dome-like feature in the center of the membrane, and the final goal is flat HMS membranes, the next step is to focus on the z displacement using phase interferometry.

3.13 Conclusion

The single objective holographic optical system shown above was rebuilt completely around 8 times in total throughout this work, with new components being added until it reached its final form, shown here. The biggest challenge in rebuilding was the small form factor (the available optical table space was less than 1x1.5 m^2), the fact that the initial system was built as close to the surface of the optical table as possible making it impossible to use 2 inch optics, and the decision to use a 30 mm cage system in order to align the optics. This was chosen in order to aid with the alignment — when all of the components are used the system consists of two illumination sources, two lasers, a camera and a spectrometer all aligned within microns of each other. The compact nature of the cage system simplifies this alignment at a cost of needing to take everything apart each time a new element needs to be added. The software used for controlling the systems is already large and complex, but could be further expanded in future in order to control the lasers and motorized mirrors. Much like the physical setup, LABVIEW has the ease of integration on it's side — with minimal knowledge of the inner workings of a machine it can be interfaced with the rest of the system, but the complexity of the software grows rapidly with more components. At this point it has reached stage where I believe the best step forward is to modularize the code and rewrite it in a traditional coding language such as MATLAB to keep it maintainable in the future.

The other optical systems have been characterized and are ready to be used for future experiments, including force sensing and biological specimens — details of these experiments can be found towards the end of Chapter 6.

The fabrication methods discussed in this Chapter do not just apply to optically manipulated membranes — all HMSs were fabricated using the same workflows, typically in less time as typical MS design accounts for at most one re-alignment as opposed to the five in a row seen here. The next Chapter serves as a intrduction to one more fabrication method not covered here, CO_2 ablation. Unlike EBL, which can be quite intimidating at takes months to learn and years to master, ablation was developed during this thesis as a simple way of forming on-chip optical traps. The next two Chapters, 4 and 5 will deal with optical trapping on-chip done during the duration of this PhD work, using the single objective holographic setup to trap particles using microstructures and HMS before returning to the experimental applications of the membranes as well as detailed future plans for the optical setups described towards the end of Chapter 6.

CHAPTER 4

Micromirrors for On-Chip Optical Trapping Arrays

After the extensive time spent fabricating complex structures using complicated cleanroom techniques and spending months building setups described in the previous Chapter, there was a curiosity about whether it would be possible to achieve optical trapping without the exhaustive process.

Over the past two decades, numerous techniques have been developed to facilitate on-chip trapping. These methods range from creating optical lattices through interference techniques [214] to near and far field trapping utilizing fibers [215]. Innovations have aimed at replacing the traditional microscope objective with high NA optical lens equivalents that maintain a smaller footprint, achieving similar focusing performance [216].

One alternative involves the use of Fresnel diffractive elements [217, 218, 219], although fabricating these elements is often costly and time-consuming, and they exhibit chromatic aberrations. These small and delicate components are also prone to damage, while still not providing the same trapping quality as the microscope objective they are designed to replace. Microlenses and micromirrors [220, 221] present a more robust solution, avoiding some fabrication and sensitivity challenges. High NA arrays of traps can be efficiently created by imprinting pre-made lenses [222, 223]. However, this approach is limited by the available variety of consumer lenses.

To address this, both this Chapter and Chapter 5 focus on methods for creating custom high-quality optical traps without needing a microscope objective. An important thing to note is that despite these devices' design not requiring an objective, all measurements are still done using one. In both this Chapter and Chapter 5, the beam would be focused on the back of the objective resulting in a collimated beam coming out of the objective as shown in Figure 3.9. The objective was used to validate the claim that our methods reached the same trapping efficiency as a commercial objective. Through this, the objective is mostly used to record the particle motion and is not strictly required.

This Chapter will cover the process of fabricating optical trap arrays on glass slides using CO_2 ablation, the characterization of the traps, and finally, demonstrating the ability to reverse the circular polarisation of light incident on the traps by rotating a vaterite particle, as shown in Figure 4.1.

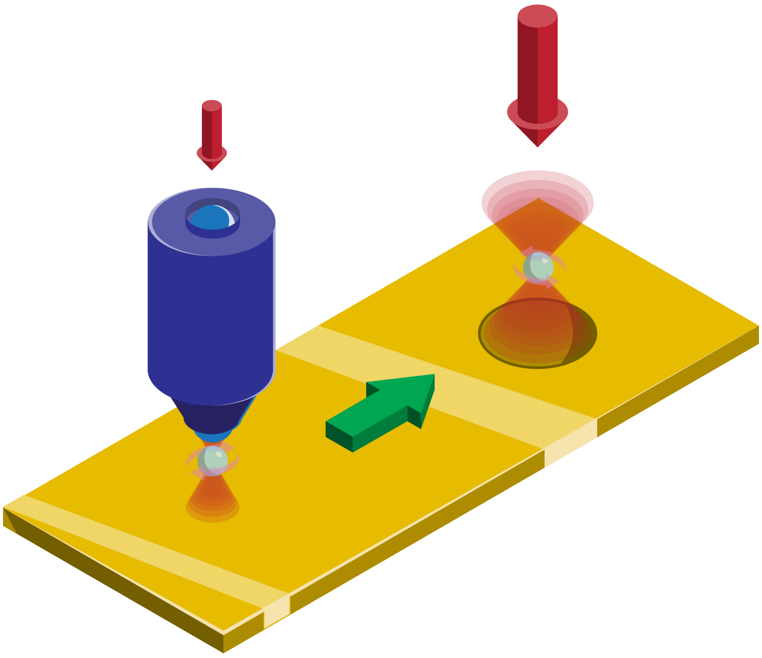

Figure 4.1 Concept image for the experiment. A clockwise-rotating vaterite particle is trapped using an objective and then handed over to a trap created by a micromirror, where it begins rotating anti-clockwise as indicated by the arrows around the particle. Taken from [204].

4.1 Micromirror Fabrication

A notable method for creating micromirrors involves silica CO_2 laser ablation, a process where a focused CO_2 laser beam, typically at a wavelength of 10.6 µm, is used to melt glass. This technique utilizes silica's high absorbance for radiation above 4 µm [224]. By delivering a short pulse ($\sim$100 ns), the laser evaporates the glass directly at the focus, creating a hemispherical mirror as the vapor pressure forms a melt front that moves away from the center, solidifying almost instantaneously [225]. This entire process is completed in less than a second [226, 227].

In our work, we enhance this method by using a CW CO_2 laser to write micromirror structures rapidly and with greater customization. The glass substrate is exposed to a focused TEM_{00} mode of the laser for about 100 ms, resulting in a nearly parabolic mirror profile [228]. Subsequently, the glass is coated with a thin layer of gold to provide a smooth, reflective surface. This technique allows for precise control over the diameter and depth of the micromirrors, making it highly adaptable to specific applications.

4.2 CO_2 Ablation Software and Optical Setup

CO_2 ablation was chosen as it enabled rapid fabrication (a single trap takes ∼100 ms to fabricate) and easy manipulation of the trapping parameters by altering the fabrication parameters. By controlling the relative position of the glass slide surface and CO_2 laser focus, laser waist size, exposure time, exposure repetition, and laser power, the mirror profile could be precisely chosen for the required application.

As shown in Figure 4.2, the ablation setup was a relatively simple one, consisting of a 27 W, 10.6 μm radio frequency modulated CW CO_2 laser (48-2KA, Synrad), which would first pass through an automated shutter, which allowed for control of exposure length down to 10 ms. An aperture was used to change the beam waist size, and a ZeSe-coated 35 mm lens was used to focus the CO_2 laser on the glass substrate. The sample was mounted on an automated 3D stage (8351 Picomotor controlled by Model 8752 Intelligent Picomotor Ethernet Controller, Newport). A 660 nm laser diode was used to align the CO_2 laser as it is not visible, and a CCD camera coupled with an LED was used for calibration and imaging of the ablated mirrors.

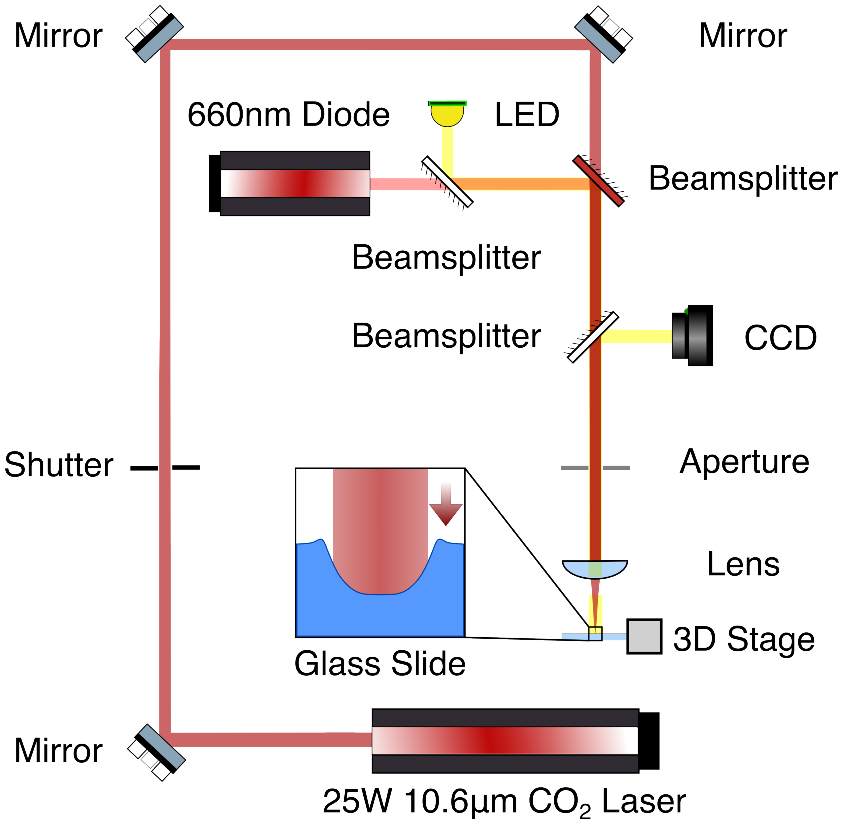

Figure 4.2 Optical setup used for the CO_2 ablation of glass slides. The 3D stage, shutter, and CO_2 laser control were automated. The inset shows the glass ablation process. Taken from [204].

The shutter was used to control the exposure time and number of exposures. The aperture controlled the beam size, and the 3D stage allowed for control of the relative position of the laser focus and glass plane and allowed for fast fabrication of arrays through x-y movement. These arrays are shown in Figure 4.3 (a) and (b) below, as well as more advanced shapes such as channels as shown in Figure 4.3 (c).

After ablation of an array of micromirrors of the glass slide substrate, the sample was transferred to an electron beam evaporator (AUTO 306, Edwards), where a 2 nm thick adhesion layer of NiCr was deposited, followed by 150 nm of gold. This thickness was chosen to ensure no heating due to plasmonic effects arising from thinner layers of gold.

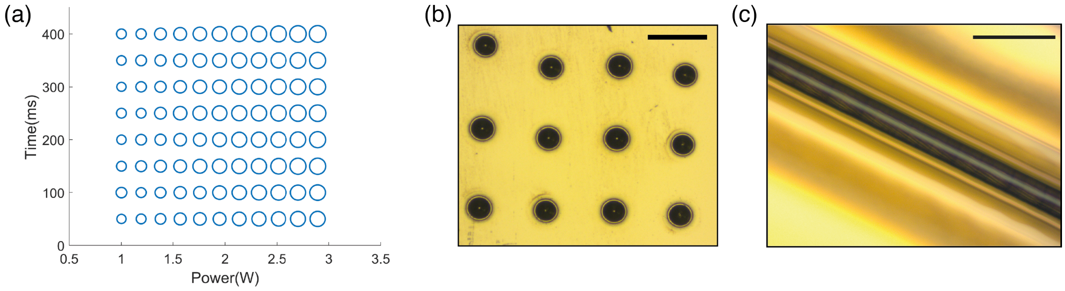

Figure 4.3 (a) Parameters used for an array of micromirrors, (b) the resulting gold coated micromirrors, scale bar is 150 µm the rows are uneven due to the stage being moved by hand in the early stages of fabrication. (c) Gold coated channel, scale bar is 200 µm. Taken from [204].

A custom LABVIEW software (also available in the research repository) was developed over multiple months to automate as much of the fabrication as possible. In the end, the software was used to control the laser's duty cycle, allowing for fine-tuned power control; it controlled the exposure time through the automated shutter and allowed for full 3D control of the sample. A screenshot of the control panel is shown below in Figure 4.4. The software was further extended to take sets of instructions similar to the g-code used in the manufacturing industry for step-by-step fabrication. This allowed for the scripting of more complex shapes, such as the channel shown in Figure 4.3 (c).

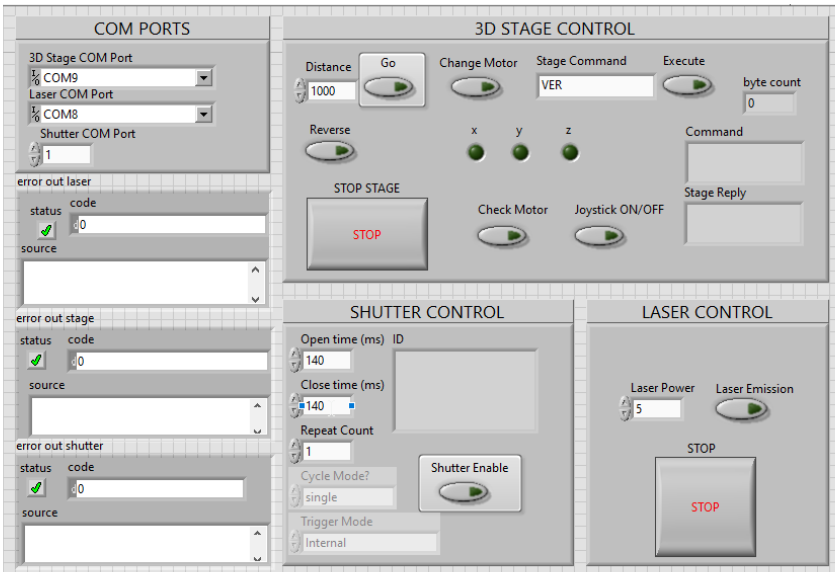

3D Stage COM Port: COM9
Laser COM Port: COM8
Shutter COM Port: 1

error out laser: status ✓ code 0
error out stage: status ✓ code 0
error out shutter: status ✓ code 0

Distance: 1000
Stage Command: VER
byte count: 0

Open time (ms): 140
Close time (ms): 140
Repeat Count: 1
Cycle Mode?: single
Trigger Mode: Internal

Laser Power: 5

Figure 4.4 Front panel of the LABVIEW software used to automate the fabrication process.

4.3 Micromirror Characterization

Over 350 mirrors were fabricated and characterized throughout this work. The vast majority were characterized optically, using a microscope to measure the diameter and depth as two key parameters from which all other relevant parameters could be calculated. The power, exposure time, exposure repetition, and substrate position were recorded during the micromirror array fabrication. The mirror diameter was extracted using ImageJ from the images of each mirror, while the depth was measured manually by focusing on the bottom of the mirror using the microscope, then on the surface and noting the distance traveled.

A microscope (Eclipse E600, Nikon), operating in brightfield mode with available magnifications of 5x, 10x, 20x, 50x, and 100x, was employed to assess the diameter and depth of the mirrors. Since most mirrors fell within the size range of approximately 40 to 120 µm, the images were predominantly captured at 100x magnification.

The effect of the fabrication parameters is shown below in Figure 4.5, Figure 4.6 and Figure 4.7.

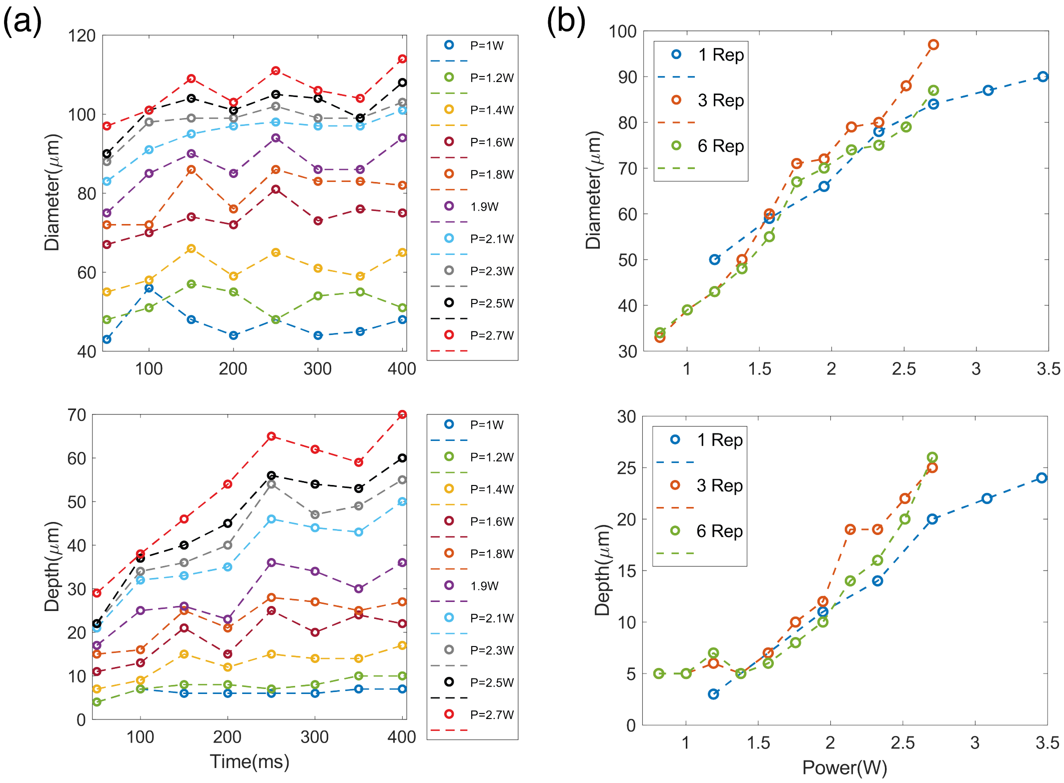

Figure 4.5 Relationship between time of exposure, the diameter of mirrors and the exposure repetition. Taken from [204].

Figure 4.5 illustrates the impact of varying exposure lengths between 50 and 400 ms. At lower power levels, the influence of extending the exposure length was almost negligible, and even at higher powers, the mirror diameter demonstrated independence from exposure length. Likewise, the depth exhibited power dependency at lower powers only below 2 W.

This phenomenon can be attributed to the ablation efficiency contingent on the focal point of the CO_2 laser beam. Assuming rapid evaporation at the exposure's onset, most ablation would occur almost instantly, primarily affecting the top layer of silica that absorbed the incident power. The layers of silica beyond the focal point, however, were unable to heat up significantly, resulting in an insignificant alteration to mirror parameters. At powers exceeding 2 W, ablation could still occur as sufficient power reached the deeper layers, allowing for evaporation and melting. Given the more pronounced influence of power, as depicted in Figure 4.6, all subsequent data is presented in terms of mirror diameter and depth as functions of the incident power of the CO_2 laser.

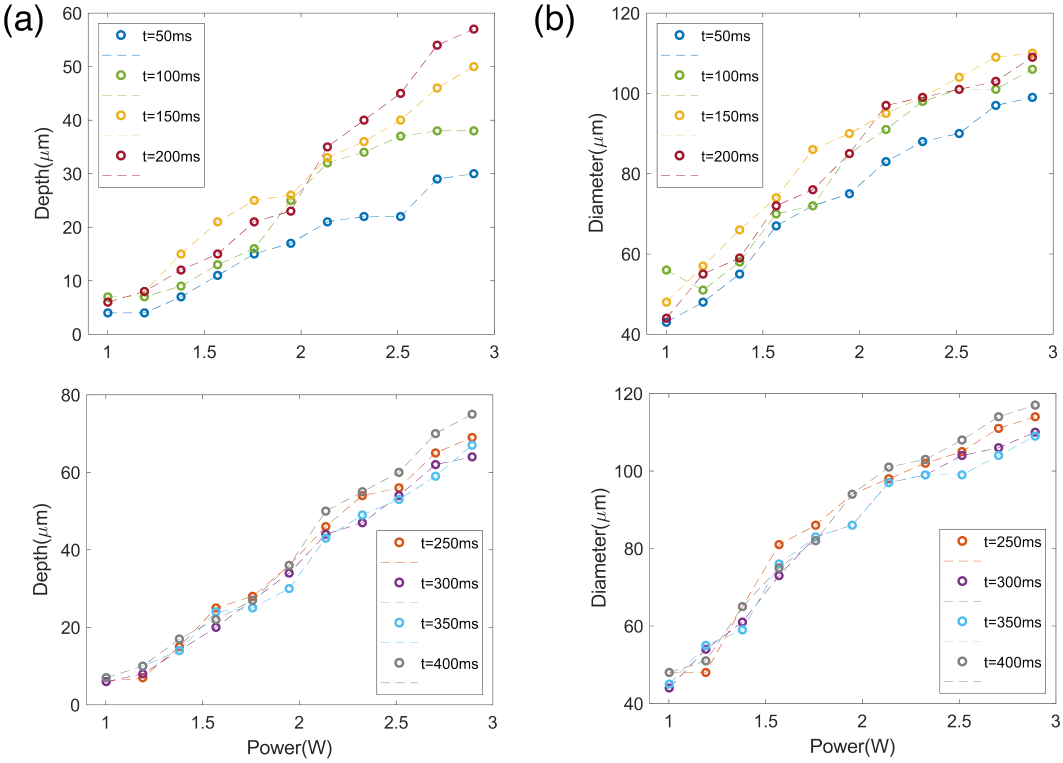

Figure 4.6 Relationship between laser power, the diameter of mirrors and the depth of mirrors. Taken from [204].

A consistent trend in the data reveals the steadfast power dependence of the micromirror's diameter, irrespective of the number of repetitions or the focal plane's position. This constancy can be rationalized by considering that even when the focal plane is 'misaligned', a sufficient amount of power reaches the surface, inducing a melt layer that spreads and determines the mirror's diameter.

Conversely, the depth, as depicted in Figure 4.7, proves to be much more sensitive to the focal point's position, defined by the motion of the Picomotor motion with a resolution of <30 nm. This sensitivity is particularly evident in the trend line corresponding to a focus position at -1 mm. Focusing the CO_2 laser behind the surface plane led to increased beam scattering by the glass, resulting in shallower mirrors. This characteristic could be advantageous at higher powers, as the 'gentler' ablation produced a smaller lip around the mirror and a visibly more curved profile while maintaining a large diameter.

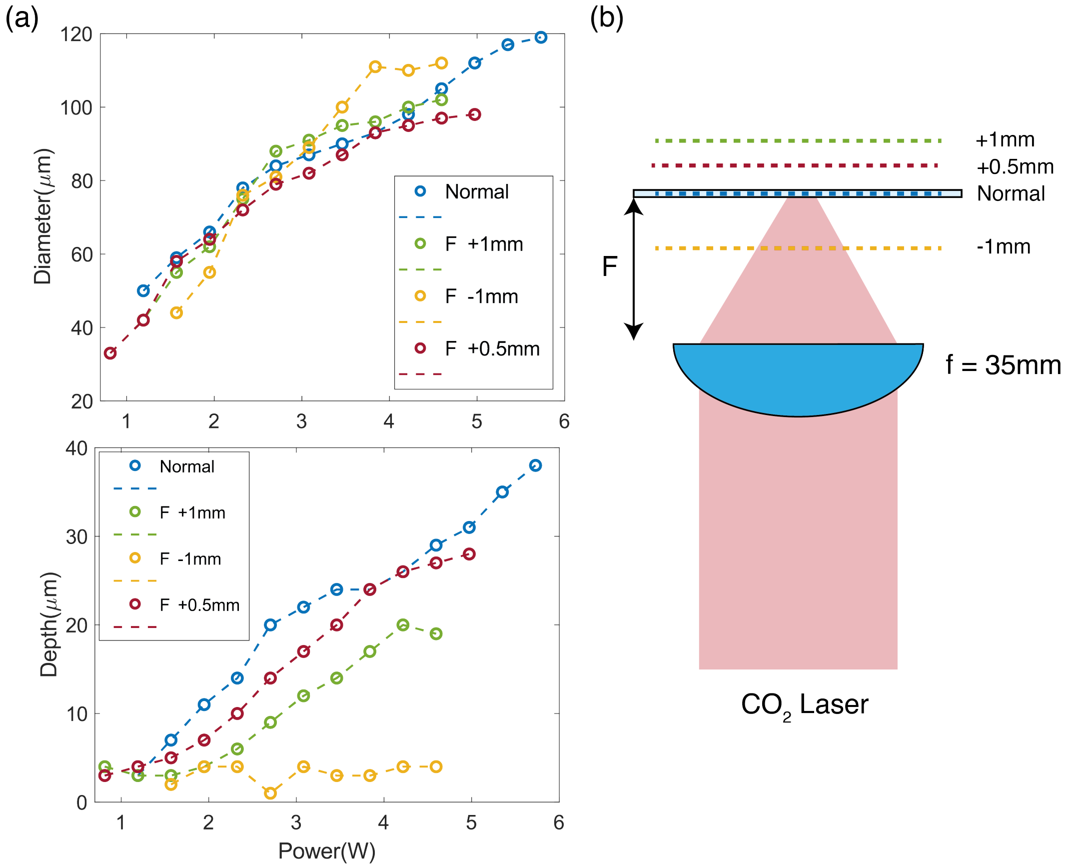

Figure 4.7 Relationship between laser power, the mirror diameter, and the position of the glass substrate relative to the laser beam focus. Taken from [204].

Importantly, this effect was most pronounced when the laser was focused behind the surface plane. The gradual evaporation of silica allowed surface tension to act over time, pulling the molten silica into a convex shape at all power levels. This differed from other mirrors created with the same parameters, which exhibited a flatter profile at the bottom due to the sudden evaporation of silica [229].

The theoretical performance of the micromirrors was first estimated by calculating the parameters relevant to the trapping, such as the focal length, radius of curvature, and NA as shown in Figure 4.8 (a). These were calculated from the measurable parameters of depth and diameter using a geometric approximation of the focal length of a parabola [230]:

$$f = \frac{D^2}{16z}, \tag{4.1}$$

where D is the mirror diameter, and z is the depth. The aperture angle θ of a parabolic mirror is defined as:

$$\frac{z}{f} = \frac{D^2}{16f^2} = \tan^2\left(\frac{\theta}{2}\right). \tag{4.2}$$

The relationship between z/D and θ is clearly illustrated in Figure 4.8 (b), where the parameters of 357 mirrors are plotted according to their estimated aperture angle. It is essential to recognize that this representation is a simple geometric approximation. Particularly for higher ratios of D and z, consideration must be given to the effects of increased fabrication power, which may lead to cracks and uneven surfaces.

Additionally, it is crucial to acknowledge that as θ surpasses $\pi/2$ degrees, the quality of trapping diminishes. This is attributed to a greater proportion of light contributing to the scattering force incident on the particle. For mirrors with $\theta < \pi/2$, a comparison can be drawn to a lens, utilizing the NA as the figure of merit.

The relationship between NA and θ is expressed as $NA = n_m \sin(\theta)$, where n_m represents the refractive index of the medium (n_m = 1.33 for D_2O). Consequently, we can define an effective NA for the micromirrors as:

$$NA = n_m \sin\left(2\tan^{-1}\left(\sqrt{\frac{16z^2}{D^2}}\right)\right). \tag{4.3}$$

It is crucial to emphasize that the comparison with lenses holds significance only for mirrors where $\theta \leq \pi/2$. In contrast, θ tends toward π for an infinitely extending parabolic mirror.

4.4 Particle Trapping

The movable mirror setup described in Chapter 3 was used to trap the particles. The 2 µm silica beads were first trapped using the 1.2 NA objective and brought to the focal point of the micromirror. The automated mirrors were then used to expand the beam coming out of the objective, trapping the particle using the micromirror. Illumination used LED light sent directly through the objective and detected in reflection, as the thick layer of gold on the micromirror substrate blocked any illumination in transmission. Another unexpected consequence of using gold as a substrate was during sample preparation. Due to the gold film being hydrophobic, the solution of particles will form into a bead and is much more likely to form air bubbles when sealed underneath the cover slip. This can be solved by oxygen plasma cleaning the gold right before the liquid is applied.

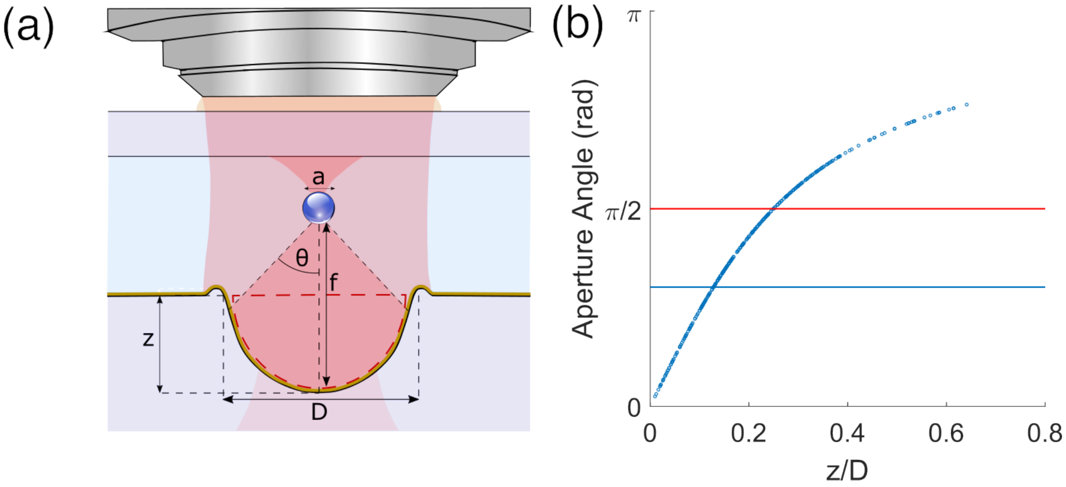

Figure 4.8 (a) Scheme showing all parameters considered when calculating the theoretical performance of a micromirror and (b) the angle of light reflected from the mirror for 350+ mirrors measured, showing the relationship between the ratio of depth and diameter and the mirror NA. Taken from [204].

The mirror parameters used for trapping in this section are shown in Table 4.1 below.

Table 4.1 Parameters of the micromirror used to trap and rotate particles. In order: diameter, depth, focal length, the radius of curvature (ROC), effective NA, trap stiffness, and the average of x and y. Taken from [204].

D (µm)	z (µm)	f_m (µm)	ROC (µm)	NA	$k_\perp$ (pN/µm/W)
56.5	7.3	54.7	109.4	1.08	52±1

Five stiffness values were acquired for each power, subsequently averaged and plotted against the power measured after the microscope objective (see Figure 4.9 (a). The dashed line represents a straight-line fit with no intercept, yielding a stiffness of $k_\perp = (52 \pm 1)$ pN/µm/W when correcting for the size of the beam incident on the mirror, shown in Figure 4.9(c) This value is approximately six times lower than that of the objective with NA = 1.2, possessing a stiffness of $k_o = (332 \pm 2)$ pN/µm/W. This can be attributed to the low quality of the CO_2 beam, resulting in a non-symmetrical power distribution. Another issue is the deposition of particles at the bottom of the mirrors during repeated experiments, increasing optical aberrations. Additionally, the slight difference between stiffness in the x and y directions can be accounted for by looking at Figure 4.9 (b), where the ellipticity of all the fabricated mirrors is shown, which can be attributed to the CO_2 beam shape.

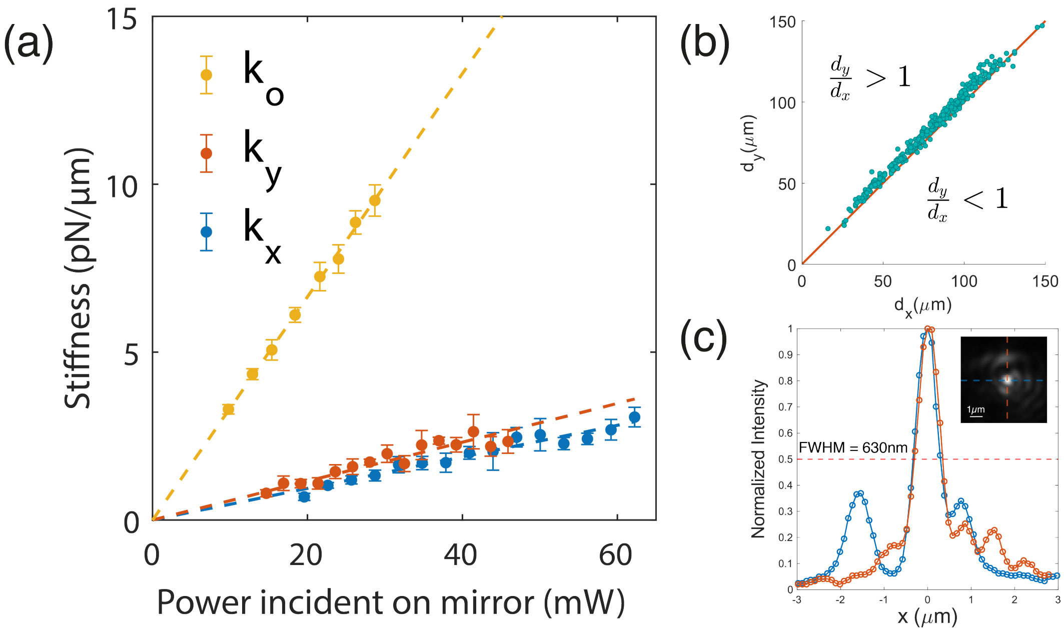

Figure 4.9 (a) Trapping stiffness of the micromirrors in x and y, compared to a 1.2 NA microscope objective. The error bars represent the standard deviation over 5 sets of measurements. (b) ellipticity of the micromirrors (c) beam profile formed by a micromirror. Taken from [204].

Although the coherence length of the laser would permit interference, the relative intensity of the incident collimated beam and the reflective focused beam at the trapping location exclude the effects of standing waves. Given the wavelength of 830 nm resulting in fringes every 415 nm and the depth of focus of the objective of ∼800 nm, any significant displacement of the particle in the z-direction would have been observed, which is not the case.

Concerns about thermal effects arise due to the presence of gold: several studies have demonstrated a notable heating effect on particles positioned less than a few microns from the surface when subjected to a focused beam incident on the gold surface [231, 232, 233]. In this scenario, however, the particle is situated over 50 µm above the gold surface, and the beam is dispersed across an area orders of magnitude larger. Considering the linear response to changes in laser power, thermal currents are also not expected to contribute significantly to the trapping dynamics.

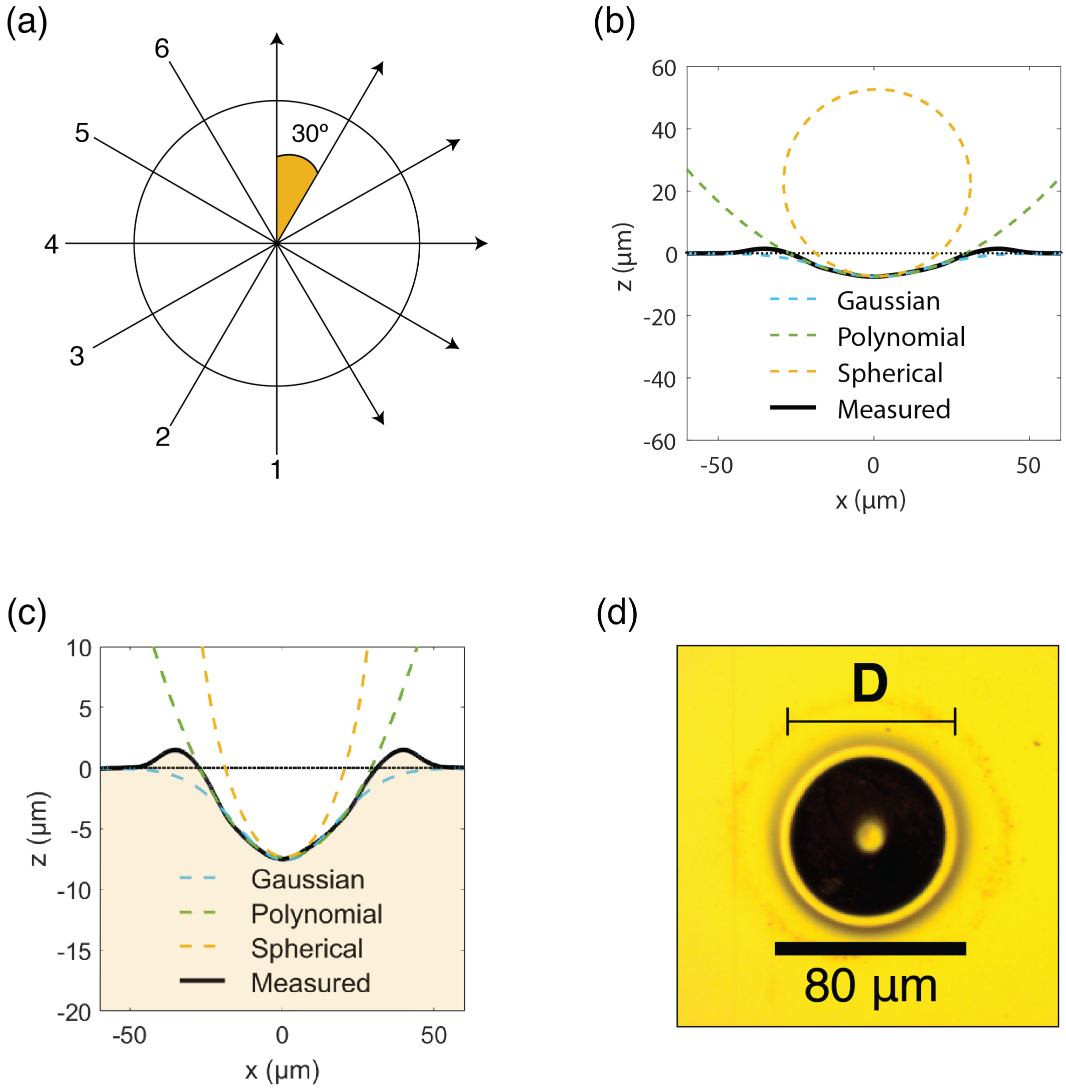

Figure 4.10 (a) Scheme for measuring the mirrors using the DekTak (b) zoomed out and (c) zoomed in profiles of the micromirror surface fitted with Gaussian, spherical, and polynomial curves, fabricated using a laser power of $1.8\,\mathrm{W}$, a pulse duration of $\tau = 120\,\mathrm{ms}$, and an aperture diameter of $2\,\mathrm{mm}$. This micromirror was utilized for particle trapping and rotation. See Table 4.1 for detailed fabrication parameters. (d) A top-down view showing a gold-coated micromirror with a diameter of $80\,\mu\mathrm{m}$, where the bright central spot indicates the lamp's reflection. Taken from [204].

To get an even more accurate profile reading, we used the DekTak profilometer (Dektak 150 with a 12 µm stylus, Veeco), scanning multiple mirrors across six axes as shown in Figure 4.10 (a). Figure 4.10 (b-d) shows the micromirror utilized for particle trapping with a depth of z = 7.3 µm and a diameter of D = 56.5 µm. Its profile aligns with the Gaussian intensity pattern of the CO_2 laser beam, albeit with deviations due to the lip forming on the mirror's edges during fabrication. These deviations suggest that a parabolic description more closely represents the mirror's profile. This parabolic profile is one of the key advantages of this process, as parabolic mirrors regularly find use in optical systems due to their unique ability to focus incoming light rays into a single point. This eliminates both spherical and chromatic aberrations, making them work over a large range of sizes and wavelengths. The ability to focus all incoming light is particularly interesting regarding optical trapping, where a high NA is required.

4.5 Particle Rotation

Transfer of optical momentum is not limited to a linear push and pull — by using circularly polarized light, it's also possible to transfer angular momentum. A noteworthy mention is the behavior of non-spherical particles in these fields. With each anisotropic shape comes a different response to the trapping beam as the objects experience both the trapping force and a torque [234, 235], with cylindrical [236]. Elliptical [237] objects such as blood cells aligning themselves to the direction of beam propagation [238], and cube-like particles rotating due to inherent form birefringence [239] when illuminated with circularly polarized light. Another method, as will be outlined below, is the use of birefringent particles of vaterite [240, 241].

This portion of the work aimed to show that the micromirrors reverse the angular momentum of the reflected light. This highlighted the ability of the micromirrors to preserve the original characteristics of the incoming light, including angular momentum. To this end, we used 5 μm diameter vaterite particles. The optical setup from Chapter 3 was modified by placing a quarter-wave plate as close as physically possible to the microscope objective to preserve the circular polarization of the beam.

Initially, we trapped the vaterite using objective-enabled optical tweezers and observed the clockwise rotation of the particle, as illustrated in the top portion of Figure 4.11. Subsequently, we switched the optical path to trap the particle using the micromirror. We observed a change in the direction of rotation, as depicted in the bottom panel of Figure 4.11.

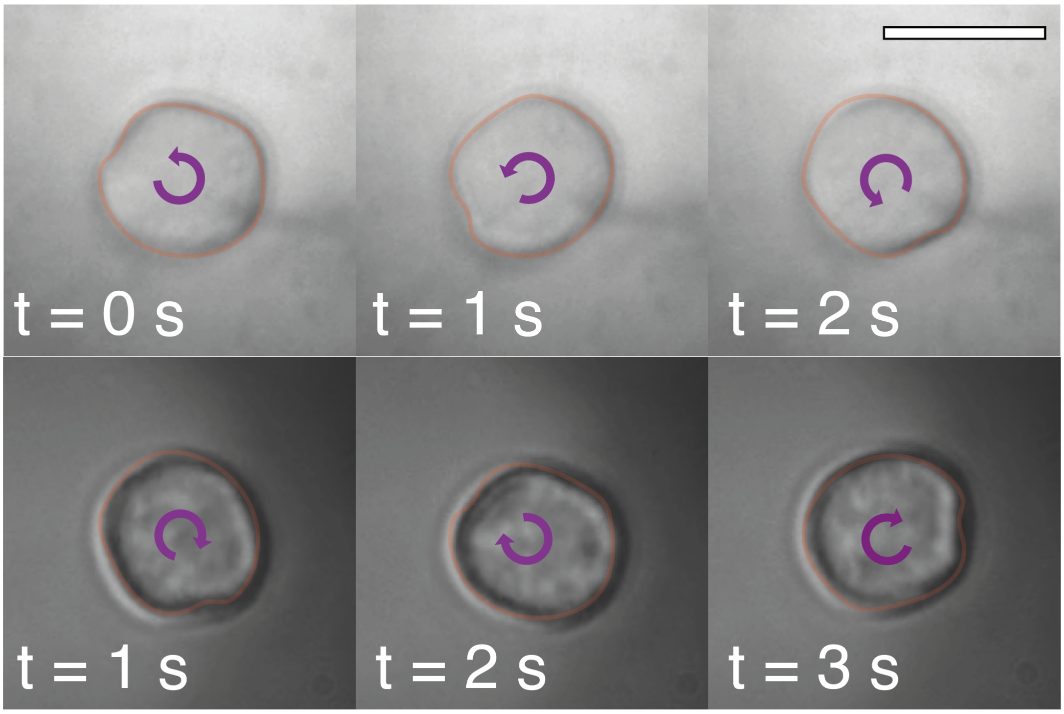

Figure 4.11 Frames showing the vaterite particle being rotated and counter-rotated by the objective trap and then the micromirror trap. The vaterite particle was rotated at 1 Hz, the scale bar is 5 µm. Adapted from [204].

4.6 Contribution

Hamid Ohadi initially installed the CO_2 optical setup, which I modified to automate all parts. I wrote the software used during the ablation process. I characterized the micromirrors primarily, with Saydulla Persheyev performing the DekTak measurements of the profile. I fabricated the majority (300+) mirrors, with Saydulla Persheyev fabricating around 50 mirrors for a total of 357 mirrors. I did the trapping experiments.

4.7 Conclusion

In conclusion, this Chapter presented a rapid and versatile fabrication process for creating 357 high-NA parabolic micromirrors with diameters in the range of 80 µm using CW CO_2 laser ablation of silica, followed by gold coating. These micromirrors prove to be suitable substitutes for microscope objectives in optical trapping applications. The trapping performance was thoroughly analyzed at various powers, resulting in an average stiffness of $k_\perp = (52 \pm 1)$ pN/µm/W for a mirror with an effective NA of 1.08, which compares favorably with values reported in the literature [205, 242].

Finally, the mirror's capability to counter-rotate a vaterite particle was demonstrated. The mirror's geometry holds promise for creating integrated dual-beam trapping [243]. Given the ability to fabricate closely spaced arrays of arbitrary size, this approach becomes a promising technique for on-chip particle trapping, sorting, and optical lattices for atoms [244, 245, 246]. Similar schemes have shown great promise in the parametric cooling of particles in vacuum [247]. With added laser writing capabilities, it would be feasible to guide particles in arbitrary circuits through 2D trapping in channels on this platform.

While incredibly promising, in the end, we could not achieve the same performance as a microscope objective when using the micromirrors. High-quality products also require more control over the fabrication parameters, even at the cost of time. The next Chapter will describe in detail the use of MSs to surpass the performance of the mirrors shown here, providing complex optical trapping landscapes in reflection and transmission.

CHAPTER 5

Metasurfaces for Optical Trapping

Encouraged by the success of the micromirror ablation, which allowed for fast and straightforward fabrication of optical trapping arrays, we wanted to explore other methods of optical trapping using integrated optical elements. The best micromirror trapping results were still an order of magnitude less efficient than a microscope objective, and the exact parameters of the trapping elements were limited in precision. The mirrors are also limited in their versatility as an optical component, usable only in reflection and capable of forming a single optical trap.

HMSs, on the other hand, can be used to create more complex photonic landscapes, allowing a greater level of control. While static, optical trapping using HMS allows for certainty where a certain particle or cell will be trapped, and so allows for single objective analysis. For example, a cell can be trapped using one MS, while light sheet microscopy is performed on it using another, with a single low NA objective collecting all the data. A range of metalenses for optical trapping has been demonstrated over the last few years [131], including polarization switchable metalenses [248], bifocal plasmonic metalenses [249], and even metalenses fabricated on top of optical fibers [130]. While successful in generating optical traps, all of these HMSs formed a single focus point. They also demonstrated trapping stiffness below that of a microscope objective.

In this portion of the thesis, we showed that a reflective HMS approach can create trapping beams with efficiency equal to that of objectives and create multiple traps using a single optical element. We also demonstrated transmissive metalenses capable of working across a broad range of wavelengths. While incredibly performant, the gold HMSs were quite fragile, and pieces would break off during use. These lenses were made of zirconia, a hard, inert ceramic known for its biocompatibility and lack of disintegration.

Shown below are concept sketches for both designs, with Figure 5.1 (a) and (b) showing the trapping HMSs working in reflection and Figure 5.1 (c) showing a HMS working in transmission.

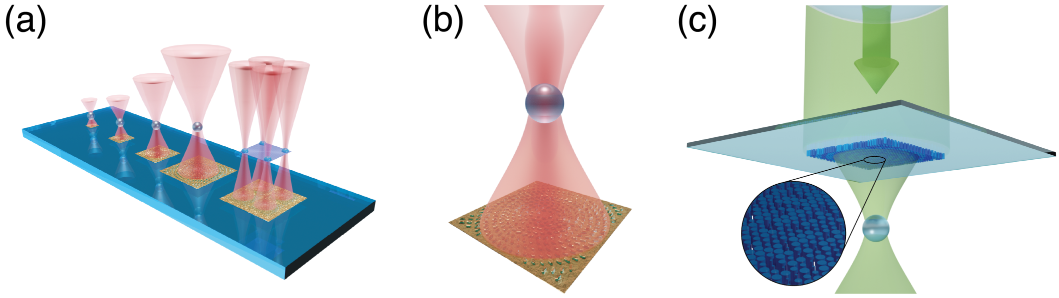

Figure 5.1 Concept images for HMS enabled optical trapping. (a) Shows the reflective trapping geometry for multiple HMS sizes and extended object trapping, taken from [128], while (b) shows in detail the trapping scheme for a single particle. (c) Shows the trapping scheme for HMSs operating in transmission, taken from [129].

5.1 Trapping with Holographic Reflective Metasurfaces

This section details the development, production, and evaluation of reflective-type HMSs featuring an NA of 1.2 and 1.3 and achieving a trap stiffness of up to 430 pN/µm/W. This stiffness is comparable to that of a traditional bulky microscope objective with an equivalent NA. Furthermore, we examined HMSs varying in size from 900 μm^2 to approximately 0.09 mm^2, with trapping distances ranging from 7.1 to 75 µm. The design of these HMSs utilized a metal-insulator-metal, three-layer configuration of PB meta-atoms, optimized for circularly polarized light with a wavelength of 830 nm. Additionally, we successfully demonstrated that these HMSs can be engineered to generate multiple focal points, enabling the trapping of non-spherical objects like fishnet membranes, which are outfitted with trapping handles to facilitate manipulation.

Holographic Metasurface Design, Fabrication and Characterization

The initial design was based on approximating the trapping geometry for the HMSs. The numerical aperture was calculated using the angle of the right-angle triangle formed by the trapped bead, the center of the HMS and the HMS edge as shown in Figure 5.2 (a), with the critical parameter of $\zeta = \frac{F}{L} = \frac{n_m}{2NA}\sqrt{1 - \left(\frac{NA}{n_m}\right)}$, where L is the HMS side length, F is the focal distance, n_m is the refractive index of the medium. This ratio is plotted against the NA in Figure 5.2 (b), showing that for an arbitrary HMS size, the focal length must be designed to be $\sim 25\%$ of the side length to achieve an NA of 1.2 (equal to the NA of the microscope objective). This was relevant as multiple sizes of HMSs were designed and fabricated to test how small a HMS could be compared to the incoming beam and still function as intended.

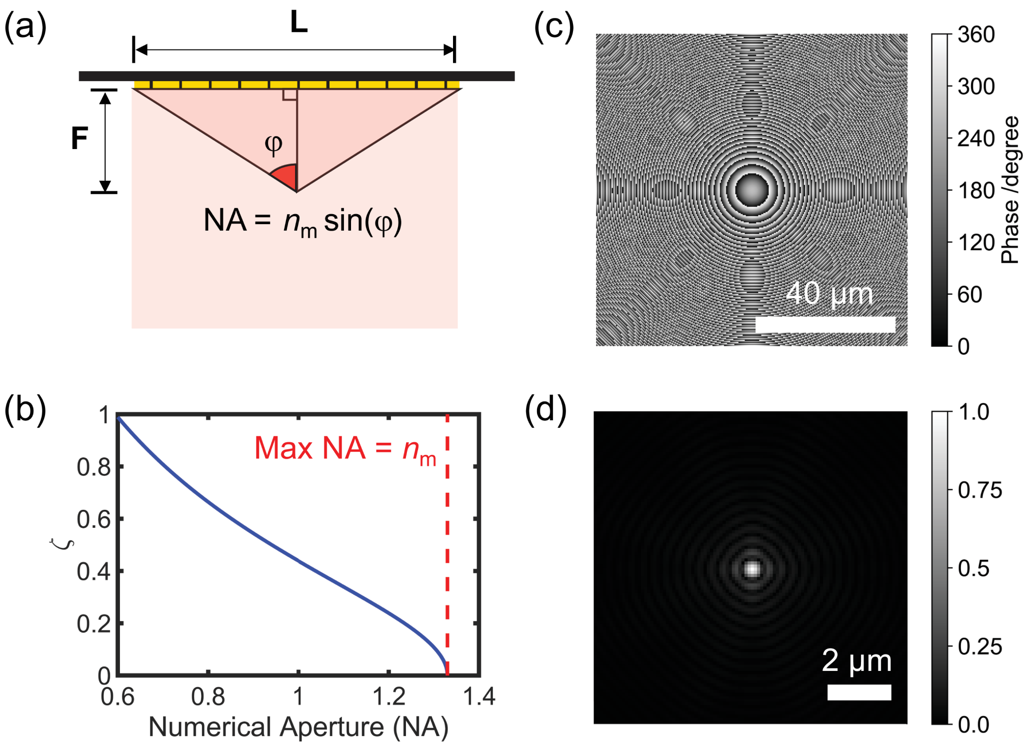

Figure 5.2 (a) Geometric approximation of the numerical aperture of the reflective HMSs, φ is the half angle of the beam (b) diagram of the variable ζ representing the ratio of the HMS side length and the focal distance against the expected NA of the HMS (c) and (d) show the single particle trapping HMS design and simulation respectively. Adapted from [128].

This resulted in a Fresnel lens-like design for HMSs with a single focal point, as shown in Figure 5.2 (c) and (d). The phase mask was generated using the standard GSA approach as described in Chapter 2. The square shape of the holograms is due to the initial goal of tiling the HMSs as closely as possible when generating trapping arrays.

The meta-atoms were based on the PB phase approach described in Chapter 2. I will only summarise the fabrication as I did not perform it. The main steps of the fabrication are shown in Figure 5.3 (a—d). First, 150 nm of gold was evaporated on a silicon sample. Then, a 180 nm layer of a negative Ma-N resist was spun on top of the gold, and individual meta-atoms were written into it using EBL. The unexposed Ma-N was then washed away using a developer, and a 40 nm gold cap was evaporated on top of the meta-atoms. The final result is shown in an SEM image in Figure 5.3 (e).

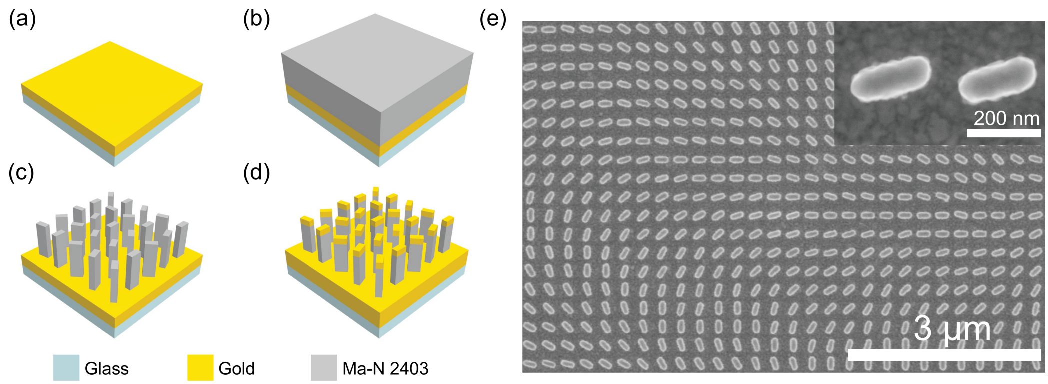

Figure 5.3 (a)-(d) major steps for the fabrication of the reflective HMSs (e) SEM image of a completed HMS. Taken from [128].

The dimensions of an individual meta-atom are shown in Figure 5.4 (a), and given in in the table.5.1 below. The periodicity P was chosen such that it would not limit the NA of the metalens as per the Nyquist sampling theorem [84]. The radiation pattern of the individual meta-atoms is also shown in Figure 5.4 (b). The radiation pattern was an important factor to consider, as the meta-atoms at the edges of the HMS would need to work efficiently at the nearly 90-degree angles required in high NA trapping. These resonators exhibited extremely good directivity, with the average angular width (3 dB) along the long and short axis being 107 deg as calculated in CST Microwave Studio.

P	T_p	L_x	L_y	T_c	T_b
300 nm	160 nm	220 nm	90 nm	40 nm	190 nm

Table 5.1 Table of the dimensions of the meta-atoms used where P is the periodicity, T_p is the pillar thickness, L_x is the top cap length, L_y is the top cap width, T_c is the top cap thickness and T_b is the bottom layer of gold thickness

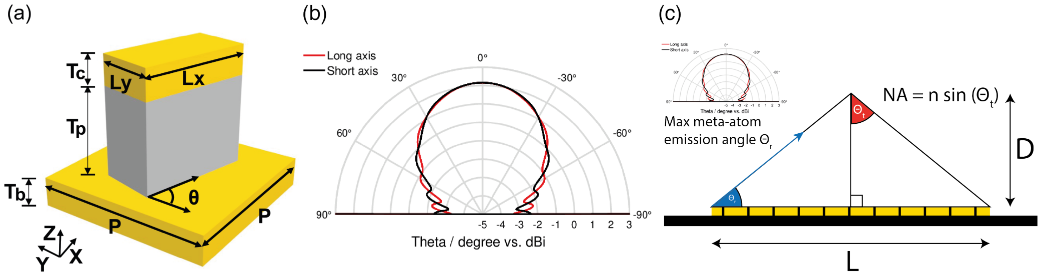

Figure 5.4 (a) individual meta-atom of the reflective trapping HMS, (b) radiation pattern of the meta-atoms, and (c) emission angle of the meta atoms depending on their position on the HMS and the design NA. Taken from [128].

The profile of the beams formed by the HMSs was measured and compared to the theoretical simulations to confirm the numerical aperture. This is shown in Figure 5.5

(e); a deviation can be seen as the HMS was underfilled due to the size of the beam being approximately 250 µm at the sample plane, while the HMS was 315×315 µm. This caused less of the HMS to be illuminated, resulting in a lower NA. Much like underfilling a microscope objective, this resulted in a larger beam than designed.

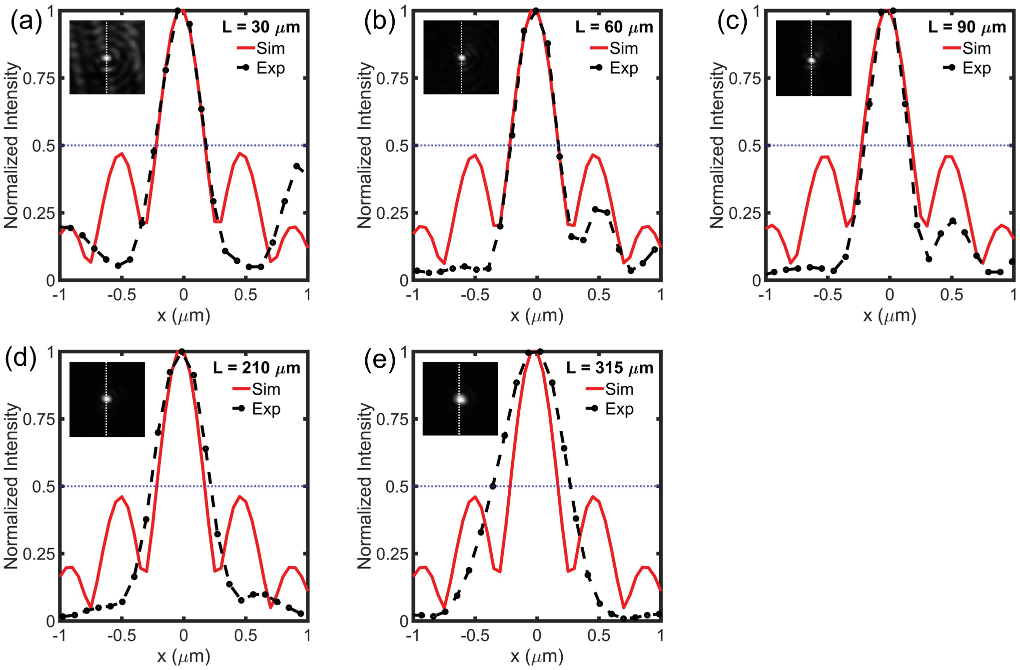

Figure 5.5 Beam profile of NA = 1.2 HMSs with side length of (a) L = 30 µm, (b) L = 60 µm, (c) L = 90 µm, (d) L = 210 µm and (e) L = 315 µm. Taken from [128].

To obtain an indicative measure of the diffraction efficiency of the HMSs, we generated a collimated beam rather than a focused spot using a separate sample. This sample with a side length of 315 µm was fabricated to project a 1 mm diameter dot, positioned 10 cm from the HMS at a 12-degree angle. During the experiment, the sample was submerged in water. The incident beam, circularly polarized and 830 nm in wavelength, had a diameter of 267 µm, ensuring the underfilling of the HMS. Measurements of the incident and reflected powers were 23 mW and 3.1 mW, respectively, yielding a calculated efficiency of 13.4%. This was done because there was no way to physically get close enough to the trapping HMSs to measure their exact efficiency.

Particle Trapping in Reflection

The optical setup used in this work is conceptually the same as the one described in Chapter 2. The main technique used was trapping a particle using objective-based optical tweezers, followed by switching the laser illumination using mechanical mirrors to trap the particle using the HMS, as shown in Figure 5.6 below. This allowed for a systematic study, as the same particle could be used to compare the HMSs' performance at different sizes and when compared to an objective, something typically impossible to achieve in such experiments where the particles are typically delivered using microfluidics, waiting for a particle to fall into the optical trap by chance.

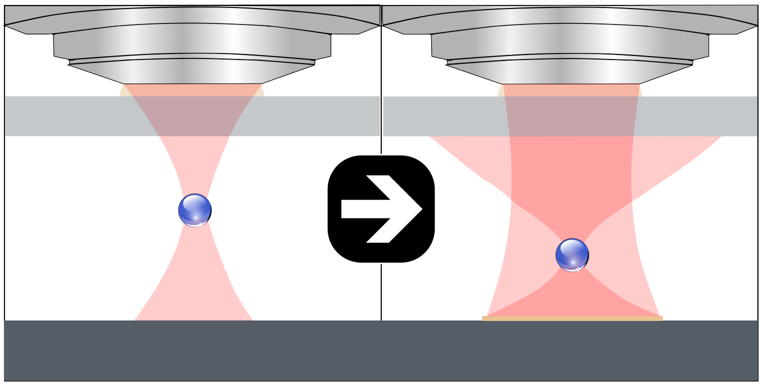

Figure 5.6 Handover process used to transport particles to the focal point of the HMSs before switching to illuminating it.

A 2 µm silica particle was trapped using the objective and HMSs, and its motion was recorded using the CCD camera recording at 1000 fps for 10 s, resulting in 10,000 frames of footage. Five separate videos were taken for each HMS, for the same bead at the same range of ten powers ranging from 23 mW at the laser to 230 mW at the laser, increasing in 10% increments. The videos were then analyzed using the MATLAB code based on the Fourier transform properties described in Chapter 3, and the x and y motions were extracted and further processed, yielding a trap stiffness from the PSD. This gave 5 separate values for trap stiffness for each power, allowing us to take an average and plot the results with error bars indicating the range of values. This is one of the key advantages of this method, as we were able to conduct an extremely systematic study with 50 trap stiffness data points for every HMS.

A comparison between the trapping performance of HMSs with side lengths of L = 315 µm and NA = 1.2 and NA = 1.3, compared to that of a microscope objective with NA = 1.2 is shown in Figure 5.7 (a). These NA values were chosen to compare like with like, and show that the HMSs can produce a trap stiffness comparable to the objective with the same NA, as well to test whether a higher NA would result in a higher trap stiffness. The orange dotted line indicates the scaling boundaries assuming a 20% efficiency of the HMS (top line) and 80% efficiency (bottom line). The trapping for both HMSs assumes 50% efficiency, as it would be extremely difficult to measure the exact efficiency given the requirements of measuring in reflection at such a short distance. It should be noted that this is a very conservative estimate, as we measured the efficiency of a MS projecting a collimated beam to be $\sim 13\%$.

The 1.3 NA HMS had a lower trapping efficiency caused by the steep angle of light re-radiated by the meta-atoms at the edges of the HMS, which can also be seen in the radiation pattern in Figure 5.4 (b). An optimized design could overcome this limitation, changing the meta-atom design at the edges to optimize for higher angles [250]. It should also be noted that for this comparison, the beam diameter was measured to be around 250 μm, meaning both the NA = 1.3 and NA = 1.2 HMSs were underfilled. This was an initial test done during the optimization of the HMSs before multiple sizes were made; not shown in the diagram are the results from trapping with HMSs with NA of 1.1 and 1. Another issue these suffered from was the increased focal distance — for the NA = 1 case, the focal point was outside of the 100 μm tall chamber. As the most optimal design was found to be NA = 1.2, all other HMSs were designed at that specification.

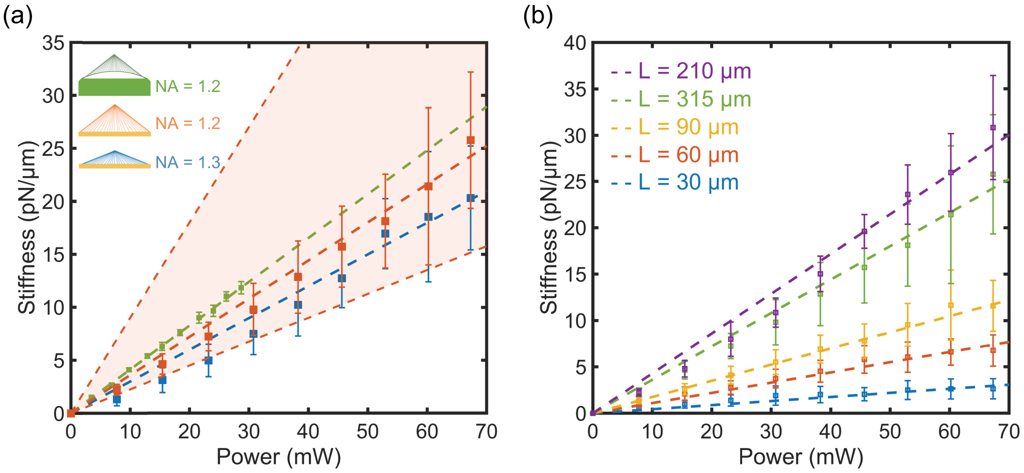

Figure 5.7 (a) Trap stiffness measurement of a HMS width side length L = 315 μm and NA = 1.2 and NA = 1.3 and a microscope objective. The orange region is bounded by a theoretical HMS efficiency of 20% and 80%. The error bars represent the standard deviation from 5 data sets taken for each point. (b) Trap stiffness comparison of HMSs of different side lengths L. The linear fit is inserted with a 0 y-intercept, following the assumption that at 0 laser power, the trap stiffness is also equal to 0. Taken from [128].

HMSs were fabricated at 5 different sizes to test the limits of how small they could be before they stopped working efficiently. As shown in Figure 5.7 (b), and even more clearly in Figure 5.8, the trap stiffness's dependency on HMS size using an NA = 1.2 design showed an initial increase in stiffness with HMS area. This can be explained by two factors: first, we did not normalize the results according to the illuminated area of the HMS as we had no way of confirming the exact efficiency. This choice conservatively underestimates the HMS' trapping efficiency, corroborated by the consistent quality of focused spots across HMS sizes shown in Figure 5.5. Second, the constant periodicity of the meta-atoms means that the smaller HMSs have a much lesser number of resonators, and as such a worse resolution and overall efficiency. The trap stiffness peaked with HMSs with L = 210 μm, explained by the measured beam diameter of 250 μm. Figure 5.8 highlights comparable efficiency across various HMS sizes and configurations despite reduced efficiency in larger HMSs due to under-filling and edge diffraction inefficiencies.

The HMSs maintained high trapping efficiency even when the stage underneath was translated in x and y, meaning the HMS only needed to be partially illuminated to function. Through the systematic study of multiple particle sizes (5, 2 and 0.5 µm) we were also able to exclude any significant thermal effects typically seen in plasmonic or metallic near-field traps due to metal absorption causing localized heating. The convection currents created by these effects have a strong effect on smaller particles, which we did not observe.

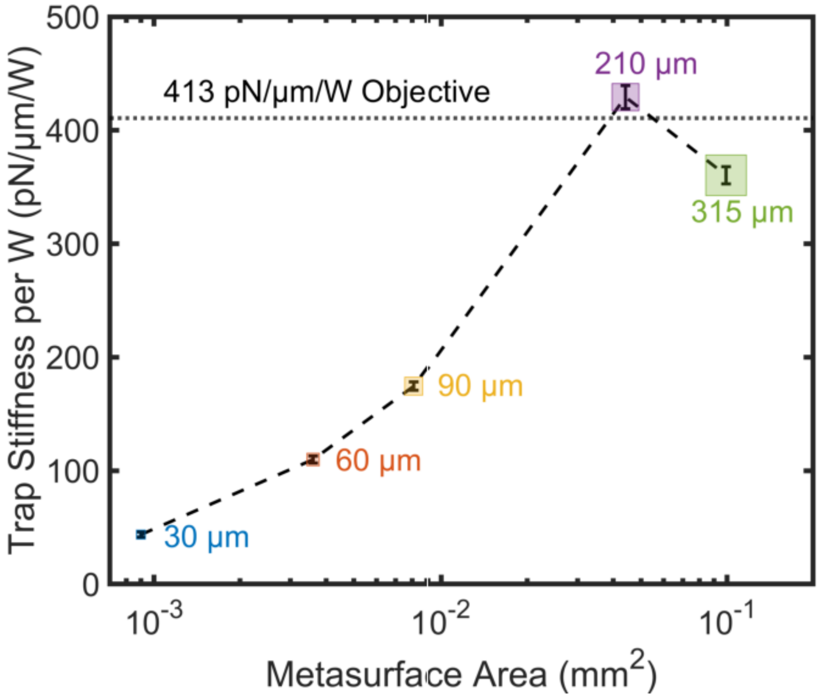

Figure 5.8 Trap stiffness vs power diagram for HMSs of different side length L. The error bars represent the standard deviation from 5 data sets taken for each point. Taken from [128].

To demonstrate that the stability of trapping extends to not only a higher trapping stiffness but also an equal trapping force experienced by the trapped particles in both x and y, Figure 5.9 shows the comparison between the x and y components of all HMS.

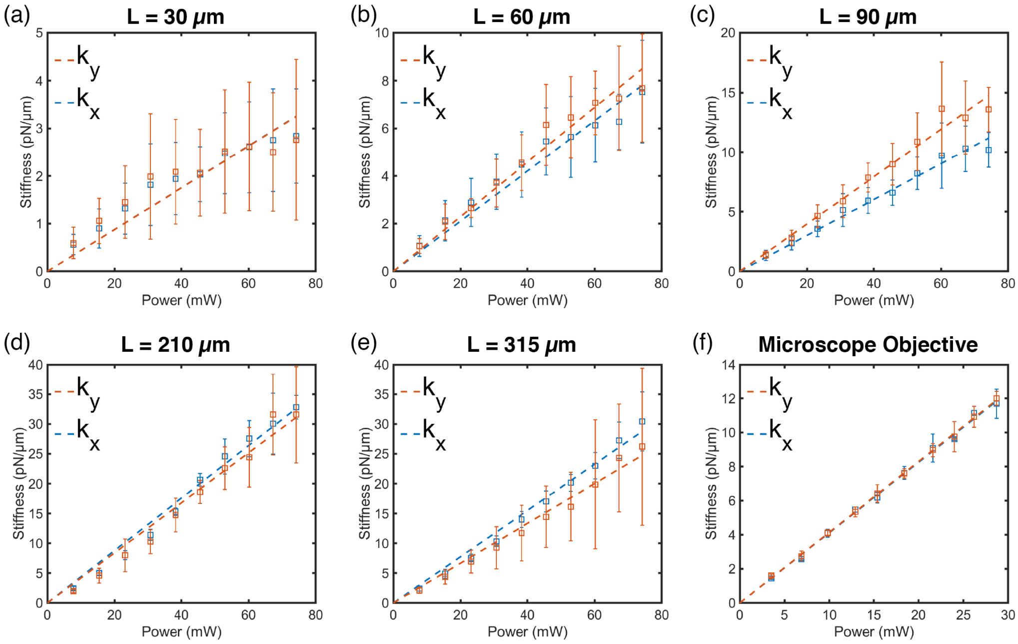

Figure 5.9 Trap stiffness in x and y of all of the metasurfaces at different sizes of MSs with side length of (a) L = 30 μm, (b) L = 60 μm, (c) L = 90 μm, (d) L = 210 μm and (e) L = 315 μm. Also shown is the trap stiffness of the microscope objective in (f). The error bars represent the standard deviation from 5 data sets taken for each point.

Another advantage of using the same system to measure the micromirrors described in Chapter 4, metasurfaces, and the microscope objective is that the PSD can be directly plotted and compared at the same laser power as shown in Figure 5.10 below. As expected, the corner frequency of the micromirror trapped sample is the lowest, followed by the microscope objective and with the L = 210 μm metasurface being the highest.

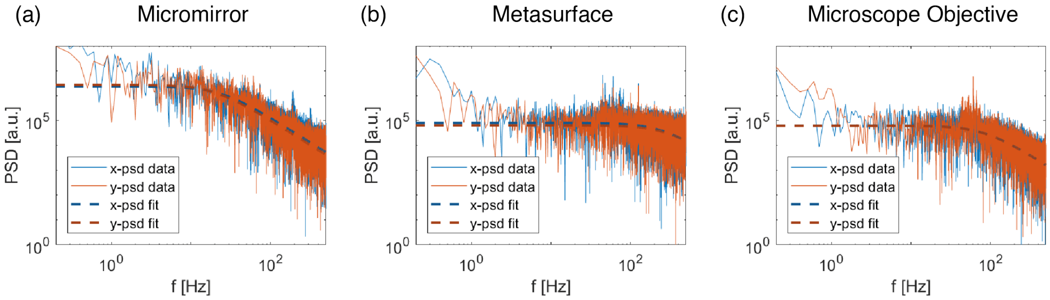

Figure 5.10 Comparison of PSD of particles trapped at 230 mW at the laser using a (a) gold micromirror, (b) L = 210 μm metasurface and (c) microscope objective.

Extended Object Trapping

Relating to the ongoing work in Chapter 4, where membranes interact with samples within the microfluidic chamber, we showed the ability to trap extended objects. We argue that while this does not have the versatility of controlling an object using an

SLM, there are multiple use cases where having a few pre-encoded positions is all that is needed. If a membrane is being used as a mirror, a metasurface can encode 2-3 positions depending on the illuminating beam polarization. This gives a fixed mirror that can be used to illuminate a sample from the side using a single objective.

Here, we looked at a simple case of a literal fishnet designed for filtering and catching larger particles. SEM images of the extended object we fabricated and trapped are shown in Figure 5.11 (a) and (b); it is a 15×15 µm^2 fishnet membrane with bead-like handles at the corners. The fishnet membrane was fabricated out of SU8 using EBL, requiring one exposure for the net and another for the handles. As with individual beads before it, the fishnet membrane was first captured using the typical holographic optical tweezers, transported above the HMS, and released as the laser was switched to illuminate the HMS. Figure 5.11 shows the fishnet membrane trapped by the HMS.

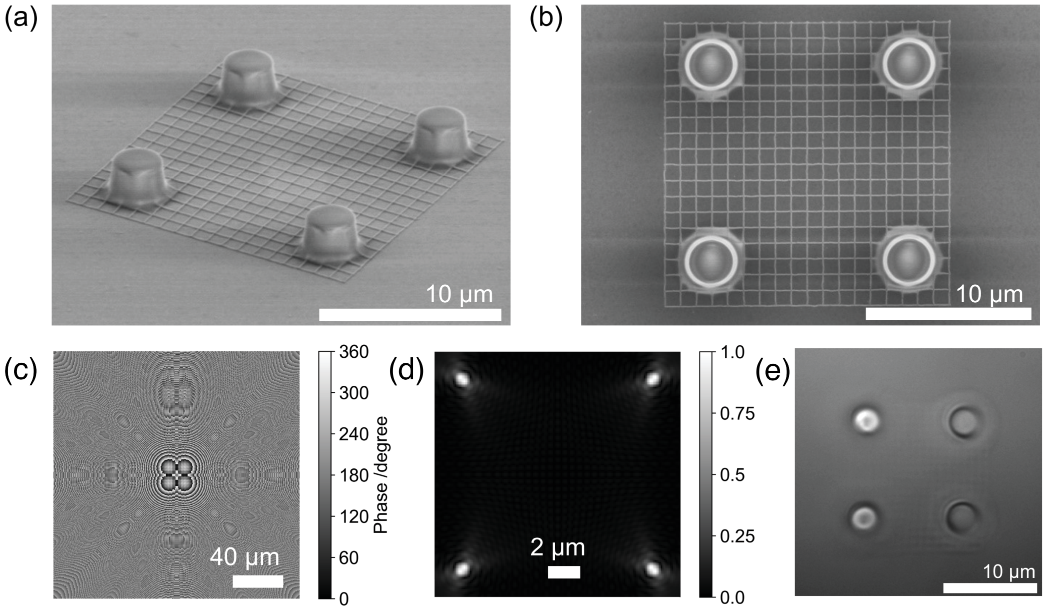

Figure 5.11 SEM images of the fishnet membrane from (a) 60 degrees and (b) from the top and (c) and (d) show the extended trapping HMS design and simulation, respectively, and (e) shows the fishnet membrane trapped by the HMS. Adapted from [128].

The initial plan for these fishnet membranes was to use them in filtering particles of different size depending on the size of the holes in the net. For this purpose HMSs with only 2 traps were designed and fabricated, and the fishnets were modified to have two long handles as seen in the center inset of Figure 5.12. A simple microfluidic chip was fabricated by first drilling two holes into a glass microscope slide, attaching two cut Eppendorf pipette tips using epoxy resin, and forming a channel on the other side using two long pieces of double-sided tape before closing the channels with a coverslip. Attaching rubber tubing to the ends of the pipette tips allowed for flowing a mixture of fishnet membranes and particles through the chip and trapping and bending of the fishnet membranes as shown in the insets of Figure 5.12. These were manipulated using an SLM, and due to the difficulty of getting a consistent slow flow rate using the pump system, as well as regular leaks in this design the scope was reduced to a simple trapping of the membranes in plane as shown in Figure 5.11 (c).

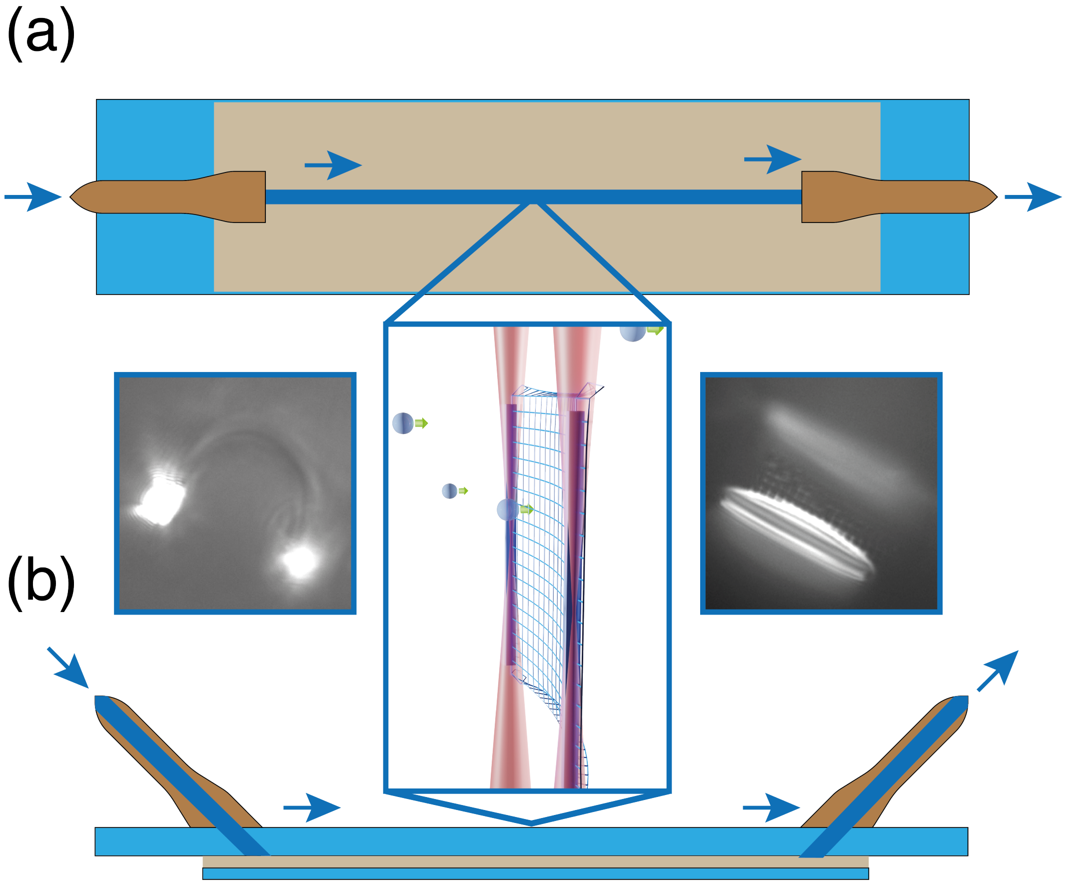

Figure 5.12 Simple microfluidic chip designed for use with holographic traps and fishnet membranes from (a) top view and (b) side view. The insets show the images from fishnet membranes being trapped in the chip, as well as the concept of the net being used for filtering particles of different sizes.

5.2 Trapping with Biocompatible ZrO2 Metasurfaces in Transmission

While the reflective HMSs' trapping performance was some of the highest recorded at the time of publishing, they were not without their drawbacks. The reflective design meant imaging and trapping could only be done from one direction, and collecting signals reflected from samples carries less information than those collected in transmission. They rely on the PB phase and require circularly polarized light, and consist of a polymer photoresist which is not necessarily biocompatible.

Additionally, the nano-sized antennas are quite fragile. Over time, the liquid in the microfluidic chamber will dry up and evaporate, making it impossible to optically trap.

At that point, with a sample such as a HMS one, the coverslip can be gently removed, and a new sample of beads inserted and re-sealed, meaning the same HMS slide can be used multiple times over weeks. Unfortunately, as the beads lie and move around on the surface, they tear up the HMS, almost like huge bowling balls, degrading it over time. As the eventual goal of the platform is to be used with biological samples, it can be easily assumed the same would happen if cells or other specimens were to move across the HMS surface as seen in Figure 5.13.

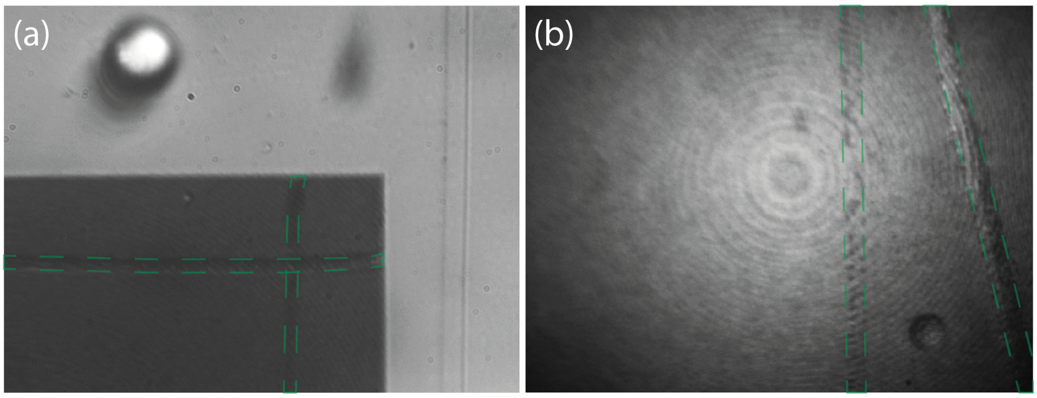

Figure 5.13 Images of HMSs destroyed by beads, with the destroyed tracks highlighted using the green dashed lines.

To address some of these issues, the work in this section focused on using ZrO_2 polarization-independent HMSs, working in transmission over a broad range of wavelengths including blue and UV wavelength where the trapping stiffness is much higher. ZrO_2 is a ceramic with a range of advantageous properties for biophotonics applications. As seen in Figure 5.14 when compared to silicon and TiO_2, which are typically used in transmissive HMSs, ZrO_2 has a remarkably consistent refractive index over the visible range with negligible losses. It's chemically inert and very hard, making it particularly suitable for biophotonic applications.

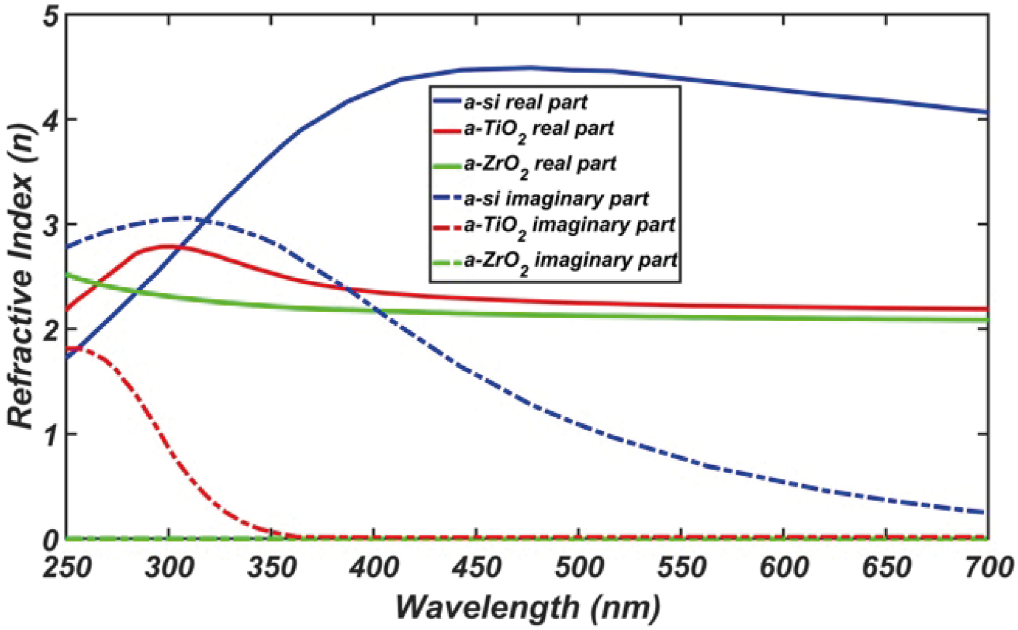

Figure 5.14 Ellipsometer measurement of the refractive index of amorphous ZrO_2 compared with amorphous TiO_2, and amorphous silicon. Taken from [129].

Fabrication and Broadband Operation Characterization

As described in Chapter 2, here, the meta-atoms function as truncated waveguides, where dephasing is dictated by the different effective refractive indices of the propagating modes. The unit cells of the HMSs are illustrated in Figure 5.15 (a), arranged in a hexagonal lattice with periodicities of 200 nm and 210 nm for the blue and green (HMSs), respectively. Each unit consists of a thick microscope glass slide substrate, a 50 nm thin layer of ITO serving as a conductive layer, 700 nm tall ZrO_2 pillars embedded in a polymethyl methacrylate (PMMA) matrix, and a 180 nm flat top layer of ZrO_2.

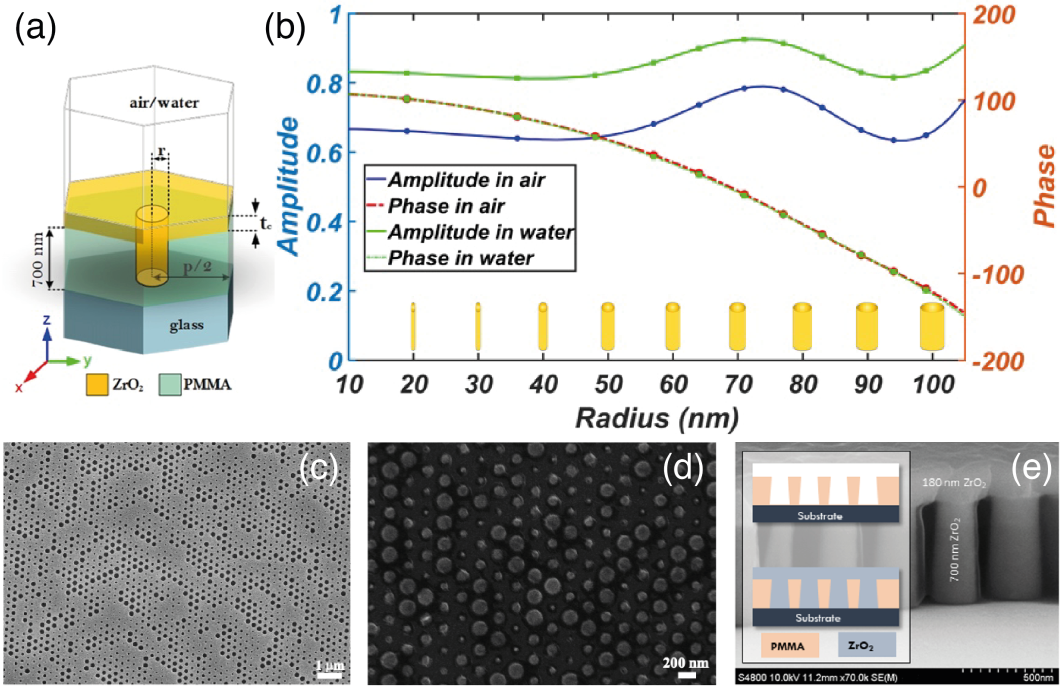

Figure 5.15 (a) Proposed unit cell perspective, (b) the transmission and phase profile of meta-atoms in air and water at 532 nm. Shown below are SEM images (c) after 40 nm gold evaporation on the developed sample, and (d) after lift-off of the photoresist and (e) image of the fabricated device, inserted are the fabrication work flow consist of EBL and ALD steps. Taken from [129].

The different fabrication steps are shown in Figure 5.15(c - e). A layer of 50 nm ITO was deposited as a thin conductive layer using a sputterer (Angstrom Engineering) to minimize electron backscattering effects. A 700 nm-thick layer of PMMA (A7 950K, Micro Resist Technology) was spin-coated at 1650 rpm for 60 s and subsequently baked for 5 min at 180 °C. The meta-atoms were defined using the EBL system, followed by development for 65 s in a 1:1 ratio of isopropanol and distilled water. This ratio was optimized to ensure the complete development of all varying-sized unit cells. Verification was performed using a sacrificial sample; a layer of gold was deposited on the PMMA and lifted off, as depicted in Figure 5.15 (c) and (d). The sample was then baked for 30 min at 95 °C, and the ZrO_2 layer was deposited via atomic layer deposition (ALD) at a rate of 1.79 Angstroms per cycle. This resulted in the HMS having a flat top layer of the ZrO_2 layer, effectively isolating it from the rest of the sample, providing medium-independent optical response and protecting the meta-atoms, as shown in Figure 5.15 (e).

As before, the HMS phase masks were designed using the GSA, resulting in Fresnel lens-like phase profiles seen in Figure 5.16 (a) and (b). Also shown in Figure 5.16 (c) and (d) are the experimental beam profiles at the focal planes for the two HMSs, demonstrating that both lenses have an NA given by $\mathrm{NA} = 0.51\lambda/\mathrm{FWHM} \approx 1.2$, resulting in diffraction limited spots formed by the HMSs.

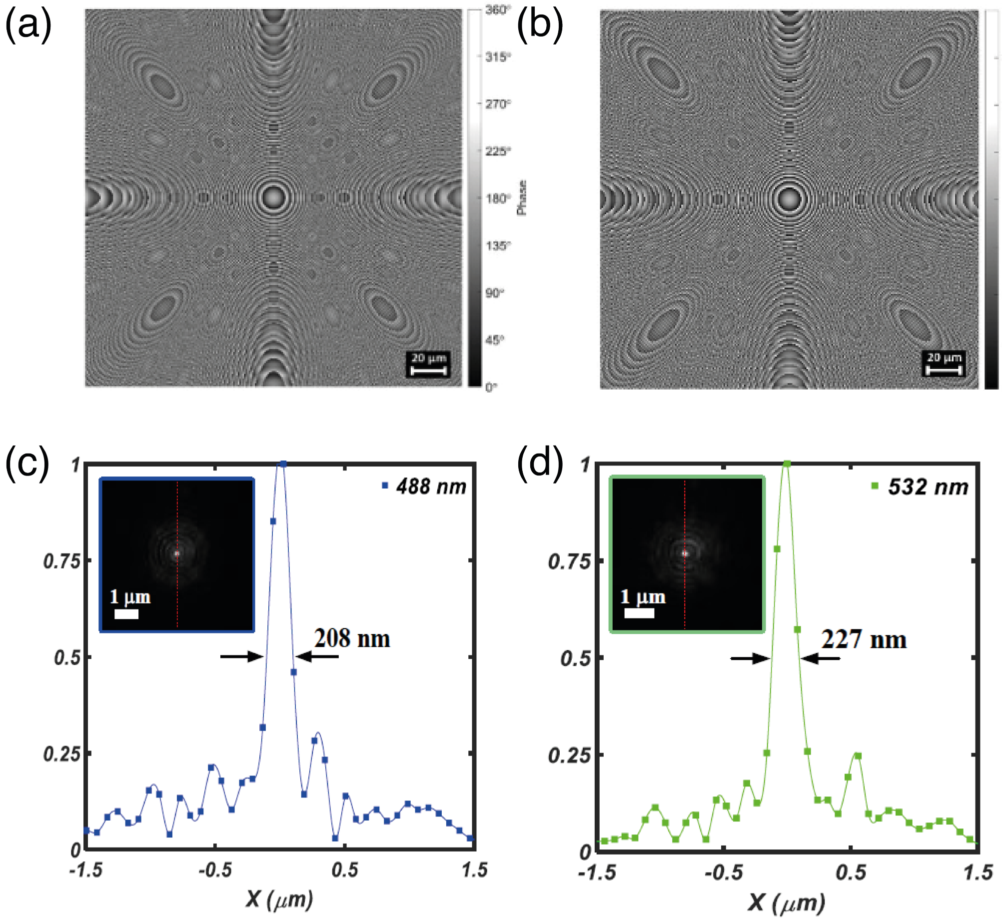

Figure 5.16 Designed phase profile at (a) 488 nm and (b) 532 nm and the experimental beam shape profile at (c) 488 nm and (d) 532 nm with its inserted image at the focal point. Taken from [129].

To characterize the HMSs, two sets of holograms were fabricated to evaluate their efficiency and image-forming capabilities. The efficiency was measured by designing the HMSs to project a collimated beam at 30 degrees relative to the normal of the HMS. The diffraction efficiency was determined by normalizing the power of the first diffracted orders against the power of the non-diffracted zeroth order, as illustrated the top section of Figure 5.17. The error bars reflect the impact of fabrication quality, including the precision in the exposure and development of the meta-atoms. The resulting efficiencies for the HMSs were 67% (HMS designed for 488 nm) and 59% (HMS designed for 532 nm). The bottom section of Figure 5.17 shows the operation of the HMS designed for 532 nm across the visible spectrum.

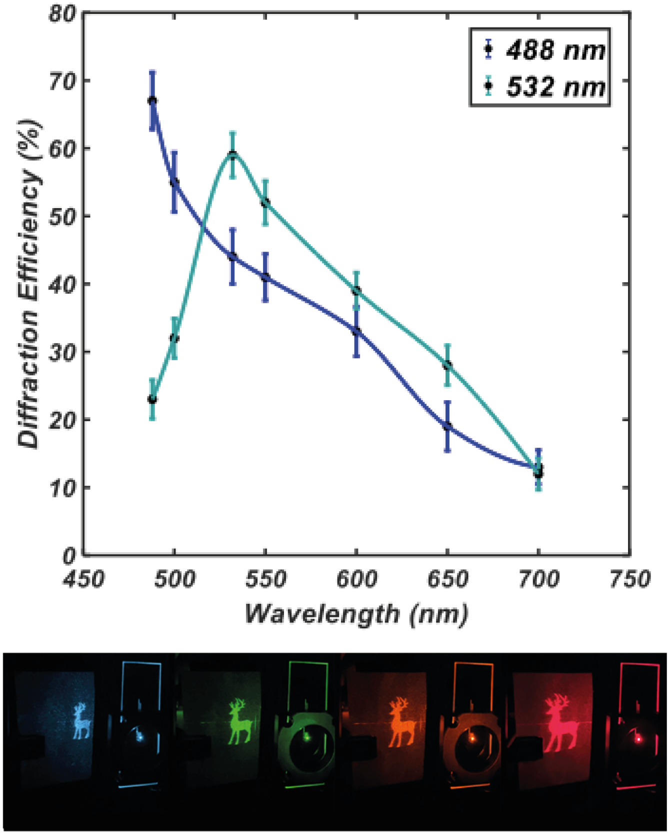

Figure 5.17 The obtained experimental efficiency at visible wavelengths regime, with the strip below showing and experimental holographic image at 488, 532, 590, and 632 nm. The error bars represent the standard deviation from 4 measured metasurfaces. The error bars reflect the impact of fabrication quality, including the precision in the exposure and development of the meta atoms. Taken from [129].

Particle Trapping in Transmission

The trapping was done using a linearly polarized green laser (532 nm, Laser Quantum) focused by a lens with a focal length of 1000 mm and directed onto the HMS. This configuration produced a spot size of approximately 250 μm in diameter on the 140×140 μm^2 HMS. The blue laser (Ibeam 488 nm, Toptica) was similarly expanded to a diameter of 1.3 mm and focused using the same 1000 mm lens. Selection between lasers was achieved using flip mirrors. The sample was imaged with a microscope (Eclipse Ti-U, Nikon) equipped with a motorized stage (PRIOR). A filter mounted on the microscope turret blocked the trapping laser while permitting white light to reach the CCD camera (VCXU-13 M, Baumer), which recorded the trapping experiments.

To facilitate the trapping experiment, the green light was directed to the rear of the microscope and used to trap 2 μm diameter SiO_2 beads using a 60X water immersion microscope objective (PlanAPO VC60xA, Nikon) with NA = 1.2. The trapped particle was positioned near the focus of the HMS before the green light was switched off. The

CCD camera was calibrated using this objective, establishing a pixel size of 80 nm.

The particle position trajectories were extracted from 10-second-long videos recorded at 1000 fps for varying laser powers using the same method described in Chapter 3. The error bars along the x-axis in Figure 5.18 are attributed to oscillations in laser power. The experiments were conducted five times for each specified power setting, resulting in the error bars along the y-axis representing variations in trap stiffness.

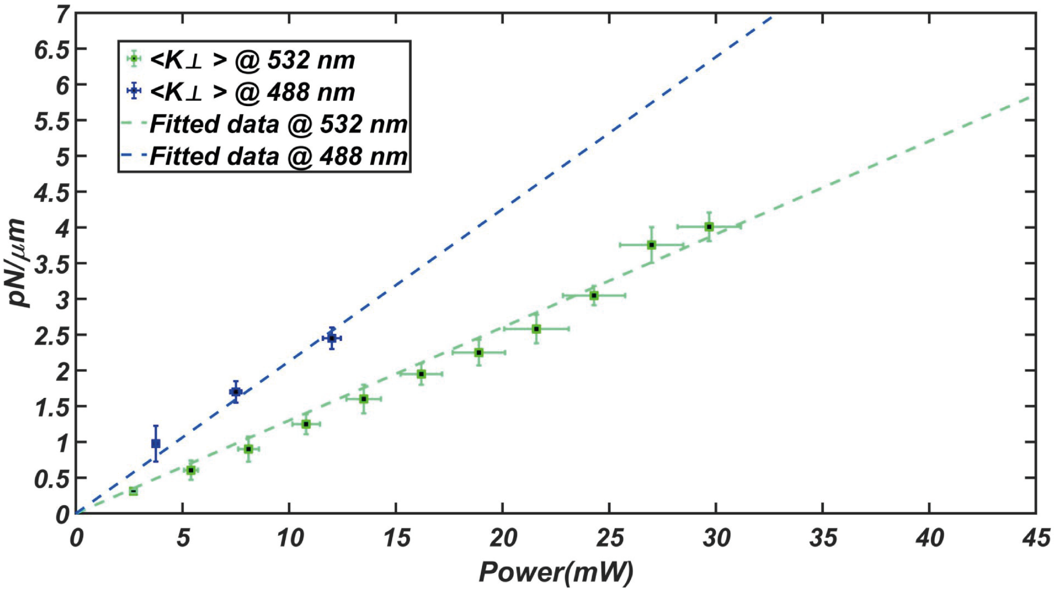

Figure 5.18 Trap stiffness measurements for optical trapping at 488 and 532 nm. The error bars along the x-axis in Figure 5.15 are attributed to oscillations in laser power. The experiments were conducted five times for each specified power setting, resulting in the error bars along the y-axis representing variations in trap stiffness. Taken from [129].

The trap stiffness $(K_\perp)$, averaged along the x and y directions, is depicted in Figure 5.18 with values of 212 pN/μm/W at 488 nm and 130 pN/μm/W at 532 nm, respectively. The power values used in Figure 5.18 and for data analysis were derived by considering the power of the Gaussian beam incident on the MSs, scaled by the geometrical overlap with the HMSs and the efficiencies previously measured for both HMSs.

5.3 Contribution

This work resulted in two publications, ”On-Chip Optical Trapping with High NA Metasurfaces” [128] described in the first portion of this chapter, and ”ZrO2 Holographic Metasurfaces for Efficient Optical Trapping in The Visible Range” [129], described in the second portion.

For both papers, I was responsible for theoretically calculating the HMS parameters such as size, numerical aperture, and focal length for optical trapping. I was also responsible for the data analysis: I extracted the trapped motion of the particles and subsequent quantification of the trapping efficiency compared to that of a microscope objective. For ”On-Chip Optical Trapping with High NA Metasurfaces” [128], I built the optical setup described in Chapter 3 and performed all of the experimental work of sample preparation and optical trap characterization. Jianling Xiao designed, simulated, and fabricated the HMSs and the extended objects for demonstration of holographic trapping. For the ”ZrO2 Holographic Metasurfaces for Efficient Optical Trapping in The Visible Range” [129], Mohammad Biabanifard performed the trapping experiments and HMS design, simulation, and fabrication. I assisted in building the optical setup and supported the experiments.

5.4 Conclusion

This Chapter explores the use of HMSs designed for optical trapping and manipulation, achieving efficiencies comparable to high-NA objectives and delivering trap stiffness up to 430 pN/µm/W.

The first section presents reflective HMSs with high NA, optimized for minimal areas under 0.001 mm^2. To demonstrate the platform's adaptability, we engineered specific HMSs for multi-site trapping, successfully capturing a large fishnet membrane. This study underscores the potential of HMSs to revolutionize lab-on-chip devices with multifunctional capabilities.

In the second section, we showcase the first demonstration of on-chip optical trapping in the blue spectrum. We report the use of ZrO_2 HMSs operating in the visible range, designed for holographic imaging and optical trapping. These HMSs were also designed with a high NA of 1.2 at 532 nm and 488 nm, with efficiencies exceeding 67% and trapping stiffness greater than 200 pN/µm/W. The capabilities of these HMSs suggest their broad applicability in fields such as holography, optical trapping, and biomedical applications.

One of the central claims in this Chapter is that these metasurfaces could eventually replace microscope objectives. While the initial process is cumbersome, requiring expensive and complex fabrication, this is simply the first step in any commercialization — the prototyping stage. Once a design is chosen, nanoimprint lithography can pattern the metasurface masks by the millions in a fraction of the time it takes to finish a single EBL writing.

With this Chapter ends the portion of the work done on on-chip trapping. The next Chapter deals with the extended objects described in both this Chapter, and the fabrication of which was covered extensively in Chapter 3. The eventual goal of this work would be to combine the two — the HMSs could be made to create custom positions for the microscopic optics fabricated using EBL, to create reconfigurable tools around any biological object of interest.

CHAPTER 6

Optically Manipulated Membranes as in-situ Optical Elements

Following the previous two Chapters on on-chip optical trapping, where static methods are used, this Chapter is motivated by the experimental challenges of working with biological samples in a lab environment. It covers the use of optically manipulated polymeric membranes, the design of which was described in Chapter 3, as both in-situ optics and sensitive force transducers for experiments involving DNA.

One of the main ways to interact with the samples is through light delivered and collected from the microfluidic chamber, whether to image, excite fluorescence, sense, or physically manipulate them through optical tweezers.

Most of these methods involve a microscope objective in some way, which provides a very limited window into the sample in terms of the small field of view of the objective and the range of detectable light moments. The main solution to this is to add more objectives, increasing the cost and complexity of the system.

Biological samples often also require an encapsulated, controlled environment. Light is shaped, focused and filtered before reaching the sample plane, adding to the bulk and maintenance of traditional optical setups.

The sample itself can be patterned to include additional elements to aid with the interactions. For example, 45-degree prisms can be used for single-objective light-sheet microscopy [251, 252], and fibers can be side-coupled into the sample chamber to optically manipulate and stretch cells without the need for an objective [253]. However, all of these methods involve inherently static elements, limiting their versatility and limiting them to systems where the samples are either grown directly next to the elements or flown through a microfluidic chamber, effectively randomizing the samples being analyzed.

Another approach is to use microtools. These can be controlled through magnetic fields [254], chemical reactions [255], and light [256]. Optical manipulation is a well-explored method with optically controlled force probes, motors, and carriers. While providing an avenue for physical interaction with the samples, they don't do much to deliver light to the sample.

The membranes we fabricated combine the advantages of both of the above solutions. They can be readily manipulated and delivered to the samples of interest, **and** they can condition the light around them in real-time, adapting to the individual samples. They do not only benefit from the ability to be patterned. Their large anisotropy significantly increases their stability in the transverse direction, dampening vibrations and essentially acting as a parachute.

4 applications of membranes, as well as a derivative microtool designed using the same fabrication methods will be described in Chapter 3. The first three will include using the membrane as a microscopic mirror, able to redirect light in the microfluidic chamber. The last two will deal with plans for using the membrane and a microtool for interacting with DNA.

The first application explored was using the membranes as steerable micromirrors, used to excite whispering gallery modes along arbitrary planes of microlasers using only one microscope objective.

6.1 Micromirrors for Exciting Whispering Gallery Modes in Microlasers

Whispering gallery modes (WGM) are supported by circular microlasers such as spheres [21], disks [257], and toroids [258]. These microlasers facilitate advanced sensing by collecting data from their entire surface. The microlasers support various resonant modes, each indicating a unique trajectory for light around their perimeter along a plane [259]. These modes, sensitive to changes in size, shape, and refractive index differences between the microlaser and its surroundings, enable the detection of minute variations. Their sensitivity comes from extremely high quality factors, which allows us to look at the spectrum of a WGM microlaser and deduce the environmental changes by observing the modes' spectral shifts.

Microlasers, as they are referred to in this Chapter, are the result of the introduction of gain media in WGMs. This enhances their sensitivity to environmental refractive index changes, as now, instead of tracking the shift of multiple modes, only few dominant lasing modes are excited with a very high intensity. This has been used in live biological samples for analytical methods; for example, the imperfections in individual microlasers can be used for tracking tens of thousands of individual cells, as each cell will ingest a microlaser with a slightly different spectrum, creating a unique 'barcode' [21]. The WGM lasers also enable force measurement within cellular structures, when ingested by heart cells. The heart cells contract, causing a change in the refractive index around the microlaser and resulting in a detectable shift of the dominant lasing mode [20].

However, despite these advancements, the current approaches primarily activate WGMs in the illumination direction, limiting their capacity to only average refractive index shifts [20] across a single plane. This constraint underscores the need for methods that offer a more diversified and comprehensive analysis, capturing the full potential of WGM sensing technology.

This section introduces a system that differentiates refractive indices across various axes of a spherical microlaser. This differentiation is facilitated by optically controlled mirrors, described in the previous section, which can alter the illumination direction and the plane of WGM laser emission. Utilizing this approach, we also conduct a time-resolved analysis of dynamic sensing by observing a glass bead in orbit around a WGM microlaser.

Shown in Figure 6.1 is the concept image for the experiment, which features a micromirror used to excite WGMs across a microlaser trapped inside a living heart cell.

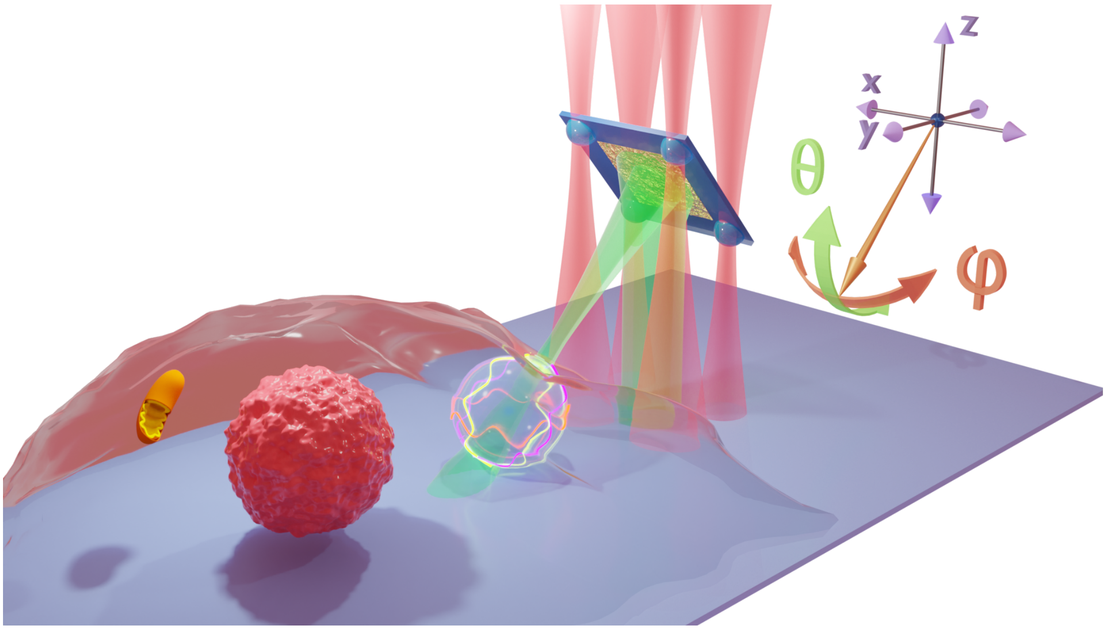

Figure 6.1 Shown is a mirror, held in place by optical trapping, being used to stimulate WGMs on various planes of a spherical microlaser sitting on glass. Before reaching the micromirror, the trapping and excitation laser beams travel in the positive z-axis direction. The central point of the micromirror is designated as the reference point for the coordinate system used throughout this section. Taken from [194].

The optical setup was the same as the one described in Chapter 3, with holographic optical tweezers used to manipulate the membrane micromirrors and individual particles, the pulsed laser used to excite WGM laser emission, and the Andor spectrometer used to collect the spectra. The microlasers were dye-doped polystyrene spheres

(PS-FluoRed, 15.35 µm particle diameter, Microparticles GmbH), and during the time-resolved experiment, a 5 µm polystyrene probe bead was used to orbit the microlaser.

Refractive Index Sensing Along Arbitrary Planes

Before WGM could be systematically excited across various planes, reference spectra were taken for validation. This involved measuring the spectra of the lasing modes at the two refractive index extremes available within the simple microfluidic chamber, the refractive index of the glass substrate ($n_g \sim 1.52$), and the refractive index of water ($n_g \sim 1.33$). This is the environment probed by the mode in the case of the microlaser sitting on the glass, the mode is only partially touching the glass, or fully touching only water. These would serve as theoretical upper and lower bounds to the refractive index shift. This portion of the experiment didn't require the use of membrane micromirrors, only finding a microlaser that could be lifted up into the center of the microfluidic chamber using an optical trap. This was also a great opportunity to establish a minimum power required for a sufficient SNR of the microlaser signal. While versatile, the reflective portion of the membranes is susceptible to being damaged at high pump laser intensities, especially if the laser is focused. The larger pump power being reflected by the micromirror also affects trapping stability due to the radiation pressure from the reflection.

As depicted in Figure 6.2 (a (i) and (ii)), two distinct spectra were obtained by directing the excitation through the microscope objective towards the microlaser. The first spectrum (i), indicated in yellow, established a baseline for the microlaser's interaction with glass (a medium of higher refractive index), while the second spectrum (ii), in orange, acted as a benchmark for the microlaser in a solely water environment (a medium of lower refractive index).

Illustrated in Figure 6.2 (b), an analysis was conducted on six modes per spectrum, considering the spectrometer's physical resolution of 35 pm and the use of comparatively low pump powers to mitigate mirror heating and light reflection onto the microlaser. The analysis focused on the average shifts across these six modes, taking into account the potential for heating and movement of the optically trapped microlaser, and was done using a MATLAB script.

This MATLAB script processes and analyzes spectral data to extract the position and characteristics of lasing peaks. It initializes with predefined constants for membrane angles, heights, and calibrates using background spectra. Calibration spectra, taken in different conditions such as water and on glass, establish reference data to calibrate the main spectral analysis. This calibration helps understand the effects of experimental setup on spectral characteristics.

The script then processes spectral files by cleaning, averaging, and reducing noise from the data and applies Gaussian fitting to identify and fit lasing peaks within a confined wavelength range based on a prominence threshold. The fitting extracts peak positions, intensities, and widths, along with confidence intervals. These parameters, alongside error measures and fit quality indicators like the coefficient of determination, are used to analyze the effect of the angle of illumination of the microlasers on the plane of the WGM being excited.

The script then organizes the data into structured formats, adjusting for data inconsistencies and saving the results in tables for further analysis.

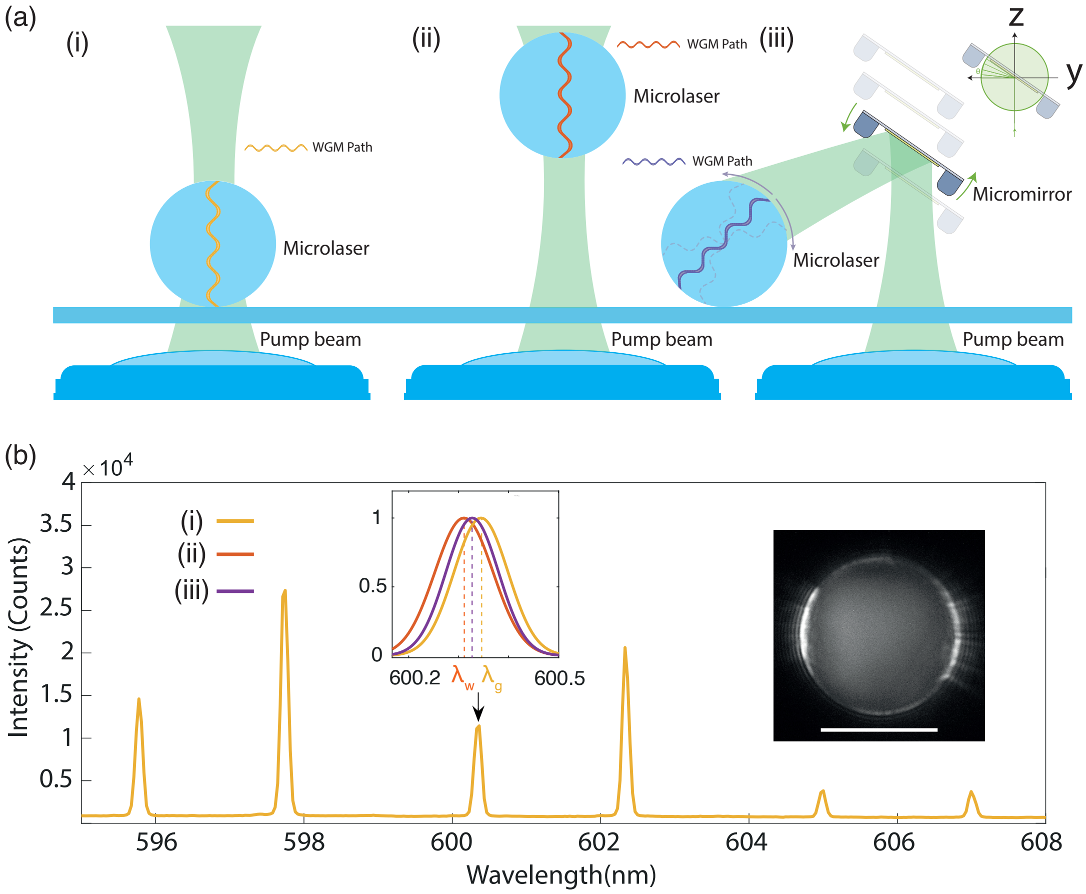

Figure 6.2 (a) the experimental setup under different illumination conditions: (i) with glass using the objective, (ii) with water using the objective, and (iii) with glass using the membrane; and (b) a typical spectrum for case (i), including an inset of the fitted normalized spectra for a specific mode across conditions (i)- (iii), where the mode excited via the membrane shifts between the water and glass modes. The scale bar is 10 µm. Taken from [194].

Subsequently, as highlighted in Figure 6.2 (a (iii)), a membrane was used to illuminate the microlaser at various heights and tilt angles, with a comprehensive mapping of these illumination positions presented in Figure 6.3 (d) displays the heights at five different levels, each examined through 20 angle combinations in θ and φ as shown in Figure 6.3 (c). To prevent direct excitation by the beam without reflection from the mirror, the microlaser was positioned 40 µm from the membrane, a distance determined through camera calibration for imaging both the microlaser and membrane. The beam was defocused by 17 µm from the microscope objective's imaging plane to ensure the membrane was adequately illuminated.

These experiments took multiple months to perfect the simultaneous manipulation of the membranes and microlasers and experiment with the optimal configuration of the spectrometer and pump beam. An attempt starts with scanning the sample (sometimes for hours) searching for a suitable membrane micromirror with all 4 handles intact. Once a membrane is found, a fresh, unstuck microlaser is searched for, which is a very slow process as it's impossible to move the membrane micromirror quickly through the medium. Once all components are placed in the field of view, the membrane is lifted and a check is performed to see if it can be tilted by 45 degrees without being pushed away by the laser. Then, the pump laser is switched on and translated in x,y, and z to ensure it's defocused when reflecting from the membrane. Multiple membranes were destroyed during this step as the membrane could be pushed into the focus of the pump beam, instantly melting the gold on top. If this happens, the attempt is restarted.

Once the setup described above is completed, all spectra need to be taken together to ensure consistent results. As the sample is constantly moving, it's never a guarantee that a sample left overnight or even for a few hours will be in the same state as before. Additionally, even during the experiment, the membrane can be pushed away by other particles being attracted into the optical traps, breaking the delicate balance of the experiment. For that reason, the spectra described in the rest of this section were acquired during a single 7-hour session.

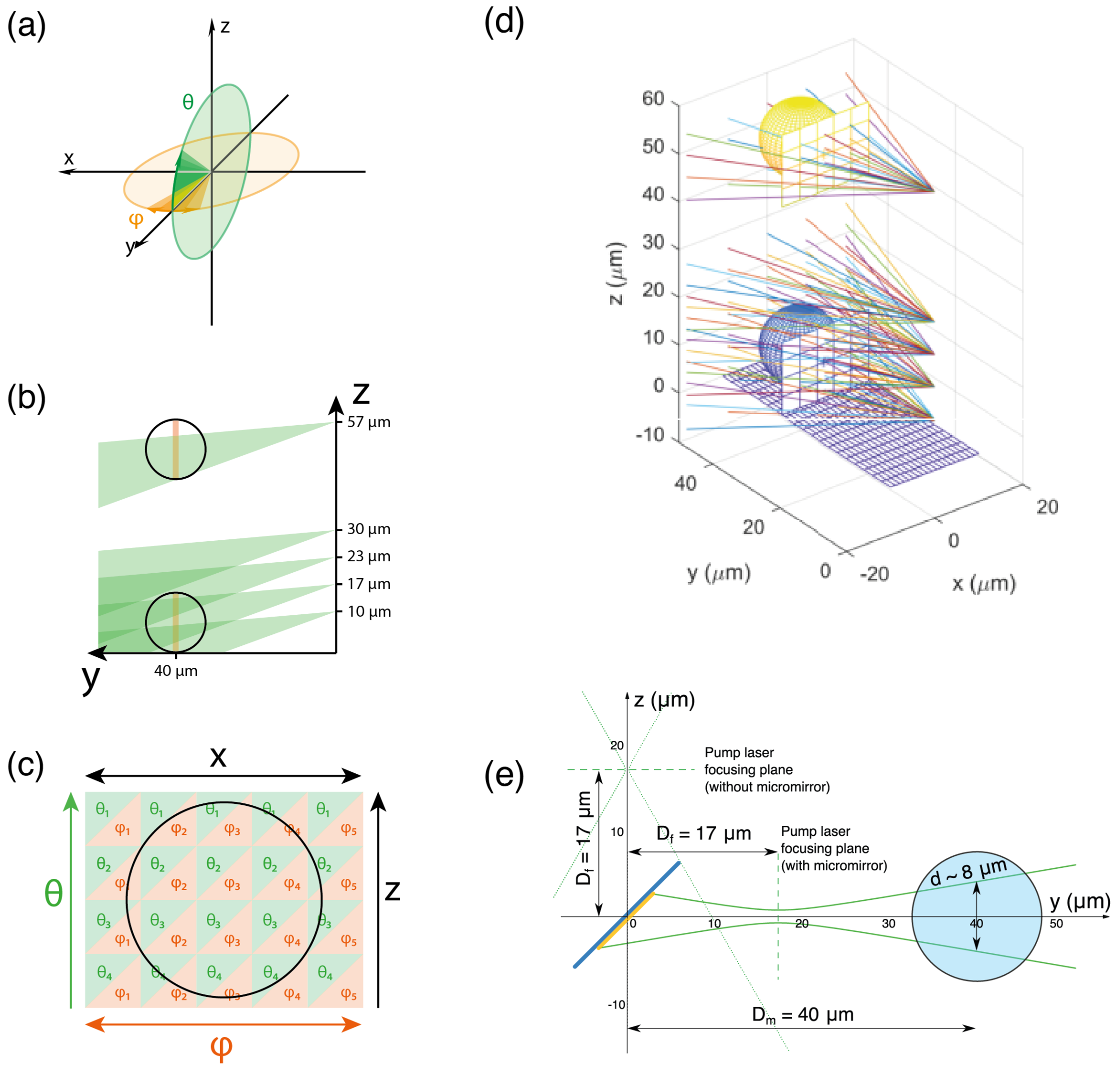

Figure 6.3 The micromirror's tilt and location are illustrated (a) in three dimensions, (b) across the x-axis, and (c) along the y-axis, with respect to the microlaser. The black circle acts as a reference point, marking the outer edge of the microlaser. (d) shows the three dimensional projection of the experiment, while (e) shows a side-view 2D ray schematic showcasing the microlaser illumination. The micromirror's center is positioned D_m = 40 µm from the microlaser's center. The pump laser's focus is offset by D_f = 17 µm from the imaging plane, which aligns with the xy plane. A dotted green line demonstrates the pump beam's trajectory if the micromirror were absent. Dashed green lines delineate the pump laser's focal plane. The angled mirror functions as a rectangular aperture, yielding a projected beam width of approximately $d \sim 8$ µm. In the perpendicular direction (not depicted), the beam's estimated width is about ~ 10 µm. Taken from [194].

A total of five sets, each comprising 20 spectra, were recorded: four sets with the microlaser positioned on glass and one with the microlaser completely immersed in water, as depicted in Figure 6.3 (b — d). The mode parameters at specific z, θ, and ϕ values were determined via fitting. The spectra preprocessing involved background subtraction to compensate for minor variations in the microscope's collection plane at different positions.

This resulted in 100 spectra (102 counting the glass and water references) with 6 mode peaks each. Each peak had potentially relevant properties: the mode number, width, height, position, and shift. Each peak also depends on the physical parameters of z, θ, and ϕ. This leaves us with 600 peaks with 7 individual parameters each, posing a significant challenge in data visualization and extracting useful information and parameter dependencies. The first attempt was to visualize both the spectral shift and peak height (intensity) as a function of the angle of the membrane pointing the beam at the microlaser as shown in Figure 6.4

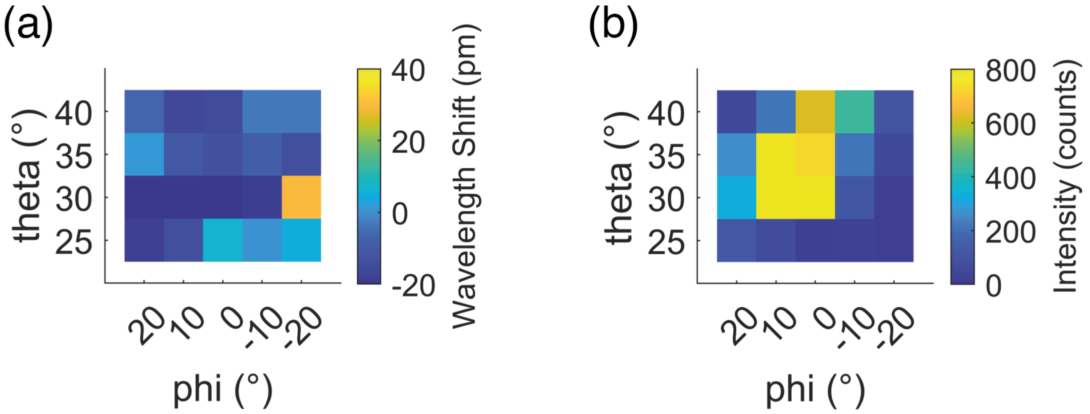

Figure 6.4 Example of a heatmap plotting of the spectra at a membrane height of 10 µm. (a) shows the shift of the spectra compared to the spectrum of the microlaser touching the glass, and (b) shows the intensity map of the spectra, showing the position of the microlaser. Taken from [194].

While visually intuitive, plotting all 100 spectra required in 5 rows was quite difficult to analyze, and limited us to only plotting one spectrum parameter at a time.

In order to show all of the parameters, as shown in in Figure 6.5 (a), spectra are normalized against the condition where the microlaser is in contact with the glass ($\Delta\lambda_g$). To enhance clarity, spectral shifts relative to this baseline ($\Delta\lambda_w$) —— occurring when the microlaser is suspended in water —— are indicated. In both reference conditions, the microlaser was excited using the orthogonal orientation of the objective, without employing the micromirror. Figure 6.5 (b) illustrates the micromirror and microlaser positions, with labels (i) — (v) marking different membrane heights. The horizontal axis displays shifts for four distinct θ angles, each assessed at five ϕ angles. The radius of each data point reflects the average spectrum intensity, normalized against other spectra at the same height, providing a visual indication of signal strength and likely accuracy due to higher SNRs. Average peak errors are represented as error bars for each data set. A histogram on the left side visualizes the distribution skewness towards either glass or water reference.

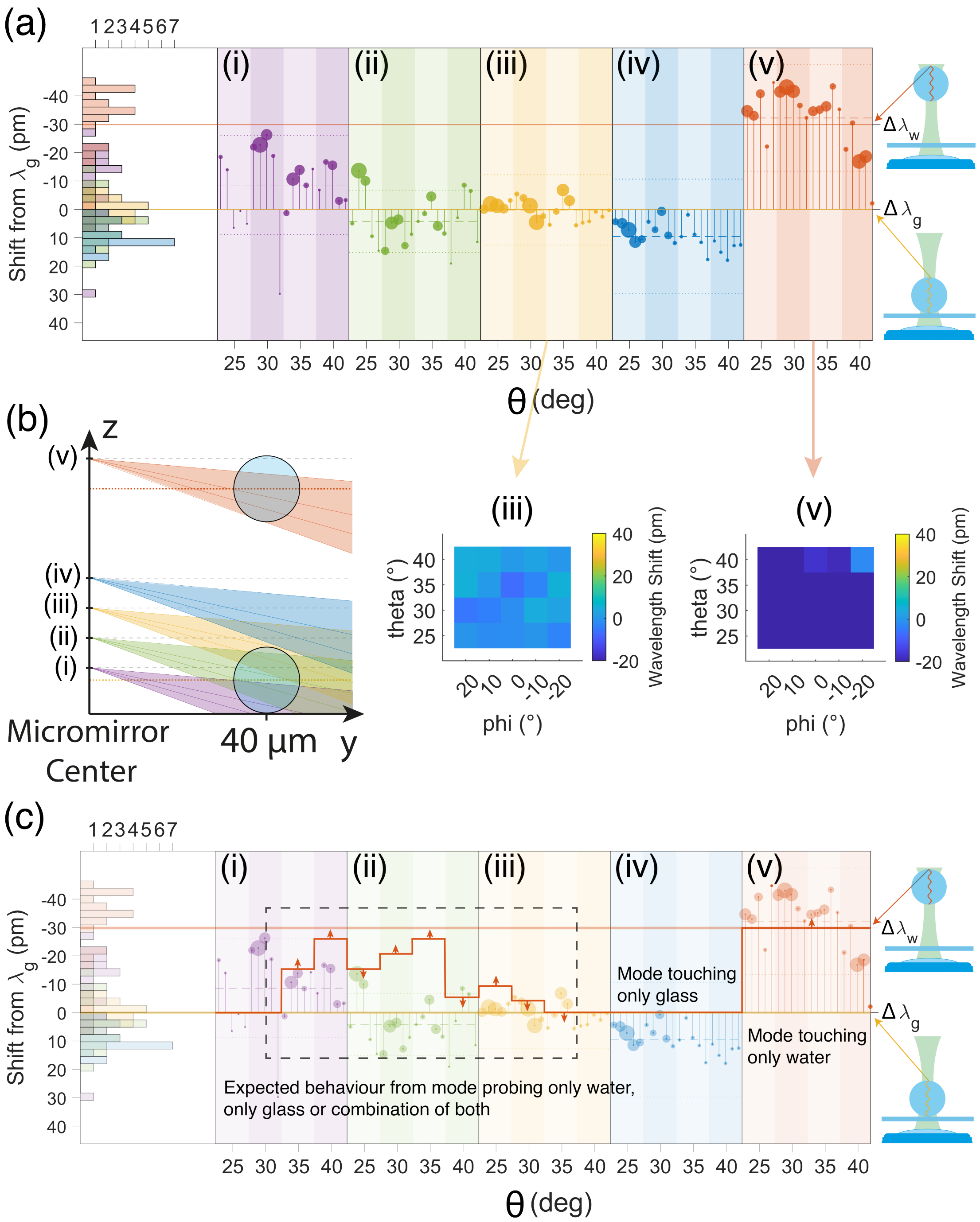

Figure 6.5 Analysis of spectral shifts and micromirror positions. (a) Graphical representation of spectral shifts observed when the micromirror is placed at different elevations above the glass slide: 10, 17, 23, 30, and 57 μm. The shifts are benchmarked against the spectrum of the microlaser on glass (λ_g), obtained through objective-direct excitation. Point sizes correspond to normalized spectral intensities. Solid horizontal lines ($\Delta\lambda_g$ and $\Delta\lambda_w$) represent average spectral shifts for excitation on glass and in water, respectively. Histograms elucidate the distribution of these shifts, with dashed lines indicating average values and dotted lines showing standard deviations. Two heatmaps of the spectra are shown below for (iii) and (v). (b) Schematic detailing the relative placements of the micromirror and microlaser for heights (i) through (v), with the microlaser dimension accurately scaled. (c) Shows the expected behaviour of the mode shifts. Taken from [194].

A clear trend can be seen as the height of the membrane is increased, where the shift from the glass being probed increases in Figure 6.5 (ii — iv). This is due to the light coupling into the microlaser at the top of the sphere, exciting a vertical WGM. This is in contrast to the spectral shift seen in Figure 6.5 (i) and (v) where the microlaser is excited from the side, and the WGM are excited along a plane that only touches the water around the microlaser. As another form of visualisaton of the spectral shift, heatmaps were plotted of the spectral shift of the modes probing the glass (Figure 6.5 (iii)) and the water (Figure 6.5 (v)).

Since we were interested in measuring the relative shift of the refractive index instead of the absolute shift per refractive index, the sensitivity is not stated in the typical units of nm/RIU. However, a sensitivity of ~0.05 nm/RIU has been obtained inside living cells [20] using the same spectrometer with our settings (resolution of 35 pm, aperture of 10 µm). This agrees with our results, with the fitting of the Gaussians being able to surpass the spectrometer's resolution. The wavelength stability of the system can be seen more clearly in Figure 6.6, where a variation of ±5 pm can be seen over the course of a few seconds at the start of the spectral recording.

6.2 Time Resolved Refractive Index Sensing

To showcase the versatility and capabilities of the micromirror platform, it was employed to observe real-time local dynamic changes in the refractive index around the microlaser. This was achieved by optically manipulating the micromirror alongside a 5µm polystyrene probe bead. The bead was actively maneuvered around the suspended and trapped microlaser while emission spectra were concurrently recorded in real-time.

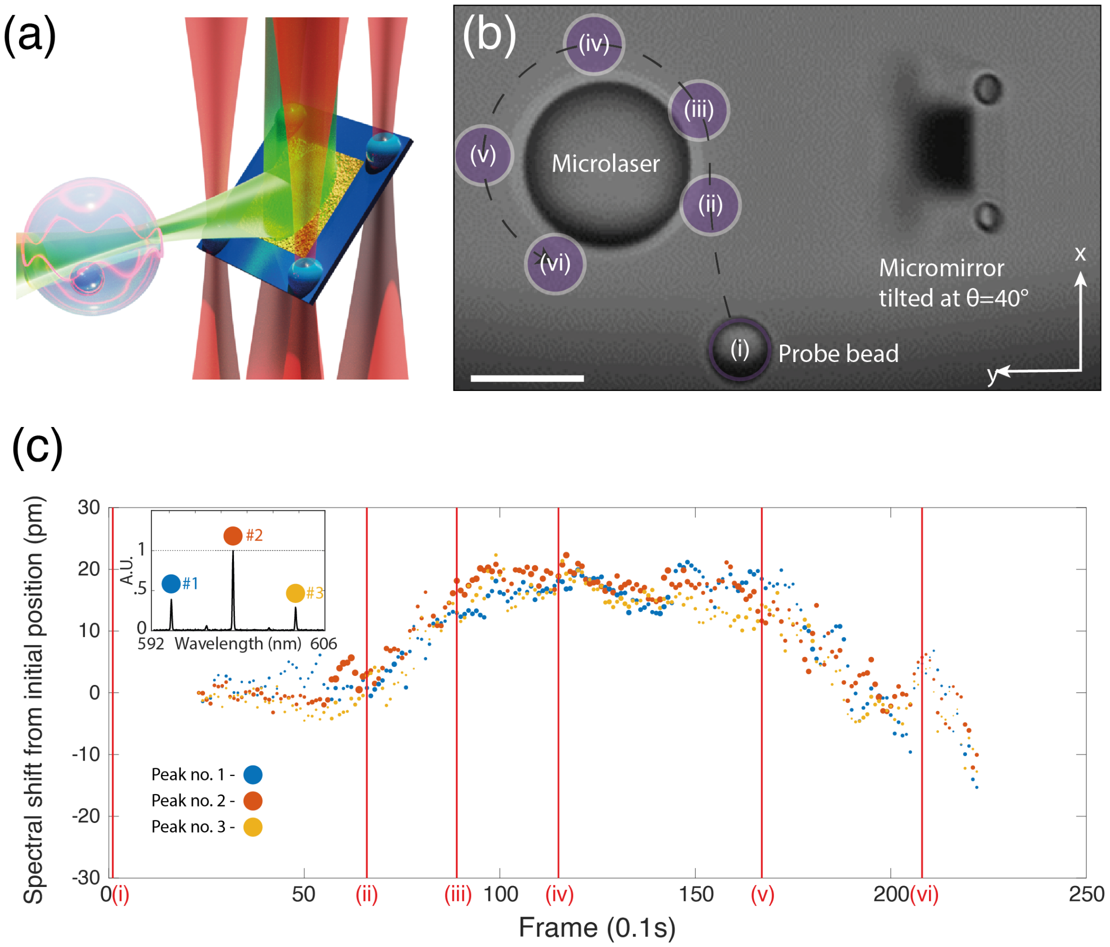

Figure 6.6 (a) Illustration of the experimental setup for detecting localized refractive index changes. The setup utilized a micromirror for directing light towards a suspended microlaser, while a 5 µm diameter polystyrene probe bead introduced local refractive index shifts at specific frame timestamps: (i) 1, (ii) 66, (iii) 89, (iv) 115, (v) 167, and (vi) 208. (b) Time-dependent spectral shift analysis for three chosen WGM peaks, illustrating peak displacements from their position at frame 20. Vertical red lines mark the spectra corresponding to the positions in (a), with the initial normalized spectrum depicted in the inset. The size of data points reflects the normalized intensity of each spectrum. A 10 µm scale bar is provided for reference. Taken from [194].

To demonstrate the micromirror platform's versatility and unique capabilities, we employed it for real-time monitoring of local dynamic changes in the refractive index near a WGM microlaser. This involved simultaneous optical manipulation of the micromirror and a 5 µm diameter polystyrene probe bead, with a refractive index of $n_b = 1.59$. The bead was actively navigated around the trapped and suspended microlaser to acquire emission spectra. To negate surface effects, the micromirror, microlaser, and probe bead were positioned 50 µm above the glass substrate, with the centers of all objects aligned with the imaging plane of the microscope objective. Figure 6.6 (a) displays the configuration of the three objects and the probe bead's path, indicated from (i) to (vi).

Figure 6.6 illustrates a typical timeline of lasing mode shifts over two hundred spectra collected over 20 seconds, synchronized with a video recorded by the CCD. For a high SNR, the shift of only the three most intense peaks per spectrum was monitored, with reference to the emission spectrum at frame 20—before the probe bead made contact with the microlaser (see Figure 6.6 (b) inset for an illustration).

As depicted in Figure 6.6 (b), the pump laser was activated around frame 20. Subsequently, the bead's gradual approach towards the microlaser, first making contact at frame 66 [(ii)], triggered a noticeable shift in the peak positions. This observed redshift is consistent with the expected influence of a high-index probe near the microlaser. The bead continued to orbit the microlaser around the equatorial plane and then moved upwards along the z-axis (out of the imaging plane) by frame 167 [(v)], causing the spectral shifts to gradually revert to the reference spectra [marked at (vi)]. Importantly, the bead's orbit was not strictly equatorial but varied in height, influenced by optical trapping and hydrodynamic coupling [260, 261]. This makes it challenging to precisely determine the bead's equatorial position around the microlaser based on the spectral shifts. However, it's still possible to clearly see the time-resolved spectral shift effect of the probe bead coupling into the WGM around the microlaser.

One key challenge is the alignment of the micromirror with the microscope's objective, which is complicated by the objective's low depth of field and aberrations caused by shifting of the trapping beam in z. To overcome these limitations, options include using objectives with lower NA to increase the field of view or deploying alternative holographic masks optimized for this purpose. Additionally, the positioning of the micromirror's central aperture affects the trade-off between the distance from the microlaser, the pump beam's spot size, and mirror dimensions.

Despite these limitations, there is a clear path to improving the platform for each limiting factor. The experiment demonstrated here serves as more proof of the platform's capabilities, highlighting just how much more information can be collected with a single steerable micromirror.

In summary, the platform showcases the potential to monitor real-time changes in the environments surrounding WGM microlasers and new possibilities for single-objective investigation of biological samples.

6.3 Future Developments of Membranes as Optical Elements

Although only the results listed above were published during this thesis, multiple experiments utilizing the membrane micromirrors were performed, as described in this section.

Exciting Photonic Jet in Nitrogen-Vacancy Nanodiamonds

While using the membranes as *in-situ* optical components, it is tempting to consider what other elements already there can perform the job of an optical component. Early on in the work of steering beams into beads, we noticed a distinct long blade of light forming at the end of the larger beads.

This turned out to be due to a phenomenon known as a photonics jet, where the bead acts as a lens to focus the beam with a waist size close to the diameter of the bead. This results in a significant increase in the field enhancement at the focal point, finding use in confocal microscopy, microsurgery, and enhanced light-matter interactions such as excitation of color centers in nitrogen-vacancy (NV) diamonds.

The excitation of these color centers produces stable emission and is immune to photobleaching [262], making it particularly appealing for biomedical applications [263]. Diamond is extremely chemically and physically inert [264], biocompatible [265], and can be chemically functionalized to interact with biological molecules [266].

After the success of using the micromirror membranes in exciting WGM, the next step was to try and use multiple membranes for the enhancment of signal collection. As we had access to TiO_2 beads with embedded nanodiamonds, the idea was for the pump beam to be steered such that it is focused by the sphere into a photonics jet, drastically increasing its emission while another micromirror membrane is used to redirect that emission back up to the microscope objective as shown in Figure 6.7

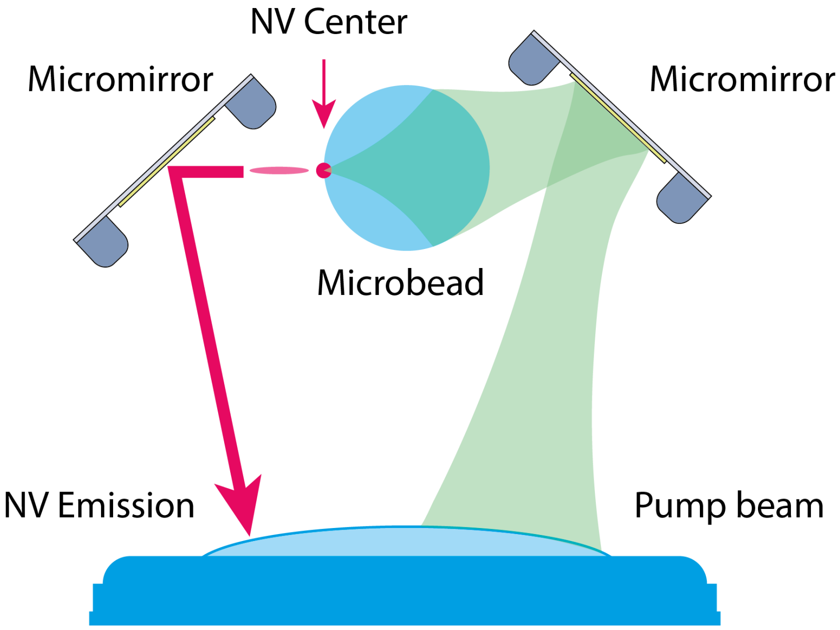

Figure 6.7 Concept schematic for the photonics jet experiment, one membrane is used to excite the NV center and the other membrane is used to collect the emission.

TiO_2 NV Microsphere Preparation

We received the samples from collaborators in ETH Zurich, consisting of synthesized TiO_2 microspheres with a nano-diamond concentration of 2% stored in hexadecane. Since the membranes are stored in water, this is a problem as water and hexadecane do not mix. Placing the membranes in hexadecane is also not an option, as it's high refractive index makes trapping impossible. Multiple methods for extracting the beads into water were experimented with, finally settling on acetone due to its high miscibility with both water and hexadecane. The exchange protocol devised was:

1. Take a small 200 µL sample of TiO_2 beads mixed with hexadecane and dilute it with 1 mL of acetone.
2. Vortex the solution, then sonicate to ensure thorough mixing.
3. Centrifuge the mixture at 4000 rpm to separate the beads and hexadecane, with the beads sedimenting at the bottom and the hexadecane, having a lower density, floating to the top.
4. Carefully remove 600 µL from the top of the liquid using a pipette.
5. Add an equal volume of 600 µL of acetone
6. Repeat the centrifugation and liquid removal steps 4-5 times to ensure effective separation.
7. Add water to the residue.
8. Vortex mix and sonicate the solution again.
9. Dry the sample on a hotplate at 80 °C to remove any remaining acetone.

The success of the extraction can be judged from the opacity of the final solution. If the sample is clear, the hexadecane has been removed completely. Otherwise, the solution will turn opaque as the water, acetone, and hexadecane emulsify.

Photonics Jet and Spectra

Two experiments were performed, one in order to characterize the photonics jet coming out of the spheres, and one to establish whether an enhanced signal could be produced by using membrane mirrors to direct the excitation and emission from and to the microscope objective.

Characterization was done by dissolving a small amount of rhodamine in a solution of 15 µm beads until the beam was clearly visible, then using the beads to form the photonics jet as shown in Figure 6.8.

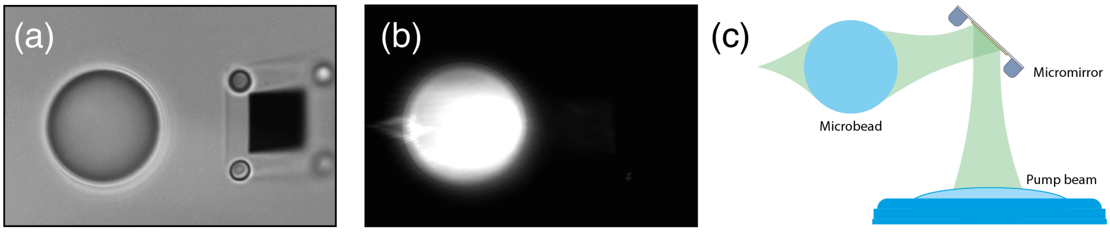

Figure 6.8 Video frames analyzing a photonics jet formed by the microsphere with (a) the LED illumination on (b) and the LED off. (c) Shows the schematic.

Once it was established the jet was formed properly, the TiO_2 nanodiamond particles were mixed with membranes in a fresh sample without rhodamine. With the same setup as in the previous section for the beads and membranes, the main challenge was finding all the necessary components for the experiments, as the extraction process destroyed most of the TiO_2 spheres as shown in Figure 6.9 (a).

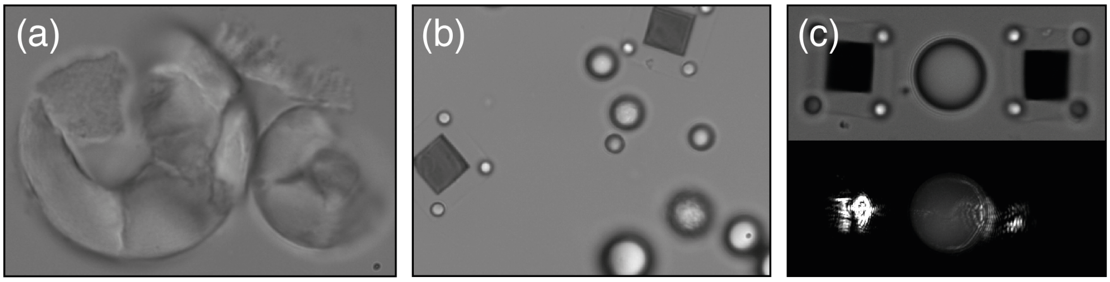

Figure 6.9 Video frames analyzing a photonics jet formed by the microsphere with (a) the LED illumination on (b) and the LED off. (c) Shows the schematic.

However due to a lot of experience at this point in searching, it was possible to locate multiple beads that produced the desired spectra and to place them together with the membranes to acquire spectra with no mirrors, one mirror and two mirrors as shown in Figure 6.9 (b) and (c).

Currently, searching for the ideal combination of membranes and beads took too long to study systematically. In future attempts, this could be solved by optimizing the exchange process to leave more of the microspheres intact.

Optical Trapping using Optically Trapped Membranes

As shown above, the membranes can adjust the laser beam to a chosen angle. This enables us to angle the membrane to deflect the trapping laser beam towards particles throughout the microfluidic chamber, even those obscured from the objective's direct view. By displacing the membrane a few micrometers from the imaging plane, we can utilize the reflected beam to capture particles within it, as illustrated in Figure 6.10.

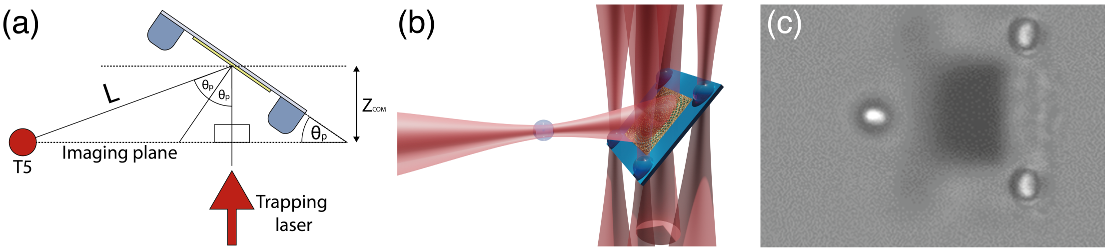

Figure 6.10 (a) Depiction of the trap created by the membrane, where θ_p denotes the polar angle at which the membrane is tilted. The membrane is shifted from the microscope's focal plane by a distance Z_{COM}, enabling particle trapping within the imaging plane. (b) Illustration of the membrane equipped with a mirror as a reflective surface. (c) Frame from a video showing a membrane micromirror trapping a particle.

This approach, while successful, was not explored fully due to an explicit geometric limitation — with the current size of the gold on top of the membranes and following the geometric approximation in the previous chapter, the approximate distance at which particles can be effectively trapped is less than 3 μm, making it impractical for most applications. This could be addressed in future works by increasing the membrane size or using more advanced beam shaping, such as reflecting a Bessel beam from the membrane.

6.4 Future Developments of DNA Manipulation Using Microstructures

This section deals with the final goal of this work, which was to create tools able to interact with DNA in ways that typical optically trapped spheres can't. First I'll explain some of the properties of DNA, before covering the two use cases of microtools for DNA analysis, membranes for DNA denaturation and paddles for DNA supercoiling.

6.5 DNA Denaturation and Supercoiling

The intricate architecture of DNA allows it to store extensive information needed for protein synthesis, replication, and cellular functions. This is achieved through its ability to twist and writhe, a process essential for fitting meters of DNA within the cell nucleus and facilitating access during transcription by forming supercoils [267]. Supercoiling not only compacts DNA to fit inside cells but is pivotal in DNA's ability to open up for transcription. The structure of double-stranded DNA, composed of two sugar-phosphate backbones and the base pairs A-T and C-G, is stabilized by hydrogen bonds [268]. To be read, DNA must unzip, breaking these hydrogen bonds through mechanisms such as enzymatic activity by helicase during replication or through physical or thermal stresses [269]. This process is known as a denaturation bubble resulting from breaking DNA base pairs. Suddenly, the DNA on either side of the bubble experiences a disturbance to the stable condition of 10.5 base pairs per turn [270], and the created stress must be relieved in some way. It can relieve that stress by coiling around itself, preserving the total number of turns — for every twist lost due to the opening of base pairs, the DNA will wrap around itself again [267], shown in Figure 6.11.

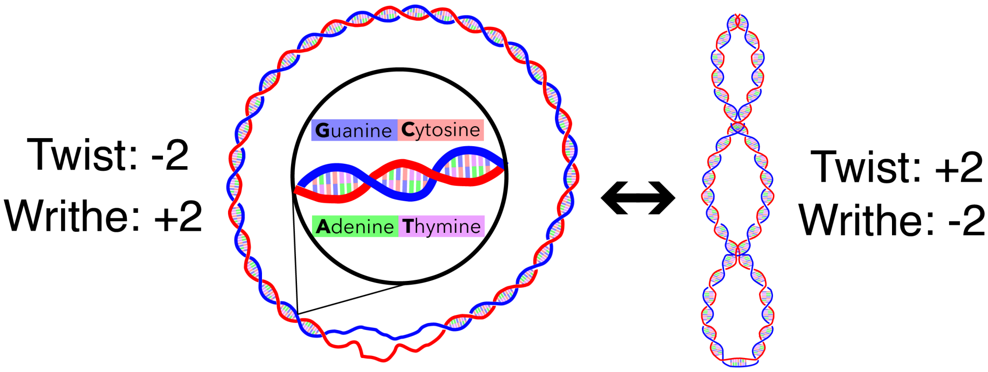

Figure 6.11

This phenomenon of DNA supercoiling and bubble formation has been a focus of extensive research, with theoretical [271] and experimental [267] approaches attempting to uncover its mechanics. Advanced imaging techniques like atomic force microscopy (AFM) have provided insights into these processes despite challenges in direct observation due to DNA's small size and low contrast [268]. However, AFM can typically only be performed this way on dried-out DNA samples, which can no longer interact with their environment. Understanding dynamic DNA behavior and properties is fundamental in the broader biophysics field. This encompasses ensemble statistics and the dynamics of single molecules, with techniques like single molecule force spectroscopy (SMFS) enabling detailed studies of DNA manipulation. SMFS methods, including AFM [272] and functionalized beads controlled by optical tweezers [273] or magnetic tweezers [274], allow us to apply force and torque to DNA, simulating conditions like supercoiling and denaturation. These approaches have led to discoveries of new DNA structures [275] and have enhanced our understanding of DNA's elasticity and response to mechanical stress [273]. Furthermore, these studies suggest that supercoiling might play a significant role in epigenetics, influencing how DNA sequences are read and which sections are actively transcribed [276]. This final section of the thesis focuses on preparing the way for work towards understanding DNA, first through mechanical bubble formation using extremely stable polymeric membranes able to detect minute forces quickly.

6.6 Membranes for Single Molecule Force Spectroscopy

Stability is important when considering the most common use case of optical tweezers as force probes in single-molecule force spectroscopy techniques. As described in Chapter 2, the motion of optically trapped particles can be precisely characterized, and any external forces acting on the particle can be resolved down to pN. This requires extremely high spatial and temporal resolution of the particle motion, down to ~ 1 Å[147]. This measurement can only be done once the particle motion has been recorded for long enough for long enough for the thermal Brownian noise to cancel out (eq. 2.1). We have previously demonstrated that the shape of the polymeric membranes results in a forty-fold decrease in transverse motion when compared to a spherical particle of equivalent mass [147]. This increased stability also translates into a much faster time of measurement of the membrane motion.

The 2D-like membranes demonstrated in Chapter 6 benefit greatly from intrinsic stability in the transverse direction. They leave us with large canvases to place HMSs, which can be used to stabilize them and shape light that interacts with them. However, with a new platform come new challenges. Due to the anisotropic shape, the motion of the membranes is not as easy to calculate analytically when compared to a sphere. Once the motion is well characterized, the work will begin on further stabilization of the membranes through circularly dichroic chiral HMSs with the final goal of incorporating the HMS membranes into biophysics experiments as shown in the concept image in Figure 6.12 below.

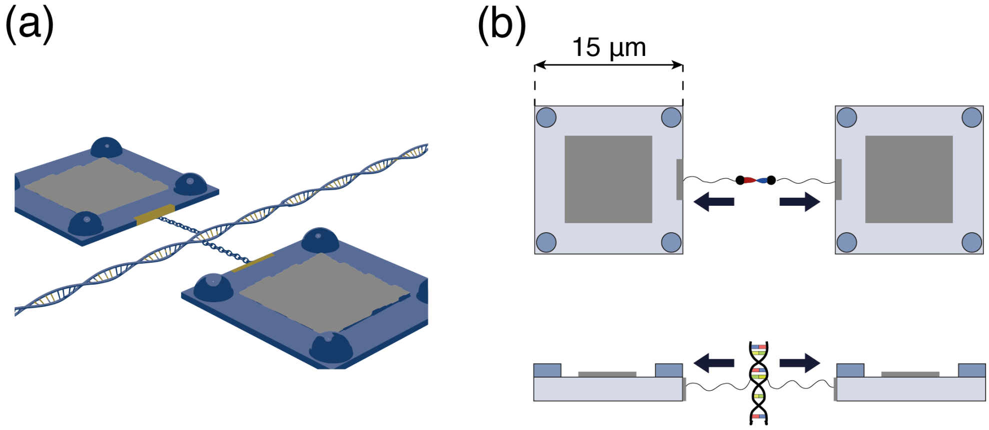

Figure 6.12 (a) Concept and (b) schematic of the DNA denaturation experiment. The mirror on top of the membrane is silver, while anchor points at the sides of the membranes are gold.

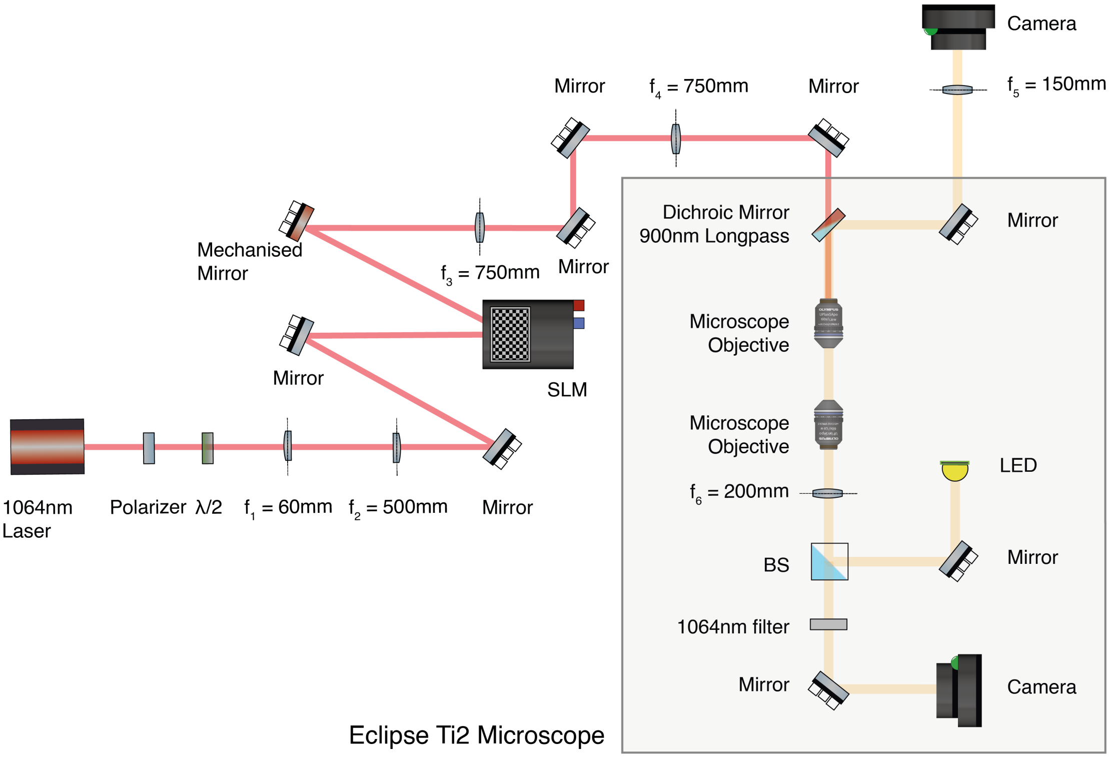

Figure 6.13 Double objective holographic optical trapping system built into a Nikon TiE2 microscope body,

The second mechanism to study was the supercoiling of DNA using polymeric paddle structures.

6.7 Paddles for DNA Coiling

In preparation for more complex experiments including membranes and inspired by the ability to quickly move the membranes with gold on them by simply focusing the laser on the metal, another idea worked on has been micro paddles for conversion of the linear momentum exerted by light pressure into angular motion.

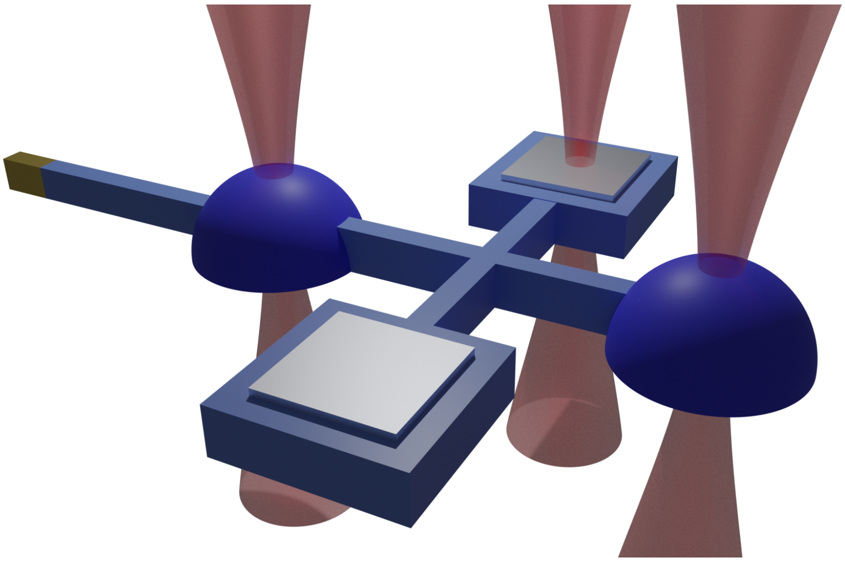

Figure 6.14 Concept design for a micro-paddle capable of conversion of linear light pressure to angular momentum.

Paddle Design and Fabrication

As shown in Figure 6.14 the paddles consist of two dome-like handles, two reflective metallic paddles, and a short rod that can be functionalized to attach to biological samples. The force exerted onto the metal paddles is significantly higher than that of the scattering or gradient force in trapping, meaning the paddles can exert significant angular torque as they spin, pushed by the laser akin to how a water wheel is pushed. The laser used to push them can also be pulsed to ensure maximum momentum transfer, resulting in angular motion without needing beam shaping or birefringence. A similar conversion of momentum was first shown in 1994 by Ohguchi *et al.* [277] with windmill-like pieces of silica, and more recently paddle [145], and water-wheel [143] like structures have been demonstrated, however in all these cases the objects were made using two-photon polymerization, and no metal deposition done — as such the forces expected would be significantly smaller. Little interaction was shown with biological samples and none with DNA.

The goal was for a pair of these paddles, with the rod section attached to two ends of a B-DNA molecule as shown in Figure 6.15, to be used to investigate the mechanical supercoiling of the molecule, which naturally occurs during DNA transcription as well as during DNA packing into cells.

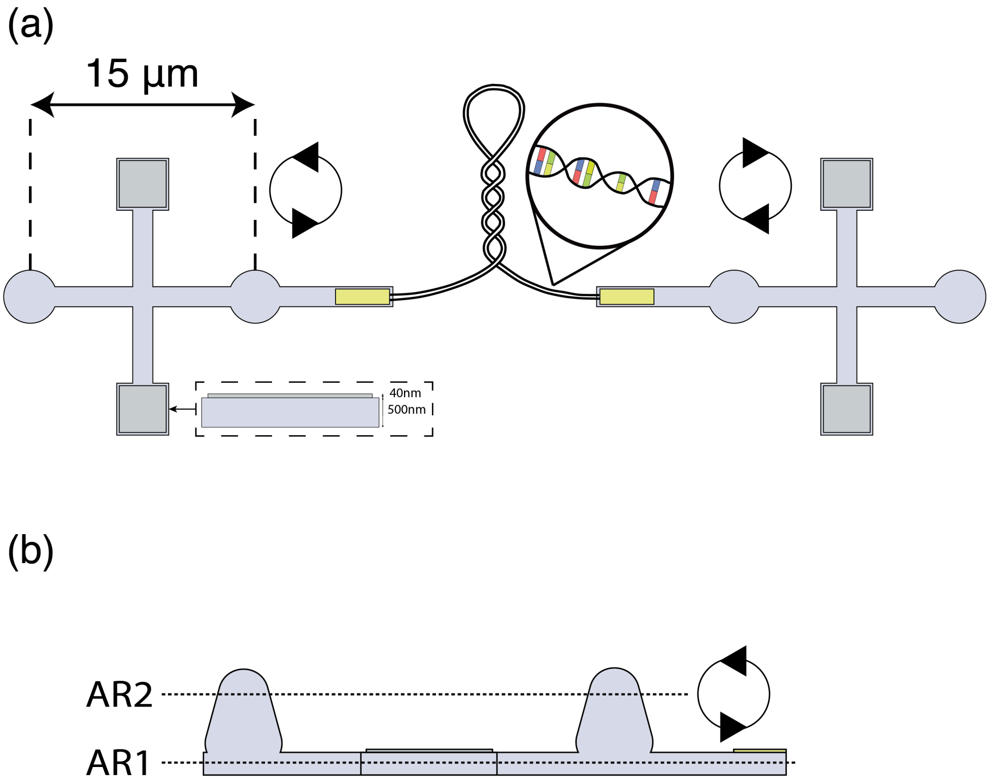

Figure 6.15 (a) DNA supercoiling using gold-tipped micro paddles and (b) side view showing the intended axis of rotation (AR1) and the effective axis of rotation observed in experiments (AR2)

DNA has been wound and unwound using optical wrenches and magnetic tweezers. However, this is done almost exclusively by attaching one end of the DNA to the substrate and the other to the bead, giving only a top-down view and the ability to manipulate one end. In this case, the DNA would be held from both ends and could be wound and unwound. At the same time, a top-down view would be available, giving a visual insight into what is happening through fluorescent functionalization and adding a pump and probe beam to the two objective setups. The DNA would be functionalized with thiol groups to allow for bonding with the gold tips of paddles.

Like the membranes, the paddles were fabricated using a combination of EBL and metal deposition. Resists were prepared on the silicon substrate as described in Chapter 3. The process is almost identical to making membranes, with markers written in PMMA and gold NiCr deposited. Then, the paddle body is written with EBL in SU8 2000.5 and developed. PMMA is patterned as a mask for the reflective surface, and NiCr is deposited. Gold is not used as the DNA will be functionalized to attach to gold. After the metal deposition, the handles are written in thick SU-8, the same as for the membranes. Finally, for the DNA experiments, a final layer of PMMA will be used to deposit gold onto the tips of the rods. A trial version was also being fabricated where a thin string of SU8 joins two sets of paddles to test the ability to spin the paddles in counter-propagating directions as seen in Figure 6.16.

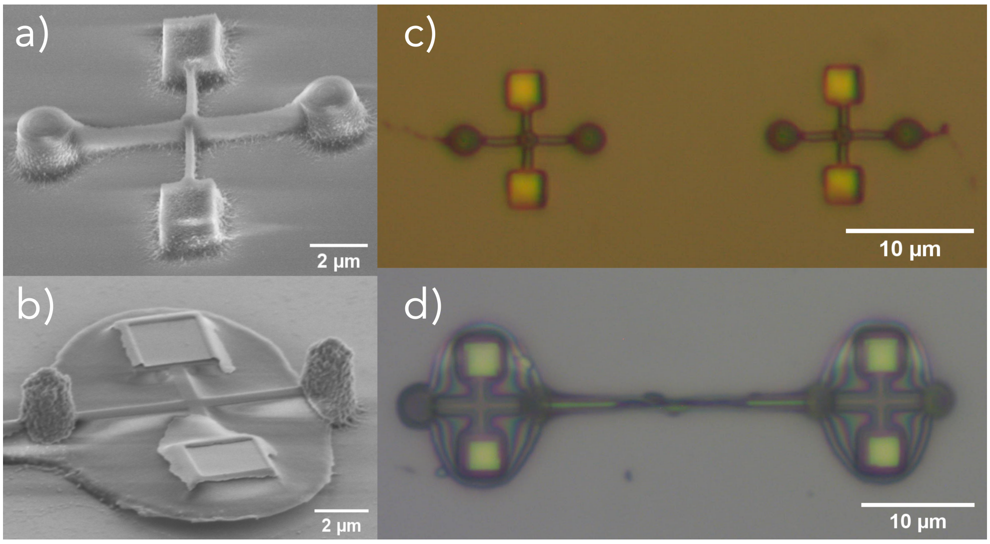

Figure 6.16 Micro-paddle fabrication. (a) shows a successfully fabricated paddle with no gold. (b) shows paddles where the fabrication succeeded, but the SU8 link was too thin. (c) and (d) show almost successful paddles, but the dose used for the initial structure was too high.

Optical Manipulation of Paddles

Like the membranes, the paddles were placed in an Eppendorf tube after being lifted off the silicon substrate and transferred to the optical trapping setup. So far, the paddles tested have been ones without metal, but even with that, rotation was achieved as shown in Figure 6.17.

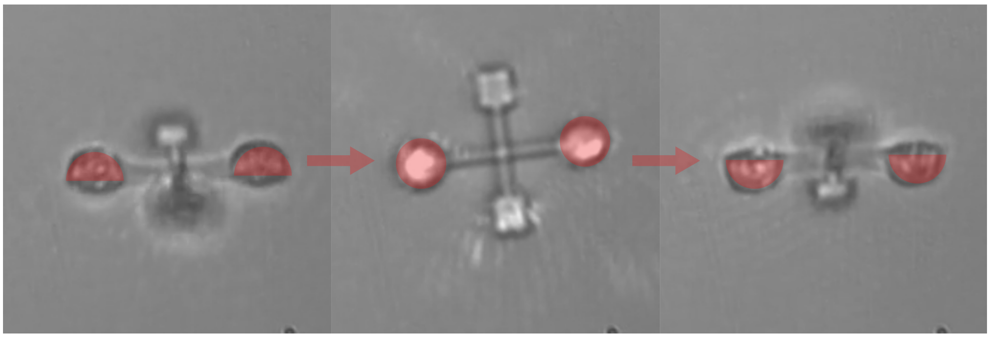

Figure 6.17 Micro-paddle manipulation, consecutive frames from a video show clearly the paddle handles rotation by 180 degrees.

The experiments on paddles were paused due to key design flaw — as shown in Figure 6.15 (b), the axis of rotation of the paddles is above the physical axis of the paddles, making it very difficult to rotate consistently.

6.8 Contribution

This work section resulted in one publication, ”Optically manipulated micromirrors for precise excitation of WGM microlasers.” [194]. For this publication, I assisted Libin Yan with the membrane fabrication and design. I did the remaining work, including building the optical setup, performing the experiments, and subsequent analysis. I wrote the paper with comments from Marcel Schubert and Malte Gather, who also provided us with guidance for the fitting of the spectral peaks and the use of the spectrometer.

6.9 Conclusion

Given the flat form factor of the membranes, our ability to manipulate them, and the response of the light that interacts with them, they are the perfect candidates for *in-situ* optics components, such as mirrors, lenses, filters, and more. This has already been shown to be viable by mixing and trapping rhodamine beads and membranes with gold features on top. The bead can be held in place by the zeroth order of the beam, while the first order is split into four and used to control and tilt the membrane. A green pump beam can then be reflected from the membrane surface and directed at the bead with a controlled angle, as shown in Figure 6.18

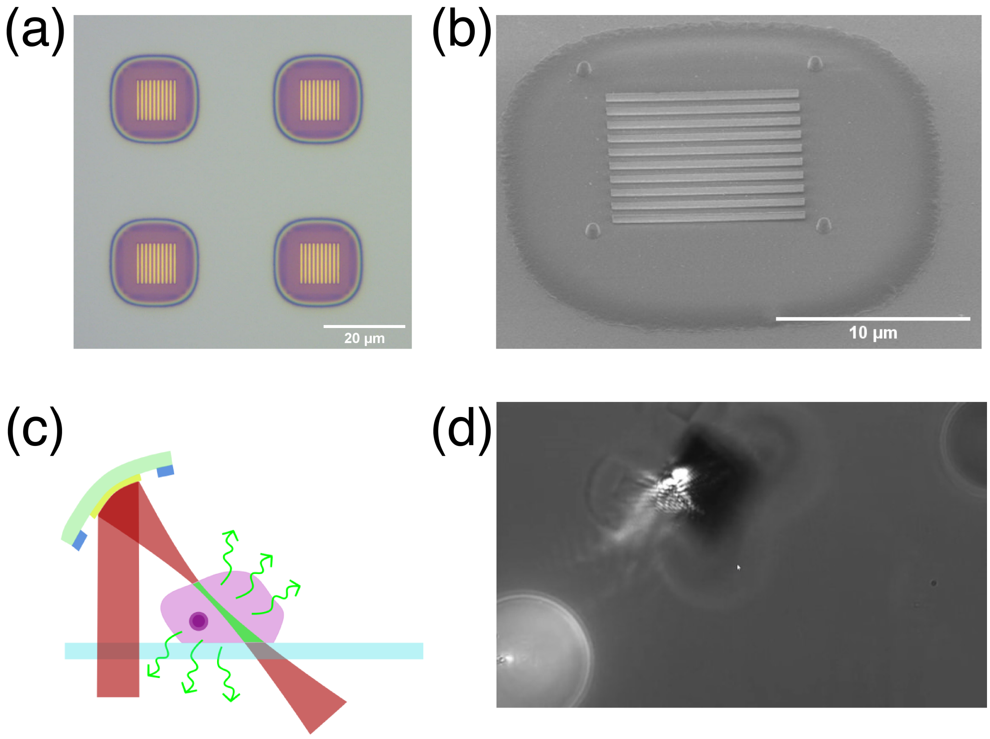

Figure 6.18 Membranes as controllable optics. (a) and (b) show a membrane with a $1\mu m$ spaced grating on top. (c) shows the eventual plan for flexible mirror membranes, and (d) shows a frame from footage where a laser is focused directly on the bead by first reflecting from the membrane surface, creating an interference pattern.

From that point, the gold membranes can also easily be modified to act as cylindrical lenses by either fabricating concave membranes or simply bending the existing ones into a curved mirror shape, acting as cylindrical lenses, and creating a light sheet. Furthermore, advanced micromirror designs with textured HMSs could revolutionize light manipulation, enabling complex illumination patterns and real-time tomographic imaging of specimens.

The future directions for using polymeric membranes in single-molecule force spectroscopy are also promising. These membranes' stability makes them ideal for optical trapping and vibration isolation, enhancing the precision and speed of force measurements at the single-molecule level. This stability is critical in overcoming the limitations of current techniques, where the timescales required for accurate measurements often exceed the duration of biological processes. The development of micro paddles for DNA manipulation further expands the experimental toolkit, enabling the conversion of light's linear momentum into angular momentum for studying mechanical supercoiling. The potential applications in understanding DNA mechanics and epigenetic influences open new avenues for research, promising significant contributions to biophysics.

CHAPTER 7

Conclusion

7.1 Thesis Summary

This thesis presented integrating optical trapping, HMSs, and microfabrication techniques to both extend the capabilities of microscope objectives and replace their function entirely for lab-on-chip biophotonics applications.

The motivation for this, as well as the background theory, is described in Chapters 1 and 2.

Chapter 3 describes the membrane fabrication and optical setup developed in order to perform optical trapping using micromirrors, HMSs and holographic optical trapping of polymeric membranes. The protocols used in all experiments, along with the software used to optically manipulate objects, are described. The software used to analyze the optical trapping data and characterize the quality of optical traps in x,y, and z is described. The exact execution of these experiments is demonstrated in the following Chapters. Chapter 4 describes the use of gold-coated micromirror arrays for the optical trapping and rotation of particles. Chapter 5 describes the use of HMSs in both reflection and transmission for trapping individual particles as well as extended objects. For the first time, HMSs with trapping stiffness equal to that of a high NA objective at a fraction of the footprint and cost.

Chapter 6 describes the work focusing on optically trapped polymeric membranes used as *in-situ* optical elements to condition light inside of a microfluidic chamber. The fabrication of the membranes using standard nanofabrication processes is described. The membranes are decorated with gold mirrors and used to excite WGM along arbitrary planes of a microlaser for extended sensing. The use of mirror membranes in exciting photonics jets for enhanced light-matter is described, as well as the use in optical trapping at an arbitrary angle. Finally, future work using these same polymeric membranes as extremely stable force transducers for SMFS of DNA and using of optically manipulated paddles for the transferring of angular momentum for DNA supercoiling.

Bibliography

[1] A. Lipson, S. G. Lipson, and H. Lipson, *Optical physics*. Cambridge University Press, 2010.

[2] H. Balasubramanian, C. M. Hobson, T.-L. Chew, and J. S. Aaron, "Imagining the future of optical microscopy: everything, everywhere, all at once," *Communications Biology*, vol. 6, no. 1, p. 1096, 2023.

[3] M. Pluta, "Phase contrast microscopy," *Advanced light microscopy*, vol. 2, 1993.

[4] C. Snoeyink, "Imaging performance of bessel beam microscopy," *Optics letters*, vol. 38, no. 14, pp. 2550–2553, 2013.

[5] J. Pawley, *Handbook of biological confocal microscopy*, vol. 236. Springer Science and Business Media, 2006.

[6] O. E. Olarte, J. Andilla, E. J. Gualda, and P. Loza-Alvarez, "Light-sheet microscopy: a tutorial," *Advances in Optics and Photonics*, vol. 10, no. 1, pp. 111–179, 2018.

[7] M. Saxena, G. Eluru, and S. S. Gorthi, "Structured illumination microscopy," *Advances in Optics and Photonics*, vol. 7, no. 2, pp. 241–275, 2015.

[8] C. J. Bustamante, Y. R. Chemla, S. Liu, and M. D. Wang, "Optical tweezers in single-molecule biophysics," *Nature Reviews Methods Primers*, vol. 1, no. 1, p. 25, 2021.

[9] K. M. McKinnon, "Flow cytometry: an overview," *Current protocols in immunology*, vol. 120, no. 1, pp. 5–1, 2018.

[10] D. Cialla, S. Pollok, C. Steinbrücker, K. Weber, and J. Popp, "Sers-based detection of biomolecules," *Nanophotonics*, vol. 3, no. 6, pp. 383–411, 2014.

[11] H. Xu, J. Aizpurua, M. Käll, and P. Apell, "Electromagnetic contributions to single-molecule sensitivity in surface-enhanced raman scattering," *Physical Review E*, vol. 62, no. 3, p. 4318, 2000.

[12] S. M. Kamali, E. Arbabi, A. Arbabi, and A. Faraon, “A review of dielectric optical metasurfaces for wavefront control,” *Nanophotonics*, vol. 7, no. 6, pp. 1041–1068, 2018.

[13] M. G. Scullion, T. F. Krauss, and A. Di Falco, “Slotted photonic crystal sensors,” *Sensors*, vol. 13, no. 3, pp. 3675–3710, 2013.

[14] Y. Xiong, Q. Huang, T. D. Canady, P. Barya, S. Liu, O. H. Arogundade, C. M. Race, C. Che, X. Wang, L. Zhou, *et al.*, “Photonic crystal enhanced fluorescence emission and blinking suppression for single quantum dot digital resolution biosensing,” *Nature communications*, vol. 13, no. 1, p. 4647, 2022.

[15] M. Chalfie, Y. Tu, G. Euskirchen, W. W. Ward, and D. C. Prasher, “Green fluorescent protein as a marker for gene expression,” *Science*, vol. 263, no. 5148, pp. 802–805, 1994.

[16] A. Pietraszewska-Bogiel and T. Gadella, “Fret microscopy: from principle to routine technology in cell biology,” *Journal of microscopy*, vol. 241, no. 2, pp. 111–118, 2011.

[17] M. Renz, “Fluorescence microscopy—a historical and technical perspective,” *Cytometry Part A*, vol. 83, no. 9, pp. 767–779, 2013.

[18] B. Huang, M. Bates, and X. Zhuang, “Super-resolution fluorescence microscopy,” *Annual review of biochemistry*, vol. 78, pp. 993–1016, 2009.

[19] A. Serrano, J. Berthelet, S. H. Naik, and D. Merino, “Mastering the use of cellular barcoding to explore cancer heterogeneity,” *Nature Reviews Cancer*, vol. 22, no. 11, pp. 609–624, 2022.

[20] M. Schubert, L. Woolfson, I. R. Barnard, A. M. Dorward, B. Casement, A. Morton, G. B. Robertson, P. L. Appleton, G. B. Miles, C. S. Tucker, S. J. Pitt, and M. C. Gather, “Monitoring contractility in cardiac tissue with cellular resolution using biointegrated microlasers,” *Nature Photonics*, vol. 14, no. 7, pp. 452–458, 2020.

[21] M. Schubert, A. Steude, P. Liehm, N. M. Kronenberg, M. Karl, E. C. Campbell, S. J. Powis, and M. C. Gather, “Lasing within live cells containing intracellular optical microresonators for barcode-type cell tagging and tracking,” *Nano letters*, vol. 15, no. 8, pp. 5647–5652, 2015.

[22] A. R. Anwar, M. Mur, and M. Humar, “Microcavity-and microlaser-based optical barcoding: A review of encoding techniques and applications,” *ACS photonics*, vol. 10, no. 5, pp. 1202–1224, 2023.

[23] M. F. Ferreira, E. Castro-Camus, D. J. Ottaway, J. M. López-Higuera, X. Feng, W. Jin, Y. Jeong, N. Picqué, L. Tong, B. M. Reinhard, *et al.*, "Roadmap on optical sensors," *Journal of Optics*, vol. 19, no. 8, p. 083001, 2017.

[24] E. C. Wait, M. A. Reiche, and T.-L. Chew, "Hypothesis-driven quantitative fluorescence microscopy–the importance of reverse-thinking in experimental design," *Journal of Cell Science*, vol. 133, no. 21, p. jcs250027, 2020.

[25] L. von Chamier, R. F. Laine, J. Jukkala, C. Spahn, D. Krentzel, E. Nehme, M. Lerche, S. Hernández-Pérez, P. K. Mattila, E. Karinou, *et al.*, "Democratising deep learning for microscopy with zerocostdl4mic," *Nature communications*, vol. 12, no. 1, p. 2276, 2021.

[26] H. Wong and H. Iwai, "The road to miniaturization," *Physics World*, vol. 18, no. 9, p. 40, 2005.

[27] P. Minzioni, R. Osellame, C. Sada, S. Zhao, F. Omenetto, K. B. Gylfason, T. Haraldsson, Y. Zhang, A. Ozcan, A. Wax, *et al.*, "Roadmap for optofluidics," *Journal of Optics*, vol. 19, no. 9, p. 093003, 2017.

[28] S. C. Terry, J. H. Jerman, and J. B. Angell, "A gas chromatographic air analyzer fabricated on a silicon wafer," *IEEE transactions on electron devices*, vol. 26, no. 12, pp. 1880–1886, 1979.

[29] H.-Y. Mu, Y.-L. Lu, T.-H. Hsiao, and J.-H. Huang, "Microfluidic-based approaches for covid-19 diagnosis," *Biomicrofluidics*, vol. 14, no. 6, 2020.

[30] A. C. R. Grayson, R. S. Shawgo, A. M. Johnson, N. T. Flynn, Y. Li, M. J. Cima, and R. Langer, "A biomems review: Mems technology for physiologically integrated devices," *Proceedings of the IEEE*, vol. 92, no. 1, pp. 6–21, 2004.

[31] R. M. Warner, "Microelectronics: Its unusual origin and personality," *IEEE Transactions on Electron Devices*, vol. 48, no. 11, pp. 2457–2467, 2001.

[32] J. S. Kilby, "Miniaturized electronic circuits [us patent no. 3,138, 743]," *IEEE Solid-State Circuits Society Newsletter*, vol. 12, no. 2, pp. 44–54, 2007.

[33] N. Convery and N. Gadegaard, "30 years of microfluidics," *Micro and Nano Engineering*, vol. 2, pp. 76–91, 2019.

[34] J. Zhu, X. Zhu, Y. Zuo, X. Hu, Y. Shi, L. Liang, and Y. Yang, "Optofluidics: the interaction between light and flowing liquids in integrated devices," *Opto-Electronic Advances*, vol. 2, no. 11, pp. 190007–1, 2019.

[35] T. Ohnstein, T. Fukiura, J. Ridley, and U. Bonne, "Micromachined silicon microvalve," in *IEEE Proceedings on Micro Electro Mechanical Systems, An Investigation of Micro Structures, Sensors, Actuators, Machines and Robots.*, pp. 95–98, IEEE, 1990.

[36] C. Iliescu, H. Taylor, M. Avram, J. Miao, and S. Franssila, "A practical guide for the fabrication of microfluidic devices using glass and silicon," *Biomicrofluidics*, vol. 6, no. 1, 2012.

[37] J. C. McDonald, D. C. Duffy, J. R. Anderson, D. T. Chiu, H. Wu, O. J. Schueller, and G. M. Whitesides, "Fabrication of microfluidic systems in poly (dimethylsiloxane)," *ELECTROPHORESIS: An International Journal*, vol. 21, no. 1, pp. 27–40, 2000.

[38] A. K. Yetisen, M. S. Akram, and C. R. Lowe, "based microfluidic point-of-care diagnostic devices," *Lab on a Chip*, vol. 13, no. 12, pp. 2210–2251, 2013.

[39] O. Reynolds, "Xxix. an experimental investigation of the circumstances which determine whether the motion of water shall be direct or sinuous, and of the law of resistance in parallel channels," *Philosophical Transactions of the Royal society of London*, no. 174, pp. 935–982, 1883.

[40] F. Bragheri, L. Ferrara, N. Bellini, K. C. Vishnubhatla, P. Minzioni, R. Ramponi, R. Osellame, and I. Cristiani, "Optofluidic chip for single cell trapping and stretching fabricated by a femtosecond laser," *Journal of biophotonics*, vol. 3, no. 4, pp. 234–243, 2010.

[41] D. Erickson, T. Rockwood, T. Emery, A. Scherer, and D. Psaltis, "Nanofluidic tuning of photonic crystal circuits," *Optics letters*, vol. 31, no. 1, pp. 59–61, 2006.

[42] X. Fan, I. M. White, S. I. Shopova, H. Zhu, J. D. Suter, and Y. Sun, "Sensitive optical biosensors for unlabeled targets: A review," *analytica chimica acta*, vol. 620, no. 1-2, pp. 8–26, 2008.

[43] X. Chen, J. Ping, Y. Sun, C. Yi, S. Liu, Z. Gong, and P. Fei, "Deep-learning on-chip light-sheet microscopy enabling video-rate volumetric imaging of dynamic biological specimens," *Lab on a Chip*, vol. 21, no. 18, pp. 3420–3428, 2021.

[44] W. Bishara, H. Zhu, and A. Ozcan, "Holographic opto-fluidic microscopy," *Optics express*, vol. 18, no. 26, pp. 27499–27510, 2010.

[45] R. Rahad, M. A. Haque, M. K. Mahadi, M. O. Faruque, S. M. T.-S. Afrid, A. S. Mohsin, A. M. N. U. R. Niaz, and R. H. Sagor, "A polarization independent

highly sensitive metasurface-based biosensor for lab-on-chip applications," *Measurement*, vol. 231, p. 114652, 2024.

[46] M. Consales, G. Quero, S. Spaziani, M. Principe, A. Micco, V. Galdi, A. Cutolo, and A. Cusano, "Metasurface-enhanced lab-on-fiber biosensors," *Laser and Photonics Reviews*, vol. 14, no. 12, p. 2000180, 2020.

[47] J. Qin, S. Jiang, Z. Wang, X. Cheng, B. Li, Y. Shi, D. P. Tsai, A. Q. Liu, W. Huang, and W. Zhu, "Metasurface micro/nano-optical sensors: principles and applications," *ACS nano*, vol. 16, no. 8, pp. 11598–11618, 2022.

[48] T. H. Maiman, "Stimulated optical radiation in ruby," *Nature*, vol. 187, no. 4736, p. 493–494, 1960.

[49] C. Simovski and S. Tretyakov, *An Introduction to Metamaterials and Nanophotonics*. Cambridge University Press, 2020.

[50] K. Yao and Y. Liu, "Plasmonic metamaterials," *Nanotechnology Reviews*, vol. 3, no. 2, pp. 177–210, 2014.

[51] S. Jahani and Z. Jacob, "All-dielectric metamaterials," *Nature nanotechnology*, vol. 11, no. 1, pp. 23–36, 2016.

[52] S. A. Tretyakov, "A personal view on the origins and developments of the metamaterial concept," *Journal of Optics (United Kingdom)*, vol. 19, no. 1, 2017.

[53] T. J. Cui, R. Liu, and D. R. Smith, *Introduction to Metamaterials*. Boston, MA: Springer US, 2010.

[54] F. Monticone and A. Alù, "Metamaterial, plasmonic and nanophotonic devices," *Reports on Progress in Physics*, vol. 80, no. 3, p. 036401, 2017.

[55] W. X. Jiang, Z. L. Mei, and T. J. Cui, *Effective Medium Theory of Metamaterials and Metasurfaces*. Elements in Emerging Theories and Technologies in Metamaterials, Cambridge University Press, 2022.

[56] Viktor G Veselago, "Soviet Physics Uspekhi THE ELECTRODYNAMICS OF SUBSTANCES WITH SIMULTANEOUSLY NEGATIVE VALUES OF AND μ Electromagnetic responses of relativistic electrons," *Sov. Phys. Usp*, vol. 10, 1968.

[57] R. A. Shelby, D. R. Smith, and S. Schultz, "Experimental verification of a negative index of refraction," *Science*, vol. 292, no. 5514, pp. 77–79, 2001.

[58] G. Dolling, M. Wegener, C. M. Soukoulis, and S. Linden, “Negative-index metamaterial at 780 nm wavelength,” *Opt. Lett.*, vol. 32, no. 1, pp. 53–55, 2007.

[59] J. B. Pendry, “Negative refraction makes a perfect lens,” *Physical Review Letters*, vol. 85, no. 18, pp. 3966–3969, 2000.

[60] N. Fang, “Sub-Diffraction-Limited Optical Imaging with a Silver Superlens,” *Science*, vol. 308, no. 5721, pp. 534–537, 2005.

[61] R. W. Ziolkowski, “Propagation in and scattering from a matched metamaterial having a zero index of refraction,” *Physical Review E - Statistical Physics, Plasmas, Fluids, and Related Interdisciplinary Topics*, vol. 70, no. 4, p. 12, 2004.

[62] N. I. Landy, S. Sajuyigbe, J. J. Mock, D. R. Smith, and W. J. Padilla, “Perfect metamaterial absorber,” *Physical Review Letters*, vol. 100, no. 20, pp. 1–4, 2008.

[63] T. Cui, B. Bai, and H.-B. Sun, “Tunable metasurfaces based on active materials,” *Advanced Functional Materials*, vol. 29, no. 10, p. 1806692, 2019.

[64] H. T. Chen, A. J. Taylor, and N. Yu, “A review of metasurfaces: Physics and applications,” *Reports on Progress in Physics*, vol. 79, no. 7, 2016.

[65] C. M. Soukoulis and M. Wegener, “Past achievements and future challenges in the development of three-dimensional photonic metamaterials,” *Nature Photonics*, vol. 5, no. 9, pp. 523–530, 2011.

[66] C. L. Holloway, E. F. Kuester, J. A. Gordon, J. O’Hara, J. Booth, and D. R. Smith, “An overview of the theory and applications of metasurfaces: The two-dimensional equivalents of metamaterials,” *IEEE Antennas and Propagation Magazine*, vol. 54, no. 2, pp. 10–35, 2012.

[67] N. Yu, P. Genevet, M. a. Kats, F. Aieta, J.-P. Tetienne, F. Capasso, and Z. Gaburro, “Light Propagation with Phase Discontinuities: Generalized Laws of Reflection and Refraction,” *Science*, vol. 334, no. 6054, pp. 333–337, 2011.

[68] L. Li, T. Jun Cui, W. Ji, S. Liu, J. Ding, X. Wan, Y. Bo Li, M. Jiang, C. W. Qiu, and S. Zhang, “Electromagnetic reprogrammable coding-metasurface holograms,” *Nature Communications*, vol. 8, no. 1, pp. 1–7, 2017.

[69] X. Ni, A. V. Kildishev, and V. M. Shalaev, “Metasurface holograms for visible light,” *Nature Communications*, vol. 4, 2013.

[70] J. Li, S. Kamin, G. Zheng, F. Neubrech, S. Zhang, and N. Liu, “Addressable metasurfaces for dynamic holography and optical information encryption,” *Science Advances*, vol. 4, no. 6, pp. 1–8, 2018.

[71] L. Yan, J. Xiao, T. Plaskocinski, M. Biabanifard, S. Persheyev, M. Askari, and A. D. Falco, “Two-tier manipulation of holographic information,” *Opt. Express*, vol. 30, pp. 19145–19151, 05 2022.

[72] F. Aieta, P. Genevet, M. A. Kats, N. Yu, R. Blanchard, Z. Gaburro, and F. Capasso, “Aberration-free ultrathin flat lenses and axicons at telecom wavelengths based on plasmonic metasurfaces,” *Nano Letters*, vol. 12, no. 9, pp. 4932–4936, 2012.

[73] T. Roy, S. Zhang, I. W. Jung, M. Troccoli, F. Capasso, and D. Lopez, “Dynamic metasurface lens based on MEMS technology,” *APL Photonics*, vol. 3, no. 2, 2018.

[74] Q. Ma, G. D. Bai, H. B. Jing, C. Yang, L. Li, and T. J. Cui, “Smart metasurface with self-adaptively reprogrammable functions,” *Light: Science and Applications*, vol. 8, no. 1, 2019.

[75] E. Bermúdez-Ureña and U. Steiner, “Self-Rolled Multilayer Metasurfaces,” *ACS Photonics*, vol. 6, no. 9, pp. 2198–2204, 2019.

[76] J. Burch, D. Wen, X. Chen, and A. Di Falco, “Conformable holographic metasurfaces,” *Scientific Reports*, vol. 7, no. 1, p. 4520, 2017.

[77] J. Burch and A. Di Falco, “Surface topology specific metasurface holograms,” *Acs Photonics*, vol. 5, no. 5, pp. 1762–1766, 2018.

[78] J. Xiao, T. Plaskocinski, M. Biabanifard, and A. Di Falco, “Self-calibrated flexible holographic curvature sensor,” *Advanced Materials Technologies*, p. 2301851, 2024.

[79] H.-S. Ee and R. Agarwal, “Tunable metasurface and flat optical zoom lens on a stretchable substrate,” *Nano letters*, vol. 16, no. 4, pp. 2818–2823, 2016.

[80] J. Sautter, I. Staude, M. Decker, E. Rusak, D. N. Neshev, I. Brener, and Y. S. Kivshar, “Active tuning of all-dielectric metasurfaces,” *ACS nano*, vol. 9, no. 4, pp. 4308–4315, 2015.

[81] M. Abb, P. Albella, J. Aizpurua, and O. L. Muskens, “All-optical control of a single plasmonic nanoantenna–ito hybrid,” *Nano letters*, vol. 11, no. 6, pp. 2457–2463, 2011.

[82] N. Dabidian, I. Kholmanov, A. B. Khanikaev, K. Tatar, S. Trendafilov, S. H. Mousavi, C. Magnuson, R. S. Ruoff, and G. Shvets, “Electrical switching of

infrared light using graphene integration with plasmonic fano resonant metasurfaces," *Acs Photonics*, vol. 2, no. 2, pp. 216–227, 2015.

[83] G. Zheng, H. Mühlenbernd, M. Kenney, G. Li, T. Zentgraf, and S. Zhang, "Metasurface holograms reaching 80% efficiency," *Nature nanotechnology*, vol. 10, no. 4, pp. 308–312, 2015.

[84] W. T. Chen, A. Y. Zhu, M. Khorasaninejad, Z. Shi, V. Sanjeev, and F. Capasso, "Immersion meta-lenses at visible wavelengths for nanoscale imaging," *Nano letters*, vol. 17, no. 5, pp. 3188–3194, 2017.

[85] Z. Li, T. Zhang, Y. Wang, W. Kong, J. Zhang, Y. Huang, C. Wang, X. Li, M. Pu, and X. Luo, "Achromatic broadband super-resolution imaging by super-oscillatory metasurface," *Laser and Photonics Reviews*, vol. 12, no. 10, p. 1800064, 2018.

[86] H. Pahlevaninezhad, M. Khorasaninejad, Y.-W. Huang, Z. Shi, L. P. Hariri, D. C. Adams, V. Ding, A. Zhu, C.-W. Qiu, F. Capasso, *et al.*, "Nano-optic endoscope for high-resolution optical coherence tomography in vivo," *Nature photonics*, vol. 12, no. 9, pp. 540–547, 2018.

[87] E. Arbabi, J. Li, R. J. Hutchins, S. M. Kamali, A. Arbabi, Y. Horie, P. Van Dorpe, V. Gradinaru, D. A. Wagenaar, and A. Faraon, "Two-photon microscopy with a double-wavelength metasurface objective lens," *Nano letters*, vol. 18, no. 8, pp. 4943–4948, 2018.

[88] Y. Zhao, A. N. Askarpour, L. Sun, J. Shi, X. Li, and A. Alù, "Chirality detection of enantiomers using twisted optical metamaterials," *Nature communications*, vol. 8, no. 1, p. 14180, 2017.

[89] C.-W. Qiu, T. Zhang, G. Hu, and Y. Kivshar, "Quo vadis, metasurfaces?," *Nano Letters*, vol. 21, no. 13, pp. 5461–5474, 2021.

[90] A. Arbabi, Y. Horie, A. J. Ball, M. Bagheri, and A. Faraon, "Subwavelength-thick lenses with high numerical apertures and large efficiency based on high-contrast transmitarrays," *Nature communications*, vol. 6, no. 1, p. 7069, 2015.

[91] L. Huang, S. Zhang, and T. Zentgraf, "Metasurface holography: from fundamentals to applications," *Nanophotonics*, vol. 7, no. 6, pp. 1169–1190, 2018.

[92] A. Ashkin and J. Dziedzic, "Optical trapping and manipulation of viruses and bacteria," *Science*, vol. 235, no. 4795, p. 1517–1520, 1987.

[93] S. M. Block, L. S. B. Goldstein, and B. J. Schnapp, “Bead movement by single kinesin molecules studied with optical tweezers,” *Nature*, vol. 348, no. 6299, p. 348–352, 1990.

[94] A. Ashkin, J. M. Dziedzic, and T. Yamane, “Optical trapping and manipulation of single cells using infrared laser beams,” *Nature*, vol. 330, no. 6150, p. 769–771, 1987.

[95] M. Wang, H. Yin, R. Landick, J. Gelles, and S. Block, “Stretching dna with optical tweezers,” *Biophysical Journal*, vol. 72, no. 3, p. 1335–1346, 1997.

[96] D. Barredo, V. Lienhard, S. D. Léséleuc, T. Lahaye, and A. Browaeys, “Synthetic three-dimensional atomic structures assembled atom by atom,” *Nature*, vol. 561, no. 7721, p. 79–82, 2018.

[97] R. Wynands and S. Weyers, “Atomic fountain clocks,” *Metrologia*, vol. 42, no. 3, 2005.

[98] K. Svoboda and S. M. Block, “Biological applications of optical forces,” *Annual Review of Biophysics and Biomolecular Structure*, vol. 23, no. 1, p. 247–285, 1994.

[99] P. H. Jones, O. M. Maragò, and G. Volpe, *Optical Tweezers: Principles and Applications*. Cambridge University Press, 2015.

[100] R. D. Vale and R. A. Milligan, “The way things move: looking under the hood of molecular motor proteins,” *Science*, vol. 288, no. 5463, pp. 88–95, 2000.

[101] A. Noy, *Handbook of molecular force spectroscopy*. Springer, 2011.

[102] C. Gosse and V. Croquette, “Magnetic tweezers: Micromanipulation and force measurement at the molecular level,” *Biophysical Journal*, vol. 82, no. 6, pp. 3314–3329, 2002.

[103] J. Lipfert, J. W. Kerssemakers, T. Jager, and N. H. Dekker, “Magnetic torque tweezers: Measuring torsional stiffness in DNA and RecA-DNA filaments,” *Nature Methods*, vol. 7, no. 12, pp. 977–980, 2010.

[104] D. Kah, C. Dürrbeck, W. Schneider, B. Fabry, and R. C. Gerum, “High-Force Magnetic Tweezers with Hysteresis-Free Force Feedback,” *Biophysical Journal*, vol. 119, no. 1, pp. 15–23, 2020.

[105] K. C. Neuman and A. Nagy, “Single-molecule force spectroscopy: optical tweezers, magnetic tweezers and atomic force microscopy,” *Nature Methods*, vol. 5, no. 6, p. 491–505, 2008.

[106] G. Longo, L. Alonso-Sarduy, L. M. Rio, A. Bizzini, A. Trampuz, J. Notz, G. Dietler, and S. Kasas, “Rapid detection of bacterial resistance to antibiotics using AFM cantilevers as nanomechanical sensors,” *Nature Nanotechnology*, vol. 8, no. 7, pp. 522–526, 2013.

[107] J. Hu, S. Jafari, Y. Han, A. J. Grodzinsky, S. Cai, and M. Guo, “Size-and speed-dependent mechanical behavior in living mammalian cytoplasm,” *Proceedings of the national Academy of Sciences*, vol. 114, no. 36, pp. 9529–9534, 2017.

[108] F. Catala-Castro, V. Venturini, S. Ortiz-Vasquez, V. Ruprecht, and M. Krieg, “Direct force measurements of subcellular mechanics in confinement using optical tweezers,” *JoVE (Journal of Visualized Experiments)*, no. 174, p. e62865, 2021.

[109] F. Català-Castro, E. Schäffer, and M. Krieg, “Exploring cell and tissue mechanics with optical tweezers,” *Journal of Cell Science*, vol. 135, no. 15, p. jcs259355, 2022.

[110] F. Czerwinski, A. C. Richardson, and L. B. Oddershede, “Quantifying Noise in Optical Tweezers by Allan Variance,” *Optics Express*, vol. 17, no. 15, p. 13255, 2009.

[111] A. Marzo and B. W. Drinkwater, “Holographic acoustic tweezers,” *Proceedings of the National Academy of Sciences*, vol. 116, no. 1, pp. 84–89, 2019.

[112] Z. Xu, W. Song, and K. B. Crozier, “Direct Particle Tracking Observation and Brownian Dynamics Simulations of a Single Nanoparticle Optically Trapped by a Plasmonic Nanoaperture,” *ACS Photonics*, vol. 5, pp. 2850–2859, 2018.

[113] K. Wang, E. Schonbrun, P. Steinvurzel, and K. B. Crozier, “Trapping and rotating nanoparticles using a plasmonic nano-tweezer with an integrated heat sink,” *Nature Communications*, no. 469, 2011.

[114] K. Setoura and S. Ito, “Opto-thermophoretic separation and trapping of plasmonic nanoparticles,” *Nanoscale*, vol. 11, 2019.

[115] M. Liu, T. Zentgraf, Y. Liu, G. Bartal, and X. Zhang, “Light-driven nanoscale plasmonic motors,” *Nature Nanotechnology*, vol. 5, no. 8, pp. 570–573, 2010.

[116] M. Righini, A. S. Zelenina, C. Girard, and R. Quidant, “Parallel and selective trapping in a patterned plasmonic landscape,” *Nature Physics*, vol. 3, no. 7, pp. 477–480, 2007.

[117] A. Ashkin, “Acceleration and trapping of particles by radiation pressure,” *Physical Review Letters*, vol. 24, no. 4, p. 156–159, 1970.

[118] J. Guck, S. Schinkinger, B. Lincoln, F. Wottawah, S. Ebert, M. Romeyke, D. Lenz, H. M. Erickson, R. Ananthakrishnan, D. Mitchell, *et al.*, “Optical deformability as an inherent cell marker for testing malignant transformation and metastatic competence,” *Biophysical journal*, vol. 88, no. 5, pp. 3689–3698, 2005.

[119] Y. Zhu, M. You, Y. Shi, H. Huang, Z. Wei, T. He, S. Xiong, Z. Wang, and X. Cheng, “Optofluidic tweezers: Efficient and versatile micro/nano-manipulation tools,” *Micromachines*, vol. 14, no. 7, 2023.

[120] K. D. Leake, B. S. Phillips, T. D. Yuzvinsky, A. R. Hawkins, and H. Schmidt, “Optical particle sorting on an optofluidic chip,” *Optics Express*, vol. 21, no. 26, p. 32605, 2013.

[121] S. Vasantham, A. Kotnala, Y. Promovych, P. Garstecki, and L. Derzsi, “Opto-hydrodynamic tweezers,” *Lab on a Chip*, vol. 24, no. 3, pp. 517–527, 2024.

[122] J. J. Curry and Z. H. Levine, “Continuous-feed optical sorting of aerosol particles,” *Optics express*, vol. 24, no. 13, pp. 14100–14123, 2016.

[123] S. Yu, J. Lu, V. Ginis, S. Kheifets, S. W. D. Lim, M. Qiu, T. Gu, J. Hu, and F. Capasso, “On-chip optical tweezers based on freeform optics,” *Optica*, vol. 8, no. 3, pp. 409–414, 2021.

[124] S. B. Wang and C. T. Chan, “Lateral optical force on chiral particles near a surface,” *Nature Communications*, vol. 5, 2014.

[125] T. Li, X. Xu, B. Fu, S. Wang, B. Li, Z. Wang, and S. Zhu, “Integrating the optical tweezers and spanner onto an individual single-layer metasurface,” *Photonics Research*, vol. 9, no. 6, pp. 1062–1068, 2021.

[126] Q. Fan, D. Wang, P. Huo, Z. Zhang, Y. Liang, and T. Xu, “Autofocusing Airy beams generated by all-dielectric metasurface for visible light,” *Optics Express*, vol. 25, no. 8, p. 9285, 2017.

[127] G. Tkachenko, D. Stellinga, A. Ruskuc, M. Chen, K. Dholakia, and T. F. Krauss, “Optical trapping with planar silicon metalenses,” *Optics Letters*, vol. 43, no. 14, p. 3224, 2018.

[128] J. Xiao, T. Plaskocinski, M. Biabanifard, S. Persheyev, and A. Di Falco, “On-chip optical trapping with high NA metasurfaces,” *ACS Photonics*, 2023.

[129] M. Biabanifard, T. Plaskocinski, J. Xiao, and A. Di Falco, “Zro2 holographic metasurfaces for efficient optical trapping in the visible range,” *Advanced Optical Materials*, vol. n/a, no. n/a, p. 2400248.

[130] M. Plidschun, H. Ren, J. Kim, R. Förster, S. A. Maier, and M. A. Schmidt, "Ultrahigh numerical aperture meta-fibre for flexible optical trapping," *Light: Science and Applications*, vol. 10, no. 1, 2021.

[131] Y. Shi, Q. Song, I. Toftul, T. Zhu, Y. Yu, W. Zhu, D. P. Tsai, Y. Kivshar, and A. Q. Liu, "Optical manipulation with metamaterial structures," *Applied Physics Reviews*, vol. 9, p. 031303, 08 2022.

[132] K. Visscher, S. P. Gross, and S. M. Block, "Construction of multiple-beam optical traps with nanometer-resolution position sensing," *IEEE Journal on Selected Topics in Quantum Electronics*, vol. 2, no. 4, pp. 1066–1076, 1996.

[133] G. Volpe, G. Volpe, and S. Gigan, "Brownian Motion in a Speckle Light Field: Tunable Anomalous Diffusion and Selective Optical Manipulation," *Scientific Reports*, vol. 4, no. 1, p. 3936, 2015.

[134] M. Padgett and R. Di Leonardo, "Holographic optical tweezers and their relevance to lab on chip devices," *Lab on a Chip*, vol. 11, no. 7, pp. 1196–1205, 2011.

[135] D. Stuart and A. Kuhn, "Single-atom trapping and transport in DMD-controlled optical tweezers," *New Journal of Physics*, vol. 20, no. 2, p. 023013, 2018.

[136] J. E. Curtis, B. A. Koss, and D. G. Grier, "Dynamic holographic optical tweezers.," *Opt. Commun.*, vol. 207, p. 169–175, 2002.

[137] A. I. Bunea and J. Glückstad, "Strategies for Optical Trapping in Biological Samples: Aiming at Microrobotic Surgeons," *Laser and Photonics Reviews*, vol. 13, no. 4, pp. 1–17, 2019.

[138] E. Engay, A.-I. Bunea, M. Chouliara, A. Bañas, and J. Glückstad, "Natural convection induced by an optically fabricated and actuated microtool with a thermoplasmonic disk," *Optics Letters*, vol. 43, no. 16, p. 3870, 2018.

[139] A. Bañas, G. Vizsnyiczai, A. Búzás, D. Palima, L. Kelemen, P. Ormos, and J. Glückstad, "Fabrication and optical trapping of handling structures for reconfigurable microsphere magnifiers," in *Complex Light and Optical Forces VII* (J. Glückstad, D. L. Andrews, and E. J. Galvez, eds.), vol. 8637, p. 86370Y, 2013.

[140] A.-I. Bunea, E. Engay, M. Chouliara, A. R. Bañas, and J. Glückstad, "Rational design of light-controlled microrobots," in *Advanced Manufacturing Technologies for Micro- and Nanosystems in Security and Defence* (A. Camposeo, Y. Dzenis, M. Farsari, and L. Persano, eds.), p. 5, SPIE, 2018.

[141] D. B. Phillips, S. H. Simpson, J. A. Grieve, R. Bowman, G. M. Gibson, M. J. Padgett, J. G. Rarity, S. Hanna, M. J. Miles, and D. M. Carberry, “Force sensing with a shaped dielectric micro-tool,” *Epl*, vol. 99, no. 5, 2012.

[142] D. Palima, A. R. Bañas, G. Vizsnyiczai, L. Kelemen, P. Ormos, and J. Glückstad, “Wave-guided optical waveguides,” vol. 20, no. 3, pp. 2004–2014, 2012.

[143] N. K. Metzger, M. Mazilu, L. Kelemen, P. Ormos, and K. Dholakia, “Observation and simulation of an optically driven micromotor,” *Journal of Optics*, vol. 13, no. 4, 2011.

[144] D. B. Phillips, G. Whyte, D. M. Carberry, S. Hanna, M. J. Miles, M. J. Padgett, and S. H. Simpson, “Fashioning microscopic tools,” *Optical Trapping and Optical Micromanipulation X*, vol. 8810, no. September 2013, p. 881029, 2013.

[145] T. Asavei, T. A. Nieminen, V. L. Loke, A. B. Stilgoe, R. Bowman, D. Preece, M. J. Padgett, N. R. Heckenberg, and H. Rubinsztein-Dunlop, “Optically trapped and driven paddle-wheel,” *New Journal of Physics*, vol. 15, 2013.

[146] B. H. Cumpston, S. P. Ananthavel, S. Barlow, D. L. Dyer, J. E. Ehrlich, L. L. Erskine, A. A. Heikal, S. M. Kuebler, I.-Y. S. Lee, D. McCord-Maughon, J. Qin, H. Röckel, M. Rumi, X.-l. Wu, S. R. Marder, and J. W. Perry, “Two-photon polymerization initiators for three-dimensional optical data storage and microfabrication,” *Nature*, vol. 398, no. 6722, pp. 51–54, 1999.

[147] M. Askari, B. C. Kirkpatrick, T. Čižmár, and A. Di Falco, “All-optical manipulation of photonic membranes,” *Optics Express*, vol. 29, no. 10, p. 14260, 2021.

[148] J. Kepler, *De Cometis: Libelli Tres*. Arpergerus, 1619.

[149] J. Ahn, Z. Xu, J. Bang, P. Ju, X. Gao, and T. Li, “Ultrasensitive torque detection with an optically levitated nanorotor,” *Nature Nanotechnology*, vol. 15, no. 2, pp. 89–93, 2020.

[150] E. J. Peterman, F. Gittes, and C. F. Schmidt, “Laser-induced heating in optical traps,” *Biophysical journal*, vol. 84, no. 2, pp. 1308–1316, 2003.

[151] K. Berg-Sørensen and H. Flyvbjerg, “Power spectrum analysis for optical tweezers,” vol. 75, no. 3, p. 594, 2003.

[152] J. A. Lock, “Calculation of the radiation trapping force for laser tweezers by use of generalized Lorenz-Mie theory I Localized model description of an on-axis tightly focused laser beam with spherical aberration,” *Applied Optics*, vol. 43, no. 12, p. 2532, 2004.

[153] J. A. Lock, “Calculation of the radiation trapping force for laser tweezers by use of generalized Lorenz-Mie theory II On-axis trapping force,” *Applied Optics*, vol. 43, no. 12, p. 2545, 2004.

[154] A. Ashkin, “Forces of a single-beam gradient laser trap on a dielectric sphere in the ray optics regime,” *Biophysical Journal*, vol. 61, no. 2, p. 569–582, 1992.

[155] A. Ashkin, J. M. Dziedzic, J. E. Bjorkholm, and S. Chu, “Observation of a single-beam gradient force optical trap for dielectric particles,” *Optics Letters*, vol. 11, p. 288–290, 1986.

[156] D. G. Grier, “A revolution in optical manipulation,” *nature*, vol. 424, no. 6950, pp. 810–816, 2003.

[157] J. Gieseler, J. R. Gomez-Solano, A. Magazzù, I. Pérez Castillo, L. Pérez García, M. Gironella-Torrent, X. Viader-Godoy, F. Ritort, G. Pesce, A. V. Arzola, K. Volke-Sepúlveda, and G. Volpe, “Optical tweezers — from calibration to applications: a tutorial,” *Advances in Optics and Photonics*, vol. 13, no. 1, p. 74, 2021.

[158] G. Pesce, G. Volpe, O. M. Maragó, P. H. Jones, S. Gigan, A. Sasso, and G. Volpe, “Step-by-step guide to the realization of advanced optical tweezers,” *Journal of the Optical Society of America B*, vol. 32, no. 5, p. B84, 2015.

[159] P. Yale, J. M. E. Konin, M. A. Kouacou, and J. T. Zoueu, “New detector sensitivity calibration and the calculation of the interaction force between particles using an optical tweezer,” *Micromachines*, vol. 9, no. 9, pp. 1–11, 2018.

[160] T. Čižmár, M. Mazilu, and K. Dholakia, “In situ wavefront correction and its application to micromanipulation,” *Nature Photonics*, vol. 4, no. 6, pp. 388–394, 2010.

[161] T. Xu, S. Wu, Z. Jiang, X. Wu, and Q. Zhang, “Video microscopy-based accurate optical force measurement by exploring a frequency-changing sinusoidal stimulus,” *Applied Optics*, vol. 59, no. 8, p. 2452, 2020.

[162] S. Helgadottir, A. Argun, and G. Volpe, “Digital video microscopy enhanced by deep learning,” *Optica*, vol. 6, no. 4, p. 506, 2019.

[163] R. Bowman, D. Preece, G. Gibson, and M. Padgett, “Stereoscopic particle tracking for 3D touch, vision and closed-loop control in optical tweezers,” *Journal of Optics*, vol. 13, no. 4, 2011.

[164] I. T. Leite, S. Turtaev, X. Jiang, M. Šiler, A. Cuschieri, P. S. J. Russell, and T. Čižmár, “Three-dimensional holographic optical manipulation through a high-numerical-aperture soft-glass multimode fibre,” *Nature Photonics*, vol. 12, no. 1, pp. 33–39, 2018.

[165] S. Knust, A. Spiering, H. Vieker, A. Beyer, A. Gölzhäuser, K. Tönsing, A. Sischka, and D. Anselmetti, “Video-based and interference-free axial force detection and analysis for optical tweezers,” *Review of Scientific Instruments*, vol. 83, no. 10, p. 103704, 2012.

[166] G. Thalhammer, L. Obmascher, and M. Ritsch-Marte, “Direct measurement of axial optical forces,” *Opt. Express*, vol. 23, pp. 6112–6129, 03 2015.

[167] R. Di Leonardo and S. Bianchi, “Hologram transmission through multi-mode optical fibers,” *Optics Express*, vol. 19, no. 1, p. 247, 2011.

[168] R. W. GERCHBERG and W. O. SAXTON, “PRACTICAL ALGORITHM FOR DETERMINATION OF PHASE FROM IMAGE AND DIFFRACTION PLANE PICTURES,” *OPTIK*, vol. 35, no. 2, pp. 237–and, 1972.

[169] T. Zhao and Y. Chi, “Modified gerchberg–saxton (g-s) algorithm and its application,” *Entropy*, vol. 22, no. 12, 2020.

[170] N. Yu, F. Aieta, P. Genevet, M. A. Kats, Z. Gaburro, and F. Capasso, “A broadband, background-free quarter-wave plate based on plasmonic metasurfaces,” *Nano letters*, vol. 12, no. 12, pp. 6328–6333, 2012.

[171] Y. Liu, X. Ling, X. Yi, X. Zhou, S. Chen, Y. Ke, H. Luo, and S. Wen, “Photonic spin hall effect in dielectric metasurfaces with rotational symmetry breaking,” *Optics letters*, vol. 40, no. 5, pp. 756–759, 2015.

[172] Y. Huang, H. Xu, Y. Lu, and Y. Chen, “All-dielectric metasurface for achieving perfect reflection at visible wavelengths,” *The Journal of Physical Chemistry C*, vol. 122, no. 5, pp. 2990–2996, 2018.

[173] Y. Yao, R. Shankar, M. A. Kats, Y. Song, J. Kong, M. Loncar, and F. Capasso, “Electrically tunable metasurface perfect absorbers for ultrathin mid-infrared optical modulators,” *Nano letters*, vol. 14, no. 11, pp. 6526–6532, 2014.

[174] A. Arbabi and A. Faraon, “Fundamental limits of ultrathin metasurfaces,” *Scientific reports*, vol. 7, no. 1, p. 43722, 2017.

[175] W. Zhu and A.-Q. Liu, *Introduction of Metasurfaces*, pp. 1–15. Singapore: Springer Nature Singapore, 2023.

[176] H. Liang, A. Martins, B.-H. V. Borges, J. Zhou, E. R. Martins, J. Li, and T. F. Krauss, "High performance metalenses: numerical aperture, aberrations, chromaticity, and trade-offs," *Optica*, vol. 6, no. 12, pp. 1461–1470, 2019.

[177] S. Zhang, C. L. Wong, S. Zeng, R. Bi, K. Tai, K. Dholakia, and M. Olivo, "Metasurfaces for biomedical applications: imaging and sensing from a nanophotonics perspective," *Nanophotonics*, vol. 10, no. 1, pp. 259–293, 2021.

[178] H.-H. Hsiao, C. H. Chu, and D. P. Tsai, "Fundamentals and applications of metasurfaces," *Small Methods*, vol. 1, no. 4, p. 1600064, 2017.

[179] N. Meinzer, W. L. Barnes, and I. R. Hooper, "Plasmonic meta-atoms and metasurfaces," *Nature photonics*, vol. 8, no. 12, pp. 889–898, 2014.

[180] S. Sun, K.-Y. Yang, C.-M. Wang, T.-K. Juan, W. T. Chen, C. Y. Liao, Q. He, S. Xiao, W.-T. Kung, G.-Y. Guo, *et al.*, "High-efficiency broadband anomalous reflection by gradient meta-surfaces," *Nano letters*, vol. 12, no. 12, pp. 6223–6229, 2012.

[181] P. Qiao, W. Yang, and C. J. Chang-Hasnain, "Recent advances in high-contrast metastructures, metasurfaces, and photonic crystals," *Adv. Opt. Photon.*, vol. 10, pp. 180–245, 03 2018.

[182] S. M. Kamali, A. Arbabi, E. Arbabi, Y. Horie, and A. Faraon, "Decoupling optical function and geometrical form using conformal flexible dielectric metasurfaces," *Nature communications*, vol. 7, no. 1, p. 11618, 2016.

[183] E. Collett, *Field Guide to Polarization*. Field Guides, SPIE Press, 2005.

[184] M. Berry, "The adiabatic phase and pancharatnam's phase for polarized light," *Journal of Modern Optics*, vol. 34, no. 11, pp. 1401–1407, 1987.

[185] W. Xu, X. Ling, D. Xu, S. Chen, S. Wen, and H. Luo, "Enhanced optical spatial differential operations via strong spin-orbit interactions in an anisotropic epsilon-near-zero slab," *Phys. Rev. A*, vol. 104, p. 053513, 11 2021.

[186] L. Huang, X. Chen, H. Mühlenbernd, G. Li, B. Bai, Q. Tan, G. Jin, T. Zentgraf, and S. Zhang, "Dispersionless phase discontinuities for controlling light propagation," *Nano Letters*, vol. 12, no. 11, pp. 5750–5755, 2012.

[187] C. Liu, Y. Bai, Q. Zhao, Y. Yang, H. Chen, J. Zhou, and L. Qiao, "Fully controllable pancharatnam-berry metasurface array with high conversion efficiency and broad bandwidth," *Scientific reports*, vol. 6, no. 1, p. 34819, 2016.

[188] S. Chen, W. Liu, Z. Li, H. Cheng, and J. Tian, “Metasurface-empowered optical multiplexing and multifunction,” *Advanced Materials*, vol. 32, no. 3, p. 1805912, 2020.

[189] Z. Tao, X. Chen, H. Jiang, C. Zhang, and S. Liu, “Polarization multiplexed all-dielectric metasurfaces for wavefront manipulation in a transmission mode,” *Journal of Optics*, vol. 19, no. 10, p. 105102, 2017.

[190] S. M. Kamali, E. Arbabi, A. Arbabi, Y. Horie, M. Faraji-Dana, and A. Faraon, “Angle-multiplexed metasurfaces: Encoding independent wavefronts in a single metasurface under different illumination angles,” *Phys. Rev. X*, vol. 7, p. 041056, 12 2017.

[191] E. Arbabi, A. Arbabi, S. M. Kamali, Y. Horie, and A. Faraon, “Multiwavelength metasurfaces through spatial multiplexing,” *Scientific reports*, vol. 6, no. 1, pp. 1–8, 2016.

[192] Q.-T. Li, F. Dong, B. Wang, W. Chu, Q. Gong, M. L. Brongersma, and Y. Li, “Free-space optical beam tapping with an all-silica metasurface,” *Acs Photonics*, vol. 4, no. 10, pp. 2544–2549, 2017.

[193] P. Moitra, B. A. Slovick, W. Li, I. I. Kravchencko, D. P. Briggs, S. Krishnamurthy, and J. Valentine, “Large-scale all-dielectric metamaterial perfect reflectors,” *Acs Photonics*, vol. 2, no. 6, pp. 692–698, 2015.

[194] T. Plaskocinski, L. Yan, M. Schubert, M. C. Gather, and A. Di Falco, “Optically manipulated micromirrors for precise excitation of wgm microlasers,” *Advanced Optical Materials*, vol. 12, no. 7, p. 2302024, 2024.

[195] Y. Chen, “Nanofabrication by electron beam lithography and its applications: A review,” *Microelectronic Engineering*, vol. 135, pp. 57–72, 2015.

[196] I. Haller, M. Hatzakis, and R. Srinivasan, “High-resolution positive resists for electron-beam exposure,” *IBM Journal of Research and Development*, vol. 12, no. 3, pp. 251–256, 1968.

[197] Z. Cui, *Nanofabrication: principles, capabilities and limits*. Springer, 2017.

[198] P. Benjamin and C. Weaver, “The adhesion of evaporated metal films on glass,” *Proceedings of the Royal Society of London. Series A, Mathematical and Physical Sciences*, vol. 261, no. 1307, pp. 516–531, 1961.

[199] A. del Campo and C. Greiner, “SU-8: a photoresist for high-aspect-ratio and 3d submicron lithography,” *Journal of Micromechanics and Microengineering*, vol. 17, no. 6, pp. R81–R95, 2007.

[200] P. Abgrall, V. Conedera, H. Camon, A.-M. Gue, and N.-T. Nguyen, "Su-8 as a structural material for labs-on-chips and microelectromechanical systems," *ELECTROPHORESIS*, vol. 28, no. 24, pp. 4539–4551, 2007.

[201] A. K. Nallani, S. W. Park, and J. B. Lee, "Characterization of SU-8 as a resist for electron-beam lithography," in *Smart Sensors, Actuators, and MEMS* (J.-C. Chiao, V. K. Varadan, and C. Cané, eds.), vol. 5116, pp. 414 – 423, International Society for Optics and Photonics, SPIE, 2003.

[202] F. Lima, I. Khazi, U. Mescheder, A. C. Tungal, and U. Muthiah, "Fabrication of 3D microstructures using grayscale lithography," *Advanced Optical Technologies*, vol. 8, no. 3-4, pp. 181–193, 2019.

[203] F. Volmer, I. Seidler, T. Bisswanger, J. S. Tu, L. R. Schreiber, C. Stampfer, and B. Beschoten, "How to solve problems in micro- And nanofabrication caused by the emission of electrons and charged metal atoms during e-beam evaporation," *Journal of Physics D: Applied Physics*, vol. 54, no. 22, pp. 1–13, 2021.

[204] T. Plaskocinski, Y. Arita, G. Bruce, S. Persheyev, K. Dholakia, A. Di Falco, and H. Ohadi, "Laser writing of parabolic micromirrors with a high numerical aperture for optical trapping and rotation," *Applied Physics Letters*, vol. 123, no. 8, 2023.

[205] A. Rohrbach, "Stiffness of optical traps: Quantitative agreement between experiment and electromagnetic theory," *Physical Review Letters*, vol. 95, p. 168102, 10 2005.

[206] J. Bayly, V. Kartha, and W. Stevens, "The absorption spectra of liquid phase h2o, hdo and d2o from 0· 7 μm to 10 μm," *Infrared Physics*, vol. 3, no. 4, pp. 211–222, 1963.

[207] M. Born and E. Wolf, *Image-forming instruments*, p. 261–285. Cambridge University Press, 2019.

[208] J. D. Ellis, *Field guide to displacement measuring interferometry*. SPIE, 2014.

[209] P. Hariharan, *Interferometers*, vol. 184. 2014.

[210] Q. Sun, W. Wabinski, and T. Bruns, "Investigation of primary vibration calibration at high frequencies using the homodyne quadrature sine-approximation method: Problems and solutions," *Measurement Science and Technology*, vol. 17, no. 8, pp. 2197–2205, 2006.

[211] M. Pisani, "A homodyne Michelson interferometer with sub-picometer resolution," *Measurement Science and Technology*, vol. 20, no. 8, 2009.

[212] S. Rerucha, Z. Buchta, M. Sarbort, J. Lazar, and O. Cip, "Detection of interference phase by digital computation of quadrature signals in homodyne laser interferometry," *Sensors (Switzerland)*, vol. 12, no. 10, pp. 14095–14112, 2012.

[213] L. Lipiäinen, K. Kokkonen, and M. Kaivola, "Phase sensitive absolute amplitude detection of surface vibrations using homodyne interferometry without active stabilization," *Journal of Applied Physics*, vol. 108, no. 11, 2010.

[214] M. P. MacDonald, G. C. Spalding, and K. Dholakia, "Microfluidic sorting in an optical lattice," *Nature*, vol. 426, no. 6965, pp. 421–424, 2003.

[215] Y. Lou, D. Wu, and Y. Pang, "Optical trapping and manipulation using optical fibers," *Advanced Fiber Materials*, vol. 1, no. 2, pp. 83–100, 2019.

[216] P. Paiè, T. Zandrini, R. M. Vázquez, R. Osellame, and F. Bragheri, "Particle manipulation by optical forces in microfluidic devices," *Micromachines*, vol. 9, no. 5, pp. 1–21, 2018.

[217] Y. Y. Sun, X. C. Yuan, L. S. Ong, J. Bu, S. W. Zhu, and R. Liu, "Large-scale optical traps on a chip for optical sorting," *Applied Physics Letters*, vol. 90, no. 3, pp. 13–16, 2007.

[218] J. N. Kuo and H. Z. Hu, "Optical trapping of beads and Jurkat cells using micromachined Fresnel zone plate integrated with microfluidic chip," *Japanese Journal of Applied Physics*, vol. 50, no. 10 PART 1, 2011.

[219] E. Schonbrun, C. Rinzler, and K. B. Crozier, "Microfabricated water immersion zone plate optical tweezer," *Applied Physics Letters*, vol. 92, no. 7, pp. 1–4, 2008.

[220] C. H. Sow, A. A. Bettiol, Y. Y. Lee, F. C. Cheong, C. T. Lim, and F. Watt, "Multiple-spot optical tweezers created with microlens arrays fabricated by proton beam writing," *Applied Physics B: Lasers and Optics*, vol. 78, no. 6, pp. 705–709, 2004.

[221] F. Merenda, J. Rohner, and J.-m. Fournier, "Multiple optical tweezers," *Optics Express*, vol. 15, no. 10, pp. 101–111, 2007.

[222] X. Zhao, Y. Sun, J. Bu, S. Zhu, and X. C. Yuan, "Microlens-array-enabled on-chip optical trapping and sorting," *Applied Optics*, vol. 50, no. 3, pp. 318–322, 2011.

[223] F. Merenda, M. Grossenbacher, S. Jeney, L. Forró, and R.-p. Salathé, "Three-dimensional force measurements in optical tweezers formed with high-NA micromirrors.," *Optics letters*, vol. 34, pp. 1063–5, 4 2009.

[224] M. D. Feit and A. M. Rubenchik, "Mechanisms of CO2 laser mitigation of laser damage growth in fused silica," No. 4932, 2003.

[225] T. Ruelle, M. Poggio, and F. Braakman, "Optimized single-shot laser ablation of concave mirror templates on optical fibers," *Applied Optics*, vol. 58, no. 14, p. 3784, 2019.

[226] D. Hunger, C. Deutsch, R. J. Barbour, R. J. Warburton, and J. Reichel, "Laser micro-fabrication of concave, low-roughness features in silica," *AIP Advances*, vol. 2, no. 1, 2012.

[227] K. M. Nowak, H. J. Baker, and D. R. Hall, "Efficient laser polishing of silica micro-optic components," *Appl. Opt.*, vol. 45, pp. 162–171, 01 2006.

[228] D. Hunger, T. Steinmetz, and Y. Colombe, "A fiber fabry-perot cavity with high finesse," *New. J. Phys.*, vol. 12, 2010.

[229] D. Hunger, T. Steinmetz, Y. Colombe, C. Deutsch, T. W. Hänsch, and J. Reichel, "A fiber Fabry-Perot cavity with high finesse," *New Journal of Physics*, vol. 12, 2010.

[230] N. Lindlein, R. Maiwald, H. Konermann, M. Sondermann, U. Peschel, and G. Leuchs, "A new 4π geometry optimized for focusing on an atom with a dipole-like radiation pattern," *Laser Physics*, vol. 17, pp. 927–934, 7 2007.

[231] D. Lu, F. Gámez, and P. Haro-González, "Temperature effects on optical trapping stability," *Micromachines*, vol. 12, no. 8, pp. 1–13, 2021.

[232] Z. Xu, W. Song, and K. B. Crozier, "Optical trapping of nanoparticles using all-silicon nanoantennas," *ACS Photonics*, vol. 5, no. 12, pp. 4993–5001, 2018.

[233] H. D. Wang, W. Bai, B. Zhang, B. W. Li, F. Ji, and M. C. Zhong, "Experimental study of transverse trapping forces of an optothermal trap close to an absorbing reflective film," *Photonics*, vol. 9, no. 7, 2022.

[234] Y. Cao, A. B. Stilgoe, L. Chen, T. A. Nieminen, and H. Rubinsztein-Dunlop, "Equilibrium orientations and positions of non-spherical particles in optical traps," *Optics Express*, vol. 20, no. 12, p. 12987, 2012.

[235] T. A. Nieminen, H. Rubinsztein-Dunlop, and N. R. Heckenberg, “Calculation and optical measurement of laser trapping forces on non-spherical particles,” *Journal of Quantitative Spectroscopy and Radiative Transfer*, vol. 70, no. 4-6, pp. 627–637, 2001.

[236] R. C. Gauthier, M. Ashman, and C. P. Grover, “Experimental confirmation of the optical-trapping properties of cylindrical objects,” *Applied Optics*, vol. 38, no. 22, p. 4861, 1999.

[237] S. H. Simpson and S. Hanna, “Optical trapping of spheroidal particles in Gaussian beams,” *Journal of the Optical Society of America A*, vol. 24, no. 2, p. 430, 2007.

[238] R. Dasgupta, S. K. Mohanty, and P. K. Gupta, “Controlled rotation of biological microscopic objects using optical line tweezers,” *Biotechnology Letters*, vol. 25, no. 19, pp. 1625–1628, 2003.

[239] R. C. Gauthier and A. Frangioudakis, “Theoretical investigation of the optical trapping properties of a micro-optic cubic glass structure,” *Applied Optics*, vol. 39, no. 18, p. 3060, 2000.

[240] Y. Arita, M. Mazilu, and K. Dholakia, “Laser-induced rotation and cooling of a trapped microgyroscope in vacuum,” *Nature Communications*, vol. 4, pp. 1–7, 2013.

[241] G. D. Bruce, P. Rodríguez-Sevilla, and K. Dholakia, “Initiating revolutions for optical manipulation: the origins and applications of rotational dynamics of trapped particles,” *Advances in Physics: X*, vol. 6, no. 1, 2021.

[242] Y. Yang, Y. X. Ren, M. Chen, Y. Arita, and C. Rosales-Guzmán, “Optical trapping with structured light: A review,” *Advanced Photonics*, vol. 3, no. 3, pp. 1–40, 2021.

[243] G. Thalhammer, R. Steiger, and S. Bernet, “Optical macro-tweezers : trapping of highly motile micro-organisms,” *Journal of Optics*, vol. 14, no. 4, 2011.

[244] T. N. Bandi, V. G. Minogin, and S. N. Chormaic, “Atom microtraps based on near-field Fresnel diffraction,” *Physical Review A - Atomic, Molecular, and Optical Physics*, vol. 78, no. 1, 2008.

[245] R. Mu, J. Lu, S. Xu, X. Ji., and J. Yin, “Generation of one- or two-dimensional arrays of hollow optical microtraps for cold atoms, molecules, or microparticles on a chip,” *Journal of the Optical Society of America B*, vol. 26, no. 1, 2009.

[246] M. Sondermann, M. Fischer, and G. Leuchs, "Prospects of trapping atoms with an optical dipole trap in a deep parabolic mirror for light–matter-interaction experiments," *Advanced Quantum Technologies*, vol. 3, no. 11, p. 2000022, 2020.

[247] J. Vovrosh, M. Rashid, D. Hempston, J. Bateman, M. Paternostro, and H. Ulbricht, "Parametric feedback cooling of levitated optomechanics in a parabolic mirror trap," *Journal of the Optical Society of America B*, vol. 34, no. 7, p. 1421, 2017.

[248] T. Chantakit, C. Schlickriede, B. Sain, F. Meyer, T. Weiss, N. Chattham, and T. Zentgraf, "All-dielectric silicon metalens for two-dimensional particle manipulation in optical tweezers," *Photonics Research*, vol. 8, no. 9, pp. 1435–1440, 2020.

[249] H. Markovich, I. I. Shishkin, N. Hendler, and P. Ginzburg, "Optical manipulation along an optical axis with a polarization sensitive meta-lens," *Nano Letters*, vol. 18, no. 8, pp. 5024–5029, 2018.

[250] J. Zhang, H. Liang, Y. Long, Y. Zhou, Q. Sun, Q. Wu, X. Fu, E. R. Martins, T. F. Krauss, J. Li, *et al.*, "Metalenses with polarization-insensitive adaptive nanoantennas," *Laser and Photonics Reviews*, vol. 16, no. 9, p. 2200268, 2022.

[251] R. Galland, G. Grenci, A. Aravind, V. Viasnoff, V. Studer, and J.-B. Sibarita, "3d high-and super-resolution imaging using single-objective spim," *Nature methods*, vol. 12, no. 7, pp. 641–644, 2015.

[252] M. B. Meddens, S. Liu, P. S. Finnegan, T. L. Edwards, C. D. James, and K. A. Lidke, "Single objective light-sheet microscopy for high-speed whole-cell 3d super-resolution," *Biomedical Optics Express*, vol. 7, no. 6, pp. 2219–2236, 2016.

[253] L. Huang, F. Liang, Y. Feng, P. Zhao, and W. Wang, "On-chip integrated optical stretching and electrorotation enabling single-cell biophysical analysis," *Microsystems and Nanoengineering*, vol. 6, no. 1, p. 57, 2020.

[254] H. Shen, S. Cai, Z. Wang, Z. Ge, and W. Yang, "Magnetically driven microrobots: Recent progress and future development," *Materials and Design*, vol. 227, p. 111735, 2023.

[255] J. Li, F. Ji, D. H. Ng, J. Liu, X. Bing, and P. Wang, "Bioinspired pt-free molecularly imprinted hydrogel-based magnetic janus micromotors for temperature-responsive recognition and adsorption of erythromycin in water," *Chemical engineering journal*, vol. 369, pp. 611–620, 2019.

[256] K. Villa and M. Pumera, "Fuel-free light-driven micro/nanomachines: Artificial active matter mimicking nature," *Chemical Society Reviews*, vol. 48, no. 19, pp. 4966–4978, 2019.

[257] N. Martino, S. J. J. Kwok, A. C. Liapis, S. Forward, H. Jang, H.-M. Kim, S. J. Wu, J. Wu, P. H. Dannenberg, S.-J. Jang, Y.-H. Lee, and S. H. Yun, "Wavelength-encoded laser particles for massively multiplexed cell tagging," *Nature Photonics*, vol. 13, pp. 720 – 727, 2019.

[258] A. Polman, B. Min, J. Kalkman, T. J. Kippenberg, and K. J. Vahala, "Ultralow-threshold erbium-implanted toroidal microlaser on silicon," *Applied Physics Letters*, vol. 84, pp. 1037–1039, 2004.

[259] D. S. Weiss, V. Sandoghdar, J. Hare, V. Lefèvre-Seguin, J.-M. Raimond, and S. Haroche, "Splitting of high-q mie modes induced by light backscattering in silica microspheres," *Optics Letters*, vol. 20, pp. 1835–1837, Sep 1995.

[260] M. Li and J. Arlt, "Trapping multiple particles in single optical tweezers," *Optics Communications*, vol. 281, no. 1, pp. 135–140, 2008.

[261] G. M. Cicuta, J. Kotar, A. T. Brown, J.-H. Noh, and P. Cicuta, "Hydrodynamic coupling in polygonal arrays of colloids: Experimental and analytical results," *Physical Review E*, vol. 81, p. 051403, May 2010.

[262] P. Reineck, A. Francis, A. Orth, D. W. M. Lau, R. D. V. Nixon-Luke, I. D. Rastogi, W. A. W. Razali, N. M. Cordina, L. M. Parker, V. K. A. Sreenivasan, *et al.*, "Brightness and photostability of emerging red and near-ir fluorescent nanomaterials for bioimaging," *Advanced Optical Materials*, vol. 4, no. 10, pp. 1549–1557, 2016.

[263] W. W.-W. Hsiao, Y. Y. Hui, P.-C. Tsai, and H.-C. Chang, "Fluorescent nanodiamond: a versatile tool for long-term cell tracking, super-resolution imaging, and nanoscale temperature sensing," *Accounts of chemical research*, vol. 49, no. 3, pp. 400–407, 2016.

[264] M. D. Torelli, N. A. Nunn, and O. A. Shenderova, "A perspective on fluorescent nanodiamond bioimaging," *Small*, vol. 15, no. 48, p. 1902151, 2019.

[265] M. Chipaux, K. J. van der Laan, S. R. Hemelaar, M. Hasani, T. Zheng, and R. Schirhagl, "Nanodiamonds and their applications in cells," *Small*, vol. 14, no. 24, p. 1704263, 2018.

[266] A. Alhaddad, M.-P. Adam, J. Botsoa, G. Dantelle, S. Perruchas, T. Gacoin, C. Mansuy, S. Lavielle, C. Malvy, F. Treussart, *et al.*, "Nanodiamond as a vector for sirna delivery to ewing sarcoma cells," *Small*, vol. 7, no. 21, pp. 3087–3095, 2011.

[267] N. J. Crisona, T. R. Strick, D. Bensimon, V. Croquette, and N. R. Cozzarelli, "Preferential relaxation of positively supercoiled dna by e. coli topoisomerase iv in single-molecule and ensemble measurements," *Genes and development*, vol. 14, no. 22, pp. 2881–2892, 2000.

[268] A. Travers and G. Muskhelishvili, "Dna structure and function," *The FEBS journal*, vol. 282, no. 12, pp. 2279–2295, 2015.

[269] M. D. Frank-Kamenetskii, "Biophysics of the dna molecule," *Physics Reports*, vol. 288, no. 1-6, pp. 13–60, 1997.

[270] G. Altan-Bonnet, A. Libchaber, and O. Krichevsky, "Bubble dynamics in double-stranded dna," *Physical review letters*, vol. 90, no. 13, p. 138101, 2003.

[271] R. M. Fye and C. J. Benham, "Exact method for numerically analyzing a model of local denaturation in superhelically stressed dna," *Physical Review E*, vol. 59, no. 3, p. 3408, 1999.

[272] A. Pyne, R. Thompson, C. Leung, D. Roy, and B. W. Hoogenboom, "Single-molecule reconstruction of oligonucleotide secondary structure by atomic force microscopy," *Small*, vol. 10, no. 16, pp. 3257–3261, 2014.

[273] K. C. Neuman and A. Nagy, "Single-molecule force spectroscopy: optical tweezers, magnetic tweezers and atomic force microscopy," *Nature methods*, vol. 5, no. 6, pp. 491–505, 2008.

[274] J. Lipfert, M. Wiggin, J. W. Kerssemakers, F. Pedaci, and N. H. Dekker, "Freely orbiting magnetic tweezers to directly monitor changes in the twist of nucleic acids," *Nature communications*, vol. 2, no. 1, p. 439, 2011.

[275] A. Sarkar, J.-F. Leger, D. Chatenay, and J. F. Marko, "Structural transitions in dna driven by external force and torque," *Physical Review E*, vol. 63, no. 5, p. 051903, 2001.

[276] V. B Teif and A. G Cherstvy, "Chromatin and epigenetics: current biophysical views," *AIMS Biophysics*, vol. 3, no. 1, pp. 88–98, 2016.

[277] E. Higurashi, H. Ukita, H. Tanaka, and O. Ohguchi, "Optically induced rotation of anisotropic micro-objects fabricated by surface micromachining," *Applied Physics Letters*, vol. 64, no. 17, pp. 2209–2210, 1994.

List of Figures

List of Tables

Acronyms and Initialisms

2D	two-dimensional	3, 9, 36, 89, 114, 125, 161, 168
3D	three-dimensional	6, 8, 10, 15, 23, 24, 27, 40, 49, 58, 61, 77, 78, 163, 164
AFM	atomic force microscopy	124
ALD	atomic layer deposition	103, 167
BPF	band-pass filter	50, 162
BS	beam splitter	50, 70, 162, 163
CCD	charge-coupled device	23, 24, 51, 56, 58, 59, 67, 68, 77, 95, 105, 106, 119
CMOS	complementary metal–oxide–semiconductor	23
CO_2	carbon dioxide	vii, 15, 76, 77, 80, 81, 84, 86, 88, 164
COM	centre-of-mass	60, 61, 64
CW	continuous wave	55, 66, 76, 77, 88
DAQ	data acquisition	71, 72, 164
DI	deionized	45, 46
DNA	deoxyribonucleic acid	2, 10, 16, 65, 123–128, 132, 133, 170
EBE	electron beam evaporator	41, 43, 48
EBL	electron beam lithography	30, 41–47, 92, 99, 103, 128, 159, 161, 167
EC	ethlyl lactate	46
EMM	electromagnetic material	7, 8
FT	Fourier transform	27, 28, 159
FWHM	full width at half maximum	56
GSA	Gerchberg-Saxton Algorithm	18, 27–30, 38, 92, 103, 159

HMS holographic metasurface 3, 4, 6, 8–10, 12, 14–18, 29–39, 42, 49, 52, 53, 65, 73, 90–97, 99–107, 125, 131, 132, 158–161, 165–167

IC integrated circuit 44

IFT inverse Fourier transform 27, 28, 159

IPA isopropyl alcohol 45

ITO indium tin oxide 9, 102, 103

LED light emitting diode 23, 50, 55, 56, 68, 77, 83, 122, 162, 169, 170

LPF long-pass filter 50, 162

MEMS micro-electromechanical systems 9, 44

MM motorized mirror 50, 52, 162

NA numerical aperture . 1, 2, 4, 10, 15, 30, 37, 48, 49, 51, 52, 55, 75, 82–85, 87, 88, 91–96, 103, 105, 107, 119, 132, 161, 164–166, 171

NV nitrogen-vacancy 120, 169

PB Pancharatnam-Berry 32–35, 37, 91, 92, 100, 160

PBS polarizing beam splitter 50, 55, 70, 162, 163

PCA principal component analysis 24

PDMS polydimethylsiloxane 6, 35

PMMA polymethyl methacrylate 42–48, 102, 103, 128, 161, 162

PSD power spectral density 38, 65, 67, 95, 98, 166

QPD quadrant photodiode 24, 67–69, 71, 72, 163, 164

RIE reactive ion etching 41, 46

ROC radius of curvature 84, 171

SEM scanning electron microscope 92, 93, 99, 103, 165–167

SLM spatial light modulator 2, 13, 15, 24–26, 28, 29, 38, 48–52, 55, 58, 59, 66–68, 100, 159, 162

SMFS single molecule force spectroscopy 124, 132

SNR signal-to-noise ratio 2, 111, 115, 119

SPF	short-pass filter	50, 162
UV	ultra violet	5, 101, 158
WGM	whispering gallery mode	3, 15, 55, 56, 109–112, 117–120, 130, 132, 167, 169